

The Experimental and Computational Modelling of the Deformation of Ceramic Composites

by
James Daniel McCafferty

Submitted to the University of Glasgow
for the degree of
Doctor of Philosophy

May 1994

© James D McCafferty

ProQuest Number: 13833798

All rights reserved

INFORMATION TO ALL USERS

The quality of this reproduction is dependent upon the quality of the copy submitted.

In the unlikely event that the author did not send a complete manuscript and there are missing pages, these will be noted. Also, if material had to be removed, a note will indicate the deletion.



ProQuest 13833798

Published by ProQuest LLC (2019). Copyright of the Dissertation is held by the Author.

All rights reserved.

This work is protected against unauthorized copying under Title 17, United States Code
Microform Edition © ProQuest LLC.

ProQuest LLC.
789 East Eisenhower Parkway
P.O. Box 1346
Ann Arbor, MI 48106 – 1346

Therist
9918
Cp71



Abstract

Ceramic composites deform in tensile states of stress by matrix micro-cracking. The deformation of SiC-Al₂O₃ and SiC-SiC composites has been modelled in two ways. Firstly a computational damage mechanics approach has been developed. In the analysis the effect of individual cracks is represented by a damaged continuum. This approach is valid over size scales which encompass multiple matrix micro-cracking, and does not attempt to model the response of a component to a single dominant crack. The damage analysis is compared with an experimental approach based on a polymer analogue of the ceramic composite. The polymer composite system has no modulus mismatch between fibre and matrix and exhibits similar deformation modes to the ceramic systems. In the computational model, micro-cracking and flow in tension and compression were represented by intersecting Mohr-Coulomb, yield, or micro-cracking surfaces. The computational model allows orthogonal arrays of cracks to be formed normal to the directions of maximum principal strain associated with the crack formation surface. This model was refined to incorporate the anisotropic effects of fibres with the introduction of reinforcing elements. Subsequent deformation was described by a combination of an incrementally damaged elastic stress-strain relationship and a classical elastic plastic relationship. The results of numerical modelling were compared with experiments on ceramic composites and the model polymer systems. The unrefined micro-damage constitutive model was also used to analyse a component of an exhaust diffuser unit of a modern air breathing engine and to discuss the micro-mechanics of single dominant crack growth in a ceramic composite.

Acknowledgements

I am grateful to thank my supervisor Professor John. W. Hancock for his help and guidance during this research. I wish also to thank him for his patience and in particular his kindness during the course of this project.

I wish also to thank and dedicate this thesis to my mother and the memory of my late father for their support during the early stages of this PhD.

Thanks are also due without doubt to my sister Maryrose for her surreptitious and at times clandestine influence in the completion of this work.

I wish also to thank my fiance, Sharon, for her love and toleration during the writing up of this thesis.

Thanks are due to Professor B.F.Scott, Head of the Department of Mechanical Engineering for providing the equipment and facilities in the engineering laboratory.

I am also glad to acknowledge the financial support of Rolls Royce Plc and the Science and Engineering Research Council.

Thanks are due to Alan Birkbeck and Alex Torry for their technical assistance in performing experiments and specimen manufacture.

I wish also to thank my friends in the Mechanical and Aero Engineering Departments for their support and advice.

Contents

	Page
Abstract	
Acknowledgments	
Contents	
Figure List	
Chapter 1. Introduction	1
Chapter 2 Mechanical Properties of Composites	3
2.1 Introduction	3
2.2 Elastic Moduli	3
2.3 Anisotropy	5
2.4 Strength	9
2.4.1 Introduction	
2.4.2 Mechanics of Fibre Pullout	
2.4.3 Mechanics of Matrix Micro-Cracking	
2.5 Toughening Mechanisms	24
2.5.1 Transformation Toughening	
2.5.2 Micro-Crack Toughening	
2.5.3 Ductile Reinforcement Toughening	
2.5.4 Fibre Reinforcement Toughening	
Chapter 2 Diagrams	34
Chapter 3 Ceramic Matrix Composite Manufacture	47
3.1 Introduction	47
3.2 Fibre Manufacture	48
3.2.1 Introduction	
3.2.2 Blow Spinning	
3.2.3 Sol-Gel Processes	
3.2.4 Crystallisation Process	
3.2.5 Vapour Phase Manufacture	
3.2.6 Chemical Transformation of a Precursor Fibre	
3.3 Preform Manufacture	52
3.3.1 Introduction	

3.3.2 Woven Preforms	
3.3.3 Braided Preforms	
3.3.4 Knitted Preforms	
3.4 Preform Densification	56
3.4.1 Introduction	
3.4.2 Sol-Gel Manufacture Process	
3.4.3 Chemical Vapour Densification	
3.4.3.1 Introduction	
3.4.3.2 Chemical Vapour Deposition (CVD)	
3.4.3.3 Chemical Vapour Infiltration (CVI)	
3.4.3.4 Forced Chemical Vapour Infiltration (FCVI)	
3.4.4 DIMOX Densification Process	
Chapter 3 Diagrams	63
Chapter 4 Materials	75
4.1 Introduction	75
4.2 Polyester Matrix Properties	78
4.3 Polyester Fibre Tests	78
4.3.1 Method	
4.3.2 Fibre Tow Results	
4.4 Composite Experiments	80
4.4.1 Specimen Manufacture	
4.4.2 Test Method	
4.4.3 Results	
4.5 Ceramic Composite and Fibre Properties	84
4.6 Model Material Verification	85
4.7 Discussion	87
4.7.1 Tensile Behaviour of Impregnated and Unimpregnated Tows	
4.7.2 Compressive and Interlaminar Behaviour	
4.7.3 Tensile Behaviour of the Woven Polyester Composite	
4.7.4 Tensile Behaviour of the Ceramic Composite	
4.7.5 Tensile Behaviour of Knitted Composites	
4.8 Conclusions	99
Chapter 4 Diagrams	100
Chapter 5 Constitutive Model Development	137
5.1 Introduction	137
5.2 Micro-damage Model	138
5.3 Reinforcement	142
5.4 Benchmarking the Constitutive Models	149
5.5 Discussion	151

5.6 Conclusions	153
Chapter 5 Diagrams	154
Chapter 6 Sub-Element Analysis	175
6.1 Introduction	175
6.2 Sub-Element Testing	175
6.2.1 Method	
6.2.2 Results	
6.3 Computational Analysis	179
6.3.1 Method	
6.3.2 Results	
6.4 Discussion	183
6.5 Conclusions	188
Chapter 6 Diagrams	189
Chapter 7 Design and Analysis of an Exhaust Diffuser Unit	237
7.1 Introduction	237
7.2 Material Selection	238
7.3 Thermal Analysis	241
7.4 Thermo-mechanical Analysis	242
7.4.1 Thermo-elastic Analysis	
7.4.2 Damage Mechanics	
7.5 Conclusions	246
Chapter 7 Diagrams	247
Chapter 8 Single Dominant Crack Growth in a Ceramic Composite	258
8.1 Introduction	258
8.2 Background	258
8.3 Numerical Method	260
8.4 Discussion	260
8.5 Conclusions	261
Chapter 8 Diagrams	262
Conclusions	265
References	266

Figure List

- 2.1 Two Phase Material in shear
- 2.2 Elastic modulus of fibre-matrix composite according to Voigt and Ruess
- 2.3 State of stress of a body defined by nine stress components
- 2.4 Composite strength for varying fibre volume fractions
- 2.5 Fibre contained within a matrix under uniform axial tension
- 2.6 Stress distribution along a fibre in tension
- 2.7 Typical probability density function for a single fibre, the fibres in a composite and in a bundle for $N=\infty$.
- 2.8 The Weibull distribution for $\beta = 8$.
- 2.9 The variation of bundle stress against the fibres stress for $\beta = 8$.
- 2.10 The onset of multiple matrix cracking for a brittle matrix ductile fibre composite
- 2.11 Schematic response of a continuous fibre brittle matrix composite with a constant matrix failure strain.
- 2.12 Fibre matrix interface model.
- 2.13 Phase transformation temperatures of zirconia.
- 2.14 Fibre crack bridging.
- 3.1 Basic weaves.
- 3.2 Triaxial weaves.
- 3.3 Four dimensional layout.
- 3.4 Two dimensional braid.

- 3.5 Three dimensional braid
- 3.6 Four dimensional triaxial braid.
- 3.7 Plain knit configurations,
- 3.8 Directionally strengthened knits.
- 3.9 Hydrolysis of an alkoxide.
- 3.10 Formation of SiO_2 from a hydroxide.
- 3.11 Surface Densification of a preform by CVI.
- 3.12 Reaction produced during the deposition of SiC.
- 3.13 The DIMOX process.
- 3.14 Cross section of a SiC-Alumina Composite.
- 3.15 Cross section of a SiC-Alumina Composite with a thermal crack.
- 4.1 Mould dimensions of the monolithic tensile test specimen.
- 4.2 Tensile response of the polyester matrix.
- 4.3 Unimpregnated gripping arrangement of the unimpregnated polyester tows.
- 4.4 Impregnated fibre gripping arrangement.
- 4.5 Stress-strain response of an unimpregnated fibre tow.
- 4.6 Load distribution of failed polyester tows.
- 4.7 Probability distribution of polyester fibres.
- 4.8 Stress-strain response of an impregnated tow.
- 4.9 Tensile test specimen.
- 4.10 Test arrangement for delamination of the polyester composite.

- 4.11 Compression test specimen.
- 4.12 Stress strain response of polymer system cycled to failure.
- 4.13 Density of micro-cracks observed as a function of the applied strain
- 4.14 Secant modulus as a function of strain prior to unloading.
- 4.15 Inelastic strain as a function of the applied strain
- 4.16 Composite modulus variation with angle of alignment.
- 4.17 Photograph of failed off axis specimen.
- 4.18 Transverse response of the polyester 0-90 laminate.
- 4.19 Uniaxial compressive stress-strain response of the polyester composite.
- 4.20 Tensile stress response of the jersey knit architecture.
- 4.21 Tensile stress strain response of the ribbed architecture in the warp configuration.
- 4.22 Tensile stress strain response of the ribbed architecture in the weft configuration.
- 4.23 Mechanical properties of knitted architectures.
- 4.24 Uniaxial tensile response of SiC-Alumina.
- 4.25 Experimental SiC fibre tow response compared to a Weibull distribution.
- 4.26 Uniaxial tensile stress strain curve comparison of SiC-SiC, the polymer system and SiC-Alumina.
- 4.27 Non-dimensionalised comparison of the polymer system, SiC-SiC and the SiC-Alumina.
- 4.28 Stress strain response of an impregnated tow compared to that of an unimpregnated tow.

- 4.29 SEM photograph of a failed 0-90 woven polyester composite.
- 4.30 Comparison of the polyester composite response with the response of the unimpregnated fibre tow.
- 4.31 SEM photograph of a failed impregnated polyester tow.
- 4.32 Unloaded composite with interfacial shear resistance producing an inelastic component of strain.
- 4.33 Average stress contribution from the fibres and the matrix of the polyester compared to the composite stress calculated from theory.
- 4.34 Average stress contribution from the fibres and the matrix of the polyester determined from the response of the unimpregnated polyester fibre tow.
- 4.35 Comparison of the average fibre stress using the calculated method and the unimpregnated experiment of the polyester tows.
- 4.36 Comparison of the average fibre and matrix contribution to the composite stress for the SiC-Alumina.
- 4.37 SEM of failure surface of the polyester knitted composite.
- 5.1 Photograph of Porosity in manufactured SiC-SiC.
- 5.2 Photograph of matrix micro-cracking.
- 5.3 Photograph of SiC-Alumina as manufactured
- 5.4 Tensile micro-crack response of a ceramic composite (Fu et al 1990)
- 5.5 Compressive and tensile Mohr Coulomb yield surfaces.
- 5.6 Stress-strain response of the polymer system cycled to failure.
- 5.7 Spring model system.
- 5.8 Spring A response.

- 5.9 Spring B response.
- 5.10 Model response.
- 5.11 Average stress contribution from fibres and matrix compared to the polymer composite stress.
- 5.12 Comparison of the first composite reinforcing model with hysteresis data.
- 5.13 Response of the two elements combined to form the reinforcing element as a function of strain.
- 5.14 Cyclic comparison of the 2nd composite reinforcing model with hysteresis data.
- 5.15 Response of micro-damaged model.
- 5.16 Cyclic response of the reinforcing model with hysteresis.
- 5.17 Reinforced model response perpendicular to the reinforcing element.
- 5.18 Cyclic comparison of the reinforcing model with the polyester uniaxial data.
- 5.19 Secant modulus against total strain for the computational model and the test data.
- 5.20 Inelastic strain as a function of the applied strain.
- 5.21 Transverse response of the polyester 0-90 laminate.
- 6.1 Bend bar dimensions.
- 6.2 T beam dimensions .
- 6.3 Thickened section dimensions.
- 6.4 Polyester bend bar response.
- 6.5 Ceramic bend bar response.

- 6.6 Polyester T beam response.
- 6.7 Ceramic T beam response.
- 6.8 Polyester thickened section response.
- 6.9 Ceramic thickened section response.
- 6.10 Bend bar polyester damaged at $\frac{v}{v_t} = 3.3$.
- 6.11 Bend bar polyester damaged at $\frac{v}{v_t} = 4.7$.
- 6.12 Bend bar polyester damaged at $\frac{v}{v_t} = 6.1$.
- 6.13 Ceramic bend bar damaged at $\frac{v}{v_t} = 13.1$
- 6.14 Ceramic bend bar damaged at $\frac{v}{v_t} = 25.0$
- 6.15 Damage in the polyester 'T' beam at a displacement ratio $\frac{v}{v_t} = 7.5$
- 6.16 Damage in the polyester 'T' beam at a displacement ratio $\frac{v}{v_t} = 7.5$
- 6.17 Damage in the polyester 'T' beam at a displacement ratio $\frac{v}{v_t} = 12.0$
- 6.18 Damage in the ceramic 'T' beam at a displacement ratio $\frac{v}{v_t} = 14.9$
- 6.19 Damage in the ceramic 'T' beam at a displacement ratio $\frac{v}{v_t} = 24.8$
- 6.20 Damage in the ceramic 'T' beam failure at a displacement ratio of 69.4
- 6.21 Damage in the polyester thickened section at a displacement ratio $\frac{v}{v_t} = 11.2$
- 6.22 Damage in the polyester thickened section at a displacement ratio $\frac{v}{v_t} = 15.0$
- 6.23 Damage in the ceramic thickened section at a displacement ratio $\frac{v}{v_t} = 18.4$

- 6.24 Damage in the ceramic thickened section at a displacement ratio $\frac{v}{v_t} = 73.6$
- 6.25 Bend bar finite element mesh.
- 6.26 T beam finite element mesh.
- 6.27 Thickened section finite element mesh.
- 6.28 Micro-damage polyester response.
- 6.29 Reinforced polyester input.
- 6.30 Ceramic reinforced material input.
- 6.31 Rebar orientations in the bend bar mesh.
- 6.32 Rebar orientations in T beam mesh.
- 6.33 Rebar orientations in thickened section mesh.
- 6.34 The response of the micro-damage, the elastic and the classical elastic plastic model.
- 6.35 Predicted damage of polyester bend bar at $\frac{v}{v_t} = 3.3$.
- 6.36 Predicted damage of polyester bend bar at $\frac{v}{v_t} = 4.7$.
- 6.37 Predicted damage of polyester bend bar at $\frac{v}{v_t} = 6.1$.
- 6.38 Principal stress distribution through the polyester bend bar.
- 6.39 Principal stress distribution of the elastic and the classical elastic plastic constitutive relations.
- 6.40 Strain distribution of polyester isotropic T beam.
- 6.41 Extent of micro-cracking in isotropic polyester T Beam.
- 6.42 Normalised load-displacement response of the polyester bend bar against reinforced bend bar.

- 6.43 Principal strain distribution of the reinforced analysis of the model material at a displacement ratio of 7.5.
- 6.44 Principal strain distribution of the ceramic 'T' beam reinforced model at a displacement ratio of 14.9.
- 6.45 Principal strain distribution in the thickened section with the polymer reinforced model at a displacement ratio of 15.0.
- 6.46 Principal strain distribution in the thickened section with the ceramic reinforced model at a displacement ratio of 18.4.
- 6.47 Uniaxial response of ceramic.
- 6.48 Elements in the polyester 'T' beam which are predicted to micro-crack.
- 7.1 Double skinned actively cooled exhaust diffuser cone.
- 7.2 Proposed single skinned exhaust diffuser cone with no cooling.
- 7.3 Thermal shock index comparison.
- 7.4 Thermal fracture index comparison.
- 7.5 Temperature variation through the cone wall with time.
- 7.6 Axial stress distribution in the cone at $t=1.6$ seconds.
- 7.7 Ideal load/unload response of a SiC/Sic Composite.
- 7.8 Principal stress distribution through the exhaust cone wall at $t=1.6$ sec.
- 7.9 Principal stress distribution through the exhaust cone wall at $t>140$ sec.
- 7.10 Principal stress distribution through the exhaust cone wall at ambient temperature.
- 7.11 Tensile and compressive yield function values through the cone wall at the maximum temperature gradient during start up.

- 8.1 Coordinate system for the crack tip analysis.
- 8.2 Normalised stress distribution ahead of a crack for an incrementally linear elastic and a linear elastic solution.
- 8.3 Normalised stress distribution at 90 degrees to the crack for an incrementally linear elastic and a linear elastic solution.

1. Introduction

Composite materials are not new, but have been extensively used throughout history in a wide variety of applications. The fundamental principle is to combine two or more materials to form a system which exhibits a desired mechanical property. A common example is the mud and straw building blocks used in ancient civilisations. Individually the constituents are brittle and flimsy, but when combined provide a solid and durable structure. This classical method of altering a material's properties is the basis of modern composite design.

The development of modern composites began with fibre reinforced plastics and has been further advanced by the introduction of tough ceramic and metal composites. This rapid expansion was spurred during the 1960's by the development of carbon and boron fibres which have high elastic moduli. This allowed the production of stiff, low weight composites. The low densities and high temperature capabilities of ceramics have made ceramic composites attractive to the aerospace industry.

The attraction to the aerospace industry has two important aspects, the first being the low density. In the aerospace industry the cost of transporting 1kg during one year of operation can be considered lost capital, if this weight is incorporated into the aircraft structure. The second aspect is more complex. In a gas turbine engine the efficiency increases with the operating temperature. If an engine operates at a higher temperature the thrust to weight ratio of the engine also increases. The use of ceramic composites allows the engine to operate at higher temperatures with improved efficiency. A higher thrust is produced which in turn allows the engine to be reduced in size and weight. The reduction in engine size and increased efficiency saves fuel, increases the cargo carrying capacity, and produces a higher profit margin due to the savings in fuel.

The aerospace industry has strict controls which must be satisfied prior to the commissioning of any components. Testing procedures for metallic components are well established, however, there is less experience with the behaviour of ceramic composites. The introduction of ceramic composites to

the harsh and demanding aerospace environment has generated a fundamental need to develop a detailed understanding of how such materials perform in high stress and high temperature environments. If the unique capabilities of these new materials are to be fully exploited it is essential that corresponding techniques for analysis and testing are developed.

The novel work in this thesis is concerned with developing techniques by which complex deformation modes inherent to ceramic composites can be more fully understood. This understanding is then exploited to produce a constitutive model describing the material characteristics. This goal has necessitated mechanical testing followed by comparisons of experiments with computational solutions. Ceramic composites involve high manufacture costs and very slow manufacturing times. For these reasons a polyester model material which has very similar deformation characteristics to the ceramic has been used in the initial development and benchmarking of the computational model.

2 Mechanical Properties of Composites

2.1 Introduction

The engineering application of composites depends on their stiffness, strength, and toughness. Composites allow these properties to be designed for a given application. This chapter is concerned with the design of ceramic composites from a knowledge of the mechanical properties of the constituent phases. The argument is developed for a two phase composite but may be extended to three or more phases.

2.2 Elastic Moduli

Consider the shear modulus (G_C) of a two phase composite material in which the volume fractions of the two phases are V_f and V_m as shown schematically in figure 2.1. The composite modulus may be expressed as a function of the moduli G_f and G_m of the two phases. A complete solution of this problem must satisfy equilibrium and compatibility. If the shear strain (γ) is assumed to be equal throughout the composite, compatibility is satisfied and the composite shear stress is:

$$\tau = \gamma G_c = \gamma V_m G_m + \gamma V_f G_f \quad (2.1)$$

This leads to an expression for the shear modulus of the composite usually attributed to Voigt (Clyne et al 1993).

$$G_{\text{Voigt}} = V_m G_m + V_f G_f \quad (2.2)$$

However in the interface between the matrix and the fibres, equilibrium is not satisfied due to the modulus difference between the two phases. The theorem of minimum potential energy (McClintock et al 1966) states "The strain energy obtained from displacements compatible with any boundary conditions, integrated over the entire volume, will be a minimum for the

exact displacement distribution." Considerations of the potential energy of a two phase material (Clyne et al 1993) where the shear strain is constant throughout leads to the relation.

$$\frac{1}{2}\gamma^2 G_c \leq \frac{1}{2}\gamma^2 V_m G_m + \frac{1}{2}\gamma^2 V_f G_f \quad (2.3)$$

$$G_{\text{CVoigt}} = V_m G_m + V_f G_f \quad G_c \leq G_{\text{CVoigt}} \quad (2.4)$$

This provided Voigt with an upper bound solution for the composite modulus. Reuss applied the minimum potential energy theorem but assumed the shear stress to be constant throughout (Clyne 1993):

$$\frac{1}{2G_c} \tau^2 \leq \frac{1}{2G_m} \tau^2 V_m + \frac{1}{2} V_f \frac{\tau^2}{G_f} \quad (2.5)$$

$$G_{\text{CReuss}} = \left(\frac{V_m}{G_m} + \frac{V_f}{G_f} \right)^{-1} \quad G_c \geq G_{\text{CReuss}} \quad (2.6)$$

This provides a lower bound solution for the composite modulus. Figure 2.2 shows equations 2.4 and 2.6 as upper and lower bounds on the shear modulus. The true composite modulus lies between the two estimates.

$$G_{\text{Voigt}} \geq G_c \geq G_{\text{Reuss}} \quad (2.7)$$

If the Poisson's ratio of the two phases match then the Young's modulus for a composite (E_c) can be bounded in a similar way.

$$V_m E_m + V_f E_f \geq E_c \geq \left(\frac{V_m}{E_m} + \frac{V_f}{E_f} \right)^{-1} \quad (2.8)$$

In general, ceramic fibre-matrix composites are anisotropic. The energetic argument has been developed for isotropic materials but can also be extended to anisotropic materials.

2.3 Anisotropy

Anisotropy is an important feature of composites, which is now reviewed, drawing on reviews by Hull (1981) and Kelly et al (1986). This leads to a brief discussion of laminate theory (Jones 1975).

The state of stress of a body can be described by six independent stress components $\sigma_{11}, \sigma_{22}, \sigma_{33}, \tau_{23}, \tau_{31}, \tau_{12}$ referred to orthogonal cartesian axes as shown in figure 2.3 where $\tau_{ij} = \tau_{ji}$. Here the first suffix defines the normal to the plane on which the stress is acting and the second defines the direction the force is acting. Hooke's Law in tensor notation relates the applied stress (σ_{ij}) to the strain (ϵ_{kl}) by a stiffness C_{ijkl} :

$$\sigma_{ij} = C_{ijkl} \epsilon_{kl} \quad (2.9)$$

Similarly the strain can be made the subject of the equation and related to the stress by a compliance tensor S_{ijkl} .

$$\epsilon_{ij} = S_{ijkl} \sigma_{kl} \quad (2.10)$$

Symmetry of the stiffness matrix requires that $C_{ijkl} = C_{jikl} = C_{ijlk} = C_{jilk}$. In order to use matrix notation it is convenient to compact the notation and replace the suffixes 11, 22, 33, 23, 31, 12 by 1, 2, 3, 4, 5, 6, writing the stiffness matrix as:

$$\begin{bmatrix} \sigma_1 \\ \sigma_2 \\ \sigma_3 \\ \tau_{23} \\ \tau_{31} \\ \tau_{12} \end{bmatrix} = \begin{bmatrix} C_{11} & C_{12} & C_{13} & C_{14} & C_{15} & C_{16} \\ C_{12} & C_{22} & C_{23} & C_{24} & C_{25} & C_{26} \\ C_{13} & C_{23} & C_{33} & C_{34} & C_{35} & C_{36} \\ C_{14} & C_{24} & C_{34} & C_{44} & C_{45} & C_{46} \\ C_{15} & C_{25} & C_{35} & C_{45} & C_{55} & C_{56} \\ C_{16} & C_{26} & C_{36} & C_{46} & C_{56} & C_{66} \end{bmatrix} \begin{bmatrix} \epsilon_1 \\ \epsilon_2 \\ \epsilon_3 \\ \gamma_{23} \\ \gamma_{31} \\ \gamma_{12} \end{bmatrix} \quad (2.11)$$

where $\tau_{23} = \sigma_4$, $\tau_{13} = \sigma_5$, $\tau_{12} = \sigma_6$, $\gamma_{23} = \frac{1}{2} \epsilon_4$, $\gamma_{31} = \frac{1}{2} \epsilon_5$ and $\gamma_{12} = \frac{1}{2} \epsilon_6$

The stiffness matrix may be simplified by arguments based on symmetry. Orthotropic symmetry requires that the material has three orthogonal axis such that a rotation of 180 degrees about any axis leaves the properties

unchanged. For an orthotropic material, referred to its material axes, equation 2.10 can be reduced to:

$$\begin{bmatrix} \sigma_1 \\ \sigma_2 \\ \sigma_3 \\ \tau_{23} \\ \tau_{31} \\ \tau_{12} \end{bmatrix} = \begin{bmatrix} C_{11} & C_{12} & C_{12} & 0 & 0 & 0 \\ C_{12} & C_{22} & C_{12} & 0 & 0 & 0 \\ C_{12} & C_{12} & C_{33} & 0 & 0 & 0 \\ 0 & 0 & 0 & C_{44} & 0 & 0 \\ 0 & 0 & 0 & 0 & C_{55} & 0 \\ 0 & 0 & 0 & 0 & 0 & C_{66} \end{bmatrix} \begin{bmatrix} \epsilon_1 \\ \epsilon_2 \\ \epsilon_3 \\ \gamma_{23} \\ \gamma_{31} \\ \gamma_{12} \end{bmatrix} \quad (2.12)$$

In uniaxial tension in the 1 direction the strain ϵ_1 is related to the stress σ_1 by the Young's modulus E.:

$$\epsilon_1 = \frac{1}{E} \sigma_1 \quad (2.13)$$

The transverse strains ϵ_2, ϵ_3 for the same loading are determined from Young's modulus, Poisson's ratio (ν) and the applied stress σ_1 :

$$\epsilon_2 = \epsilon_3 = \frac{-\nu}{E} \sigma_1 \quad (2.14)$$

From equations 2.13 and 2.14, equation 2.12 may be written for an isotropic material as:

$$\begin{bmatrix} \sigma_1 \\ \sigma_2 \\ \sigma_3 \\ \tau_{23} \\ \tau_{31} \\ \tau_{12} \end{bmatrix} = \begin{bmatrix} E(1-\nu^2) & \nu E(1-\nu^2) & \nu E(1-\nu^2) & 0 & 0 & 0 \\ \nu E(1-\nu^2) & E(1-\nu^2) & \nu E(1-\nu^2) & 0 & 0 & 0 \\ \nu E(1-\nu^2) & \nu E(1-\nu^2) & E(1-\nu^2) & 0 & 0 & 0 \\ 0 & 0 & 0 & G & 0 & 0 \\ 0 & 0 & 0 & 0 & G & 0 \\ 0 & 0 & 0 & 0 & 0 & G \end{bmatrix} \begin{bmatrix} \epsilon_1 \\ \epsilon_2 \\ \epsilon_3 \\ \gamma_{23} \\ \gamma_{31} \\ \gamma_{12} \end{bmatrix} \quad (2.15)$$

These equations show that the stresses and strains are a function of modulus and Poisson's ratio. The shear modulus (G) is also a function of E and ν .

$$G = \frac{E}{2(1+\nu)} \quad (2.16)$$

Consider now a state of plane stress where σ_3 , τ_4 and τ_5 are zero. For an orthotropic material in plane stress, equation (2.12) can be written as:

$$\begin{bmatrix} \sigma_1 \\ \sigma_2 \\ \tau_{12} \end{bmatrix} = \begin{bmatrix} C_{11} & C_{12} & 0 \\ C_{12} & C_{22} & 0 \\ 0 & 0 & C_{66} \end{bmatrix} \begin{bmatrix} \epsilon_1 \\ \epsilon_1 \\ \gamma_{12} \end{bmatrix} \quad (2.17)$$

This theory may be applied to a laminate in plane stress. The relation between the principal stresses and the strains for a laminate is often written in terms of a reduced stiffness matrix Q:

$$\begin{bmatrix} \sigma_1 \\ \sigma_2 \\ \tau_{12} \end{bmatrix} = \begin{bmatrix} Q_{11} & Q_{12} & 0 \\ Q_{12} & Q_{22} & 0 \\ 0 & 0 & Q_{66} \end{bmatrix} \begin{bmatrix} \epsilon_1 \\ \epsilon_1 \\ \gamma_{12} \end{bmatrix} \quad (2.18)$$

The reduced stiffness matrix Q can also be written as a function of Young's modulus and the Poisson's ratio. The fundamental difference between the stiffnesses Q_{11} and Q_{22} arise from dissimilar moduli E_1 and E_2 in the 1 and 2 directions. The difference in transverse modulus affects the Poisson's ratio term such that it depends on the orientation of the applied tensile stress. Poisson's ratio is defined by the ratio of the transverse strain to the strain in the direction of loading ($\nu_{12} = \frac{-\epsilon_2}{\epsilon_1}$). Similarly $\nu_{21} = \frac{-\epsilon_1}{\epsilon_2}$. It follows that for an orthotropic material the stress-strain relation in plane stress are.

$$\begin{bmatrix} \sigma_1 \\ \sigma_2 \\ \tau_{12} \end{bmatrix} = \begin{bmatrix} \frac{E_1}{(1 - \nu_{12}\nu_{21})} & \frac{\nu_{21}E_1}{(1 - \nu_{12}\nu_{21})} & 0 \\ \frac{\nu_{21}E_1}{(1 - \nu_{12}\nu_{21})} & \frac{E_2}{(1 - \nu_{12}\nu_{21})} & 0 \\ 0 & 0 & G_{12} \end{bmatrix} \begin{bmatrix} \epsilon_1 \\ \epsilon_1 \\ \gamma_{12} \end{bmatrix} \quad (2.19)$$

Equation (2.19) applies to loading in a principal direction. If a specimen is tested off the principal axes then the resultant stress must include shear terms. The stiffness matrix is then expanded and takes the form:

$$\begin{bmatrix} \sigma_x \\ \sigma_y \\ \tau_{xy} \end{bmatrix} = \begin{bmatrix} \bar{Q}_{11} & \bar{Q}_{12} & \bar{Q}_{16} \\ \bar{Q}_{12} & \bar{Q}_{22} & \bar{Q}_{26} \\ \bar{Q}_{16} & \bar{Q}_{26} & \bar{Q}_{66} \end{bmatrix} \begin{bmatrix} \epsilon_x \\ \epsilon_y \\ \gamma_{xy} \end{bmatrix} \quad (2.20)$$

This is the transformed reduced stiffness matrix. The components of this matrix (\bar{Q}) include terms to describe the angle of offset coupled with principal stiffness components Q .

Consider now a cross-ply laminate manufactured from two unidirectional laminate layers orientated perpendicular to each other. The stress-strain relationship will have form:

$$\begin{bmatrix} \sigma_{c1} \\ \sigma_{c2} \\ \tau_{c12} \end{bmatrix} = \begin{bmatrix} Q_{c11} & Q_{c12} & Q_{c16} \\ Q_{c21} & Q_{c22} & Q_{c26} \\ Q_{c16} & Q_{c26} & Q_{c66} \end{bmatrix} \begin{bmatrix} \epsilon_{c1} \\ \epsilon_{c2} \\ \gamma_{c12} \end{bmatrix} \quad (2.21)$$

Here the suffix (c) relates to the cross-ply orientation. For an orthotropic laminate in plane stress the shear terms are zero (i.e. $Q_{c26} = Q_{c16} = 0$) in the direction of the principal axes. The stiffness matrix can then be determined by summing the stiffness of the two layers weighted by the volume fraction of the laminates (V_a, V_b).

$$\begin{aligned} Q_{c11} &= V_a Q_{11} + V_b Q_{22} \\ Q_{c12} &= V_a Q_{12} + V_b Q_{12} = Q_{12} \\ Q_{c22} &= V_a Q_{22} + V_b Q_{11} \\ Q_{c66} &= V_a Q_{66} + V_b Q_{66} = Q_{66} \end{aligned} \quad (2.22)$$

The off axis stress-strain relationship can also be developed using the same theory as in equation (2.20) and (2.21). From these it is possible to determine the modulus of laminates.

Simple laminate theory is limited since no account is taken of the interlaminar stress and only in plane stresses are considered (Jones 1975). As a result classical laminate theory is incapable of predicting the high interlaminar shear stresses that in many cases actually cause failure. This is demonstrated more fully at a free edge of a laminate where the interlaminar shearing stresses are very high and may become singular (Jones 1975).

2.4 Composite Strength

2.4.1 Introduction

The prediction of the strength of a fibrous composite loaded parallel to the fibres, requires a knowledge of the failure stresses and strains of individual fibres. Initially it is appropriate to assume that both the fibres and the matrix are linear elastic and perfectly reliable. In this scenario there are two possible modes of deformation which are determined by the relative failure strains of the constituents. In the case where the fibre failure strain is lower than that of the matrix then the fibres will fail. If however the fibre failure strain is greater than the matrix then the matrix fails after which the fibre-matrix interface debonds with the fibre sliding inside the matrix. This section describes the essential strength characteristics of these two deformation mechanisms drawing on reviews by Kelly (1966) and Aveston et al (1971).

2.4.2 Mechanics of Fibre Pullout

Kelly (1966) considered a composite of a ductile matrix and brittle fibres with ultimate tensile strengths σ_{mu} and σ_{fu} . In any fibrous composite there is a limiting fibre volume fraction (V_{min}) which must be exceeded before the fibres contribute to the composite strength such that:

$$\sigma_c = \sigma_{mu}(1 - V_f) \quad V_f < V_{min} \quad (2.23)$$

Below V_{min} the matrix dominates the response, and the strength of the composite is a function of the ultimate tensile strength of the matrix. Above this fibre volume fraction the strength of the composite is largely determined by the fibres, and composite failure occurs at the fibre failure strain. The contribution of the matrix to the composite stress is therefore limited by the stress in the matrix at the fibre failure strain (σ'_m).

$$\sigma_c = \sigma_{fu} V_f + \sigma'_m (1 - V_f) \quad V_f > V_{min} \quad (2.24)$$

Figure 2.4 shows the composite strength for varying fibre volume fractions of ductile and brittle continuous fibres. There is a minimum fibre volume fraction V_{crit} , that must be exceeded in order to provide a composite with an ultimate breaking strength greater than that of the matrix alone.

The effect of discontinuous fibres in a matrix was considered by Kelly (1966). Figure 2.5 shows a fibre of length L contained within a matrix under uniform axial tension. Equilibrium of a small element of fibre requires:

$$d\sigma_f \pi r^2 + 2\pi r \tau dx = 0 \quad (2.25)$$

Here r is the fibre radius, $d\sigma_f$ is the change in fibre stress over the element and dx is the length of the fibre over which a constant interfacial shear stress (τ) acts. Integrating equation (2.25) with $\sigma_f = 0$ at $x = 0$ gives:

$$\sigma_f = \frac{-2\tau x}{r} \quad (2.26)$$

At $x = \frac{L}{2}$ the stress in the fibre is a maximum. This produces a stress distribution along the fibre similar to that shown in figure 2.6 for increasing fibre lengths. Substituting the fibre failure stress (σ_{fu}) into equation 2.26 gives the critical fibre length (L_c) or length to raise the stress in the fibre to its failure stress.

$$L_c = \frac{-\sigma_{fu} r}{\tau} \quad (2.27)$$

The critical fibre length (L_c) determines whether the fibres will pullout or break. If the fibre length is less than the critical fibre length then all the fibres pull out. If however the fibre length is greater than the critical fibre length then the fraction of fibres that pullout is given by $\frac{L_c}{L}$. This applies only when the fibres all have the same failure stress and are very reliable.

The average stress ($\bar{\sigma}_f$) in the fibre is given by:

$$\bar{\sigma}_f = \sigma_{fu} \left(1 - \frac{L_c}{2L}\right) \quad (2.28)$$

The average stress $\bar{\sigma}_f$ can be incorporated into equation 2.23 in place of the fibre stress σ_f to give an expression for the strength of a composite with discontinuous aligned fibres.

$$\sigma_c = \sigma_{fu} \left(1 - \frac{L_c}{2L}\right) V_f + \sigma'_m (1 - V_f) \quad V_f > V_{\min} \quad (2.29)$$

The fibres used in ceramic composites are generally brittle and exhibit large strength variations. Due to the inherently variable strength of fibres a statistical approach must be taken in determining the mode of failure (Rosen 1970). Consider a composite containing high modulus fibres with large variations in strength (ie low reliability). The strength of a composite depends on the strength and reliability of the fibres. The probability that an individual fibre contained within a population of fibres will break can be represented by a probability density function $p\left(\frac{\sigma}{\sigma_o}\right)$ as shown in figure 2.7. Here σ is the fibre stress while σ_o is a normalising curve fitting constant. This expresses the variable strengths of individual fibres by the probability $p\left(\frac{\sigma}{\sigma_o}\right) d\sigma$ that a fraction of the fibres will break between a given stress σ and $\sigma + d\sigma$. The fraction of fibres breaking below a stress $\left(\frac{\sigma}{\sigma_o}\right)$ is given by a cumulative probability density function $P\left(\frac{\sigma}{\sigma_o}\right)$.

$$P\left(\frac{\sigma}{\sigma_o}\right) = \int_0^{\sigma} p\left(\frac{\sigma}{\sigma_o}\right) d\sigma \quad (2.30)$$

Curve fitting functions can be used to describe $P\left(\frac{\sigma}{\sigma_o}\right)$ as long as the following boundary conditions are satisfied.

$$P\left(\frac{\sigma}{\sigma_o}\right)_{\sigma=\infty} = 1 \quad \text{and}$$

$$P\left(\frac{\sigma}{\sigma_o}\right)_{\sigma=0} = 0 \quad (2.31)$$

The fraction of broken fibres $P\left(\frac{\sigma}{\sigma_0}\right)$, as shown in figure 2.8 can be expressed by a two parameter Weibull distribution as:

$$P\left(\frac{\sigma}{\sigma_0}\right) = 1 - \exp\left(-\left(\frac{\sigma}{\sigma_0}\right)^\beta\right) \quad (2.32)$$

Here σ_0 and β are curve fitting constants. Differentiating allows the probability density function $p\left(\frac{\sigma}{\sigma_0}\right)$ to be expressed as:

$$p\left(\frac{\sigma}{\sigma_0}\right) = \beta\left(\frac{\sigma}{\sigma_0}\right)^{\beta-1} \exp\left(-\left(\frac{\sigma}{\sigma_0}\right)^\beta\right) \quad (2.33)$$

Consider a bundle of fibres not in contact with each other and subject to the same stress. At a fibre stress $\left(\frac{\sigma}{\sigma_0}\right)$ the fraction of broken fibres is $P\left(\frac{\sigma}{\sigma_0}\right)$ and the fibre stress borne by the bundle $\left(\frac{\sigma_b}{\sigma_0}\right)$, is given by:

$$\left(\frac{\sigma_b}{\sigma_0}\right) = \left(\frac{\sigma}{\sigma_0}\right)\left(1 - P\left(\frac{\sigma}{\sigma_0}\right)\right) = \left(\frac{\sigma}{\sigma_0}\right) \exp\left(-\left(\frac{\sigma}{\sigma_0}\right)^\beta\right) \quad (2.34)$$

This expression indicates that as the applied stress $\left(\frac{\sigma_b}{\sigma_0}\right)$ increases, fibres break, and the stress in the remaining fibres increases further. At a point dependent on the fibre reliability and the normalising fibre strength (σ_0) a critical fraction of fibres remain that support the applied stress. Increasing the individual fibre stress $\left(\frac{\sigma}{\sigma_0}\right)$ results in a reduction in the stress borne by the bundle as shown in figure 2.9 due to the reduction in the number of remaining fibres. The maximum stress borne by the bundle $\left(\frac{\sigma_b}{\sigma_0}\right)_{\max}$ is determined by differentiating and equating equation (2.32) to zero, giving the expression.

$$\left(\frac{\sigma_b}{\sigma_0}\right)_{\max} = \left(\beta\right)^{\left(\frac{-1}{\beta}\right)} \exp\left(\frac{-1}{\beta}\right) \quad (2.35)$$

at a fibre stress of:

$$\frac{\sigma}{\sigma_0} = (\beta)^{-\frac{1}{\beta}} \quad (2.36)$$

From the probability density function the fibre stress at which the probability of fibre failure is maximum can be determined by putting the differential of equation (2.33) to zero. This gives the modal failure stress for an individual fibre as:

$$\left(\frac{\sigma}{\sigma_0}\right) = \left(\frac{(\beta-1)}{\beta}\right)^{\frac{1}{\beta}} \quad (2.37)$$

Comparing the mean strength of an individual fibre to the mean bundle strength it can be seen from equations (2.36) and (2.37) that the modal fibre strength is significantly stronger than the bundle strength. This analysis applies when the bundle contained a very high number of fibres (N). The central limit theorem (Daniels 1945) shows that the distribution of bundle strength is Gaussian with a standard deviation proportional to \sqrt{N} . This predicts a standard deviation approaching zero and complete reliability for a bundle where $N = \infty$. This produces a highly reliable configuration with an infinitely narrow probability density curve, as shown in figure 2.7, compared to the individual fibre strength distribution curve. The disadvantage of a low average bundle strength is compensated by an increase in reliability with the number of fibres.

The effect of embedding the fibres in a matrix is now considered. The principal difference between a fibre composite and a fibre bundle is that in a bundle when a fibre breaks it can no longer sustain a load. When this happens in a composite the load can be transferred to the matrix and back to the fibre on the other side of the break. This can only occur in fibres with a length $L \geq L_c$ where L_c is the critical transfer length. The composite can then be visualised as a chain of fibre bundles of length L_c . It becomes apparent that the length of the fibres in the composite will then affect the overall strength (Rosen 1970)

A single fibre (of length $L > L_c$) may break in more than one place simultaneously. The probability of failure not occurring in a fibre is given by:

$$(1 - P(\sigma)) = \exp - \left(\frac{\sigma}{\sigma_o} \right)^\beta \quad (2.38)$$

The probability of a fibre of length $L > L_c$ not failing is given by the product of the probability of the individual component lengths L_c not failing:

$$(1 - P(\sigma))^{\frac{L}{L_c}} = \exp - \frac{L}{L_c} \left(\frac{\sigma}{\sigma_o} \right)^\beta \quad (2.39)$$

By following the argument leading to equation (2.35) the contribution of the fibres $\left(\frac{\sigma_{fu}}{\sigma_o} \right)_{\max}$ to the composite strength is given by:

$$\left(\frac{\sigma_{fu}}{\sigma_o} \right)_{\max} = \left(\frac{L\beta}{L_c} \right)^{\frac{1}{\beta}} \exp - \left(\frac{1}{\beta} \right) \quad (2.40)$$

Figure 2.7 compares the strength distribution for a single fibre with a composite and a bundle. In this diagram the fibre lengths are $L \gg L_c$ with both the bundle and the composite containing an infinite number of fibres. From this diagram it can be seen that the composite has a greater average strength than both the bundle and the single fibre with an added increase in reliability for large numbers of fibres.

Substituting σ_{fu} for $\bar{\sigma}_f$ in equation 2.23 gives the strength of a composite in terms of matrix strength (σ'_m), the fibre reliability (β), nominal strength (σ_o), the fibre volume fraction (V_f) and the length ratio of the fibres $\left(\frac{L}{L_c} \right)$.

$$\sigma_c = \left(\left(\frac{L}{L_c} \right) \beta \right)^{\frac{1}{\beta}} \exp \left(\frac{-1}{\beta} \right) \sigma_o V_f + \sigma'_m (1 - V_f) \quad (2.41)$$

2.4.3 Mechanics of Matrix Micro-Cracking

The deformation and final failure mode of composites may involve either single, or multiple cracking. Initially one of the phases will start to fail with the formation of a single crack. This transfers the load to the remaining phase. If the load cannot be supported by this phase then the composite will fail and the crack will propagate leading to a single failure. If however the transferred load is supported by the remaining phase then multiple cracking can occur before final failure of the composite.

Aveston et al (1971) considered two specific cases: brittle fibres in a ductile matrix and a brittle matrix with ductile fibres. For brittle fibres in a ductile matrix the failure strain of the fibres, ϵ_{fu} , is significantly lower than that of the matrix, ϵ_{mu} . In the case of a composite in which the fibre failure strain is higher than matrix failure strain, cracking will initiate in the matrix. When the matrix cracks, the fibres bridging the crack support the load and lead to multiple fracture. If the fibres fail with the onset of the first micro-crack then single fracture is observed. In this case the load borne by the fibres at failure cannot be supported by the matrix, resulting in single fracture.

$$\sigma_{fu} V_f > (1 - V_f)(\sigma_{mu} - \sigma'_m) \quad (\epsilon_{fu} < \epsilon_{mu}) \quad (2.42)$$

Here σ'_m is the stress in the matrix at a strain equal to the failure strain of the fibre and V_f is the fibre volume fraction. Multiple fibre fracture will occur when:

$$\sigma_{fu} V_f < (1 - V_f)(\sigma_{mu} - \sigma'_m) \quad (\epsilon_{fu} < \epsilon_{mu}) \quad (2.43)$$

In the case of a brittle matrix and ductile fibres, the fibre failure strain is higher than that of the matrix. In this case a similar relation describes the onset of multiple fracture of the matrix:

$$\sigma_{fu} V_f > (1 - V_f) \sigma_{mu} + \sigma'_f V_f \quad (2.44)$$

This is represented graphically in figure 2.10 where σ'_f is the fibre stress at a strain equal to the failure strain of the matrix. In this figure a critical value of the fibre volume fraction V_f dictates the occurrence of single or multiple fracture.

Figure 2.11 shows the stress-strain response of a unidirectional composite where multiple matrix micro-cracking is stabilised by ductile fibres. In this diagram the stress strain curve is broken down into three regions. The first zone is linear elastic. The stress in the fibres and matrix is $\epsilon_c E_f$ and $\epsilon_c E_m$ respectively. Here ϵ_c is the composite strain while E_f and E_m denote the elastic moduli of the fibre and the matrix. In the second region micro-cracking has occurred in the matrix which breaks into blocks of average length $2L$ producing stress gradients along the fibre and the matrix. Figure 2.12 shows the stresses acting on the matrix and the fibre as well as the notation and the coordinate system which will be used. At the crack ($\eta = L$) the matrix stress in the direction of loading must be zero since this is a free surface. During micro-cracking a mode II or shear crack in the fibre-matrix interface causes debonding over a length L_s on either side of the matrix crack. Following debonding, sliding occurs between the fibre and the matrix over the length L_s along which a constant frictional shear stress (τ) is assumed to act. From figure 2.12, the matrix stress increases linearly from zero over the debonded length L_s . The relation between the stress in the fibre and the debond length L_s is given in equation 2.26 where L_s replaces the fibre length x . The resulting fibre stress is caused by the fibre sliding in the matrix and transferring a stress to the matrix through a constant interfacial shear resistance. The remainder of the matrix is fully bonded to the fibre and is assumed to have the same strain ($\epsilon_f = \epsilon_m = \epsilon_c$).

Equations 2.25 and 2.26 show the stress distribution along a fibre of length (x) as a result of a constant interface shear stress. For a constant shear stress (τ) acting over a length (x) on the fibre radius (r), the force in the fibre is $2\pi r \tau x$. In figure 2.12 if the shear stress (τ) is constant along the debonded length L_s , then from equilibrium the force in a fibre of radius R and cross sectional area A_f is given by:

$$\sigma_{f(\eta)} A_f = \sigma_{f(\eta=0)} A_f + 2\tau \pi R \{\eta - (L - L_s)\} \quad (2.45)$$

The fibre stress $\sigma_{f(\eta)}$ is a function of the distance η from the mid point of a matrix block of half length L where sliding is occurring over a length L_s . The bracketed term $\{\eta - (L - L_s)\}$ adopts the Macauley notation in which a negative argument is taken to be zero. This gives the stress in the fibre as:

$$\sigma_{f(\eta)} = \sigma_{f(\eta=0)} + \frac{2\tau}{R} \{\eta - (L - L_s)\} \quad (2.46)$$

At the crack ($\eta = L$) the stress in the composite is borne totally by the fibre and:

$$\sigma_{f(\eta=L)} = \frac{\sigma_c}{V_f} = \sigma_{f(\eta=0)} + \frac{2\tau}{R} \{L_s\} \quad (2.47)$$

It follows that the stress in the fibre $\sigma_{f(\eta=0)}$ is given by

$$\sigma_{f(\eta=0)} = \frac{\sigma_c}{V_f} - \frac{2\tau}{R} \{L_s\} \quad (2.48)$$

The stress along the fibre may now be written:

$$\sigma_{f(\eta)} = \frac{\sigma_c}{V_f} - \frac{2\tau}{R} \{L_s\} + \frac{2\tau}{R} \{\eta - (L - L_s)\} \quad (2.49)$$

The average stress in the fibre ($\bar{\sigma}_f$) is determined by integrating over the block length.

$$\bar{\sigma}_f = \frac{1}{L} \int_0^L \sigma_{f(\eta)} d\eta \quad (2.50)$$

$$\bar{\sigma}_f = \frac{\sigma_c}{V_f} - \frac{2\tau}{R} \{L_s\} + \frac{\tau}{R} \frac{\{L_s\}^2}{L} \quad (2.51)$$

The matrix is now considered. From figure 2.12 the axial force in an annulus of matrix of area A_m and length L by equilibrium is:

$$\sigma_{m(\eta)} A_m = \sigma_{m(\eta=0)} A_m - 2\tau \pi R \{\eta - (L - L_s)\} \quad (2.52)$$

Here the matrix stress is $\sigma_{m(\eta)}$ and the radius over which the shear stress (τ) acts is R . The bracketed term $\{\eta - (L - L_s)\}$ again adopts Macauley notation. This gives the stress in the matrix as:

$$\sigma_{m(\eta)} = \sigma_{m(\eta=0)} - \frac{2\tau}{R} \frac{V_f}{V_m} \{\eta - (L - L_s)\} \quad (2.53)$$

At the crack, the stress in the matrix $\sigma_{m(\eta=L)} = 0$. Hence from equation (2.53) the matrix stress $\sigma_{m(\eta=0)}$ is:

$$\sigma_{m(\eta=0)} = \frac{2\tau}{R} \frac{V_f}{V_m} \{L_s\} \quad (2.54)$$

Thus far it has been assumed that the matrix is perfectly reliable with a constant matrix micro-cracking stress (σ_{mu}). In these circumstances the stress in the matrix cannot exceed σ_{mu} hence:

$$\sigma_{mu} = \frac{2\tau}{R} \frac{V_f}{V_m} \{L_s\} \quad (2.55)$$

It follows that for a composite with a deterministic matrix micro-cracking stress (σ_{mu}) and a known interfacial shear stress then the debond length (L_s) is fixed. The stress in the matrix as a function of η will then be:

$$\sigma_{m(\eta)} = \sigma_{mu} - \frac{2\tau}{R} \frac{V_f}{V_m} \{\eta - (L - L_s)\} \quad (2.56)$$

The average stress in the matrix ($\bar{\sigma}_m$) is given by the integral.

$$\bar{\sigma}_m = \frac{1}{L} \int_0^L \sigma_{m(\eta)} d\eta \quad (2.57)$$

$$\bar{\sigma}_m = \sigma_{mu} - \frac{\tau}{R} \frac{V_f}{V_m} \frac{(L_s)^2}{L} \quad (2.58)$$

The stress in the composite ($\sigma_{c(\eta)}$) is obtained from the rule of mixtures.

$$\sigma_{\alpha(\eta)} = V_m \sigma_{m(\eta)} + V_f \sigma_{f(\eta)} \quad (2.59)$$

The composite stress at any section η is the sum of the fibre and matrix stresses.

$$\sigma_{\alpha(\eta)} = V_m \left[\sigma_{mu} - \frac{2\tau}{R} \frac{V_f}{V_m} (\eta - (L - L_s)) \right] + V_f \left[\frac{\sigma_c}{V_f} - \frac{2\tau}{R} (L_s) + \frac{2\tau}{R} (\eta - (L - L_s)) \right] \quad (2.60)$$

$$\sigma_{\alpha(\eta)} = V_m \sigma_{mu} + \sigma_c - \frac{2\tau V_f}{R} (L_s) \quad (2.61)$$

$$\sigma_{\alpha(\eta)} = \sigma_c + V_m \left[\sigma_{mu} - \frac{2\tau}{R} \frac{V_f}{V_m} (L_s) \right] \quad (2.62)$$

From equation 2.55 $\left[\sigma_{mu} - \frac{2\tau}{R} \frac{V_f}{V_m} (L_s) \right]$ is zero hence.

$$\sigma_{\alpha(\eta)} = \sigma_c \quad (2.63)$$

This demonstrates the consistency of the argument which results in equations 2.49 and 2.56 where their addition weighted by the volume fractions, is equal to the composite stress on every section.

The average stress in composite ($\bar{\sigma}_c$) is the sum of the average stresses in the fibres ($\bar{\sigma}_f$) and the matrix ($\bar{\sigma}_m$).

$$\bar{\sigma}_c = V_m \bar{\sigma}_m + V_f \bar{\sigma}_f \quad (2.64)$$

$$\bar{\sigma}_c = V_m \left[\sigma_{mu} - \frac{\tau}{R} \frac{V_f}{V_m} \frac{(L_s)^2}{L} \right] + V_f \left[\frac{\sigma_c}{V_f} - \frac{2\tau}{R} (L_s) + \frac{\tau}{R} \frac{(L_s)^2}{L} \right] \quad (2.65)$$

$$\bar{\sigma}_c = V_m \sigma_{mu} + \sigma_c - V_f \frac{2\tau}{R} (L_s) \quad (2.66)$$

$$\bar{\sigma}_c = \sigma_c + V_m \left[\sigma_{mc} - \frac{2\tau}{R} \frac{V_f}{V_m} (L_s) \right] \quad (2.67)$$

From equation 2.43 $\left[\sigma_{mu} - \frac{2\tau}{R} \frac{V_f}{V_m} (L_s) \right]$ is zero hence.

$$\bar{\sigma}_c = \sigma_c \quad (2.68)$$

This again demonstrates the consistency of the argument leading to average stresses in the fibre and matrix $\bar{\sigma}_{f,m}$. This now allows the calculation of the average contribution to the composite stress of the fibre and the matrix in the micro-cracking region of the response curve.

In the third region of figure 2.11, micro-cracking has saturated and further micro-cracking can not occur in the matrix. This happens when the block lengths are not long enough to raise the stress in the matrix to the matrix micro-cracking stress. Subsequently the matrix can only be broken into blocks of length greater than or equal to L_s , since this is the minimum length required to raise the stress in the matrix to micro-cracking. It follows that at saturation the matrix is broken into blocks of lengths between L_s and $2L_s$. Kimber et al (1982) gave the average spacing of cracks in a brittle matrix with continuous fibres as $1.33L_s$. Taking the average block length $2L$ as $1.33L_s$ the average stress in the fibre taken from equation 2.51 is therefore given by:

$$\bar{\sigma}_f = \frac{\sigma_c}{V_f} - \frac{\tau}{2R}(L_s) \quad \text{for } 2L = \frac{4}{3}L_s \quad (2.69)$$

Similarly the average stress in the matrix from equation 2.58 is given by:

$$\bar{\sigma}_m = \sigma_{mu} - \frac{3\tau}{2R} \frac{V_f}{V_m} L_s \quad \text{for } 2L = \frac{4}{3}L_s \quad (2.70)$$

From these two equations the average stress in the composite ($\bar{\sigma}_c = V_m \bar{\sigma}_m + V_f \bar{\sigma}_f$) correctly reduces to σ_c . After micro-crack saturation the average fibre stress given in equation 2.69 is dependent on the composite stress minus a constant stress ($\frac{\tau}{2R}(L_s)$). Consequently the matrix stress is constant past micro-crack saturation and dependent on the average block length. Knowledge of the block length ($2L = 1.33L_s$) therefore allows the interfacial shear stress to be calculated for a given distribution of micro-cracks and a known matrix micro-cracking stress:

$$\tau = \frac{\sigma_{mu} R}{1.5038 L} \frac{V_m}{V_f} \quad (2.71)$$

The strain distribution along the length of the block is now considered. The initial loading is linear elastic up to the failure strain of the matrix whereupon matrix micro-cracking occurs. The matrix continues to micro-crack, until the density of micro-cracks eventually saturates. After this point the stiffness of the composite is dictated by the fibre modulus and the fibre volume fraction up to the failure stress $\sigma_{fu}V_f$. Micro-crack initiation occurs when the strain in the composite reaches the failure strain of the matrix ϵ_{mu} . A stress of magnitude $\frac{\sigma_{mu}}{V_f}$ corresponding to the load in the matrix then transfers to the fibre bridging the crack. The additional stress on the fibre ($\frac{\sigma_{mu}}{V_f}$) decays to zero at distance L_s either side of the crack. The average additional strain on the fibre over the block length $2L_s$ is therefore:

$$\frac{1}{E_f} \left(\frac{\sigma_{mu}}{2V_f} \right) = \frac{E_m \epsilon_{mu}}{2 E_f V_f} \quad (2.72)$$

Where E denotes the modulus and the subscripts f and m the fibre and the matrix.

For a composite with continuous fibres, the average fibre strain is identical to the average composite strain. If the matrix is broken into blocks of length $2L = 2L_s$, the total strain in the fibres is given by the micro-cracking strain plus an additional strain given by equation 2.72:

$$\epsilon_{mu} \left(1 + \frac{E_m}{2V_f E_f} \right) \quad (2.73)$$

This represents a lower bound for the strain at micro-crack saturation.

If all the block lengths are L_s the additional stress in the fibre is still given by $\frac{\sigma_{mu}}{V_f}$ but reduces to $\frac{\sigma_{mu}}{2V_f}$ over a length $L_s/2$. This means that the additional strain in the fibre does not go to zero but to strain of $\frac{E_m \epsilon_{mu}}{2 E_f V_f}$. The average additional strain in the fibre over a block length L_s is:

$$\frac{E_m \epsilon_{mu}}{2 E_f V_f} + \frac{E_m \epsilon_{mu}}{4 E_f V_f} = \frac{3 E_m \epsilon_{mu}}{4 E_f V_f} \quad (2.74)$$

If at micro-crack saturation the block length is L_s then the strain in the fibres is:

$$\epsilon_{mu} \left(1 + \frac{3 E_m}{4 V_f E_f} \right) \quad (2.75)$$

This is an upper bound for the strain to cause micro-crack saturation in the composite. It is assumed that the failure strain of the fibre is constant. For block lengths of $2L_s$ and L_s there is a distribution of strain along the fibre. For this reason failure of the composite occurs when the local strain in the fibre reaches the fibre failure strain ϵ_{fu} . The composite failure strain (ϵ_{cu}) is therefore lower than the fibre failure strain. This provides upper and lower bounds on the composite failure strain (ϵ_{cu}) corresponding to block lengths of L_s and $2L_s$.

$$\left(\epsilon_{fu} - \frac{E_m \epsilon_{mu}}{2 E_f V_f} \right) < \epsilon_{cu} < \left(\epsilon_{fu} - \frac{E_m \epsilon_{mu}}{4 E_f V_f} \right) \quad (2.76)$$

In the micro-cracking region the number of micro-cracks per unit length increases with strain. For a block length of $2L_s$ the micro-crack density, ρ , cannot exceed $\frac{1}{2L_s}$ cracks per unit length, the average additional strain in the fibres is:

$$\frac{\rho}{\frac{1}{2L_s}} \frac{E_m \epsilon_{mu}}{2 V_f E_f} = \frac{\rho L_s E_m \epsilon_{mu}}{V_f E_f} \quad (2.77)$$

Therefore the total strain in the composite is:

$$\epsilon_{mu} \left(1 + \frac{\rho L_s E_m}{V_f E_f} \right) \quad (2.78)$$

If the composite is unloaded, the region between the lengths $L_s/2$ and L_s is

considered to be elastic for a constant shear resistance to sliding. In this case the residual strain is half the average additional strain on the composite. This gives the strain on unloading as:

$$\frac{\rho L_s E_m \epsilon_{mu}}{2 V_f E_f} \quad (2.79)$$

If the fibres are linear elastic to failure the inelastic strain after micro-crack saturation for block lengths of $2L_s$ is then a maximum at $\frac{E_m \epsilon_{mu}}{2 V_f E_f}$. For block lengths of L_s a similar process is followed resulting in a maximum unload strain from micro-crack saturation of $\frac{E_m \epsilon_{mu}}{4 V_f E_f}$.

The theories documented in this section attempt to describe the strength and mode of deformation of a fibrous composites. A general understanding of the mechanics of these materials is required to tailor these properties for a specific task. More specifically an understanding of the micro-mechanics of deformation allows the development of computational continuum models of fibrous composite.

2.5 Toughening Mechanisms

Fracture toughness is the ability of a material to resist crack propagation. Ceramics have inherently low resistance to fracture due to the strongly directional nature of their interatomic forces which inhibit plastic deformation. Understanding the mechanisms which drive or arrest crack propagation in ceramic composites can be used to design high toughness components.

Two fundamentally different approaches to this problem have been adopted: flaw control and the introduction of toughening mechanisms. The first accepts the inherent brittleness of the material and attempts to limit the size of flaws produced by processing. The second is a more recent advance in which toughness is enhanced by modifying the micro-structure or inclusion of a reinforcement. Individual mechanisms include, transformation toughening, micro-crack toughening, ductile reinforcement and fibre or whisker reinforcement (Ruhle et al 1989). Each of these mechanisms has produced critical stress intensity factors ranging from $10\text{MNm}^{\frac{3}{2}}$ to greater than $30\text{MNm}^{\frac{3}{2}}$ with the higher values produced by fibre reinforcement. These toughening mechanisms are now reviewed briefly.

2.5.1 Transformation Toughening

A variety of lattice transformations have been identified in inorganic materials. The most widely used for toughening is the ZrO_2 (zirconia) martensitic transformation. ZrO_2 undergoes two phase transformations. Three of the crystallographic modifications that exist are cubic (c), tetragonal (t) and monoclinic (m) symmetry. Stability of these structures occurs over temperature ranges as shown in figure 2.13

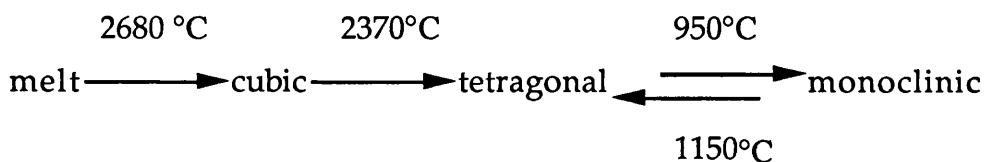


Figure 2.13 Phase transformations of ZrO_2

Tough ZrO_2 alloys typically contain t- ZrO_2 particles within a ceramic matrix where the start of the martensite transformation is suppressed below room temperature. The martensitic transformation is induced in t- ZrO_2 particles not by thermal effects but by stress, and specifically by the hydrostatic tensile stress field ahead of a crack. This transformation is essentially the source of toughness for ceramics containing ZrO_2 as discussed by Evans et al (1986).

ZrO_2 toughened ceramics are based on several micro-structures as described by Ruhle et al (1989). An important micro-structure arises from the densification in the t- ZrO_2 phase, followed by cooling to room temperature. Providing the grain size is less than the critical size required for the transformation. This produces a single phase material t- ZrO_2 called tetragonal zirconia polycrystals (TZP). This can also be used as one of the components in a ceramic composite referred to as a zirconia dispersed ceramic (ZDC).

An alternative micro-structure comprises t- ZrO_2 in a cubic matrix. This material is generally formed by sintering in the cubic phase field and cooling to the two phase field where the tetragonal phase forms as precipitates. These precipitates, if small, remain tetragonal down to very low temperatures. This type of material is commonly referred to as partially stabilized zirconia (PSZ). If however the precipitates are large then they transform thermally to m- ZrO_2 . The processing route by which these materials are formed therefore govern the size and distribution of ZrO_2 phases.

Stress induced transformations can be regarded as processes dominated by a volume increase. Similarly t - m transformations, ahead of a crack relax the strain and resist further crack propagation. This transformation occurs ahead of the pre-existing cracks which implies the absence of toughening for crack initiation. Further crack extension causes a zone ahead of the crack to unload inducing hysteresis and toughening.

After substantial crack growth steady state transformation is achieved. A transformation zone profile is created bounding the diminished transformed material ahead of the crack. The zone size is governed by a martensitic nucleation law. More specifically the size of the zone reduces with increasing

temperature and reduction in particle size. Ruhle et al (1989) has expressed this as a function of temperature and particle size. More specifically the operating temperature range of the material is limited by the transformation phase selected during composite manufacture.

2.5.2 Micro-Crack Toughening

Micro-crack toughening has been documented by Buresch (1978), Hoagland et al (1975) and Evans (1976). Microcracks occur in areas of local tensile stress. This stress can be induced by thermal expansion mismatch and/or by phase transformations. The toughening mechanism is based on a similar toughening to transformation toughening, in that the volume increase results in strain relaxation and consequent stress relief. Microcracking thus results in a reduction in Young's modulus within the process zone. Consequently constitutive relations for microcracking solids are nonlinear.

The initiation of microcracks ahead of a macrocrack provides a toughening mechanism for the extension of the main crack. However the toughness varies during crack propagation due to the reducing modulus. An example of this toughening is Al_2O_3 toughened by monoclinic ZrO_2 given by Ruhle et al (1989). Here the reduction in modulus and level of plastic strain are dependent on the micro-structure. This also effects the location of the microcracks in the ZrO_2 particles or the Al_2O_3 matrix. The distribution of micro-cracks also depend on the particle size and local stress distribution.

A potentially detrimental effect of microcrack toughening is the incidence of thermal microcracks at the largest particles due to thermal mismatch (Ruhle 1976). These cracks can be strength limiting and result in a tough material with moderate strength. The levels of toughening achieved by microcracking are the lowest of the toughening mechanisms described in this study. Its use is however enhanced when coupled with fibre reinforcement.

2.5.3 Ductile Reinforcement Toughening

Ductile reinforcement toughening has the ability to increase the toughness of ceramics significantly (Ruhle 1989). The reinforcement mechanisms include crack bridging (Ashby et al 1989, Sigl et al 1988) and crack shielding as well as energy dissipation associated with a plastic zone (Marshall et al 1989).

Crack shielding mechanisms operate by creating a process zone which inhibits stress concentrations at the crack tip. Crack shielding occurs when the stress field of a single crack nucleates micro-cracks around the crack tip. Kelly (1986) discusses two toughening mechanisms involving crack shielding. The first mechanism operates by shielding the crack from the applied stress intensity by means of a process zone. The second mechanism, and arguably the more dominant, arises from the increase in surface area from the nucleation combined with the depletion of the modulus through micro-cracking and dilation of the micro-cracking zone.

Ruhle (1989) identified crack bridging as the most effective toughening mechanism using ductile reinforcement. This was analysed by considering the local stresses at the crack tip producing plastic deformation of the toughener bridging the crack. The plastic deformation observed can be large and yield considerable increases in toughness. Crack bridging can be affected by both particulate reinforcements and a continuous ductile phase.

Gerberich (1971) produced ductile reinforcement of an aluminium matrix by the introduction of stainless steel fibres. This composite produced twice the value of K_{IC}/σ_{YS} compared to the best steels at the time where K_{IC} is the stress intensity factor and σ_{YS} is the yield stress. This was primarily attributed to an increased work to fracture caused by the high strength fibres ductile necking. This extended work by Cooper et al (1967) who established a relationship for the fracture toughness of laminated composites using both ductile and brittle tungsten fibres and silica fibres in a copper matrix.

Cao et al (1989a) experimented with Nb and Nb-alloy wire reinforcements in a TiAl cylinder. The composite cylinders were manufactured by hot isostatic pressing generally referred to as HIPing. Toughening was again achieved by ductile fibres which exhibited extensive plastic deformation after

matrix failure. Experimental results produced a stress intensity factor of 13 MPa m^{1/2}. It was estimated that by using reinforcements of 1mm diameter that a toughness of 115MPa m^{1/2} could be achieved.

Sigl et al (1988) demonstrated crack bridging by cemented carbides in the form of a continuous ductile network, for a tungsten-carbide cobalt composite. In this composite the cobalt is the ductile phase binding the carbide together. More commonly these are sometimes referred to as "cermets" and are widely used for machine tool tips (Reed 1987). The crack propagates between the carbide particles and across the cobalt matrix. At the cobalt yield stress small voids appear on the crack plane. These grow deforming the cobalt plastically and bridging the crack hence contributing to the toughness of the composite.

2.5.4 Fibre Reinforcement Toughening

The fracture toughness and strength of ceramic composites remain competing requirements. Altering the structure of the material to enhance toughness generally has the effect of reducing strength. However the toughness of a composite can be very much greater than either of its constituents. An example given by Kelly (1986) involves a glass-reinforced plastic. Here the resistance to crack propagation of the polyester resin and the glass is 100 Jm⁻² and 10 Jm⁻². In contrast the resistance to crack propagation of the composite is of the order 10⁵ Jm⁻². This increase in toughness is significant and much higher than the sum of the constituent resistances to fracture. Similarly high strength ceramics are relatively common and levels of strength can be an order of magnitude higher than those produced by metals. This allows for a sacrificial reduction in strength compensated by an increase in toughness. The highest levels of toughness in ceramic composites are produced by fibre reinforcement toughening.

Fibre toughening has similarities to ductile fibre reinforcement toughening, in which matrix cracking transfers the stress onto the fibre (Cox et al 1991). Incorporating this method of toughening can substantially increase the fracture toughness of a composite (Laird et al 1991). Evans et al (1989)b attributed the toughness in these composites to fibre pullout where

the fibre-matrix interface dictates the toughness. Figure 2.14 shows fibres bridging a crack. As the crack opens the fibres have three basic mechanisms of failure which may occur separately or concurrently. These are brittle fibre fracture, the plastic deformation of ductile fibres and finally fibre pullout. The brittle failure of the fibre requires the least work and provides a negligible contribution to toughness. With ductile fibres, the contribution to toughening is limited to the plastic deformation of the fibre. The pulling out of a fibre produces a shear stress on the fibre matrix interface significantly increasing the fracture toughness. Work reviewed by Kelly (1986) describes how the work of fracture is affected by the length of fibres in a composite (L) as well as the critical fibre length (L_c , equation 2.27). From this review, the work done in pulling a fibre out of a matrix is force on the fibre times the distance moved. As the fibre pulls out so the surface area of the fibre in contact with matrix reduces. The work done withdrawing a fibre whose end is a distance x from the matrix crack is given by:

$$\text{Work done} = \pi r^2 \int_0^x \sigma_f dx \quad (2.80)$$

From equation (2.26) $\sigma_f = \frac{-2\tau x}{r}$ and hence the work done is:

$$\text{Work done} = \pi r \tau x^2 \quad (2.81)$$

If the fibre length is greater than the critical fibre length then the fraction of fibres that pullout is $\frac{L_c}{L}$. The work done per unit area of specimen cross section to withdraw all the fibres which pull out is:

$$W = \frac{V_f(L_c)}{\pi r^2(L)} \int_0^{\frac{L_c}{2}} \pi r \tau x^2 \frac{dx}{L_c/2} = \frac{V_f(L_c)}{12(L)} \left(\frac{\tau L_c^2}{r} \right) \quad \text{For } L < L_c, L_c = L \quad (2.82)$$

In this equation the maximum work is achieved by maximising L_c and keeping the fibre length L close to L_c . For increasing L the work decreases. If the fibre length L is below the critical value then work of fracture is

determined by setting $L_c = L$ producing a reduction in the work. Equation (2.82) also indicates that increasing the interfacial shear resistance (τ) will increase the work. However from equation (2.27), increasing τ reduces the critical fibre length, reducing the work and hence the toughness.

The toughness of a fibre-matrix composite may be optimised by balancing the fibre, the matrix and the interface mechanical properties (Thouless 1989). The effect of the interface on the mechanical behaviour of the composite is strongly affected by its debond strength (Charalambides et al 1989) and its interfacial shear stress (Cao et al 1990). In the case of a brittle matrix and brittle fibre composites the interfacial properties characterise the response. High debond and interfacial shear resistance results in small fibre pullout lengths and low composite fracture toughness. It follows that the interface must be balanced with the fibre strength to encourage large fibre pullout lengths and high work to fracture.

The toughening mechanisms of a composite has been considered for materials in which the fibres failure strain is significantly higher than that of the matrix. Reviews by Hutchinson et al (1990), Evans et (1989)b Bao et al (1993) and Thouless (1989) discuss and model the influence of the interface on the fibres bridging a macroscopic crack. Enhanced toughness requires that a crack propagating through the brittle matrix leaves in its wake intact undamaged fibres bridging the crack. To achieve this, the strength of the fibre-matrix interface must be sufficiently low to favour fibre debonding on the crack flanks and maximise the growth of the debond crack before fibre failure. If the interfacial shear resistance is too large, fibre debond lengths will be small and the resulting pullout lengths and work to fracture reduced accordingly. Conversely if the interface resistance is too small then large fibre debond lengths are produced resulting in low pullout work hence low toughness.

Hutchinson et al (1990) modelled fibre debonding and fibre pullout using constant friction and also Coulomb friction. Both analyses consider debonding arising from a mode II crack growing from the mode I crack face. As the debond crack grows contact between the fibre and the matrix is prevented over a critical length and thus offers no resistance to sliding. At this point the load curve levels remaining unchanged until the failure stress

in the fibre is reached, after which pullout is observed. A similar model by Bao et al (1993) considered the effects of cycling of broken fibres in the wake of a mode I fatigue crack.

Aveston et al (1971) considered the energy involved in producing multiple cracking in a brittle matrix surrounding fibres with higher failure strains than the matrix. When the crack initially traverses the matrix under conditions of fixed load the strain in the matrix will be ϵ_{mu} . The formation of the crack must be energetically favourable.

Work is done (ΔW) by the applied stress since the body increases in length. The extension can only occur over the length of fibre that has debonded given by $2L_s$ with a shear resistance (τ). By symmetry the increase in length is $\left(\frac{E_m V_m}{E_f V_f} L_s \epsilon_{mu}\right)$. If the stress in the composite is $E_c \epsilon_{mu}$, the work done per unit area of composite is

$$\Delta W = \frac{E_m^2 V_m^2}{2\tau V_f} \epsilon_{mu}^3 r \left(1 + \frac{E_m V_m}{E_f V_f}\right) \quad (2.83)$$

Here E is the elastic modulus and V the volume fraction with the subscripts f and m denoting fibre and matrix. Work must also be done in debonding the fibre from the matrix over the length $2L_s$ in a mode II type crack with a shear resistance τ . Here the energy absorbed γ_{db} will be:

$$\gamma_{db} = \frac{2\sigma_{mu} V_m G_{II}}{\tau} \quad (2.84)$$

Here G_{II} is the energy per unit area of debond. After debonding the matrix slides back over the fibre thus work is done against the sliding resistance τ . This energy per unit area of the crack surface is

$$U_s = \frac{E_m^2 V_m^2}{6\tau V_f} \epsilon_{mu}^3 r \left(1 + \frac{E_m V_m}{E_f V_f}\right) \quad (2.85)$$

Here r is the fibre radius. After sliding occurs the matrix strain decreases thus reducing its strain energy by ΔU_m :

$$\Delta U_m = \frac{E_m^2 V_m^2}{3\tau V_f} \epsilon_{mu}^3 r \quad (2.86)$$

Consequently there will be an increase in the fibre strain energy described by:

$$\Delta U_f = \frac{E_m^2 V_m^2}{2\tau V_f} \epsilon_{mu}^3 r \left(1 + \frac{E_m V_m}{3E_f V_f} \right) \quad (2.87)$$

In the matrix the work done creating a fracture surface is γ_m . A crack may only form in the matrix when:

$$2\gamma_m V_m + \gamma_{db} + U_s + \Delta U_f = \Delta W + \Delta U_m \quad (2.88)$$

Substituting equations 2.83-2.87, allows 2.88 to be written as:

$$2V_m \left(\gamma_m + G_{II} \frac{\sigma_{mu}}{\tau} \right) \leq \frac{E_c E_m^2 V_m^2}{6\tau V_f} \epsilon_{mu}^3 r \quad (2.89)$$

The energy G_{II} cannot be estimated but is assumed to be less than γ_m therefore by setting G_{II} equal to γ_m a limit is set given by:

$$2V_m \gamma_m \left(1 + \frac{\sigma_{mu}}{\tau} \right) \leq \frac{E_c E_m^2 V_m^2}{6\tau E_f V_f^2} \epsilon_{mu}^3 r \quad (2.90)$$

With the assumption that $G_{II} < \gamma_m$ then a lower limit on equation 2.89 can be established by setting $G_{II} = 0$ hence:

$$2V_m \gamma_m \leq \frac{E_c E_m^2 V_m^2}{6\tau E_f V_f^2} \epsilon_{mu}^3 r \quad (2.91)$$

Rearranging equation (2.91) gives the micro-cracking strain as:

$$\epsilon_{mu} = \left(\frac{12\tau\gamma_mE_fV_f^2}{E_cE_m^2V_mr} \right)^{\frac{1}{3}} \quad (2.92)$$

For a matrix with a constant failure strain incremental increases in strain past initial matrix micro-cracking will result in sets of cracks normal to the direction of loading with crack spacing between L_s and $2L_s$. In an ideal composite this results in a constant stress over the micro-cracking region. In practical terms this is not observed due to a variation of the micro-cracking strain in the matrix causing the composite stress to rise during micro-cracking.

For a composite with fixed fibre and matrix material properties, a constant fibre volume fraction and a constant interfacial shear stress then the matrix micro-cracking strain is a function of the fibre radius. Aveston et al (1971) documented an example of this where values relating to a general ceramic composite were applied to equation (2.92). These included a matrix and fibre elastic moduli of 140GPa and 440GPa, a fibre volume of 0.5 and an interfacial shear stress estimated at 20MPa. The failure strain of many ceramic materials is $\sim 10^{-3}$ hence from equation (2.92) a fibre radius of 350 μm was predicted. To raise the failure strain to 0.01 with the material and interfacial properties remaining constant would require a fibre radius of 0.35 μm . In addition from equation (2.44) the required fibre strength for multiple matrix micro-cracking to occur would be of the order 50GPa. Hence to increase the failure strain of ceramics requires very strong fibres.

Aveston et al (1971) also considered a case where the matrix cracks as a result of thermal stress. For a composite with matrix thermal expansion coefficient (α_m) greater than the fibre equivalent α_f then when the composite is cooled by a temperature difference ΔT , cracking will not occur until a strain $\epsilon_T = (\alpha_m - \alpha_f)\Delta T$. Following the argument developed by equations (2.83) to (2.88) but with ΔW equal to zero and ΔU_f having a negative value Aveston developed the expression:

$$2V_m\gamma_m \leq \frac{E_c E_m^2 V_m^2 r}{6\tau E_f V_f^2} \left[\frac{\epsilon_T E_f V_f}{E_c} \right]^3 \quad (2.93)$$

Using a similar argument to that which leads to equation (2.92) it must therefore be possible to limit the thermal strain ϵ_T in the composite via the variation in the fibre radius. It follows that increasing the radius would ensure that the composite would not micro-crack during processing. This is however in direct competition with the requirement to increase the failure strain of the matrix.

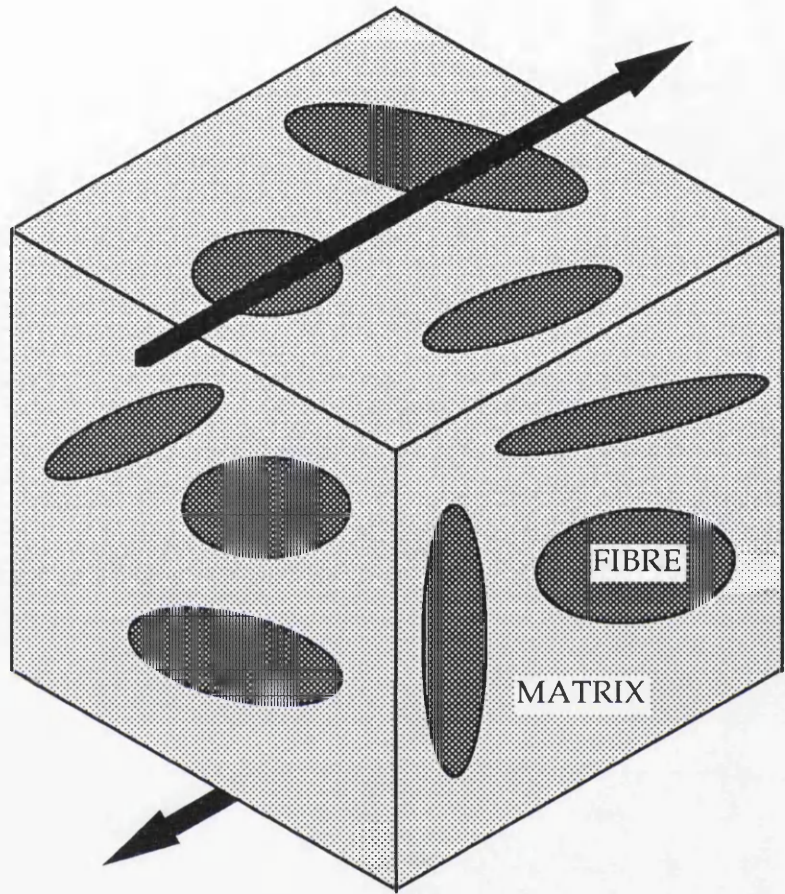


Figure 2.1 Two phase material in shear

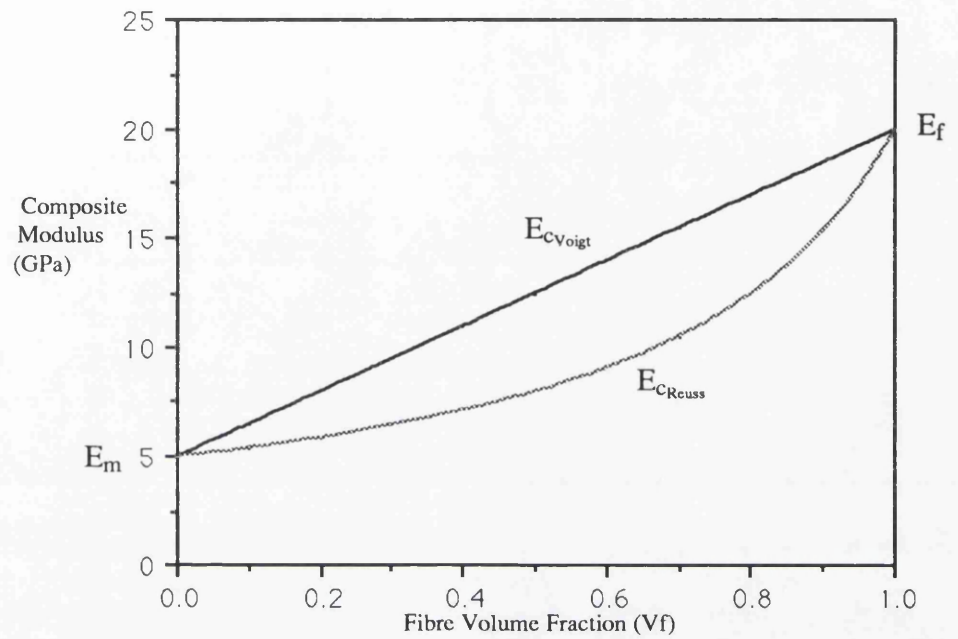


Figure 2.2 Elastic Modulus of a fibre-matrix composite according to Voigt and Reuss taking a fibre modulus of 20 GPa and a matrix modulus of 5GPa

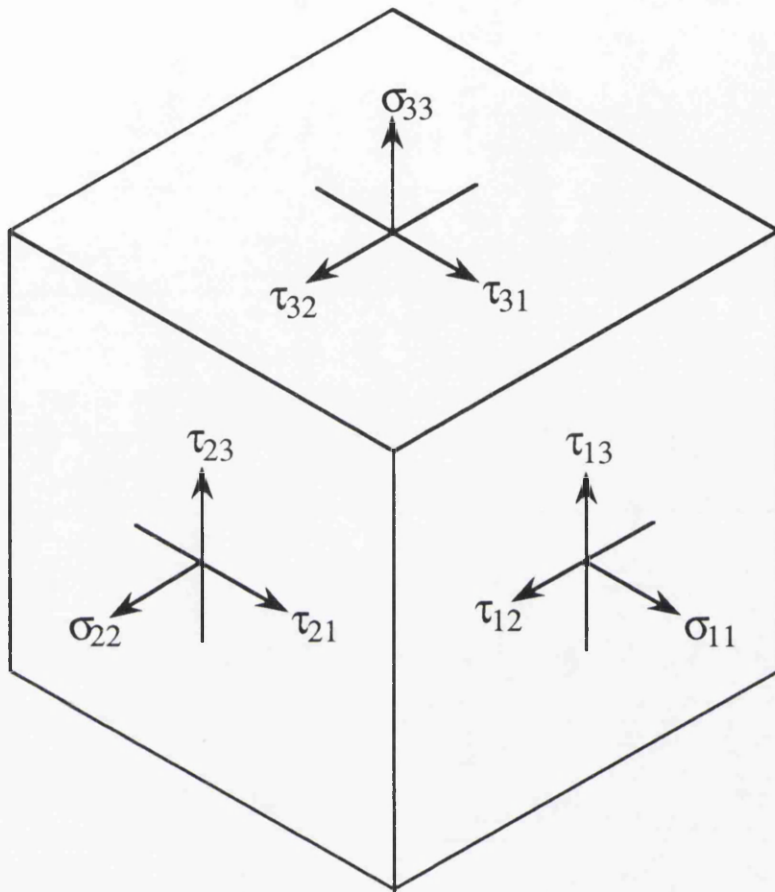


Figure 2.3 State of stress of a body defined by nine stress components

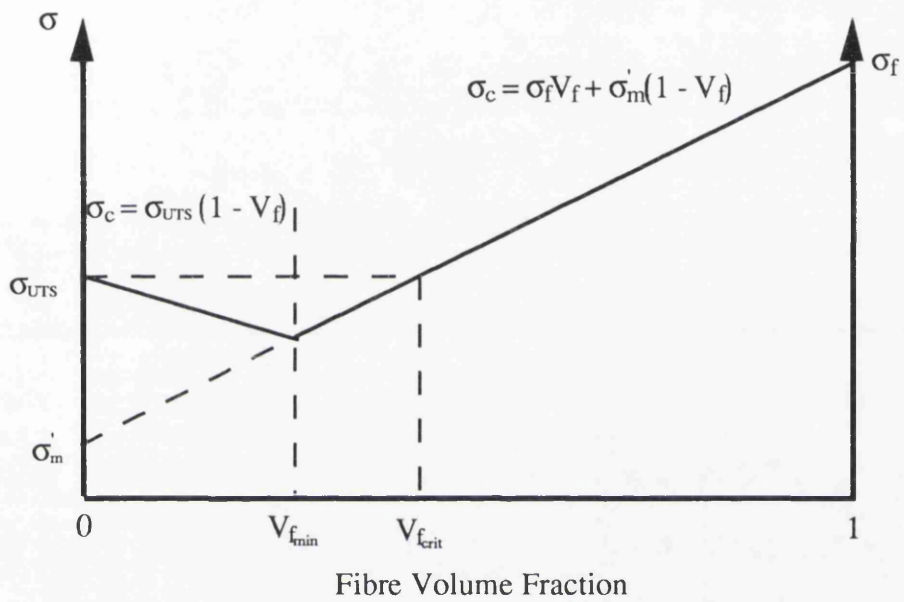


Figure 2.4 Composite strength for varying fibre volumes

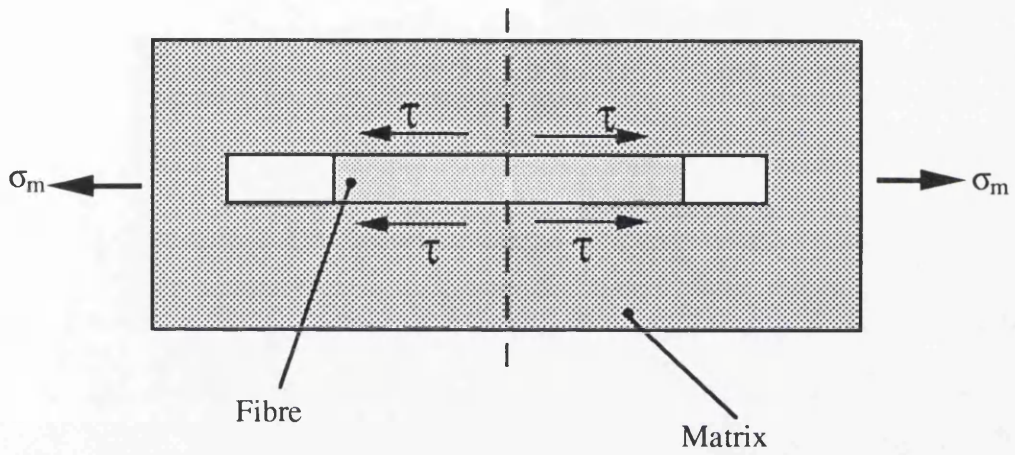


Figure 2.5 Fibre contained within a matrix under tension

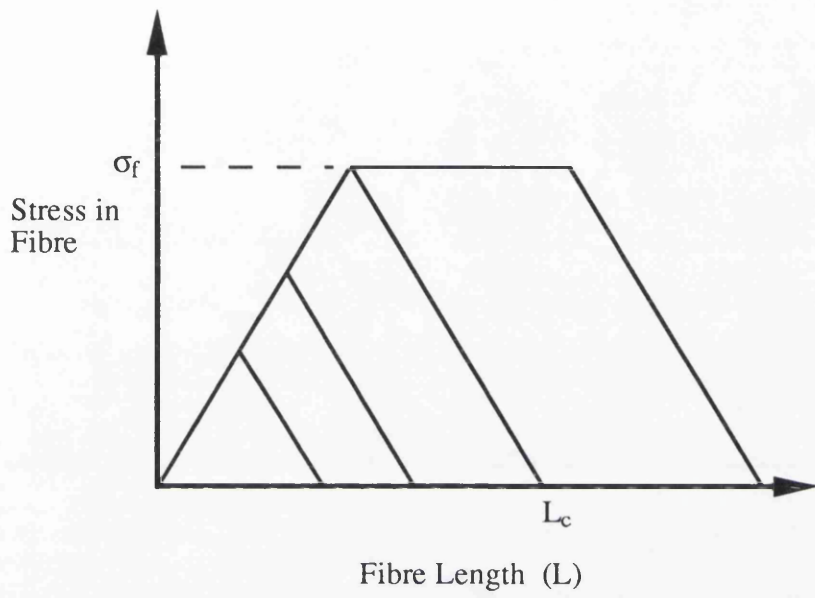


Figure 2.6 Stress distribution along a fibre in tension

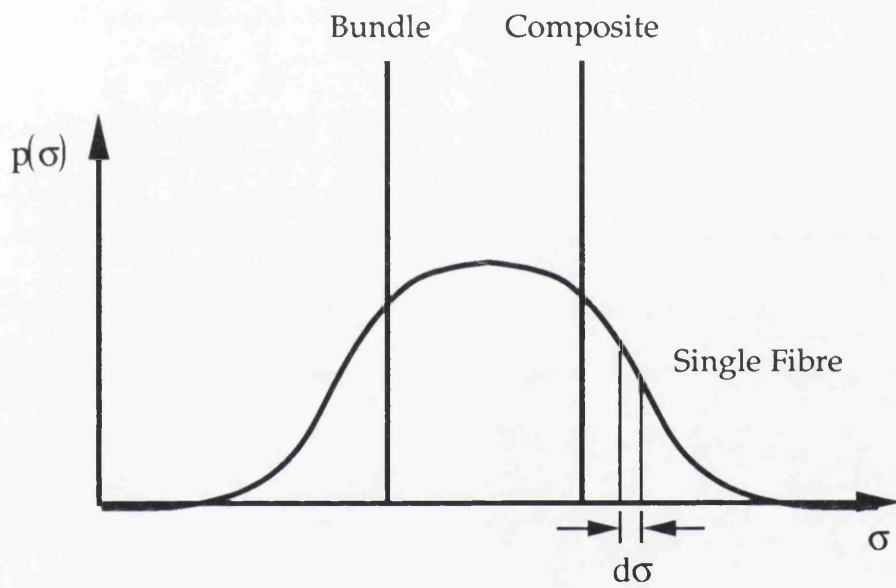


Figure 2.7 Typical probability density function for the fibres in a composite, in a bundle and a single fibre with $N = \infty$.

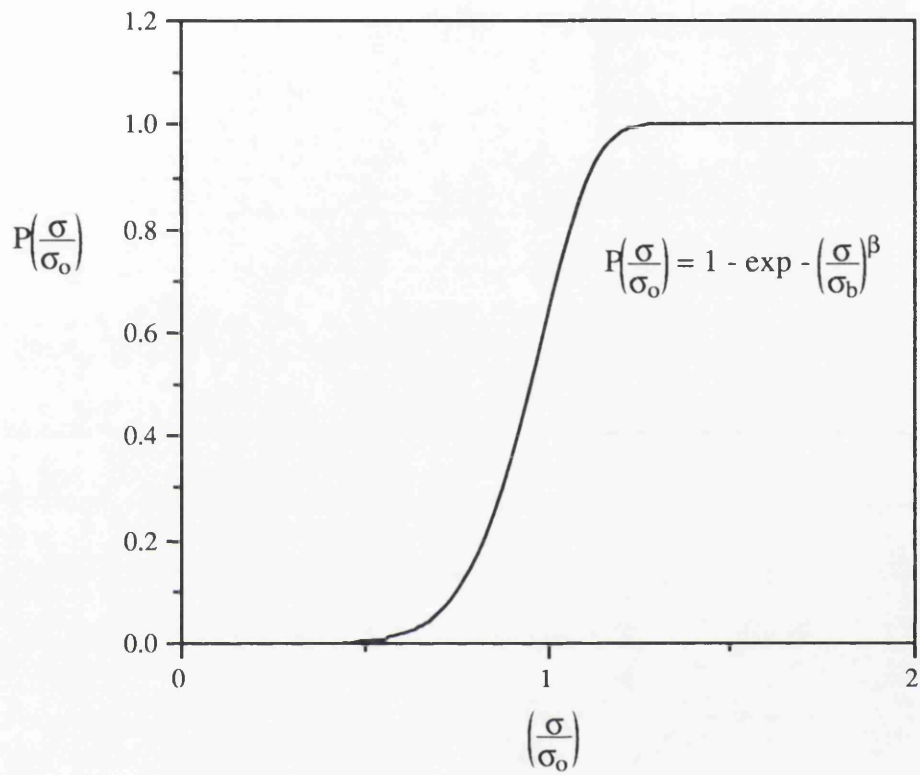


Figure 2.8 The Weibull Distribution for $\beta = 8$

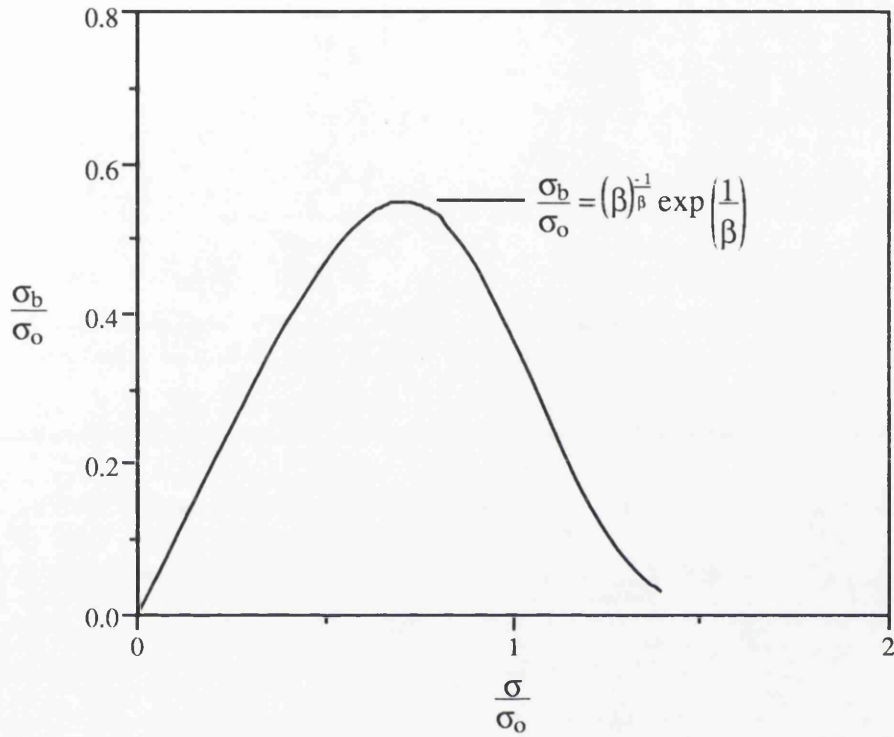


Figure 2.9 The variation of the bundle stress $\left(\frac{\sigma_b}{\sigma_o}\right)$ against the fibre stress $\left(\frac{\sigma}{\sigma_o}\right)$ for $\beta = 8$

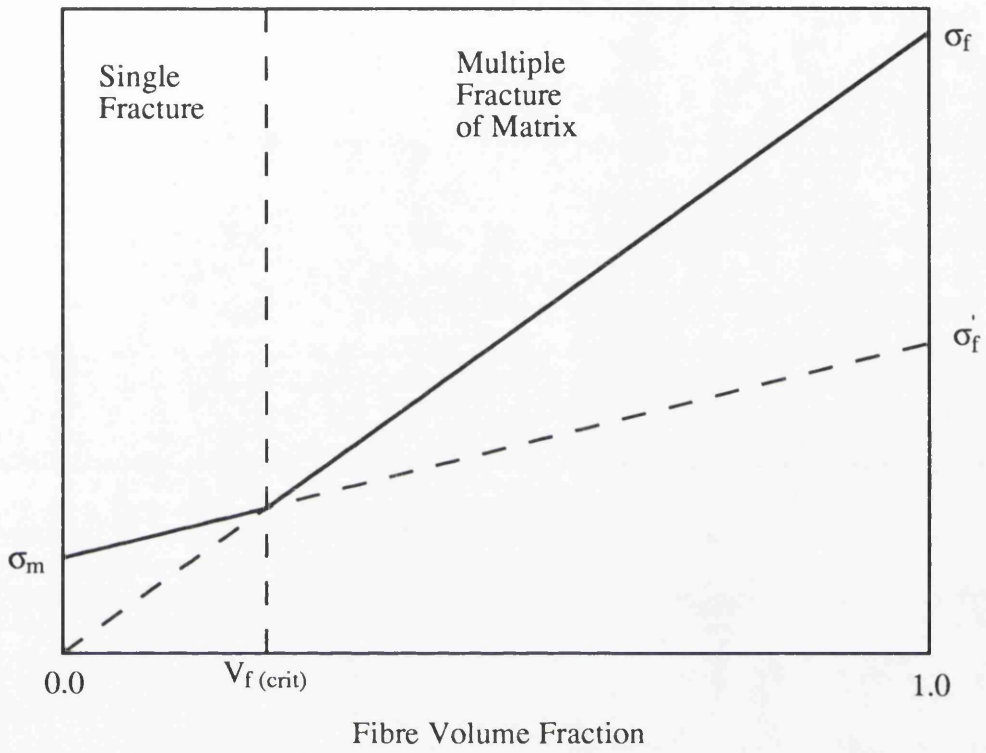


Figure 2.10 The Onset of Multiple Matrix Cracking for a Brittle Matrix - Ductile Fibre Composite

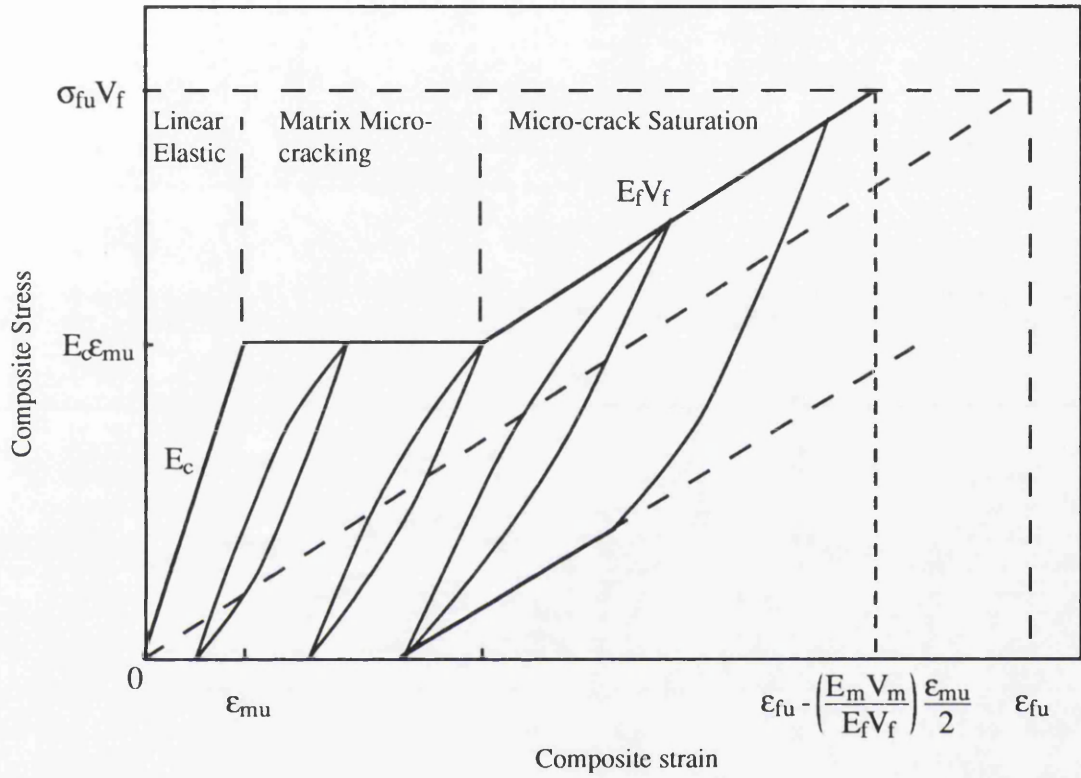


Figure 2.11 Schematic response of a continuous fibre brittle matrix composite with a constant matrix failure strain.

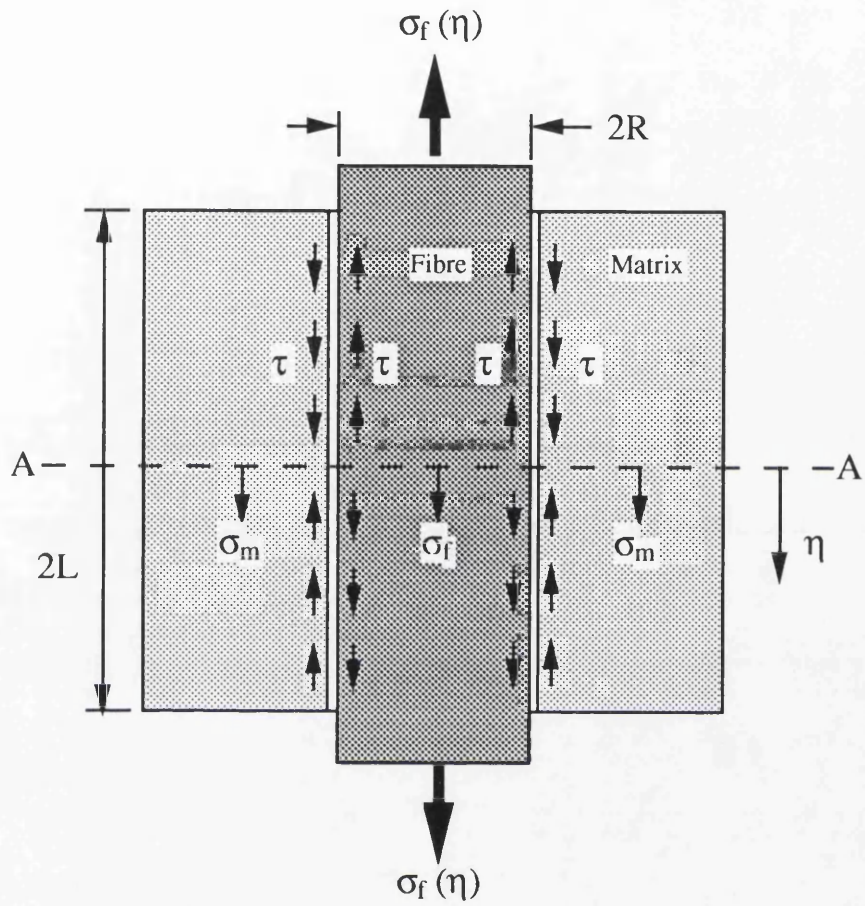


Figure 2.12 Fibre matrix Interface Model

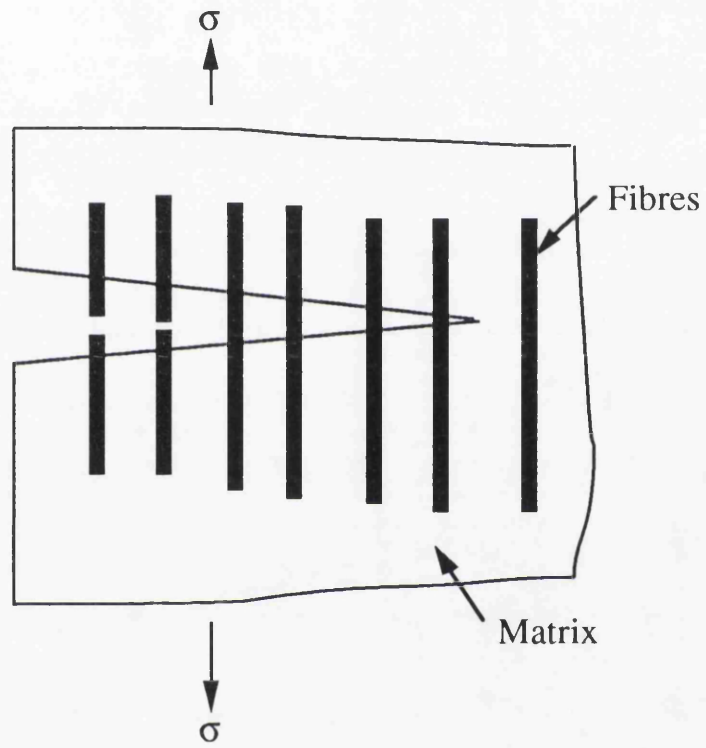


Figure 2.14 Fibre crack bridging

3.Ceramic Composite Manufacture

3.1 Introduction

Ceramic composites are manufactured in an attempt to create a material that exhibits high temperature capabilities, low density and an acceptable level of toughness for structural engineering applications. The initial step in creating a ceramic composite is the manufacture of the fibre. This is followed by the fabrication of a fibre preform and finally by densification with a compatible matrix.

The processing of ceramic fibres prior to the formation of the preform may involve drawing or extruding. These processes are reviewed along with alternative fibre manufacturing routes. Preform manufacture techniques such as knitting, weaving and braiding are also reviewed. The preform essentially controls the fibre architecture and toughness of the composite. Densification techniques described include sol-gel, chemical vapour processing, hot pressing and the DIMOX process. This chapter outlines the main manufacture processes used in the manufacture of ceramic matrix composites.

3.2 Fibre Manufacture

3.2.1 Introduction

The development of viable engineering composites is dependant on the production of fibres. The evolution of carbon, boron and kevlar fibres central to reinforced plastics has been reviewed by Hull (1981). Interest is restricted to ceramic fibres for high temperature ceramics or metal-matrix composites, drawing on reviews by McColm et al (1986) and Mathews et al (1994).

3.2.2 Air Drag or Blow Spinning

Manufacture of a fibre by the air drag process begins with a molten ceramic reservoir extruded through a die. High velocity air jets are forced over the fibre. This both cools and exerts a frictional force, to draw the fibre. The air flow cools the fibre over a length after which it is wound onto a mandrel. The fibre diameter can be altered by varying the distance from the die to the air jets and the air jet velocity.

Drag from the air accelerates the fibre from the initial contact of the air jets. Between this point and the mandrel the air velocity drops and the fibre travels faster than the air. The air slows the motion of the fibre through a drag effect causing the fibre to bend and vibrate. For this reason the distance to the mandrel must be kept below a critical value to prevent the fibre breaking.

A variation of this process is blow spinning in which a thin stream of the molten liquid is cooled by compressed air or steam prior to the fibre being wound. This process is more commonly applied to glass fibre but is used to manufacture ceramic fibres with compositions in the $\text{Al}_2\text{O}_3\text{-SiO}_2$ system in the temperature range 1800-2000 C.

3.2.3 Sol-Gel Processes

Modern sol-gel techniques allow processing temperatures of the order of 100°C. The manufacture of a sol gel begins with a solution (sol) or viscous

medium. The content of the initial solution includes a mixture of colloidal suspension (gel forming medium) and solutions. The sol is passed through a liquid removing processes such as vacuum drying after which a gel is formed. The gel may now follow the blow-spin process coupled with a drying process which prevents binding of neighbouring fibres on the mandrel. Careful monitoring of the water content and viscosity of the gel are crucial for consistent fibre manufacture. In comparison to the fibre melt process the sol gel process results in inferior mechanical properties. The strength of SiO_2 fibres formed from the sol gel process (600MN/m^2) is less than the melt fibre (700MN/m^2) due to surface defects created during the drying process.

The extrusion of modern ceramic fibres is usually based on the sol gel process. The viscosity of the gel is adjusted during its formation to allow extrusion with modest forces. After this the fibre is heat treated to crystallize the gel then wound onto a mandrel. In this process the applied force and the viscosity of the gel limit the fibre diameter. The applied force in this case may be used to either drawn or extruded fibres. After the initial forming process, moisture is removed by passing the fibre through heating chambers prior to winding to eliminate binding.

The extrusion process can be modified to manufacture short fibres. By altering the viscosity of the gel, droplets can be produced. Forcing the droplets through a high velocity spinning disc produces short fibres with aspect ratios (fibre length/fibre diameter) of the order 60 which then collect on the inside of the drum. The distance from the disk to drum is adjusted to allow for the fibres to dry to eliminate binding.

3.2.4 Crystallization Process

Manufacture of an Al_2O_3 fibre using the crystallization process begins with a concentrated solution of AlCl_3 impregnated into a rayon or cotton thread. The thread is rapidly heated, crystallising the solution and evaporating the solvent. The thread is burned off leaving the crystallised medium. Full saturation of the thread prior to burning results in the formation of an oxide skeleton through the finished fibre. Problems occur when saturation is not achieved due to the transport of the solution along the thread, commonly

termed wicking. Oxidation of the thread in this state results in hollow fibres. This may be avoided if threads with low wicking rates are used in conjunction with a rapid oxidation process. Other examples of fibres made from this process include MgO, ZrO₂ and TiO₂

3.2.5 Vapour Phase Manufacture

In this process a filament is heated in a chemical vapour. A reaction is caused and the fibre grown from deposited vapour. This process is used to manufacture large diameter boron fibres (greater than 20 μm). Here a mixture of H₂ and BCl₃ vapours are deposited onto a 10 μm tungsten filament resistance heated to 1100 C causing a reaction hence deposition. As the fibre diameter grows so the temperature to cause the reaction falls to a critical level where deposition ceases. This limits the maximum fibre diameter to 100 μm . In this process careful temperature control is required to ensure repeatability and small crystal sizes. Problems are encountered when this fibre is used above 1100C with the possibility of interdiffusion leading to boron phases and flaw generation. A common failure of this fibre occurs through longitudinal splitting as a result of thermal mismatch of expansion coefficients at the fibre-matrix interface.

Continuous Silicon Carbide and Nicalon SiC fibres are also formed by chemical vapour deposition. In this case of SiC fibres, a mixture of SiH₄ and H₂ vapour is passed over a resistance heated graphite coated monofilament at 1300 C. During this passage the thickness of the deposited layer increases and the temperature of the outside of the fibre drops. The lower deposition temperature affects the structure of the depositing SiC. Coarser grains are then produced in the fibre over a diameter of 40 μm in the outer layers of the fibre during the final stages of deposition. Finally a 1 μm protective coating of carbon is deposited onto the fibre to prevent degradation and sustain fibre strength.

3.2.6 Chemical Transformation of a Precursor Fibre

The classical route to manufacture high performance carbon fibres has

been through the chemical transformation of a polyacrylonitrile (PAN) fibre (McColm et al 1986). The PAN fibre has a 2 dimensional molecular arrangement of the C-C...N-C-C bonds forming the nucleus of the hexagonal graphite ring structure. Light oxidation provides shape stabilisation, after which the fibre is pyrolysed to remove N₂ and H₂O. The fibre is finally graphitised at temperatures of the order 2200 C.

The finished fibre properties are affected by the process route prior to oxidation. Pre-oxidation treatments can be used to enhance the structure, crystallinity and the orientation of the polymer chains. These treatments can be achieved by stretching the precursor fibre at temperature in various mediums. The most effective treatment is stretching in N₂ gas at 220 C. This produces a finished fibre with a failure stress of 2.75 GPa and a modulus of 207GPa. This is significantly improved when compared to an untreated fibre with a failure stress of 1.38 GPa and a modulus of 145 GPa.

3.3 Preform Manufacture

3.3.1 Introduction

The manufacture of preforms using continuous ceramic fibres follows paths established by the textile industry in the manufacture of cloth by weaving and knitting. An alternative method utilises knowledge gained in the manufacture of ropes through braiding. All these methods aim to create, a high fibre volume composite with the fibres arranged in an architecture that introduces toughening to the densified preform. This section summarises the techniques and configurations developed for preform manufacture drawing on reviews by Ko (1989) , Klein (1986) and McColm et al (1986)

3.3.2 Woven Preforms

The weaving of a preform can take many forms of which the simplest is the plain weave shown in figure 3.1. Klein (1986) describes variations of this weave, some of which are also shown in figure 3.1. These variations exhibit the basic 2D characteristics associated with the plain configuration but with a bias to one axis. Composites created from 2D weaves consist of layers of woven fibre cloths pressed together, densification follows and a 2D laminate is produced. Such composites are highly anisotropic with the main strength and modulus in the direction of the fibres. Through thickness properties are often of an order of magnitude lower, giving rise to delamination under out of plane loading (Cao et al 1989)b.

In an attempt to reduce the anisotropy, the woven layers can be stitched together to increase the through thickness strength. Offsetting the layers combined with the stitching reduces the maximum directional strength and stiffness but results in a more isotropic material (Yang et al 1986). Other methods of increasing the through thickness properties are to weave a number of layers simultaneously allowing individual fibres to share layers. This can be done by weaving a fibre in one layer, taking it out and weaving it into another layer. If this is repeated with several fibres then the layers are

joined. This can have greater effect on the through thickness properties than stitching the layers but results in a reduction in the maximum mechanical properties.

Triaxial weaving, as shown in figure 3.2, typically consist of three yarns interwoven at an angle of sixty degrees to one another. This form of weaving is two dimensional and results in similar disadvantages to that of the plain weave with similar remedies. The main advantages of this weave are its high in plane shear resistance, its large fibre volume fraction and an improved resistance to unravelling.

Weaving is not restricted to two dimensions. Complex three dimensional preforms can be created using 3 and 4D weaves with improved isotropic properties but with a significant increase in cost. Figure 3.3 shows typical 4D layup. The 3D weave can be used to create solids as in a 3D block billet weaving where the fibres are aligned orthogonally. Typical uses of the 3D cylindrical weave include rocket nozzles where reinforcement in the through thickness properties are required.

The 4D layup as shown in figure 3.3 has similar improving characteristics to that of the triaxial weave. These weaves are used in cases where strength is needed in more than three directions, introducing strength where it is required as in complex components and resistance to interlaminar shear failure.

3.3.3 Braided Preforms

Ko (1989) defined braiding as 'a fabric formation process that intertwines three or more yarns in the bias direction.' This intertwining is the basic method through which ropes are typically formed. Braiding is however not restricted to cylindrical components but can be used to manufacture a large variation in shapes. The most basic of these processes is the 2D braid.

Figure 3.4 shows a typical example of a 2D braid. The nature of braiding allows the formed braid to be stretched or contracted. This is utilised in the formation of cylindrical 2D braids where the braid is formed over a shaped mandrel, with high production rates achieved at low cost. Braiding also has the advantage of allowing fibre orientation in a specified direction adding

strength where required. One disadvantage of braiding is a susceptibility to fibre crimping resulting in a loss of composite strength.

Triaxial braiding advances the 2D braid by introducing a stiffener in the direction where added strength is required. This can be used to create a hollow cylindrical form over a mandrel. In this process 0° fibres are laid along the mandrel axis with the braid formed round these. This is as versatile as the standard 2D braid but with added shear resistance. An example of a structure based on this braid is that of a 3/4 size formula one chassis created using a 144 carrier braider and a monocoque unibody chassis (Ko 1988).

The 2D and triaxial braiding processes are used to create a layered or hollow preforms. Solid objects can be formed using 3D braiding. In this process the same basic braiding action is similar to the 2D braid. Carriers are moved in orthogonal directions followed by a compacting motion. With this process a variation of shapes may be formed by the positioning of the carriers. Figure 3.5 shows a typical 3D braid. A large number of fibre strands can be used in the formation of solid 3D braids, a particular example being a cartesian 3D braiding machine that can handle 12,222 fibres (Bittence 1987).

When additional directional strength is required 4D braiding can be used. A 4D braid is formed by the addition of stiffened fibres laid in a particular direction and a 3D braid created around them. An example of this is the 4D Triaxial braid shown in figure 3.6 which is radial reinforcement added to a 3D triaxial braid.

3.3.4 Knitted Preforms

Knitting interloops continuous fibres to form a preform layer. The process is identical to those developed for textile manufacture. The basic form of this is the plain knit as shown in figure 3.7. Knit geometries can vary considerably to control the loop density. However the bending imparted to the fibres in the formation of the loops can significantly reduce the strength of stiffer ceramic fibres. To counter this, solid fibres or tows may be laid into the knit as shown in figure 3.8. Two dimensional laminates may be formed by knitting together solid fibres aligned perpendicular to each other. An advantage of this is that the fibres are not damaged through bending as in the

0-90 woven process. A disadvantage is that lower fibre volumes are created.

Three dimensional knits are available incorporating solid fibres as in the strengthened 2D laminates. In this case layers or mats of fibres can be laid in the direction required for maximum strength and systematically knitted together to form a solid. An example of a component manufactured using this process is carbon/carbon aircraft disc brakes (Ko 1989). These are knitted as a continuous helical strip with radial strengtheners. This strip is then collapsed and impregnated to form the disc.

3.4 Preform Densification

3.4.1 Introduction

The densification of a fibre preform is the final process in the manufacture of a modern ceramic composite. The prime objective of the process is to densify the preform with the absence of voids or inclusions and in a finished shape requiring no surface finishing. This section reviews techniques used in attaining these requirements by sol-gel, chemical vapour and directed metal oxidation processes.

3.4.2 The Sol Gel Manufacture Process

Composite manufacture using a solution gelatinous (sol-gel) technique has been developed at G.E.C. Alstom Engineering Research Centre (Hyde 1988). In this technique the matrix is formed from solutions containing refractory precursors. Densification of the preform is achieved either by impregnating the fibre preform or by coating the fibres prior to preform manufacture with the precursor solution. In both cases the composite undergoes a heat treatment during which the solution solidifies forming the matrix.

The sol-gel technique used to densify a fibre preform can best be described in four steps. The technique is very similar to polymerisation in that it chemically bonds small molecules together to form large chains and networks. A typical starting point for formation of a silica matrix is hydrolysis of an alkoxide (in this case tetraethoxysilane). In the presence of acids this process yields solutions containing hydroxides as shown in figure 3.9.

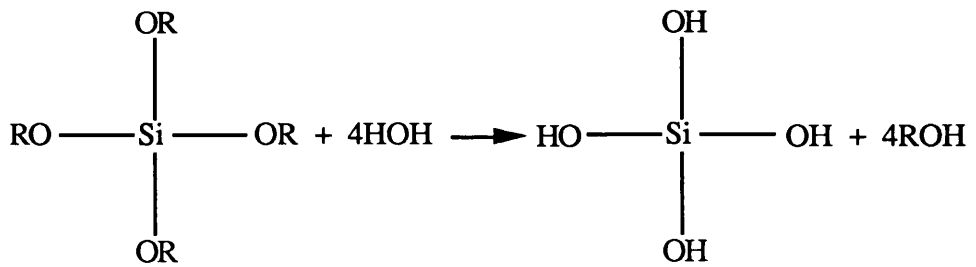


Figure 3.9

The second stage involves the loss of water through condensation as shown below in figure 3.10.

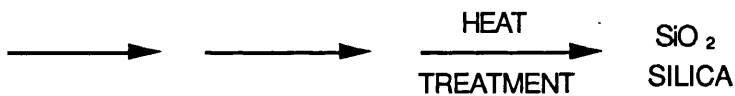
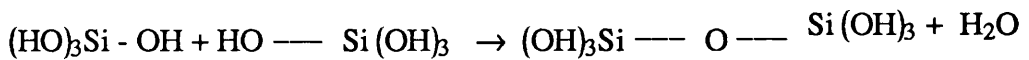


Figure 3.10

Repetition of this reaction results in the formation of a solution containing small chains and networks of the metal oxide, known as a sol. Cross linking between the chains and networks results in larger groups until a solid is formed. The solid is generally gelatinous and termed a gel. Following a heat treatment at a temperature of 1000°C, the gel produces a uniform dense ceramic matrix. Conventionally prepared powders of similar composition require processing at softening temperatures of the order 1700°C. Due to the high softening temperatures it is acceptable to use a sol-gel processed composite in applications where the operating temperature is continuously above the gel-matrix processing temperature.

3.4.3 Chemical Vapour Densification

3.4.3.1 Introduction

The formation of a composite through a chemical vapour process

requires a surface reaction and a mass transfer of the ceramic precursors in a gaseous state. Gases containing the precursors diffuse through the preform via gaps or pores between the fibres. On contact with the fibres a reaction takes place which results in the decomposition of the ceramic on the fibre. This surface reaction can be achieved between several ceramics. Problems are immediately encountered with the process, the most prominent being that of surface densification. Resulting in little, or no, further vapour infiltration of the preform as shown in figure 3.11. The adoption of sensitive manufacture techniques can succeed in producing highly densified composites. An attribute of chemical vapour processing is the ability to deposit ceramics at medium and low temperatures, depending on the nature of the activation of the reaction. The processes to be examined are chemical vapour deposition, isobaric/isothermal, and forced chemical vapour infiltration.

3.4.3.2 Chemical vapour deposition

Chemical vapour deposition is a process used to form coatings on metals, ceramics and ceramic fibres. Various coatings, including borides, carbides, nitrides and silicides, can be formed by this process. In chemical vapour deposition the thin layer is formed molecule by molecule. The parent material is vaporised and thermally decomposed to form a reaction product which forms a coating. In many cases fibres are pre-coated prior to preform manufacture to create an interface between the fibre and the matrix. This allows better control of the interfacial properties of the fibres during pullout, enhancing the toughness of the composite.

This process is useful in producing a uniform coating on a complex surface, but can result in surface densification when used to densify ceramic preforms. Reed (1987) described the reaction to produce silicon carbide deposited below 1000°C from CH_3SiCl_3 in the presence of hydrogen as:

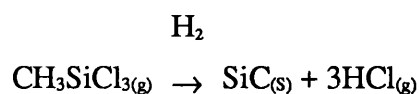


Figure 3.12

The purity of the deposit, and the deposition rate, are dependent on the initial composition, the pressure and the temperature of the process. This process forms the basic mechanisms on which all other chemical vapour processes are based.

3.4.3.3 Chemical Vapour Infiltration (CVI)

The chemical vapour infiltration process is concerned with densifying a ceramic preform through pores or gaps between the fibres. The deposition rate is extremely sensitive to temperature and pressure gradients. Deposition depends on the reactant gas diffusing into the preform to allow a uniform growth of the ceramic. The deposition rate is therefore dependent on surface kinetics governing the diffusion rate. Forcing the deposition rate above that of the diffusion will result in surface densification and a dramatic reduction in the densification of the preform.

Rossignol et al (1984) modelled a porous fibre preform as a cylindrical pore in which a matrix was deposited through chemical vapour infiltration. This extended work by Van Den Breckal et al (1981) who showed that the deposition rate on a flat surface was controlled by a dimensionless group known as the Sherwood number. Van Den Breckal (1981) established that low deposition rates were achieved with low Sherwood numbers.

Naslain et al (1989) examined the effect of temperature and pressure on the deposit profile of a cylindrical pore. An incremental computational procedure allowed the pore to be gradually sealed by the deposit and a measure of the uniform deposit depth made. This was then be used to estimate ideal conditions for high densification of preforms. These findings indicated that low temperatures and pressures combined with large pore diameters (of the order 100 μ m) produced high deposition over the length of the pore, and low Sherwood numbers.

Using a similar dimensionless grouping to the Sherwood number, Fitzer et al (1986) derived the maximum depth at which a pore could be deposited uniformly with a ceramic. The findings were consistent with those of Naslain et al (1989) where low temperatures and large pore diameters produced highly

densified preforms.

3.4.3.4 Forced Chemical Vapour Infiltration (FCVI)

Methods of accelerating the manufacture of isobaric/isothermal chemical vapour infiltration have been the subject of much recent research. Work documented by Besmann et al (1989) claimed a reduction in manufacture time of a composite from weeks to less than 24hrs. The process, known as forced chemical vapour infiltration, produced specimens with 90% of the theoretical density and strengths of 400-450MPa and noncatastrophic failure.

This process replaces the steady state conditions used in isobaric/isothermal chemical vapour infiltration for one containing temperature and pressure gradients. In isobaric/isothermal chemical vapour infiltration processes, low deposition rates are required to prevent surface densification of the preform. FCVI encourages surface densification on one side of the preform with densification proceeding it from that surface to the other.

The introduction of pressure and temperature gradients allows the deposition of the ceramic and the direction of matrix formation to be controlled. Gases entering the ceramic preform are at a low temperature and high pressure. At the low temperature the gas does not react with the preform and no deposition occurs. Continuing through the preform the gas pressure drops whereupon it encounters the hot surface resulting in rapid deposition at the outer surface of the preform. As the deposition grows so heat is transferred towards the cooled gas inlet via conduction through the newly formed matrix. The process continues until complete densification is achieved. Extremely sensitive control of pressure, temperature and rate of cooling are required to create a composite using this process.

3.4.4 DIMOX Densification Process

The Directed Metal Oxidation (DIMOX) process was developed by the Lanxide Corporation to densify preforms with the product of a liquid metal-gas reaction (Newkirk et al 1987). For example molten aluminium and oxygen are reacted to form alpha aluminium oxide. Similarly the use of nitrogen forms aluminium nitride. The nature of the reaction product allows it to form in and around porous preforms.

The preform is placed in contact with the parent molten metal as shown in figure 3.13. During the reaction a reaction product grows from the original metal surface. To sustain the reaction wicking occurs along microscopic channels in the reaction product. The resulting matrix is a ceramic/metal composite interconnected in three dimensions with a metal content typically between 3-15% by volume (Schiroky et al 1989). The matrix is free of impurities at the grain boundaries. This is a desirable feature for high temperature applications. An advantage of this process is the ability densify shapes too intricate for CVI with low levels of porosity. The final shape of the composite may be controlled during processing by fixing a barrier or casing around the preform restricting the growth of the reaction product.

Of particular relevance to the present work is SiC/Al₂O₃ whose manufacture by the DIMOX process is now described. Nicalon fibres, with diameters of the order of 20 µm and a boron nitride coating of the order 1µm thick, are woven into a 0-90 cloth. Layers of the woven cloth were laid and compressed in a porous mould then partially densified with a 2µm layer of SiC by the CVI process. This serves the dual purpose of binding the preform into a stable shape and providing a suitable reaction surface for metal oxide deposition. An alumina matrix is formed by the DIMOX process followed by a nitriding treatment to reduce the level of metal in the matrix. The finished component is therefore a multiphase composite. Figures 3.14 and 3.15 show the cross sections of an undeformed SiC/Al₂O₃ composite. Figure 3.14 shows the SiC fibre with the boron nitride interface, the CVI layer and densified Alumina matrix. The crack shown in figure 3.15 is a result of the thermal stresses produced during cooling from the process temperature to ambient.

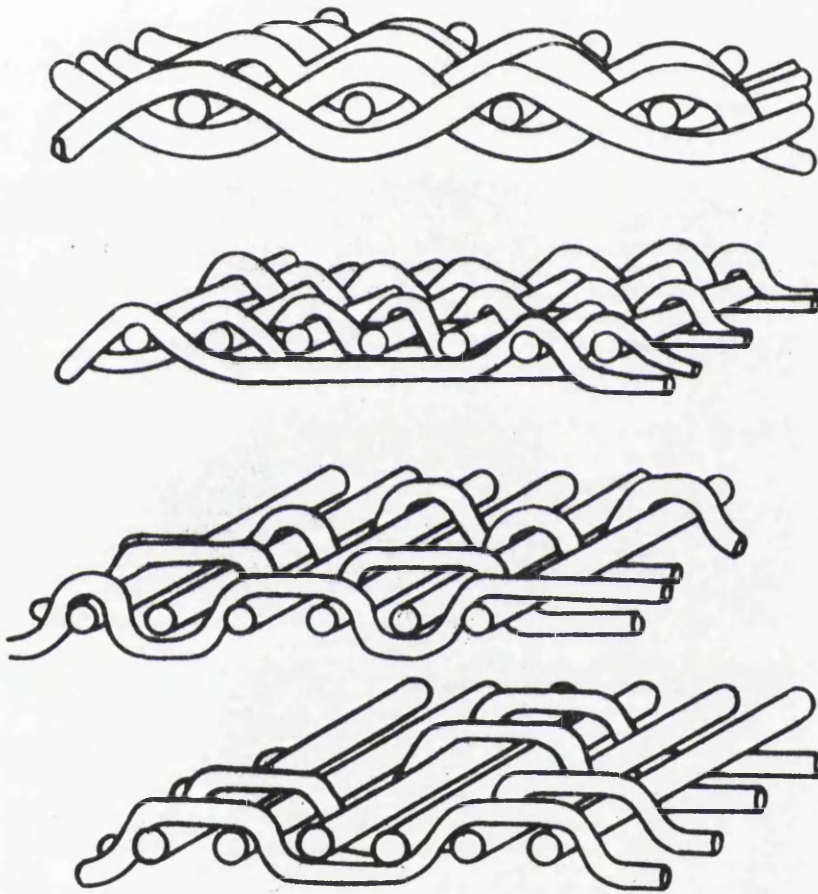


Figure 3.1 Basic Weaves

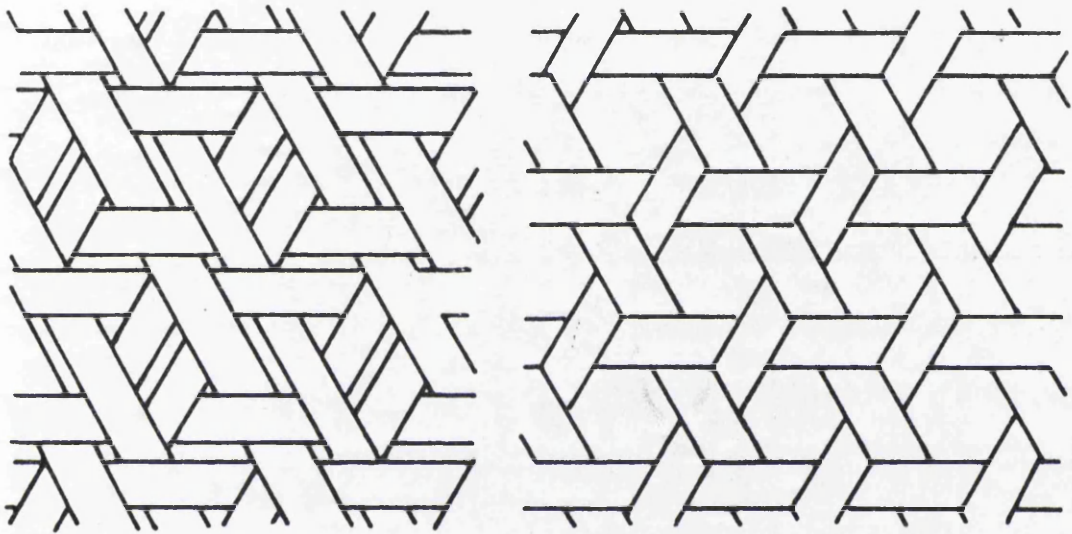


Figure 3.2 Triaxial Weaves

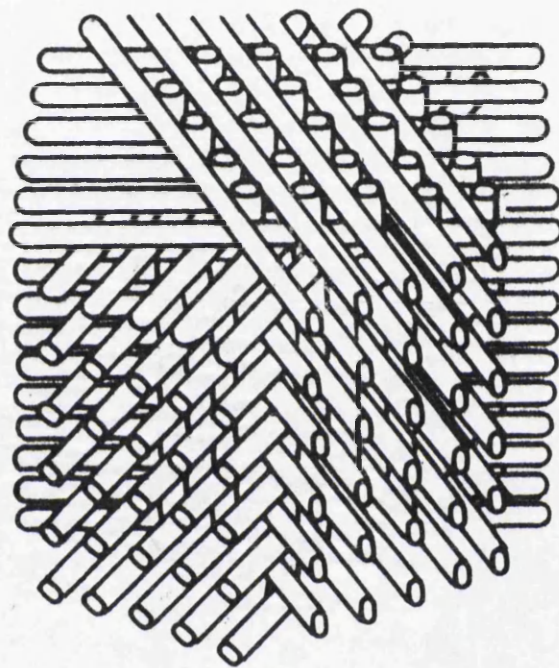


Figure 3.3 Four Dimensional Layout

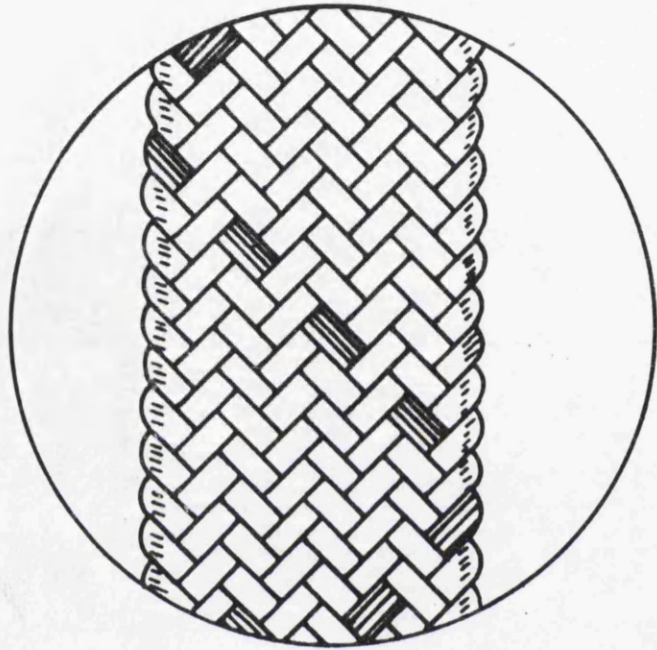
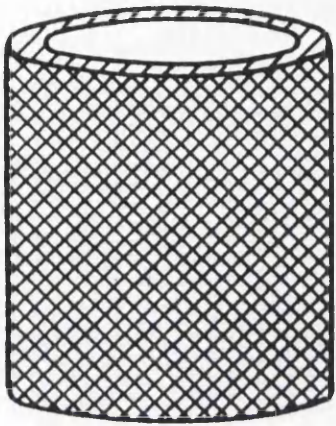


Figure 3.4 Two Dimensional Braid

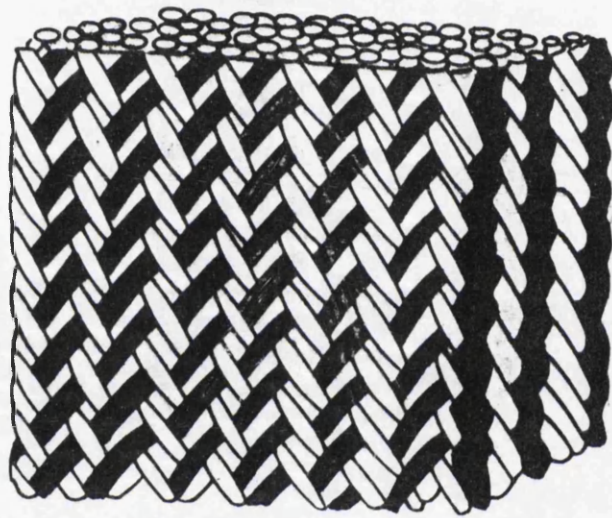


Figure 3.5 Three Dimensional Braid

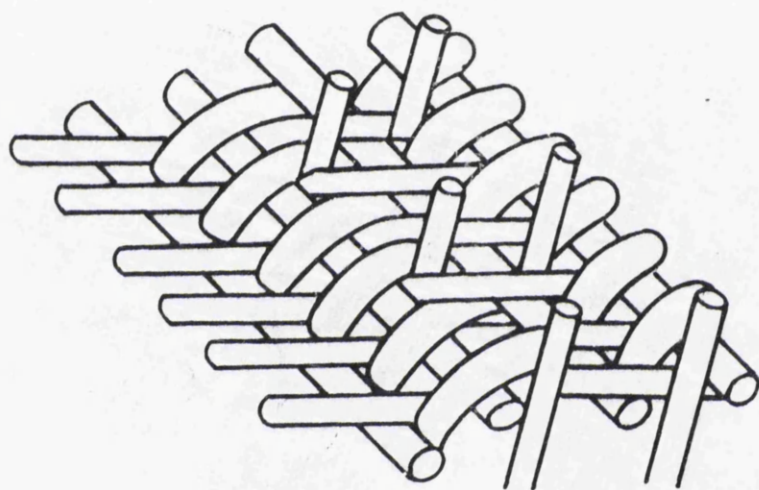


Figure 3.6 Four Dimensional Triaxial Braid

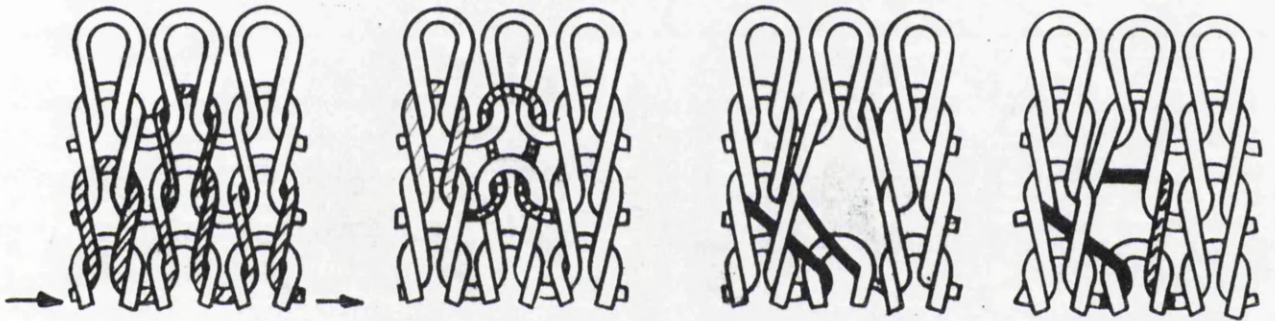


Figure 3.7 Plain Knit Configurations

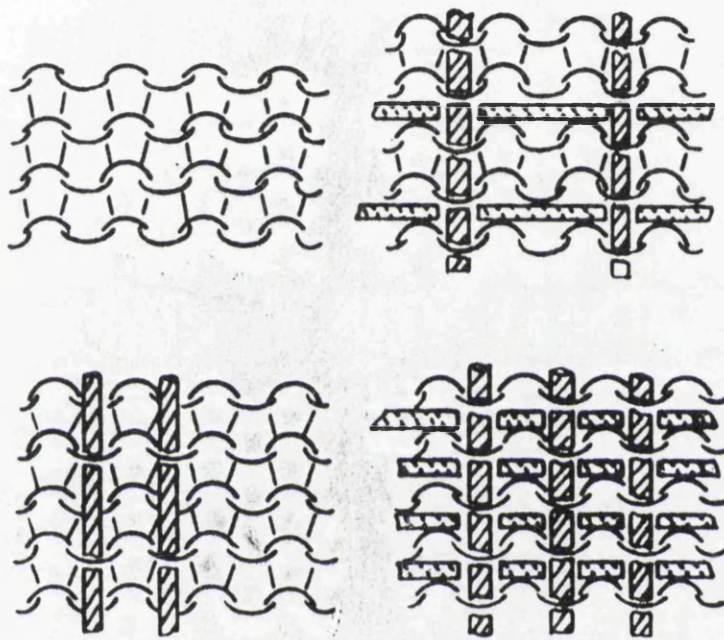


Figure 3.8 Directionally Strengthened Knits

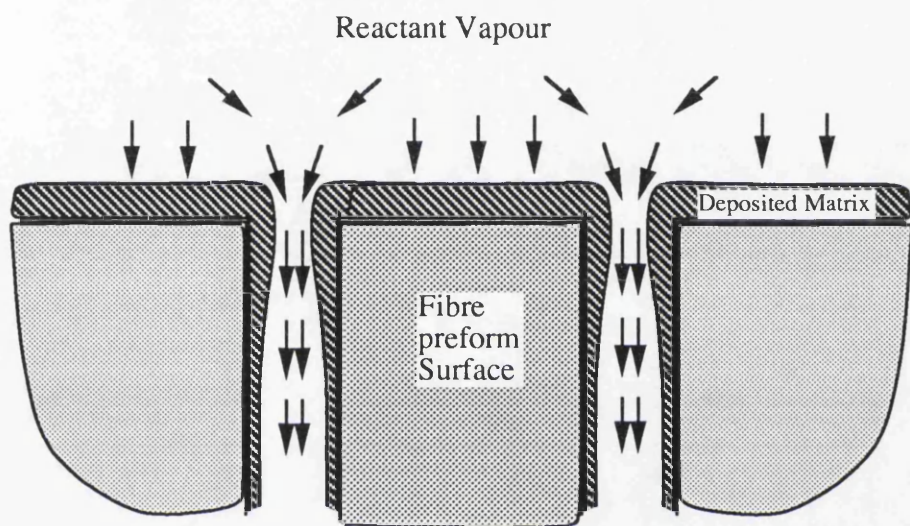


Figure 3.11 Surface densification of a preform caused by closing of pores in the preform surface thus preventing the oxide vapour flowing into the centre and densifying.

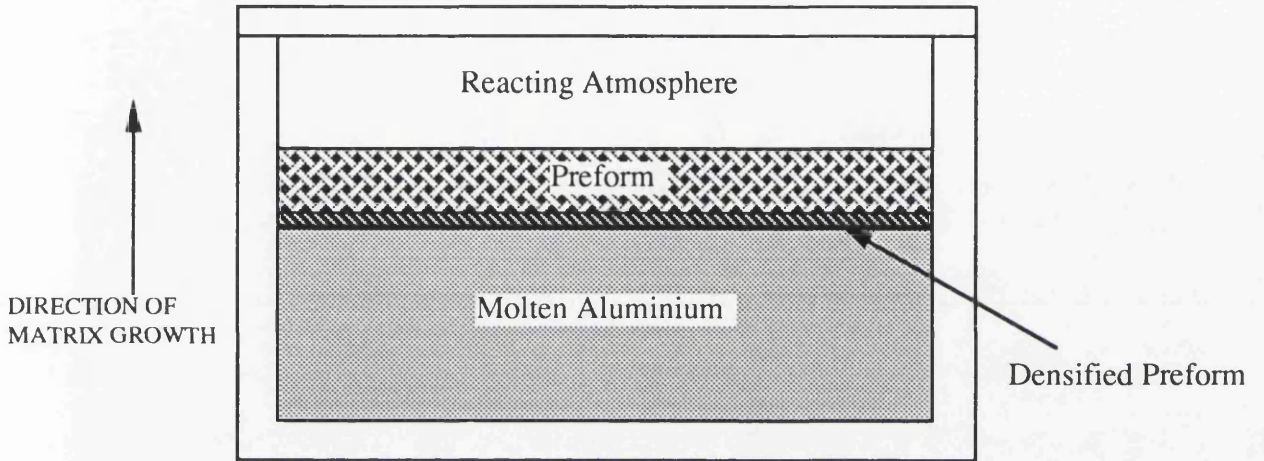


Figure 3.13 The DIMOX process configuration

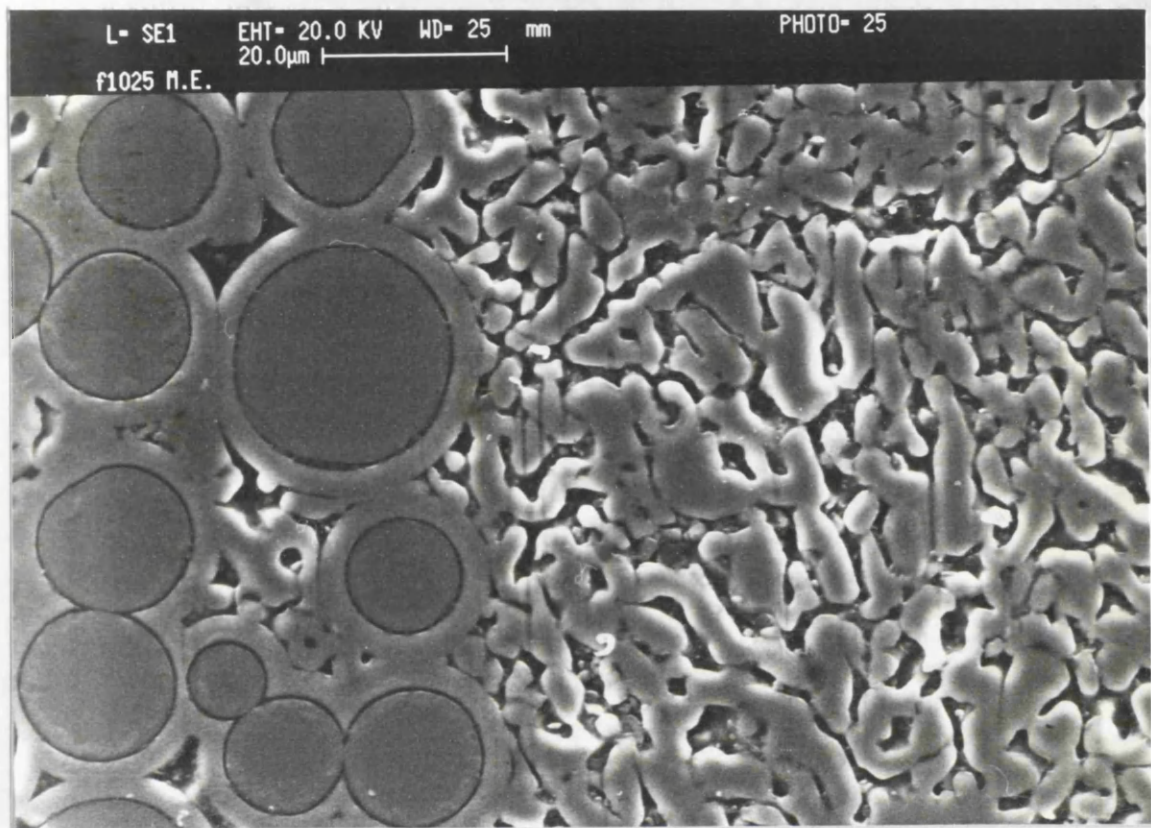


Figure 3.14 Cross section of a SiC-Alumina composite with the SiC Fibre, Boron coating, a CVI layer of SiC and the Alumina Matrix.

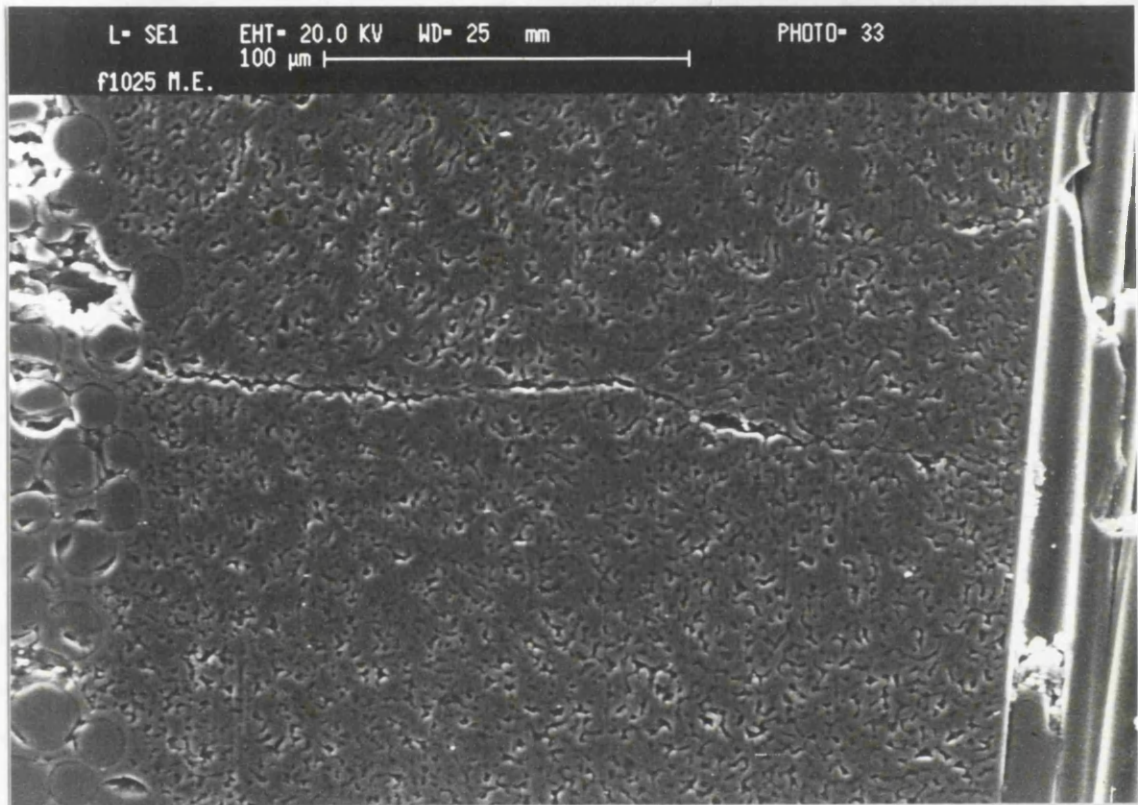


Figure 3.15 Cross section of a SiC-Alumina composite with a thermal induced crack traversing the Alumina matrix.

4 Materials

4.1 Introduction

From an engineering viewpoint the use of ceramic composites in high temperature environments is an inviting prospect. However the expense of manufacturing these materials is very high and there is the added disadvantage of long manufacture times. The expense can be balanced by the technical advantage gained over a company's competitors. Laboratory testing has demonstrated the potential of these materials at high temperatures although little is known regarding design guidelines for ceramic composites.

It is proposed to use ceramic composites to upgrade high temperature aero engine components where the super alloys currently used are at the peak of their performance. Particular interest has focused on the exhaust diffuser unit of an EJ 200 engine manufactured by Rolls-Royce. This non-critical component in the engine serves as a test bed into which advanced materials may be introduced. Information currently available on ceramic composites is limited. This can be partly attributed to the difficulties of fabrication which are hampered by problems of producing reliable material properties. By the nature of the manufacturing processes, the composites frequently contain damage in the form of matrix micro-cracking or porosity. Porosity is an inherent byproduct of the densification process. Micro-cracking can occur during cooling from the manufacturing temperature as a result of a modulus mismatch between the fibres and matrix. It is desirable that this damage is minimised and as a result a candidate materials for the exhaust diffuser unit of the engine include SiC-SiC composites whose low modulus and thermal expansion mismatch prevents thermo-elastic cracking. This material is manufactured using chemical vapour deposition which is both an expensive and slow process. The structure of such composites usually consists of continuous woven fibres embedded in a brittle matrix with a weak fibre-matrix interface. The failure strain of the matrix is significantly lower than the fibre so that the resulting tensile

deformation is through matrix micro-cracking.

The development of the necessary knowledge for effective design requires initial testing of generic shapes followed by prototype manufacture and testing. This process is slow and requires a right first time approach. For these reasons a model material has been investigated with the aim of using this to accelerate and reduce the cost of the development of the design guidelines for ceramic composites. Butler (1992) has proposed a polymer model of SiC-SiC which is intended to have similar deformation modes to the ceramic composite. The material is inexpensive and has a processing time of a day as against months for the ceramic composite. It was proposed to investigate the use of the polymer system to provide an experimental benchmark of the constitutive relations without the complication of processing damage. This work was extended into testing generic shapes or sub-elements representing configurations expected in aero-engine components. The sub-elements featured changes in cross section and 'T' joints. The results of the sub-element tests were then be compared with computational solutions using developed constitutive relations.

Although the polymer system was intended to provide vital information regarding the design of composite components there was still be a requirement to benchmark the constitutive relations using a ceramic composite. Currently, the expense and slow manufacture of the SiC-SiC composite has resulted in a lack of material with uniaxial data produced by Hillier (1991). The requirement to benchmark the polymer against a ceramic was satisfied using sub-elements of SiC-Al₂O₃ manufactured using the DIMOX process. This material deforms through matrix micro-cracking as in the SiC-SiC and the polymer systems. This chapter examines the characteristics of the polymer composite and the SiC-Al₂O₃ composite.

Initial testing focused on the properties of the constituents of the polyester composite. Matrix tensile specimens were manufactured and tested to failure. Fibre data was produced by experiments on bundles of unimpregnated polyester fibre tows and single tows impregnated with the polyester matrix. The response of the polyester composite was then examined. Tests were performed to determine the elastic modulus and the failure modes in tension and compression. The effect of a tensile load acting

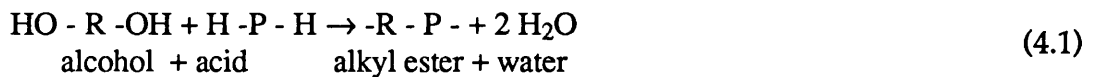
at an angle to the fibres was investigated by testing specimens with fibre orientations ranging from 0-90 to 45-45. The uniaxial 0-90 testing was extended to include cycling of specimens to failure. The analysis of the hysteresis loops formed provided information of the development of micro-damage, the extent of micro-cracking and the development of inelastic strains. In addition to the testing of woven preforms, the experiments on the polymer examined the uniaxial response of knitted fibre architectures. These experiments investigated the effect of fibre volume fraction on the mechanical properties as well as the failure modes

Testing was extended to included the constituents of the SiC-Al₂O₃ system with tests limited to individual SiC fibre tows. Uniaxial composite data was supplied by Merril (1993). Compared to the polymer system the test data available on the ceramic is restricted. However due to the similar deformation modes of the ceramic and the polymer it was hoped to apply any principles developed for the polyester to the SiC-Al₂O₃ system.

The experimental work provided input data for a computational model of both the polymer and the SiC-Al₂O₃ system. This was based on the work of Aveston et al (1971). The computational model was then used to analyse the sub-elements.

4.2 Polyester Matrix Properties

The matrix was prepared from polyester resin (Spectra 1991) and hardener (Pergan 1991) in the ratio 50:1 by weight, mixed and stirred until the hardener was completely dissolved. The mixture was left to stand in an ultrasonic bath for two minutes to remove any air bubbles. The matrix material was then poured into tensile specimen mould, the dimensions of which are shown in figure 4.1. This was allowed to stand for 4 hours during which time the matrix set. The basic thermoset reaction is:



The resulting composite was cured for two hours at a temperature of 180C, removed from the oven and allowed to cool in situ. The tensile specimens were tested on a Lloyds 10000 testing machine at a displacement rate of 0.2mm/min with an extensometer mounted directly onto the specimen.

Figure 4.2 shows a typical stress strain response of the polyester matrix. The average elastic modulus was 3.8GPa. Micro-cracking and failure were coincident at a stress of 24MPa and a strain of 0.0065. The material exhibited a brittle linear elastic response with no indication of yield prior to failure.

4.3 Polyester Fibre Tests

4.3.1 Method

Unimpregnated fibre bundles were formed from strips of woven polyester cloth containing between fourteen and sixteen fibre tows. These were wound around a mandrel to which they were bonded with polyester resin. The mandrel was then gripped as shown in figure 4.3. This removed any pinching and reduced the stress concentration at the grips. The specimens were tested on an Instron testing machine with the specimen

displacement recovered by an extensometer mounted between the grips. The fibre radius was measured using a SEM to be 11µm with an average of 220 fibres in a tow.

Individual tows were removed from the woven cloth and saturated in the polyester matrix. The tows were lightly stretched, to remove any “wrinkles” produced by the weaving, then cured. The impregnated tows were cut to length, wrapped, bonded to a mandrel and gripped between rubber pads, to remove any stress concentrations, as shown in figure 4.4. Displacements were recorded using a laser extensometer with reflective tape attached directly onto the fibres.

4.3.2 Fibre Tow Results

Figure 4.5 shows the stress-strain response of two fibre bundles of unimpregnated tows. The load is normalised to give the stress/fibre. To determine the cross section area of a single tow, a 0-90 woven composite was considered. Here the composite has a fibre volume fraction of 36% containing eighty eight tows in the direction of loading over a section area of $4 \times 10^{-5} \text{m}^2$. The volume fraction incorporates both the axial and the transverse tows. The area fraction of the tows aligned in the direction of loading of the composite was therefore 18%. This gave an average tow area of $8.2 \times 10^{-8} \text{m}^2$. Using this area the modulus, taken over the gauge length, was 5.4 GPa with an initial failure stress of 760MPa at a strain of 16.5%.

It was observed during the test that the sudden reductions in the load were associated with the failure of individual tows. It is assumed that the failure load of each tow corresponds directly to the magnitude of the step. Figure 4.6 shows the distribution of failure loads for both tests against the percentage of failed tows. From this the average stress of the tows was calculated to be 990 MPa. The failure loads of all the fibres from experiments on unimpregnated bundles were collated and expressed as a two parameter Weibull distribution.

$$P(\sigma) = 1 - \exp\left(-\left(\frac{\sigma}{\sigma_0}\right)^\beta\right) \quad (4.2)$$

Here the fraction of broken tows which failed below a stress σ is denoted by the cumulative probability $P(\sigma)$, which is a function of the fibre stress (σ) and two curve fitting constants σ_0 and β . The distribution in figure 4.6 was expressed as the fraction of broken fibres and a function of the fibres stress as shown in figure 4.7. From this the Weibull curve fitting constants σ_0 and β were determined to be 1 GPa and 1.85.

The stress-strain response of the impregnated fibres are shown in figure 4.8. The initial elastic response correspond to an elastic modulus of 7.7 GPa with failure occurring at a stress of 366 MPa and a strain of 0.1625.

4.4 Composite Experiments

4.4.1 Specimen Manufacture

A composite was manufactured as a sheet 125mm square by 3mm thick from woven 0-90 polyester filament yarn (Enka 1991), polyester resin Spectra (1991) and hardener Pergan (1991). The matrix was prepared by the method described in section 4.2. Matrix material was poured into a mould whereupon the polyester fibre preforms were pressed into the resin. This process was repeated until the required thickness was achieved. A pressure of 3.2 MN/m² was applied to the composite for 4 hours during which time the matrix set. The composite was cured and tensile specimens cut from the sheet to the dimensions shown in figure 4.9. The fibre volume fraction of the composite determined by weight was 36%. Over the gauge length the composite had an average area of 4×10^{-5} m² containing eighty eight tows. Off axis woven specimens were manufactured following the same procedure but with the laminates cut to the required angle of alignment. The 0-90 woven sheet was also tested to determine the delamination stress of the laminate using a 50mm square specimen cut from the prepared laminate sheets. This was bonded using an epoxy resin Araldite 2005 (Ciba-Geigy 1991) to metal grips as shown in figure 4.10.

The knitted composite sheets were made by Butler (1991) then cut to the dimensions in figure 4.9. Tubular specimens were manufactured to the

dimensions shown in figure 4.11 The matrix was prepared as before, the woven cloth was dipped into the matrix and wrapped around a mandrel. This continued until a nominal thickness of 3 mm was achieved. The mandrel was encased in a sleeve exerting a radial compressive load and allowed to set. The tube composite was then cured and cut into 15mm lengths for testing. In all the polyester specimens the fibre volume fractions were determined by weight of fibres measured prior to manufacture compared to the final weight of the composite, assuming the fibres and matrix to have the same density

4.4.2 Test Method

Composite tensile and interlaminar specimens were manufactured from the woven polymer composite containing eight layers of woven cloth with an average fibre volume fraction of 36% by weight. The knitted architectures tested included Jersey and Ribbed patterns. The latter was tested in warp and weft configurations at fibre volume fractions ranging from 24.2% to 47.2% by weight. The configuration of these architectures is defined in section 3.0. The specimens were tested on an Instron testing machine at a cross head displacement of 0.5 mm/min with an extensometer mounted directly onto the specimen. In the case of the tensile delamination tests, an extensometer was mounted across the grips as shown in figure 4.10.

Of the nine woven tensile specimens tested, three were taken to failure. The remainder were taken to varying levels of strain between initial micro-cracking and failure. The objective was to measure the development of micro-cracking and the decay in modulus with strain. From this information the interfacial shear stress and the matrix and fibre contributions to the overall composite response were determined

From the knitted materials supplied by Butler (1991) it was possible to machine only two specimens for any one fibre volume. This limited the information gained from the load curves to micro-cracking, the failure modes and failure levels of stress and strain.

4.4.3 Results

Figure 4.12 shows the stress-strain response of the composite, cycled to failure normalised by the micro-cracking stress and strain. Tensile micro-cracking was observed to start at an average stress of 35 MPa and an average strain of 0.0104 corresponding to an elastic modulus of 3.37GPa. Tensile failure occurred at a stress of 125MPa and a strain of 0.16.

As the 0-90 specimen was strained, the number of micro-cracks increased until micro-crack saturation occurred and no further micro-cracking damage was observed. Figure 4.13 shows the micro-crack density ($\rho_{\text{cracks/cm}}$) non-dimensionalised by the saturation density (ρ_{sat}) as function of strain normalised by the micro-cracking strain. The micro-crack density saturated at a strain of 0.108 and an average crack density of 10.6 cracks/cm measured over a 5cm length. This corresponds to the final rise in the original stress strain response shown in figure 4.12.

The cycles shown in figure 4.12 show a decay in the secant modulus of the material. This secant modulus was calculated between the initial unload point and the zero load point. This was repeated for several points taken from the specimens tested. The secant modulus (E_{sec}) was normalised by the initial elastic modulus ($E_{\text{ela}}=3.4\text{GPa}$) and is given as a function of the applied strain non-dimensionalised by the micro-cracking strain ($\frac{\epsilon}{\epsilon_m}$) in figure 4.14.

To examine the inelastic response of the material the permanent strain after unloading was plotted as a function of the applied strain, both normalised by the micro-cracking strain ($\epsilon_m=0.0104$) as shown in figure 4.15.

The results of tensile tests for the off axis fibre layups indicated a reduction in modulus with an increase in mis-orientation as shown in figure 4.16. Figure 4.17 shows a typical failed off axis specimen, from which the apparent mode of failure is through fibre tow-matrix interface failure followed by pullout.

The tensile delamination response is shown in figure 4.18. The initial elastic modulus was 0.26 GPa at a strain of 0.003. The specimen cracked but continued to load up to a stress of 0.688MPa and a strain of 0.00856 when the

stress began to drop to a final value of 0.042MPa at a strain of 0.1

The result of a uniaxial compressive test is shown in figure 4.19. The compressive yield stress was 55 MN/m² at a strain of 0.013. The specimen was tested to a total strain of 0.18 before large scale delamination occurred. After yield, the stress fluctuated with the applied strain between stresses of 55 MPa and 45 MPa up to a strain of 0.15 during which large scale delamination was observed to occur.

Figures 4.20, 4.21 and 4.22 show the stress-strain curve for the Jersey knit, the Ribbed warp and the Ribbed weft as a function of the fibre volume fraction V_f . The elastic modulus, micro-cracking stress, failure stress and strain are tabulated as a function of V_f in figure 4.23. The data shows a decrease in modulus with an increase in V_f for all the configurations. The initial micro-cracking stress was independent of V_f but the final failure stress dropped with V_f . The strain to failure of the Jersey knitted specimens increased with increasing fibre volumes. The failure strain of the ribbed Weft was seen to increase with a reduction in V_f while the failure strain of the Ribbed Warp dropped with V_f .

4.5 Ceramic Composite and Fibre Properties

The properties of a 0-90 woven SiC-Al₂O₃ composite manufactured by Du Pont Lanxide (Newkirk et al 1987) by the DIMOX process were required for a computational analysis. Uniaxial tensile data was produced for a composite by Du Pont Lanxide (1992) shown in figure 4.24. The composite contained a volume fraction of 36% of SiC fibres arranged in tows which contained 475 fibres with a fibre radius of 16µm. The modulus of the SiC-Al₂O₃ was 112 GPa with micro-cracking occurring at a stress of 78.5 MPa and a strain of 0.0007. Failure of the composite occurred at a stress of 238MPa and a strain of 0.0051.

To provide information on the constituents of the Du Pont SiC-Al₂O₃ system, individual SiC fibre tows were tested in tension. To prevent stress concentrations, the specimens were wound and bonded to a mandrel then gripped between rubber pads as shown in figure 4.4. The tests were performed on an Instron testing machine with a cross head displacement rate of 0.5mm/min. The specimen displacement was measured using a laser extensometer with reflective tap mounted directly onto the specimen. Figure 4.25 shows the response of the SiC fibre. The initial modulus is 259 GPa. Failure occurred at a stress of 1.45 GPa and a strain of 0.012.

The ceramic fibre tow response in figure 4.25 displays a non-linear curve after the initial elastic region. If it is assumed that the individual fibres in the tow are linear elastic but the post elastic response can be attributed to a distribution of failure stresses of the fibres. It follows that the stress in the tow can be described the two parameter Weibull distribution.

$$\sigma_{\text{tow}} = \sigma \exp - \left(\frac{\sigma}{\sigma_0} \right)^\beta \quad (4.3)$$

Here the fibre tow stress (σ_{tow}) is a function of the fibre stress (σ) and two curve fitting constants σ_0 and β . Figure 4.25 shows the response of the ceramic fibre tow compared to the tow stress (σ_{tow}) with curve fitting constants $\sigma_0= 3.48\text{GPa}$ and $\beta =1.871$.

4.6 Model Material Verification

Although the polymer system was initially developed to model SiC-SiC composites, the stress strain relations were also compared with the SiC-Al₂O₃ composite. The polymer response is produced from a 0-90 woven composite as described in section 4.4 with a fibre volume fraction of 36%. The SiC-SiC data was as produced by Rolls Royce (Meril 1992) for a 0-90 woven composite manufactured by CVI. The SiC-Al₂O₃ is as described in section 4.5 manufactured using the DIMOX process by Du Pont Lanxide.

Figure 4.26 shows the tensile response of SiC-SiC, SiC-Al₂O₃ and the model material in tensile tests at room temperature. Although the levels of stress and strain are very different, the mechanisms of failure are similar. Both the polymer and the ceramic composite have a brittle matrix reinforced with continuous fibres separated by a weak interface. As a result of these properties the mode of deformation in both the ceramics and the polymer was dominated by matrix micro-cracking. This was followed, in the case of the SiC-SiC and the polymer, by a region of loading in which micro-crack saturation is observed. The stress-strain curves of the ceramics and the model material were non-dimensionalised by their respective micro-cracking stress and strain. Figure 4.27 compares the non-dimensionalised stress and strain curves of the ceramics and the model material. For the polymer, the SiC-SiC and the SiC-Al₂O₃ the normalising parameters are the micro-cracking stress and strain (σ_c , ϵ_c) with values 35MPa and 0.0104, 100MPa and 0.00065, 78.5MPa and 0.0007 respectively. From this diagram it can be seen that the non-dimensionalised stress strain curves of the SiC-SiC and the model material are closely similar. The similarity of these two curves can be attributed to both materials having a weak interface and low modulus mismatch. This combined with a brittle matrix and relatively ductile fibres supports the use of the model material as a test bed for the SiC-SiC material. The SiC-Al₂O₃ does however produce a different response to the model material. This may be a result of different interface properties and a significant modulus mismatch introducing processing damage in the form of matrix micro-cracking. It should be noted however that the deformation

and failure mechanisms will be similar allowing any knowledge accumulated from the testing of the model material to be used in the design of components manufactured from SiC-Al₂O₃.

An advantage of the similarity of the SiC-SiC and the model material normalised responses allowed the testing of specimens manufactured from these materials to be compared directly. In addition careful normalising of the results of computational analysis of components allows these to be related directly to the ceramic. With a properly developed constitutive model it is therefore be possible to analyse components prior to manufacture.

4.7 Discussion

4.7.1 Tensile behaviour of Impregnated and Unimpregnated Tows

The stress-strain response of the unimpregnated polyester tows shown in figure 4.5 can be divided into three regions. Section (1) corresponds to the straightening of the fibres due to the wrinkles produced during weaving of the cloth. The second region shows a linear elastic response of the bundle. In the third section individual fibre tows fail and give rise to distinct steps in the stress-strain relation.

In the case of the unimpregnated polyester tows the unloading curve may be described in two ways. The first assumes that the tows are unreliable and the response arises from a statistical distribution of tow strengths. The second description considers the tows to be highly reliable, and the response is the result of a distribution of strains in the individual tows at the start of the experiment. The reliable tow argument would require the last fibre that failed, to have a 15% residual "slack" strain or 15mm over the 100mm working section prior to the experiment starting. This is not unreasonable if sliding in the grips is considered and would only require a 7.5% residual strain or 15mm over 200mm (inclusive of the grip length of the specimen). A more realistic scenario is a combination of unreliable fibres with a distribution of initial strains. The fibre strength distribution of the unimpregnated polyester fibre tows can be compared with those of Cao (1990) for Nicalon fibres. In this case Cao (1990) determined the strength to break individual fibres by measuring the mirror radius on the fractured fibres and by taking the fibre fracture toughness as $1 \text{ MPa}\cdot\text{m}^{\frac{1}{2}}$. Nicalon fibres made by differing processing routes gave Weibull distribution parameters (σ_0, β), of 2.47 GPa, 2.1 and 1.38GPa, 3.1. Although the Nicalon fibre strengths are 3 and 5 times the strength of polyester fibres it should be noted that the reliability parameters (β) are comparable. In the case of the SiC fibre tows tested the Weibull parameters (σ_0, β) were 3.58GPa and 1.871. This is comparable to the results of Cao (1990), although the mean strength is higher. The Weibull parameters of the SiC and the polyester tows were

closely similar in terms of the reliability parameter but varied by 3 to 4 times in strength. The variation in strength between the polyester and the ceramic composites would be predictable. However the comparison of fibre reliability parameter (β) is important as this has a strong effect on the mode of toughening of the composite.

The deformation of the impregnated tow can be compared to the analysis of Aveston et al (1971). The impregnated response shown in figure 4.8 may be characterised by three regions, linear elastic, micro-cracking region and micro-crack saturation. The failure stresses of the impregnated and the unimpregnated tows are closely similar. However at any given strain the stress born by the impregnated tow is always greater than the unimpregnated tow as a result of the matrix contribution. Aveston's model assumes linear elastic fibres, so that when micro-cracking saturates the composite stiffness becomes $E_f V_f$. In the case of the impregnated tow the response of the reinforcement or fibre tow was non-linear. In the case of the impregnated tow where the fibre volume fraction was high ($V_f=0.48$) it would be expected that its response would be less affected by the matrix and more closely associated with that of the unimpregnated tow. This is shown in figure 4.28 where the response of the impregnated tow is compared with the unimpregnated tow. From this it can be seen that while the failure stresses are comparable, the strain to failure of the impregnated tow is less than the unimpregnated tow, as expected from Aveston's analysis. In the case of the failure stress, Aveston et al (1971) predicted this to be $\sigma_f V_f$. This compares well with the experiment as shown in figure 4.28.

To predict the failure strain of a composite Aveston considered two limiting cases where the matrix is broken into block lengths of L_s or $2L_s$. Failure of the composite will occur when the localised strain in the fibre reaches the fibre failure strain ϵ_{fu} . It follows that the failure strain of the composite (ϵ_{cu}) will always be lower than that of the fibre. Using the two block lengths L_s and $2L_s$, Aveston predicted the composite failure strain ϵ_{cu} to be bounded by the inequality:

$$\epsilon_{fu} - \frac{E_m \epsilon_{mu}}{E_f 2 V_f} < \epsilon_{cu} < \epsilon_{fu} - \frac{E_m \epsilon_{mu}}{E_f 4 V_f} \quad (4.4)$$

The matrix failure strain is ϵ_{mu} . The failure strain of the impregnated polyester tow is now considered. For this system the matrix modulus was 3.8GPa with a failure strain of 0.0065. For the unimpregnated tow the elastic modulus over the final portion of loading was calculated to be 5.4 GPa with a failure strain of 0.165 and a volume fraction of 0.48. Avestons prediction of the composite failure strain are taken from the failure strain of the fibre and are therefore associated with the micro-cracked region. The use of the polymer fibre modulus as 5.4 GPa is therefore justified. The predicted failure strain was calculated using equation (4.4) to be between 0.160 and 0.163. The experimental failure strain of the impregnated tow was 0.1625 in accord with Aveston's analysis.

4.7.2 Compressive and Interlaminar Behaviour

The results of the compressive tests shown in figure 4.19 are now discussed. Sammis et al (1986) considered the response of a brittle porous solid in compression. Here cracking transverse to the direction of compressive loading initiates at tensile stress concentrations at the top and bottom of pores. The overall response is described by four strain regions. The first region is attributed to alignment of the specimen and the test machine. The second region is a linear elastic up to the initiation of transverse cracking. In the third region continued crack initiation and growth provides a non-linear section of loading to failure. During the fourth region the specimen experiences delamination through buckling of the layers of the laminate. A similar response was observed by Rossignol et al (1987) who conducted compressive tests on a 2 D Carbon-Carbon composite.

The interlaminar or through thickness tensile response is shown in figure 4.18. In this direction there is no reinforcement hence it would be expected that the response would be largely dependent on the matrix properties. However a through thickness modulus and strength of 0.26GPa and 0.688MPa when compared to matrix properties of 3.8GPa and 24MPa suggests this not to be the case. This is supported by Voigt's bound of the composite modulus given by.

$$E_c = V_m E_m + V_f E_f \quad (4.5)$$

For the case of the polymer in the through thickness direction there was no reinforcement (ie $V_f = 0$). From equation (4.5) the composite stiffness would be 2.47GPa for a matrix volume fraction $V_m = 0.64$. Examination of the failed interlaminar specimens showed cracks initiating in between laminate layers from one side of the specimen. This would partly explain the low stresses measured, since the area of the specimen considered is much larger than the area over which the cracking is occurring. However the low elastic modulus cannot be explained as simply. In the direction of loading the composite modulus is dominated by the matrix modulus and the volume fraction of matrix ($E_c = V_m E_m$). In this direction cracks will form at the fibre matrix interface where debonding is favoured against matrix micro-cracking. This will reduce the apparant matrix modulus and a hence the composite modulus.

4.7.3 Tensile Behaviour of the Woven Polyester Composite

The tensile stress-strain curve of the 0-90 polymer woven specimen illustrated in figure 4.18 may be divided into three domains. The first is a linear elastic region up to the micro-cracking strain. The second section represents the strain region over which the matrix micro-cracks. In the third region matrix micro-cracking reached saturation and the load was primarily borne by the fibres.

Micro-scopic examination of the specimens showed the woven tensile specimen to be segmented into blocks of matrix bridged by tows as shown in figure 4.29. Figure 4.30 shows the composite stress-strain response compared to that of the stress in the unimpregnated tow weighted by the fibre volume fraction ($V_f = 0.35$). The response in the third region is therefore dictated by the fibre properties as modified by the frictional interaction with the matrix blocks (Evans et al 1989b).

The average block length or distance between micro-cracks in the composite past saturation can be compared with those in the impregnated tows. The average spacing of matrix cracks in the composite and impregnated tow were 1.06mm and 0.39mm with corresponding fibre volume fractions $\left(\frac{V_f}{V_m}\right)$ of 0.18 and 0.48. From Aveston the maximum stress in the matrix of block length $2L$ past micro-crack saturation where sliding is occurring over its total length is given by

$$\sigma_{m(max)} = \frac{2\tau L}{R} \frac{V_f}{V_m} \quad (4.6)$$

Here R is the radius of the reinforcement and τ the interfacial shear resistance. If it is assumed that the matrix micro-cracking stress in the composite and the tow are the same then:

$$\left(\frac{2\tau}{R}\right)_{IT} (L)_{IT} \left(\frac{V_f}{V_m}\right)_{IT} = \left(\frac{2\tau}{R}\right)_C (L)_C \left(\frac{V_f}{V_m}\right)_C \quad (4.7)$$

Here the suffices IT and C refer to the impregnated tow and the composite respectively. Incorporating the average block lengths and the fibre volume fractions of the impregnated tow and composite into equation 4.7 gave.

$$\left(\frac{\tau}{R}\right)_{IT} = 1.019 \left(\frac{\tau}{R}\right)_C$$

To a close approximation

$$\left(\frac{\tau}{R}\right)_{IT} = \left(\frac{\tau}{R}\right)_C \quad (4.8)$$

This may be interpreted in one of two ways. The first assumes the radius of the reinforcement R to be the radius of an individual fibre in the impregnated tow and the radius of the tow in the composite. Using a tow radius of 0.16mm and a fibre radius of $11\mu\text{m}$ measured using an SEM gives the ratio of the interfacial shear stress as.

$$\frac{\tau_{IT}}{\tau_C} = \frac{R_{IT}}{R_C} = 0.069 \quad (4.9)$$

The second interpretation of equation 4.8 assumes the shear stress acting on the reinforcement in the composite and the impregnated tow to be the same hence the reinforcing radii (R_{IT} and R_C) are equal. Figure 4.31 shows a failed impregnated tow with evidence of fibre pullout. This indicates the reinforcing in the impregnated tow to be the fibres. From the failure of the composite there is evidence that suggests the reinforcing element is the tow as shown in figure 4.29. Hence from equation 4.9 the interface shear resistance differs from the tow to the single fibre. A more realistic scenario arises if the area over which the stress is acting is considered. In the case of the single fibre in the impregnated tow, the area is accurately defined by the fibre radius. However in the case of the composite, the tow area cannot be properly described by a radius since the tow circumference is not round and is formed by many individual fibres. It is possible for the area of contact to be significantly higher than that predicted by the previous tow radius. This would therefore support the argument that the shear resistance is comparable while the size of reinforcing elements are different in the two experiments.

In the composite the ultimate strength is governed by tow failure between the blocks where the tow stress is maximum and is comparable with the unimpregnated tow failure in figure 4.30. SEM examination of the failed composite specimen, shown in figure 4.29, confirms this and shows little evidence of tow pullout.

During SEM examination of the composite the micro-cracking was also observed to occur perpendicular to the applied load. At the edge of the specimen transverse micro-cracks parallel to the applied load were observed between individual laminates as shown in figure 4.29. This is distinct from interface debonding as discussed by Evans et al (1989b) for composites with weak interfaces. Possible causes of this are thought to be a result of fibre straightening between the layers producing a tensile stress of a sufficient order to cause tensile delamination. This is supported by the interlaminar experiment where very low interlaminar strengths were observed.

Micro-cracking saturation occurs in the third region. The density of micro-cracks shown in figure 4.13 reached saturation at a strain where no further reduction in the secant modulus was observed ($\frac{\epsilon}{\epsilon_m} > 10$). Figure 4.15 shows the inelastic strain as a function of the applied strain up to micro-crack saturation. After micro-crack saturation the inelastic strain is linearly proportional to the applied strain. If the interface frictional resistance was sufficiently weak and the fibres were completely elastic, Aveston et al (1971) argued that there would be a limit on the inelastic strain which is dependant on the block length (2L) during micro-crack saturation. The maximum inelastic strain according to Aveston is a function of the constituent moduli, the micro-cracking strain of the matrix (ϵ_{mu}) and limited by the block length such that:

$$\frac{\epsilon_{mu} V_m E_m}{4 V_f E_f} \leq \epsilon_{\max \text{ unload}} \leq \frac{\epsilon_{mu} V_m E_m}{2 V_f E_f} \quad L_s \leq \text{Block length} \leq 2L_s \quad (4.10)$$

This assumes the shear stress during sliding to be the same during loading and unloading.

The results of the uniaxial tests showed a linear increase in the inelastic strain component after micro-crack saturation. This suggests the interface resists reverse sliding. This results in an increase in the inelastic strain component after unloading throughout micro-crack saturation.

An increment of strain ($d\epsilon$) applied past saturation (ϵ_{sat}) acts on the embedded section of the fibre and equally on the matrix bridging section of the fibre resulting in a composite stiffness $E_c = E_f V_f$. Upon unloading, the elastic component arises from the elasticity of the cracked matrix block E'_m and the bridged fibres E_f .

$$E_c = V_f E_f + (1 - V_f) E'_m \quad \epsilon > \epsilon_{sat} \quad (4.11)$$

The inelastic component of strain must be provided by the section of the fibre surrounded by the matrix since the remainder is unrestrained. Unloading, past micro-crack initiation, will produce a residual strain in the composite which will increase up to the point of micro-crack saturation.

The Aveston analysis compared favourably with the results for the

woven polymer system in the micro-crack saturation region. The composite stiffness was correctly predicted by the model. As in the case of the impregnated tow, the elongation to failure of the composite was as predicted by Aveston et al to be bounded by:

$$\left(\epsilon_{fu} - \frac{E_m \epsilon_{mu}}{2E_f V_f} \right) < \epsilon_{cu} < \left(\epsilon_{fu} - \frac{E_m \epsilon_{mu}}{4E_f V_f} \right) \quad (4.12)$$

Here ϵ_{fu} and ϵ_{mu} are the failure strains of the tow and the matrix. From the results of tests on the unimpregnated tow and the matrix, the failure strain of the composite was calculated from equation (4.12) to be between 0.152 and 0.159. The composite failure strain from figure 4.12 was 0.16. This is acceptable if it is considered that not all of the tows in the composite will start the test aligned in the direction of loading.

It is necessary to predict the contribution of the reinforcement and the matrix for use in a finite element analysis of both the polymer system and the SiC-Al₂O₃. In the case of the polymer, two methods have been developed and compared. The information developed from the polymer model is then applied to the ceramic. The first method uses the approach developed by Aveston et al (1971) while the second adopts an experimental approach.

The computational input requires an individual response for both components of the composite. To achieve this for the polymer system, the average stress in the fibre and the matrix must be determined. In section 2.4.3 the fibre and matrix stress are described as a function of distance from the crack face in equations 2.49 and 2.53. Integrating this over the length of the block gives an average stress on the fibre ($\bar{\sigma}_f$) and the matrix ($\bar{\sigma}_m$) as:

$$\bar{\sigma}_f = E_f \epsilon_c \quad \epsilon_c < \epsilon_{mu} \quad (4.13)$$

$$\bar{\sigma}_m = E_m \epsilon_c \quad \epsilon_c < \epsilon_{mu} \quad (4.14)$$

$$\bar{\sigma}_f = \frac{1}{L} \int_0^L \sigma_{f(\eta)} d\eta \quad \epsilon_c > \epsilon_{mu} \quad (4.15)$$

$$\bar{\sigma}_f = \frac{\sigma_c}{V_f} - \frac{2\tau}{R}\{L_s\} + \frac{\tau}{R} \frac{\{L_s\}^2}{L} \quad \epsilon_c > \epsilon_{mu} \quad (4.16)$$

$$\bar{\sigma}_m = \frac{1}{L} \int_0^L \sigma_{m(\eta)} d\eta \quad \epsilon_c > \epsilon_{mu} \quad (4.17)$$

$$\bar{\sigma}_m = \sigma_{mu} - \frac{\tau}{R} \frac{V_f}{V_m} \frac{\{L_s\}^2}{L} \quad \epsilon_c > \epsilon_{mu} \quad (4.18)$$

For the polymer system the shear stress τ was calculated from equation 4.6 to be 13.38MPa using $\sigma_{m(max)} = 24\text{MPa}$, $\frac{V_m}{V_f} = 0.36$, an average block length of $1.33L_s = 1.06\text{mm}$, and an average tow radius (R) of 0.16mm. This gave an average matrix stress at saturation of 12MPa. Immediately prior to matrix micro-cracking, the average stress in the matrix was 24MPa. The average stress in the matrix is related to the block length of the composite. As micro-cracking extends, the block length reduces corresponding to a fall in the average matrix stress. To calculate the average stress from equations 4.16 and 4.18 in the fibre and the matrix therefore requires the history of block length as a function of the applied strain. This can be achieved from knowledge of the micro-cracking density at all strains. The average matrix and fibre stress in the polymer was calculated as a function of strain shown in figure 4.33.

The average matrix term in equation 4.18 is now examined. Here the stress is transferred from the fibre to the matrix by the the interfacial shear resistance (τ). It follows that from equation 4.18 that the average matrix stress includes a term which is a function of the interfacial shear stress given by $\left(\frac{\tau}{R} \frac{V_f}{V_m} \frac{\{L_s\}^2}{L}\right)$. This term is subtracted from the matrix micro-cracking stress such that the average matrix stress is independant of the interface. Comparing equations 4.16 and 4.18 therefore shows the interface term to be removed from the average matrix and contained wholly within the average fibre stress. This is a useful solution in the computational model where the response transverse to the reinforcement is matrix dependent and independent of the interface effects.

In the absence of information regarding the interface and micro-

cracking block length history, a second approach to predicting the average stress in the matrix and fibres is considered. This method assumes the average fibre stress in the composite can be determined from tensile tests on fibres. The matrix term is therefore determined by the rule of mixtures:

$$\sigma_c = V_f \sigma_f + (1 - V_f) \sigma_m \quad (4.19)$$

Figure 4.34 shows the response of the matrix and the fibre compared to the composite. This method allows the stress in the matrix to include the interface term which is acceptable during the loading in the direction of the reinforcement. However in the transverse loading the matrix term is over predicted resulting in a stiffer response than indicated by the experiments.

The two fibre responses are compared as shown in figure 4.35. The difference between the two predictions is not significant as a result of the low interface shear term and would allow either to be used in a computational model. However in the case of a composite with a high interface strength, the first is favoured in terms of a more correct transverse response.

4.7.4 Tensile Behaviour of the Ceramic Composite

The computational input for analysis of the deformation of SiC-Al₂O₃ is now considered. In this case the micro-crack density is not known as a function of strain. For this reason the computational model input was determined from the response of the unimpregnated ceramic fibre tows. Figure 4.36 shows the response of the composite compared with the unimpregnated tow response weighted by the fibre volume fraction. Using equation 4.19 the average matrix stress was calculated as shown in figure 4.36. From this figure, the failure stress of the composite is closely similar to the fibre failure stress ($V_f\sigma_f$), in agreement with Aveston et al (1971). However the ceramic composite does not exhibit micro-crack saturation. This may be attributed to a high interface shear resistance.

4.7.5 Tensile Behaviour of Knitted Composites

In the transverse direction the fibre has little or no influence on the strength of the woven composite and the response is matrix dependent. In the case of the knitted and ribbed fibre architectures the fibre is only aligned with the applied load over a portion of its length. The strength of the composite is therefore strongly influenced by the fibre architecture with strong, but anisotropic, composite design being favoured by high levels of fibre alignment.

A consistent trend with all the knitted configurations was the reduction in modulus with increasing fibre volume. A characteristic of knitted architectures is the low volume fraction of fibres aligned in any one direction. Following Aveston et al (1971) the response was dominated by the matrix, such that low V_f gave rise to a higher stiffness but lower strains to failure.

The post micro-cracking response is dominated by the extent of fibre alignment in the direction of loading. Comparing figures 4.20 and 4.22, the Jersey knit provided the highest failure stresses and strains which increased with V_f . This indicated that the fibre alignment of the Jersey knit had a

higher volume fraction of fibres parallel to the applied load. To further this point the Jersey knit was compared with the woven architecture for comparable fibre volumes. Failure occurred at similar strains with the woven architecture displaying higher stress levels at the same fibre volume.

The stress strain curves of the ribbed warp and weft composites are compared, in figures 4.21 and 4.22 and again show that the highest strengths were achieved in the most aligned fibre architectures. The ribbed weft knit showed lower failure strengths and a decreasing failure strain with increasing fibre volume. The lower failure strengths of the weft knit suggests that the level of fibre alignment corresponding to the direction of loading is low. To describe the result of reducing failure strain with increasing fibre volumes, a failed ribbed weft specimen was examined and photographed as shown in figure 4.37 shows. The surface of the failed specimen showed fibre bundles with segmented volumes of matrix. For this particular architecture and orientation an increase in fibre volume increases the local density of the fibre bundles. This lowers the local matrix volume fraction. The low levels of matrix present reduces the shear resistance to fibre pullout giving rise to low strains to failure, and the observed result.

4.8 Conclusions

The polymer system has very similar characteristics to the SiC-SiC composite, both through comparable responses in compression and tension. The fibre-matrix interface is weak and the fibre reliability is low in both system. This allows the use of the polymer system to model the ceramic composite.

From experiments on the matrix, the tow and composite the matrix and fibre contribution was determined in two different ways. These were comparable and showed that the fibre and matrix contribution can be predicted from knowledge of the fibre response, the fibre volume fraction and the composite response. This was applied to a SiC-Al₂O₃ composite where good interface data is difficult to determine. The contribution of the fibre and the matrix was therefore determined for both the polymer and the ceramic for use in a computational model.

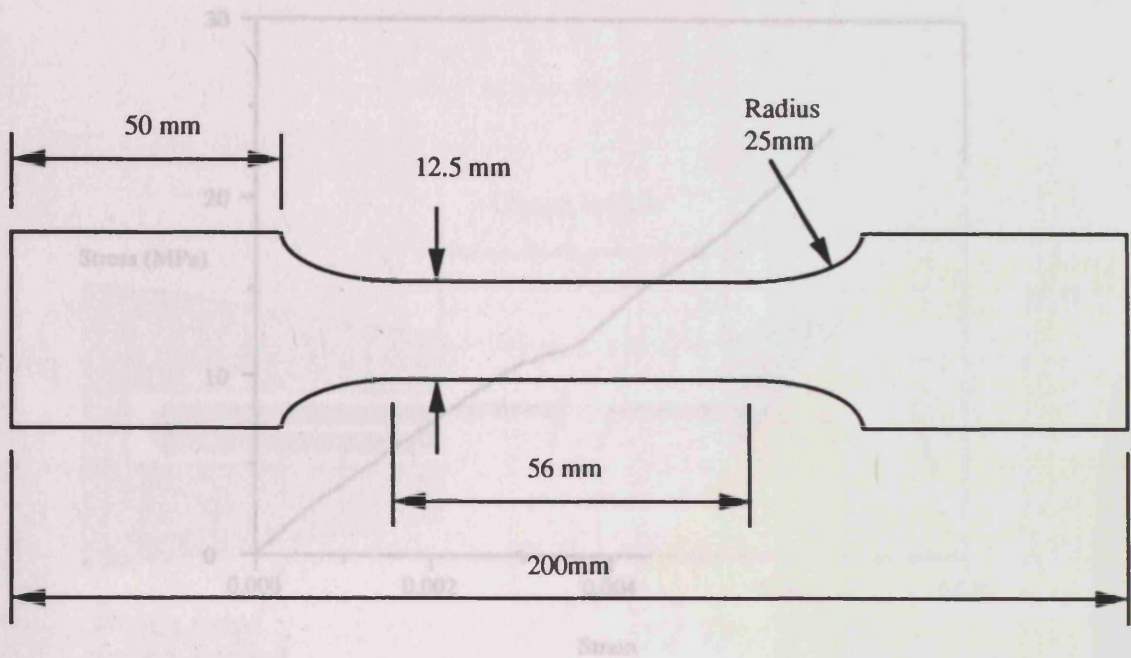


Figure 4.2 Tensile response of the polymer.

Figure 4.1 Mould Dimensions of the Monolithic Tensile Test Specimen

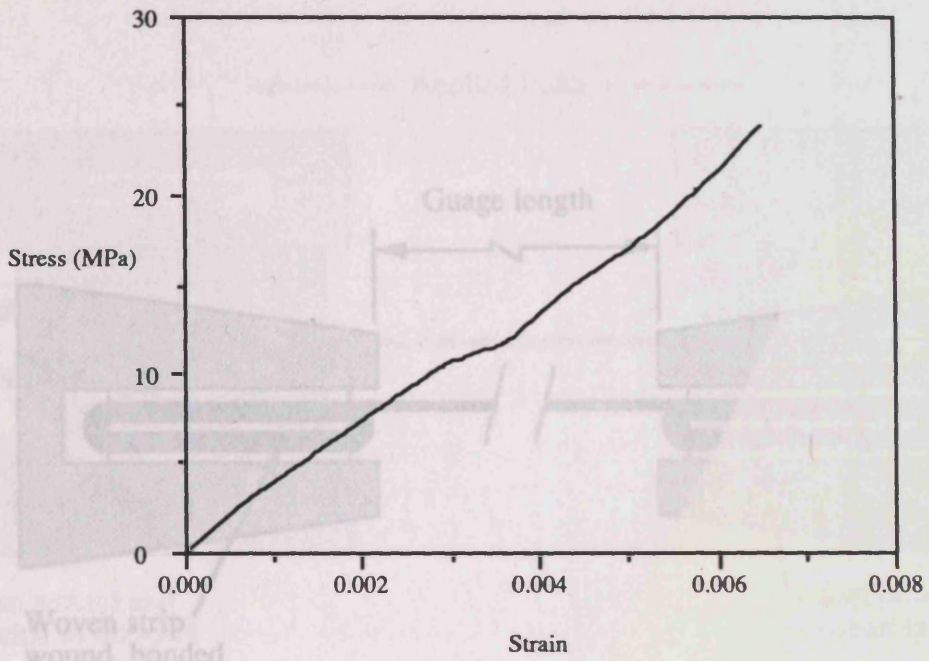


Figure 4.2 Tensile response of the polyester matrix

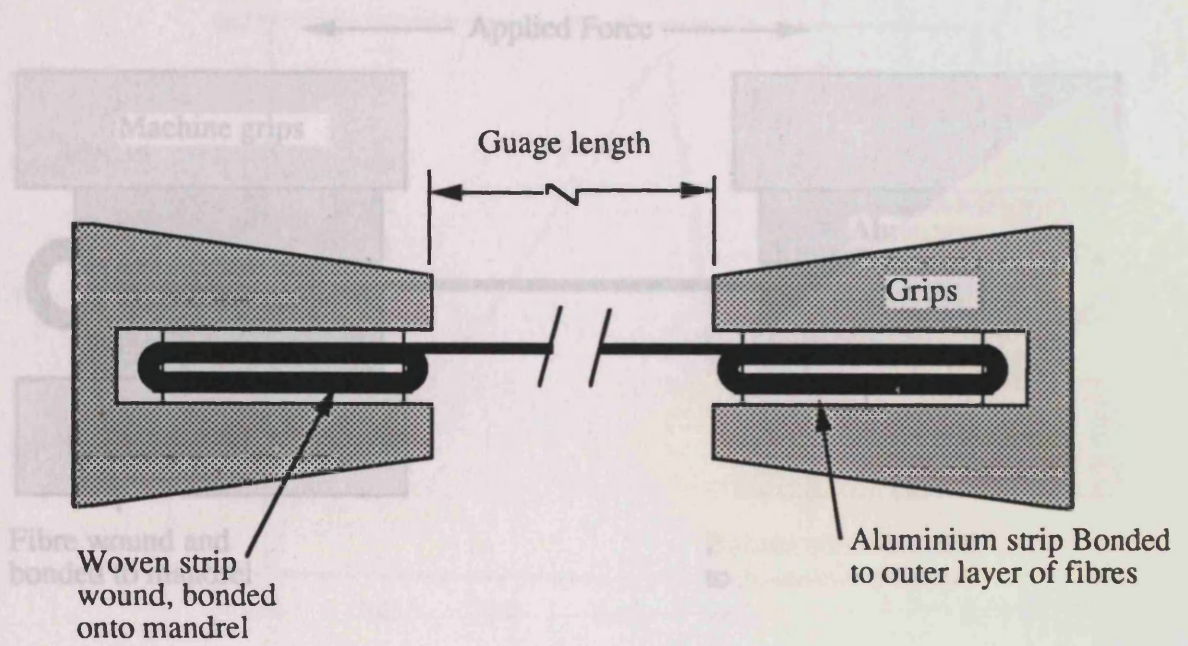


Figure 4.3 Unimpregnated gripping arrangement

Figure 4.4 Impregnated Fibre Gripping Arrangement

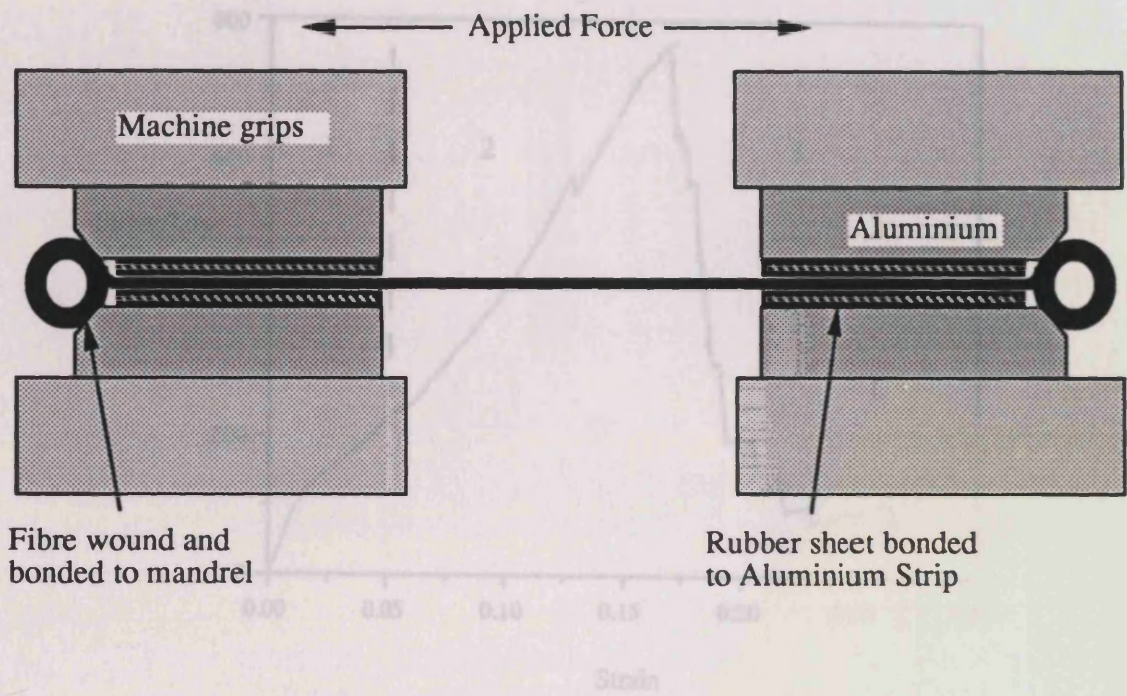


Figure 4.4 Impregnated Fibre Gripping Arrangement

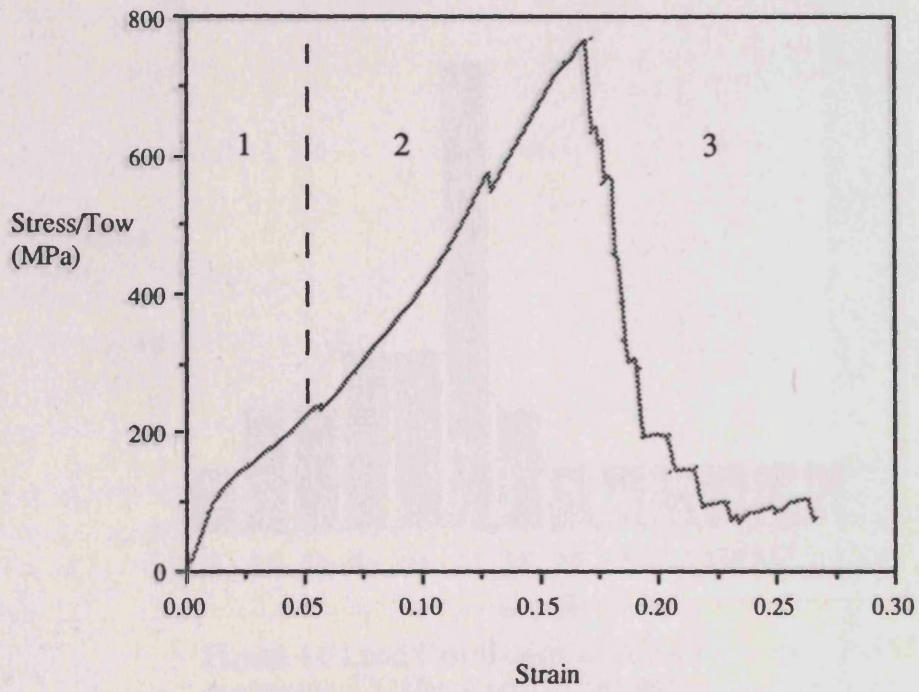


Figure 4.5 Stress-Strain Response of an unimpregnated Fibre Tow

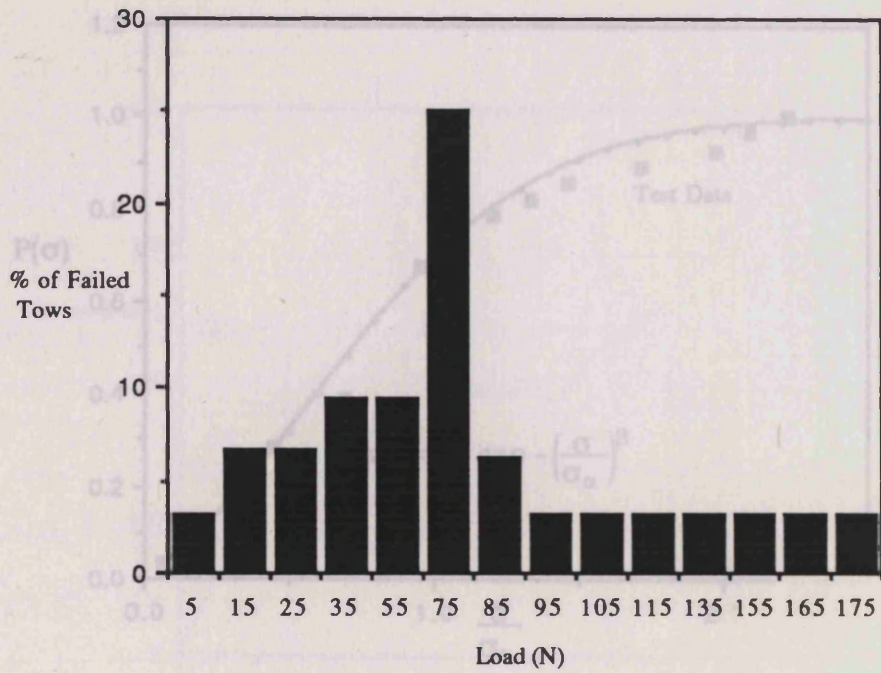


Figure 4.6 Load Distribution of failed tows, each tow containing 220 fibres with a fibre radius of 11 μ m

Figure 4
of polyester tows

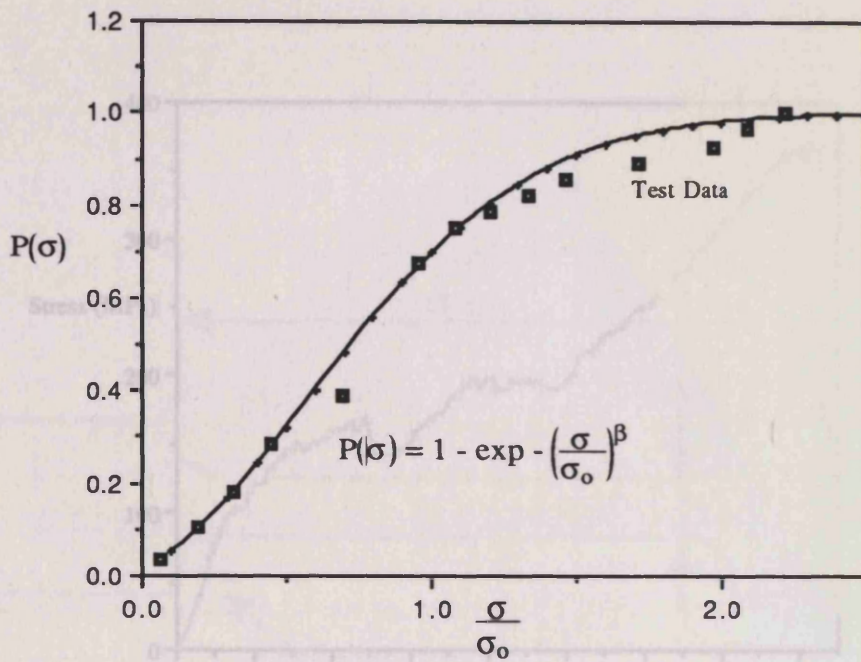


Figure 4.7 Probability distribution with $\sigma_0 = 495\text{MPa}$ and $\beta = 1.85$ of polyester tows

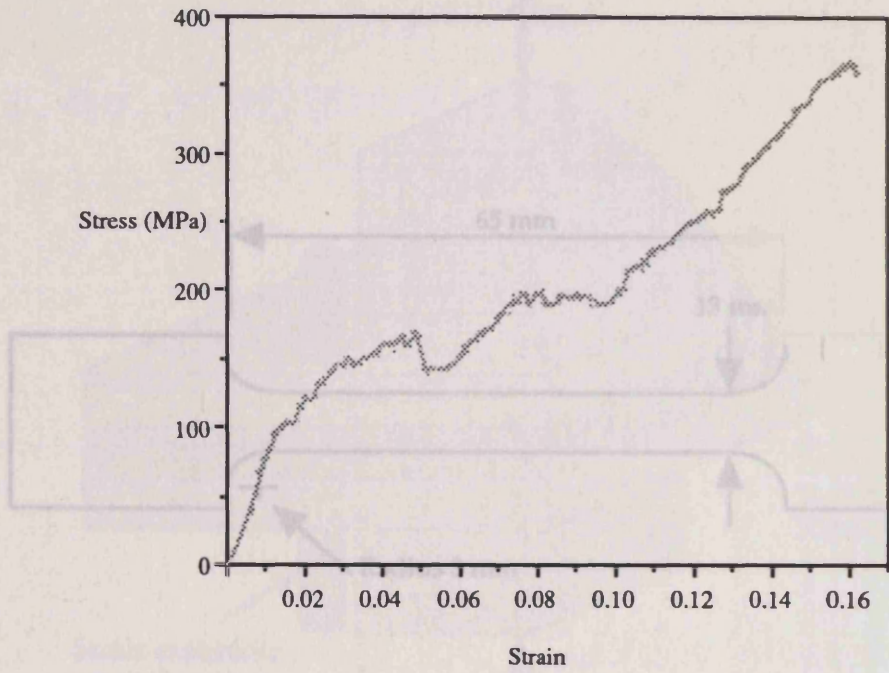


Figure 4.8 Stress-strain response of an impregnated tow

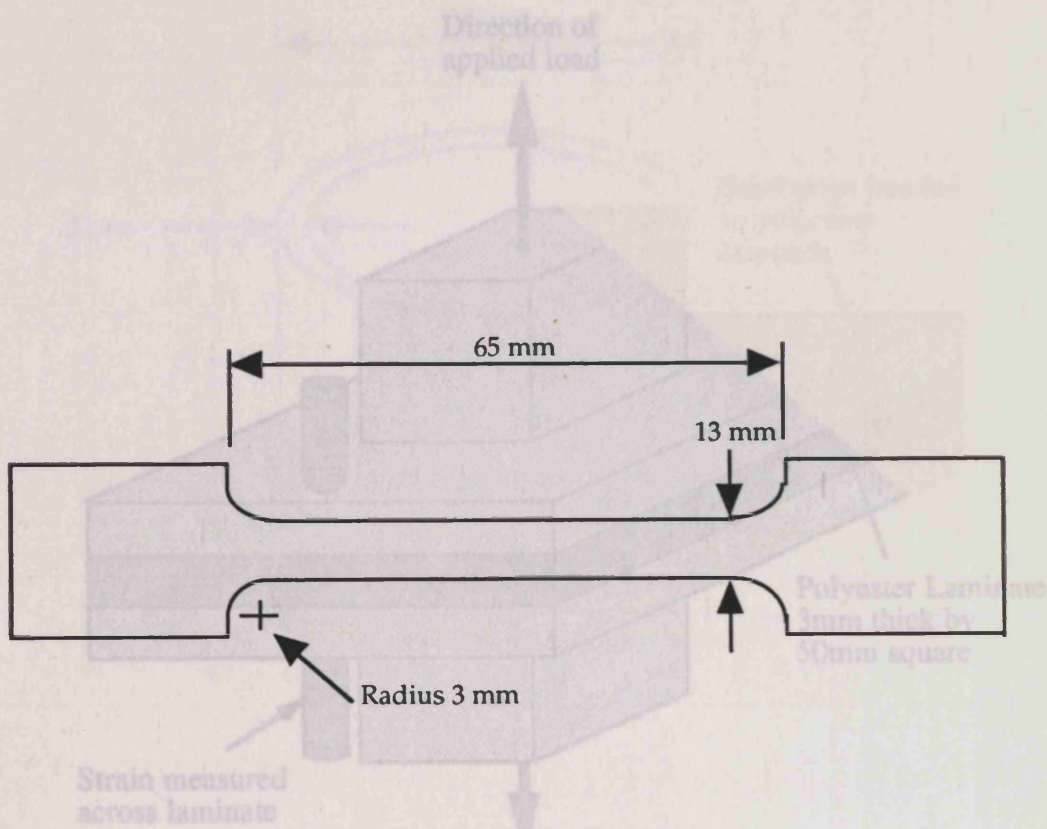


Figure 4.9 Tensile Test Specimen

Figure 4.10 Experimental arrangement of the woven polyester composite delamination test.

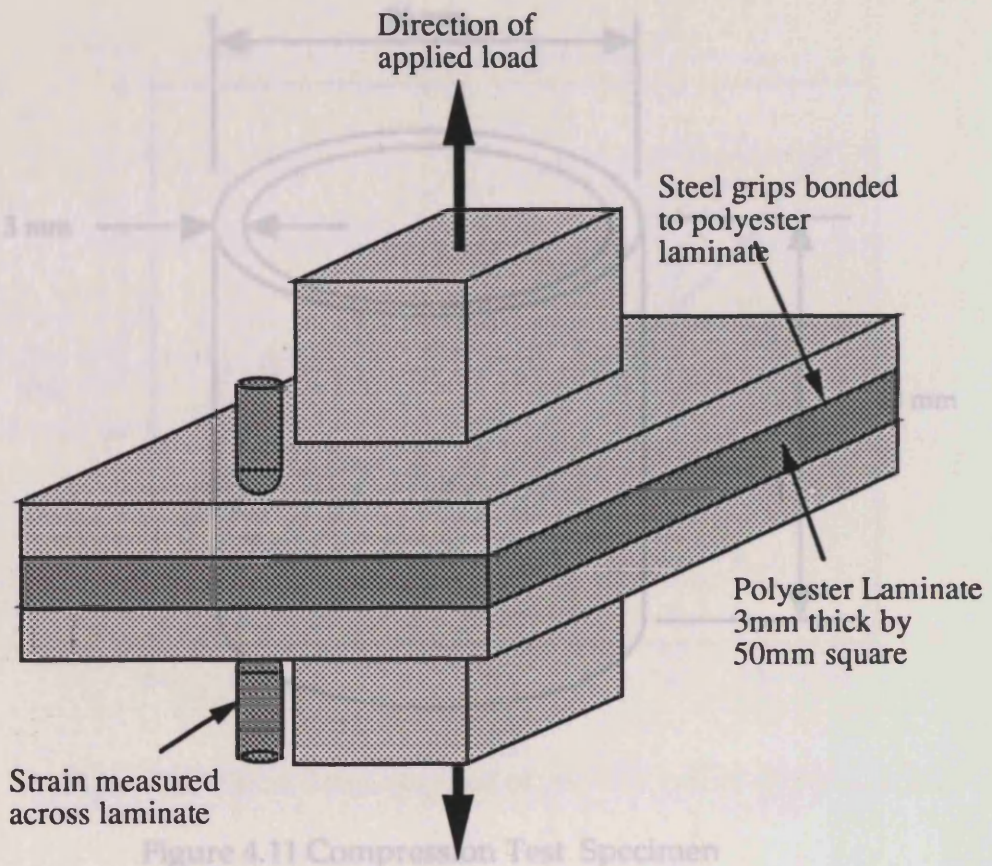


Figure 4.10 Experimental arrangement of the woven polyester composite delamination test.

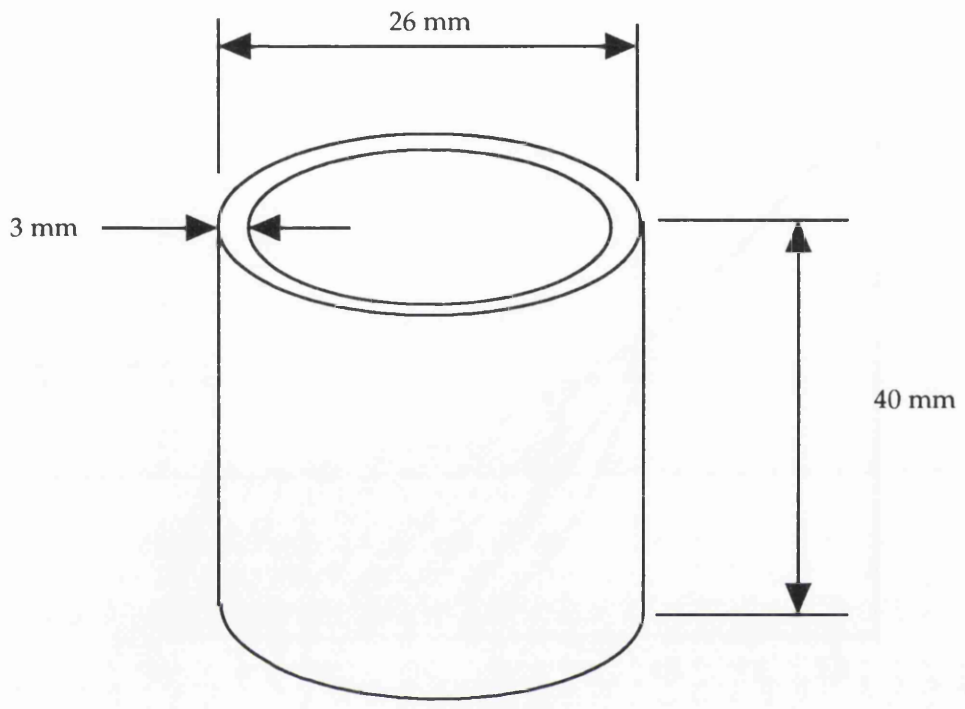


Figure 4.11 Compression Test Specimen

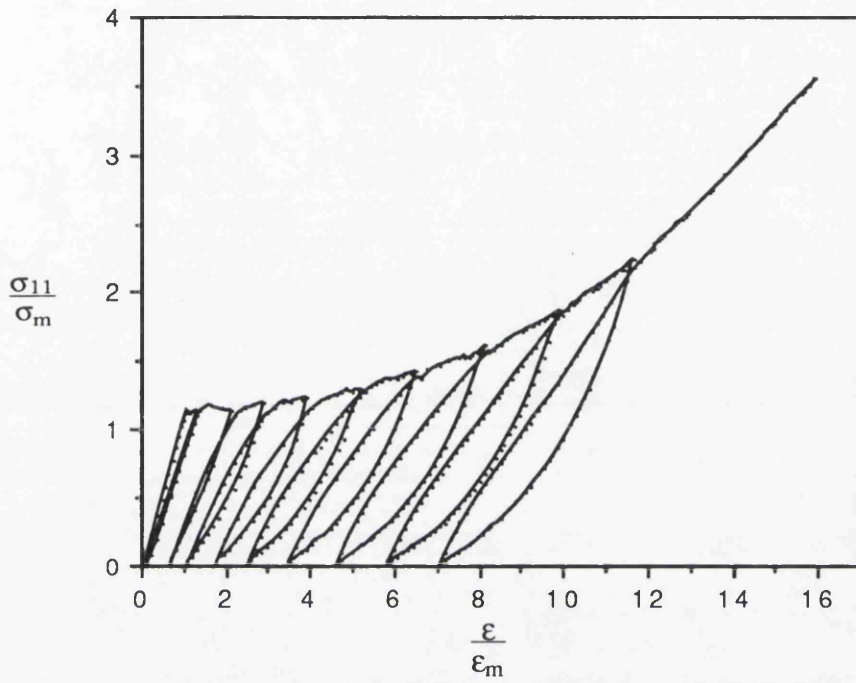


Figure 4.12 Stress Strain response of polymer system cycled to failure

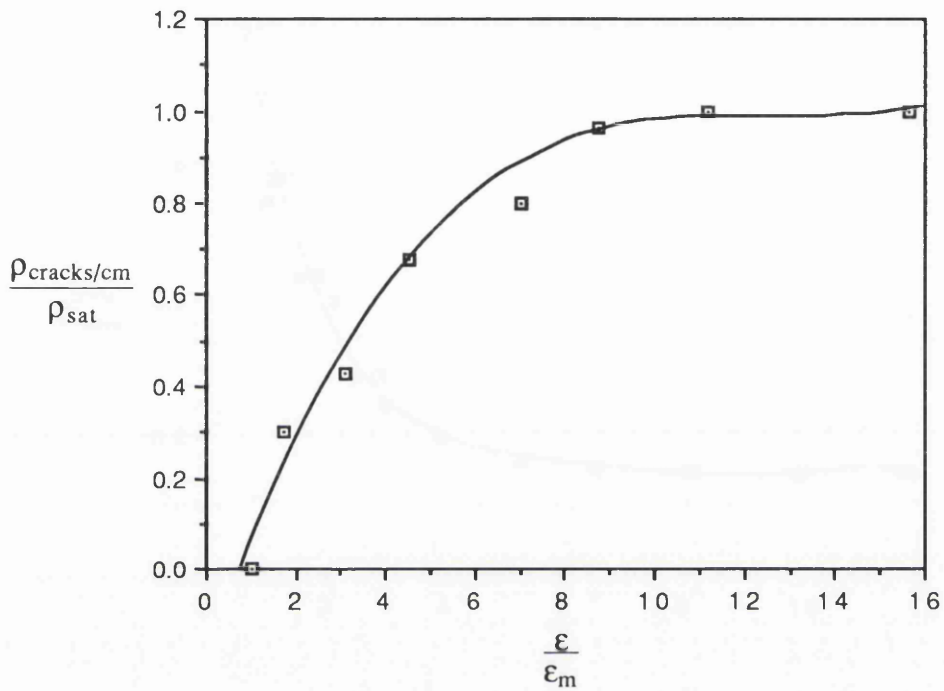


Figure 4.13 Density of micro-cracks observed as a function of the applied strain ($\rho_{\text{sat}}=9.96$ cracks /cm, $\epsilon_m=0.0104$) for the polyester composite

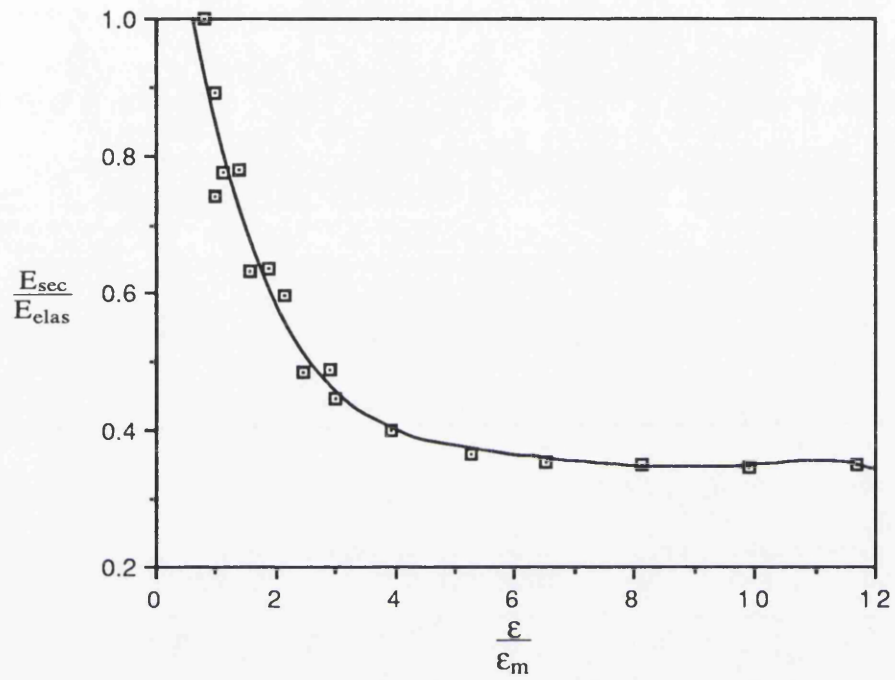


Figure 4.14 Secant modulus as a function of strain prior to unloading
 $E_{elas}=3.8\text{GPa}$

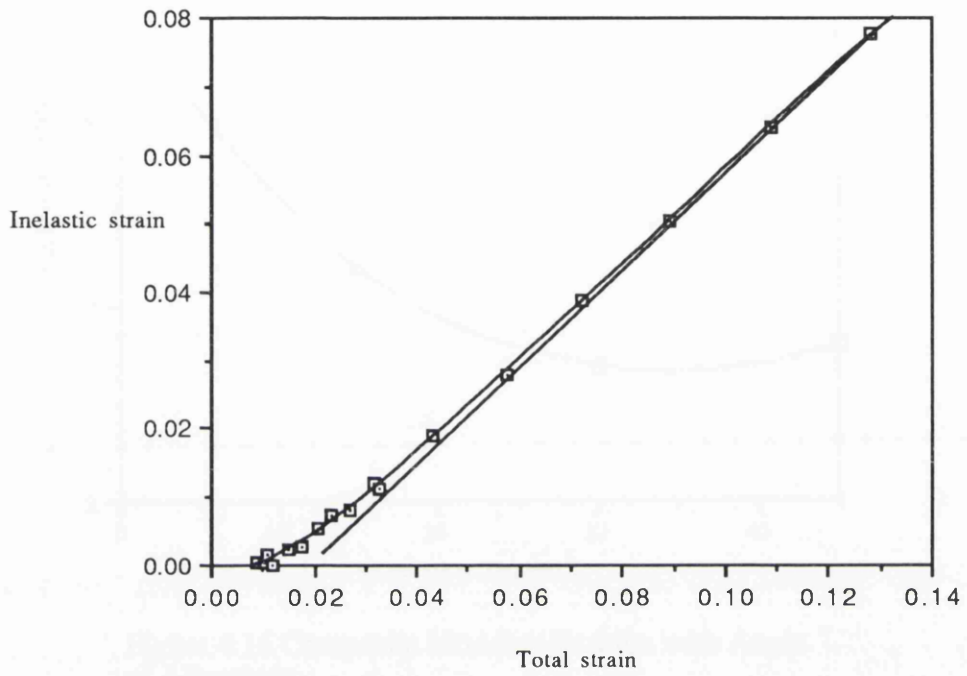


Figure 4.15 Inelastic strain as a function of the applied strain

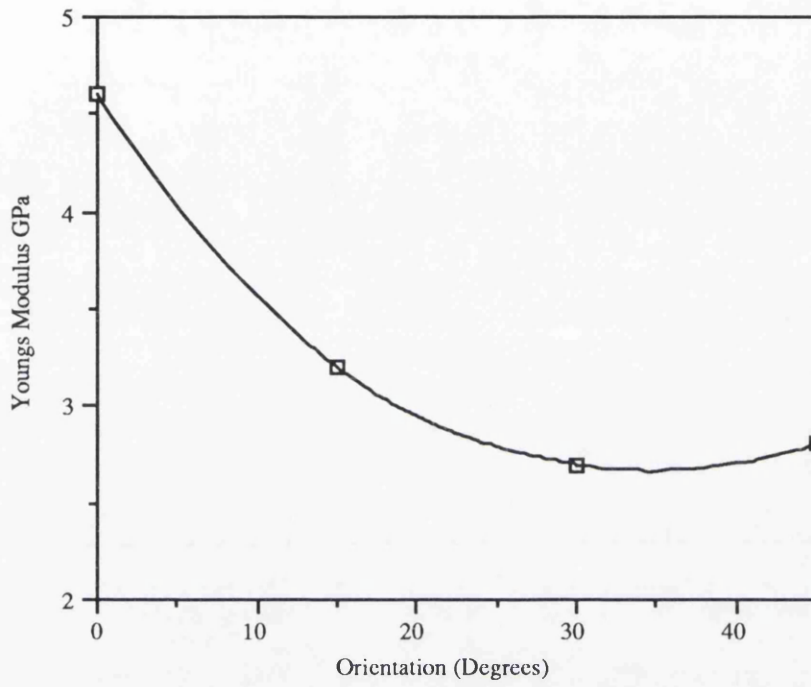


Figure 4.16 Composite Modulus Variation with Angle of Alignment

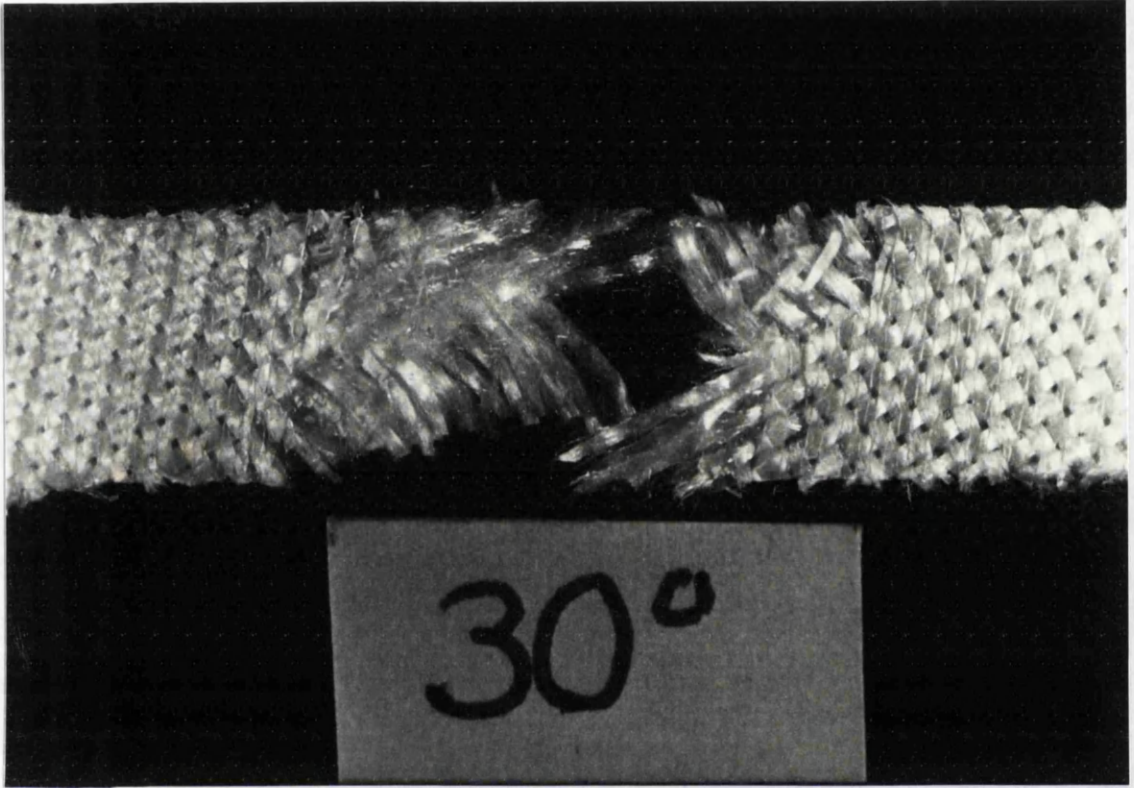


Figure 4.17 Photograph of a failed off axis woven composite.

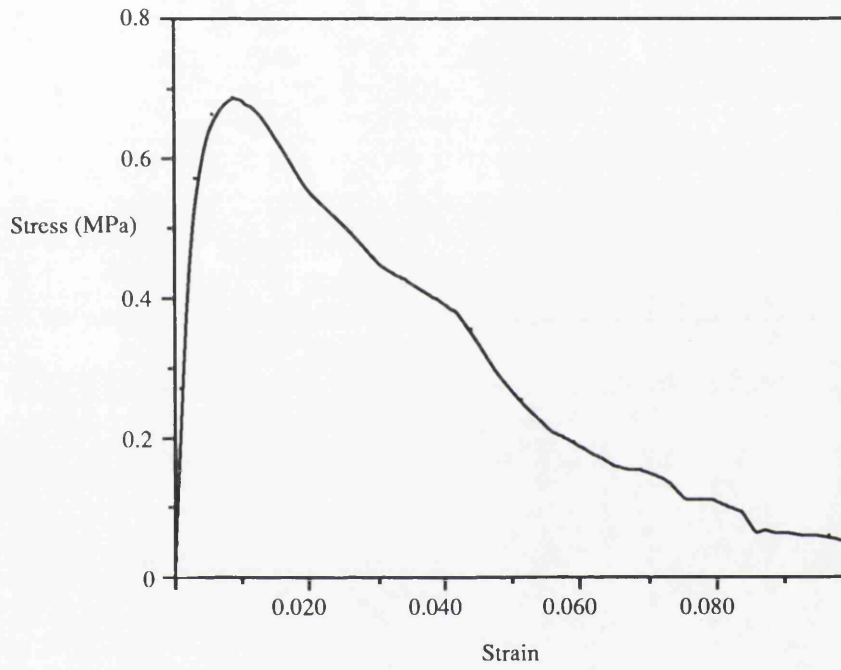


Figure 4.18 Interlaminar response of the polyester 0-90 laminate.

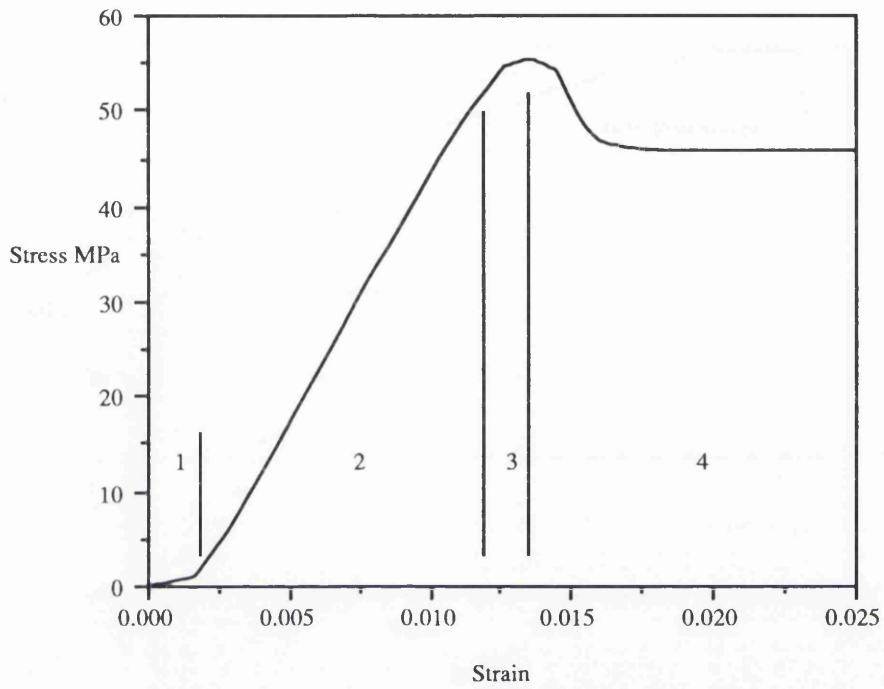


Figure 4.19 Uniaxial Compressive Stress/Strain Response for a Polyester-Polyester Composite

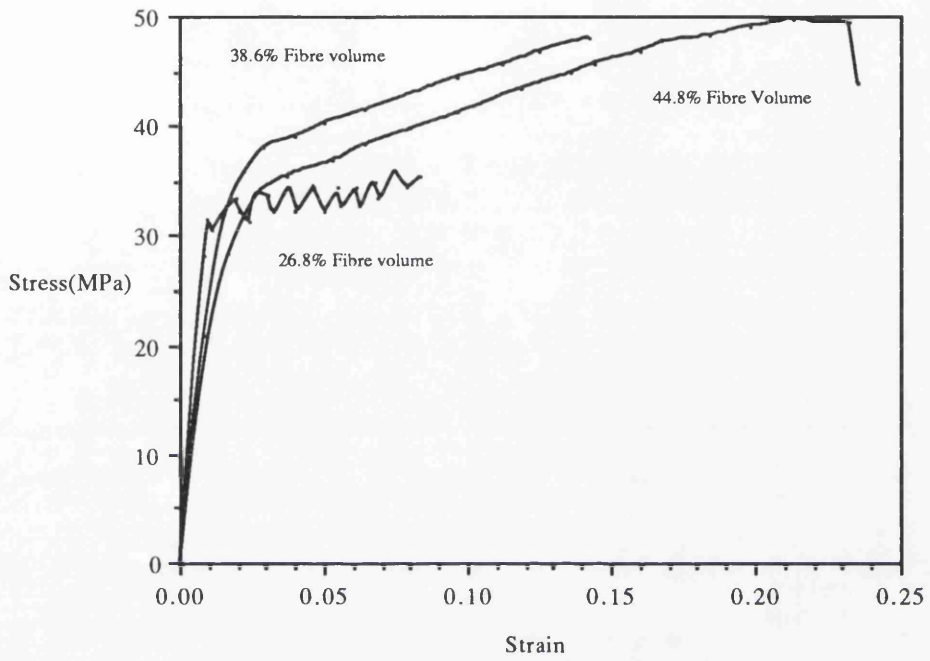


Figure 4.20 Tensile stress strain response of the Jersey knit architectures

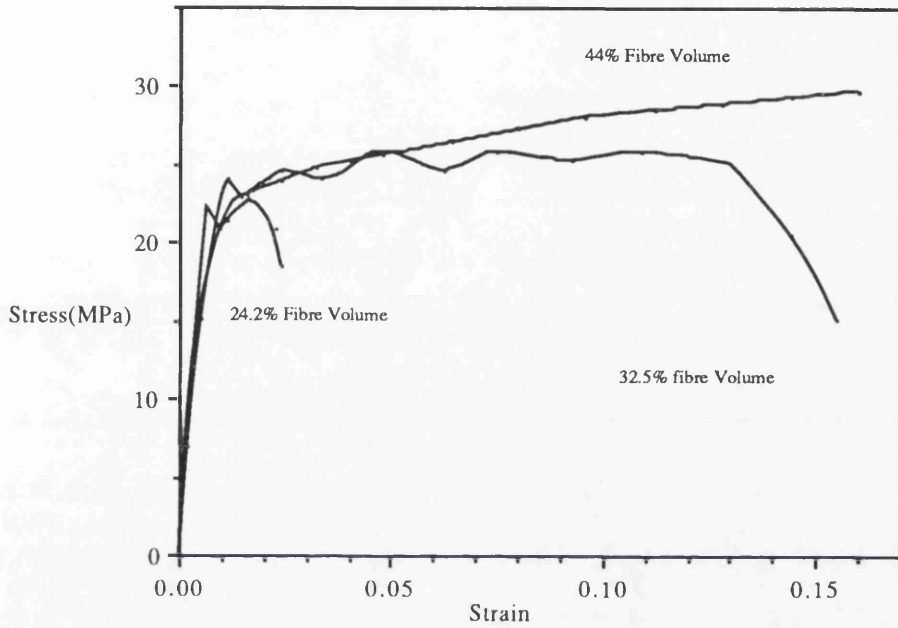


Figure 4.21 Tensile stress strain response of the Ribbed architecture tested in the warp configuration

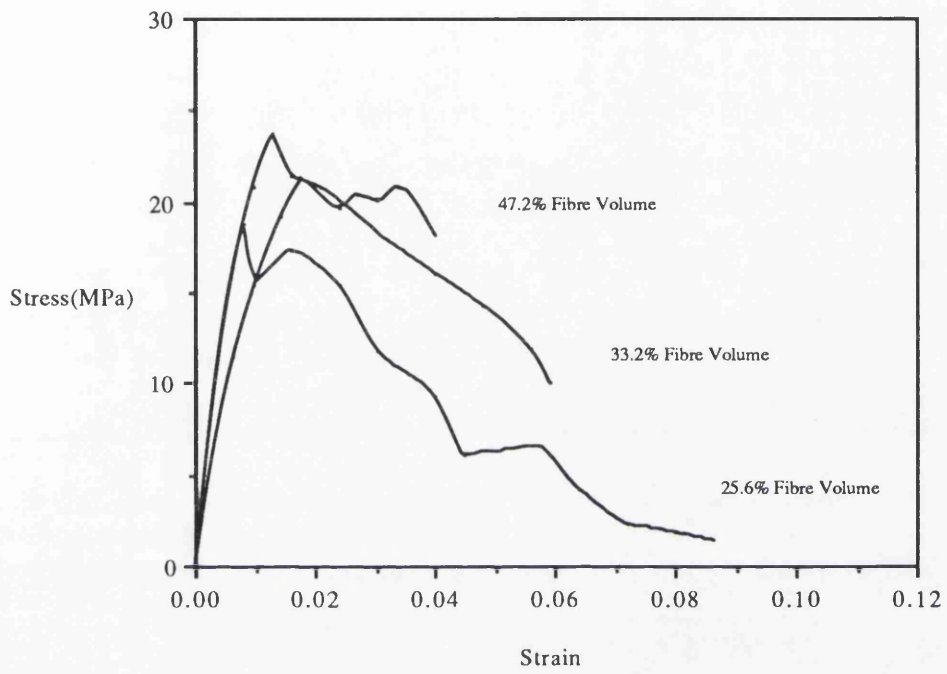


Figure 4.22 Tensile stress strain response of the Ribbed architecture tested in the weft configuration

Layers	Fibre volume Fraction (%)	Youngs Modulus (GPa)	Microcracking Stress (MPa)	Tensile Strength (MPa)	Ultimate Tensile Strain
4	44.8	1.78	35.51	49.72	0.15
6	38.6	2.24	37.45	47.9	0.15
4	26.8	3.26	32.03	35.94	0.08

Table 1 Mechanical Properties of the Jersey Warp

Layers	Fibre volume Fraction (%)	Youngs Modulus (GPa)	Microcracking Stress (MPa)	Tensile Strength (MPa)	Ultimate Tensile Strain
2	44.1	1.45	22.73	29.13	0.15
2	32.5	2.51	24.85	26.36	0.15
1	24.2	3.07	22.57	22.92	0.025

Table 2 Mechanical Properties of the Ribbed Warp

Layers	Fibre volume Fraction (%)	Youngs Modulus (GPa)	Microcracking Stress (MPa)	Tensile Strength (MPa)	Ultimate Tensile Strain
2	47.2	1.21	20.08	20.08	0.1
2	33.2	1.88	23.81	23.81	0.05
1	33.2	2.45	18.08	18.08	0.07

Table 3 Mechanical Properties of the Ribbed Weft

Figure 4.23 Mechanical Properties of Knitted Architectures

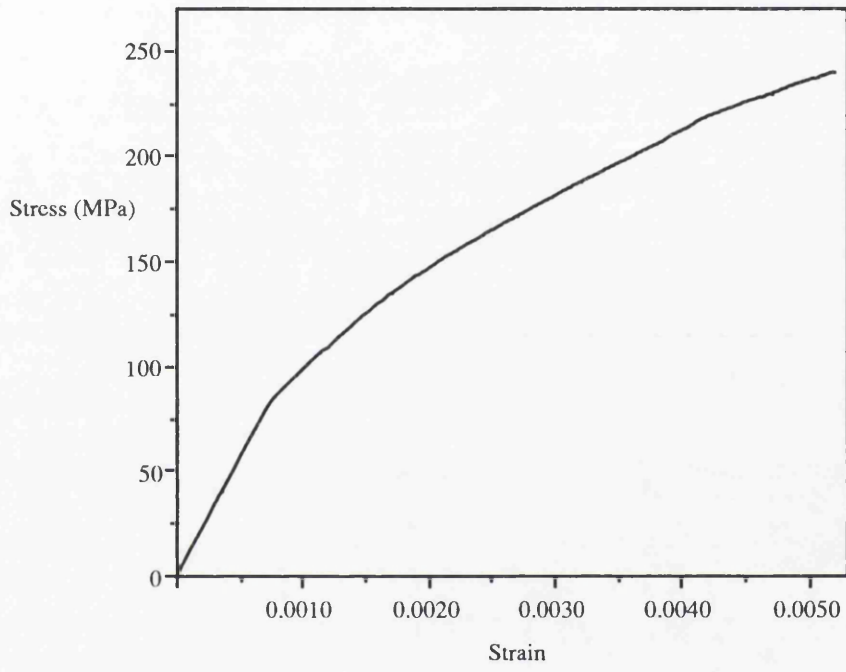


Figure 4.24 Uniaxial tensile response of SiC-Alumina

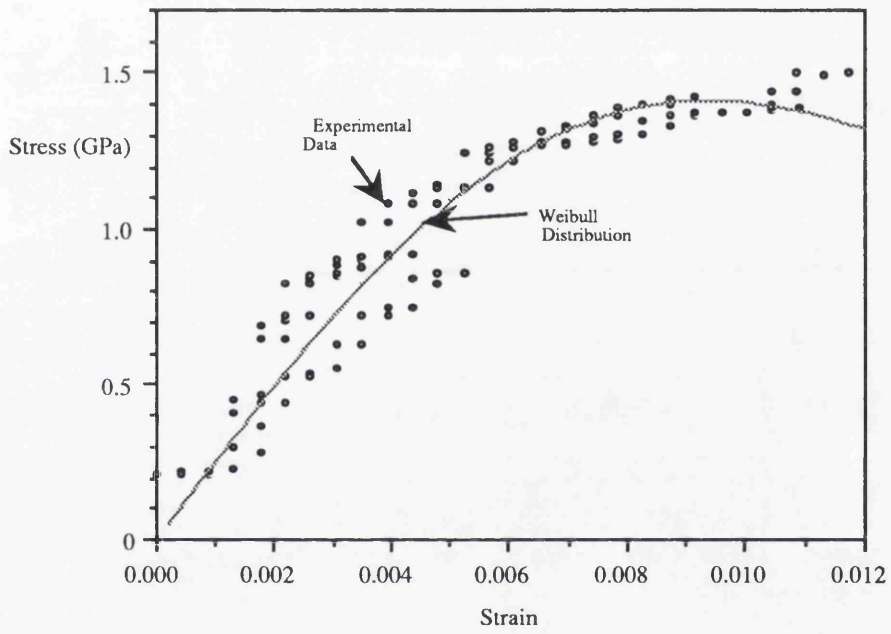


Figure 4.25 Experimental SiC fibre tow response compared to a Weibull distribution with parameters $\sigma_0 = 3.58\text{GPa}$ and $\beta = 1.871$

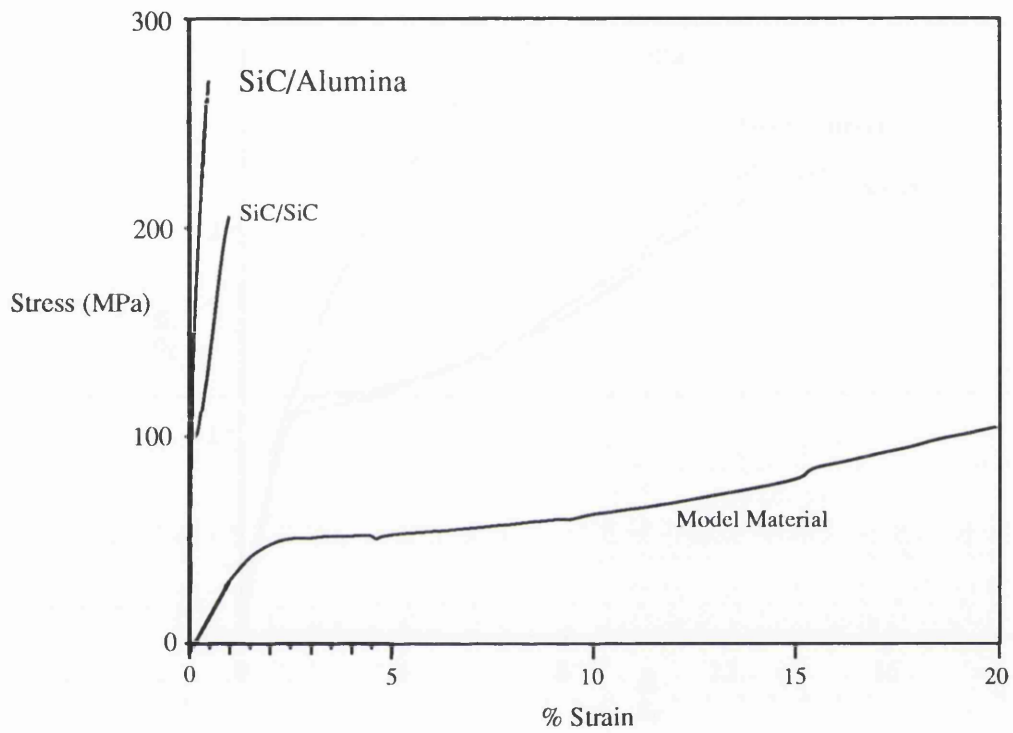


Figure 4.26 Uniaxial Tensile Stress/Strain Curve Comparison of SiC/SiC, Polymer System and SiC/Alumina

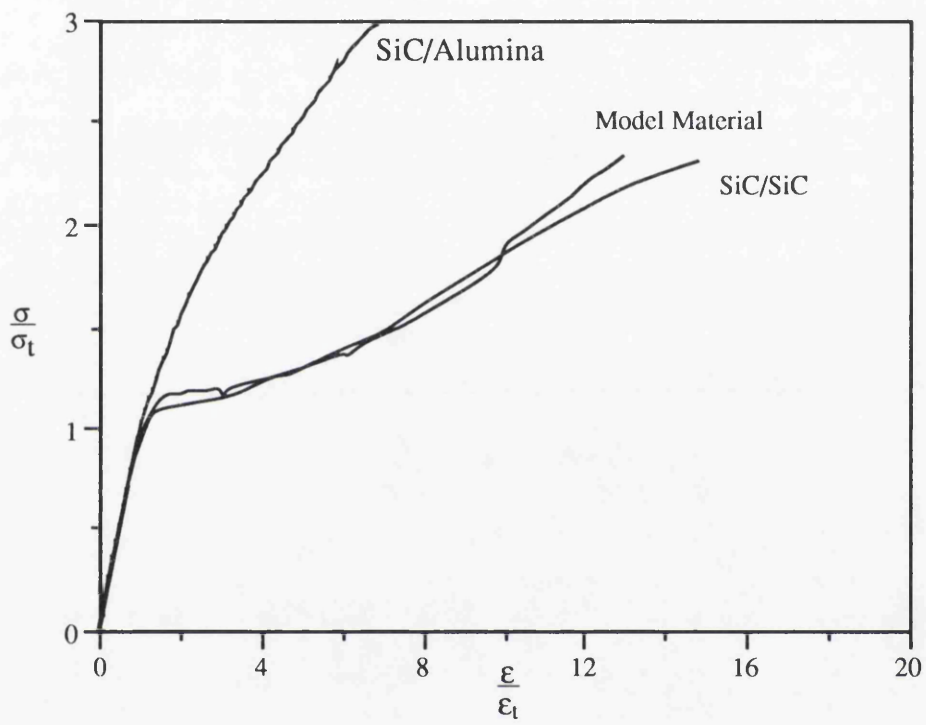


Figure 4.27 Non-Dimensionalised Comparison of the Polymer System SiC/SiC and SiC/Alumina

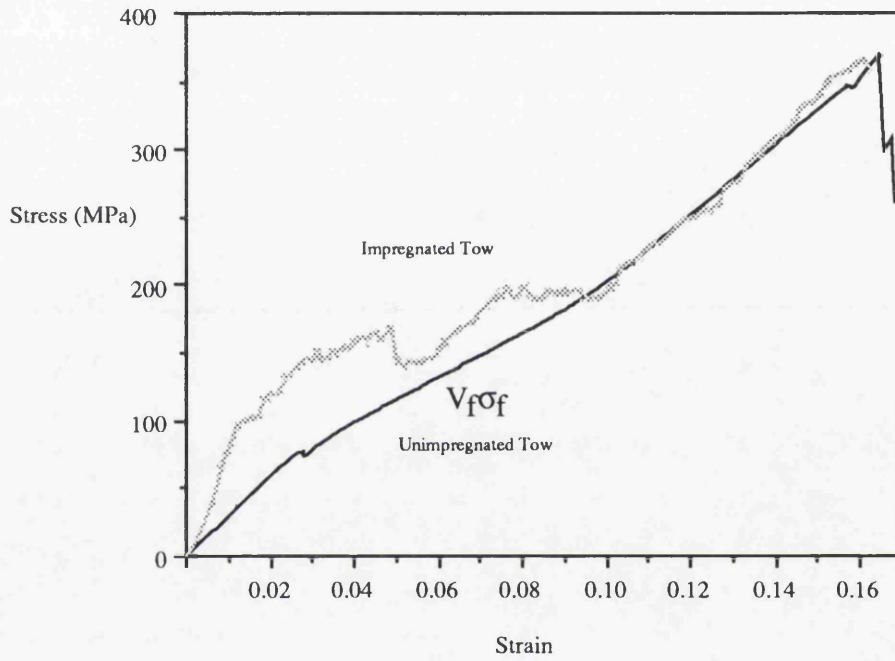


Figure 4.28 Stress-strain response on an impregnated tow with a volume fraction $V_f=0.48$ compared to an unimpregnated tow



Direction of Loading

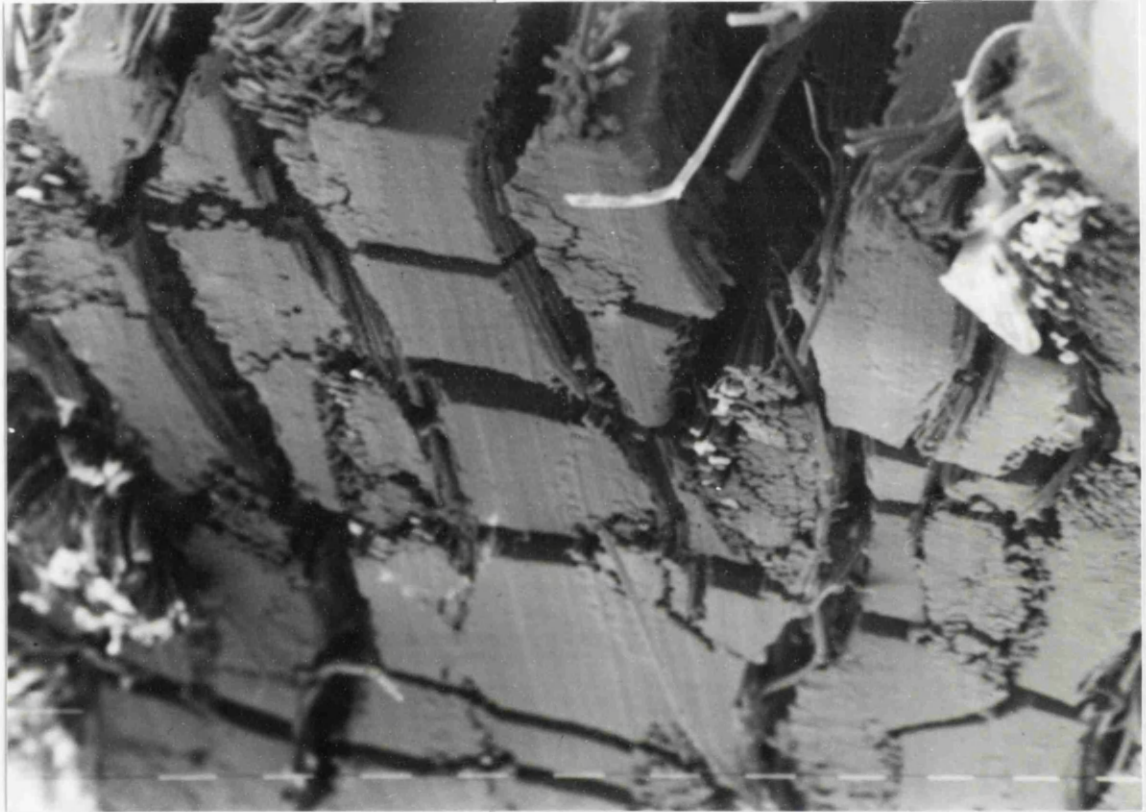


Figure 4.29 SEM photograph of a failed uniaxial tensile 0-90 woven polyester composite showing transverse micro-cracking

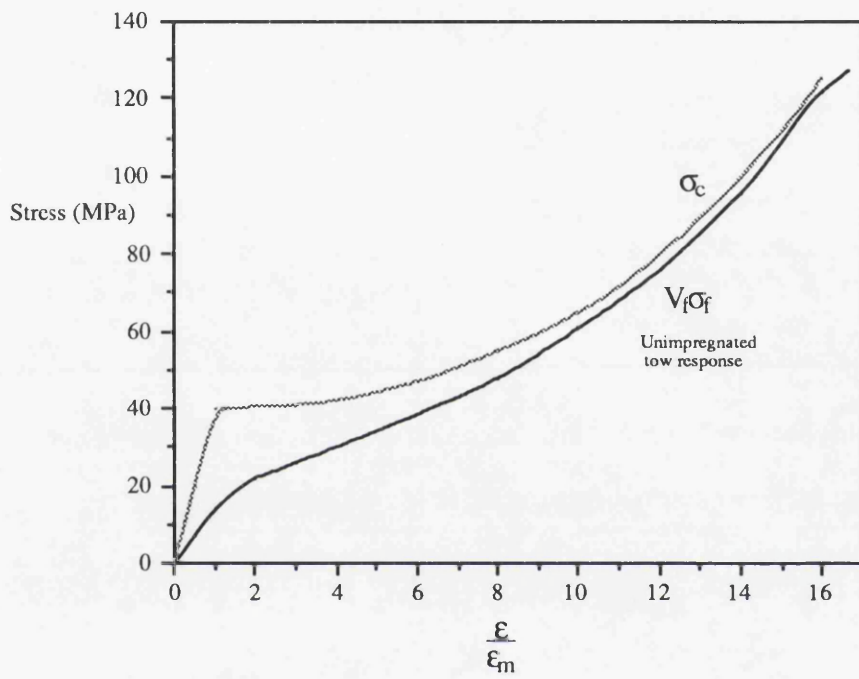


Figure 4.30 Comparison of the polyester composite response with the response of the unimpregnated fibre tow.

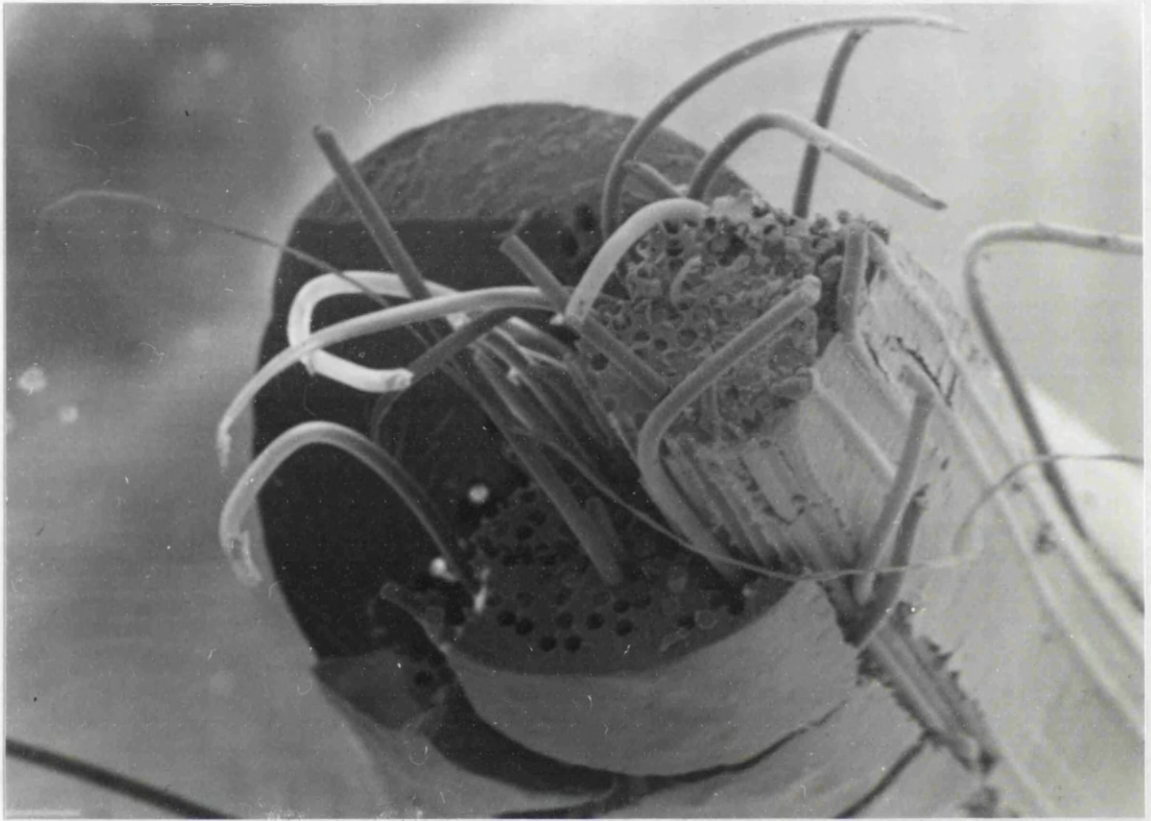


Figure 4.31 SEM photograph of a failed impregnated polyester tow

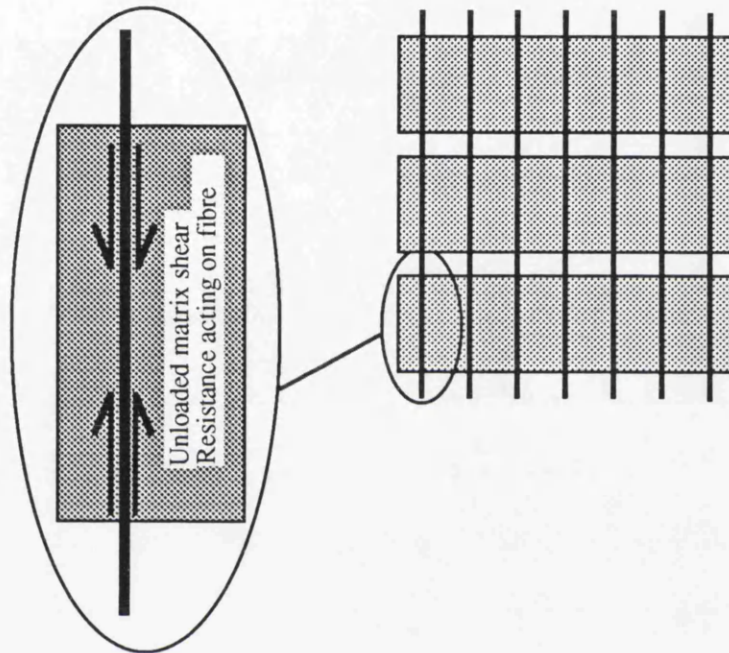


Figure 4.32 Unloaded composite with interfacial shear resistance producing an inelastic component of strain

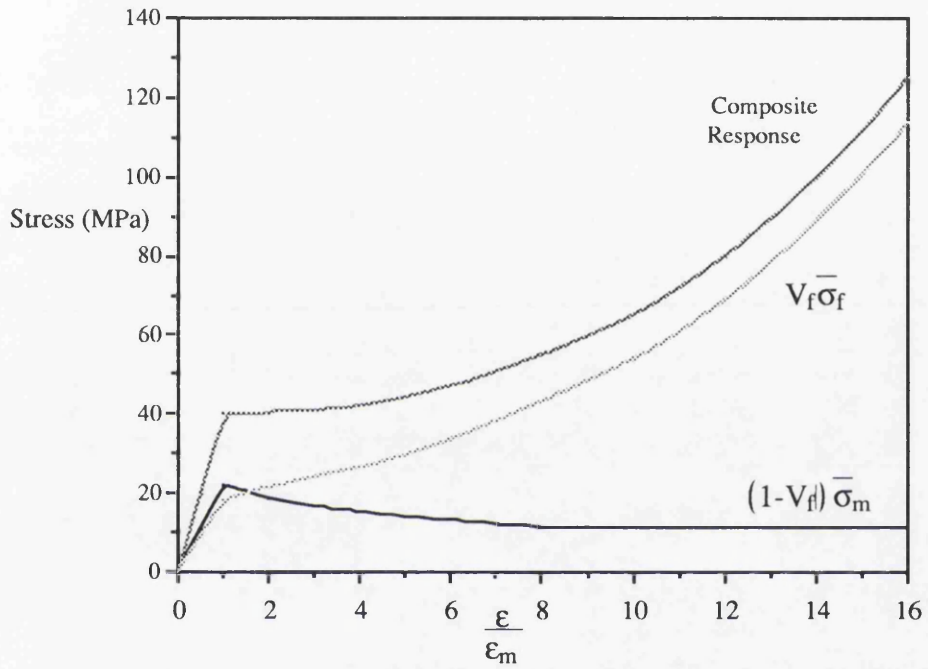


Figure 4.33 Average stress contribution from fibres and matrix of the polyester compared to the composite stress calculated from composite theory in equations (4.16) and (4.18)

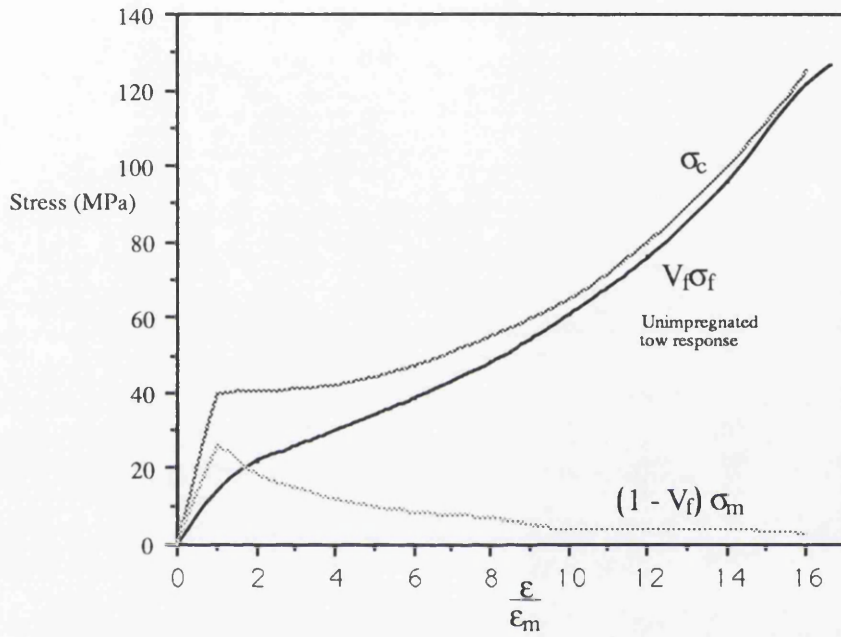


Figure 4.34 Average fibre and matrix contribution to the polyester composite stress determined from the response of the unimpregnated polyester fibre.

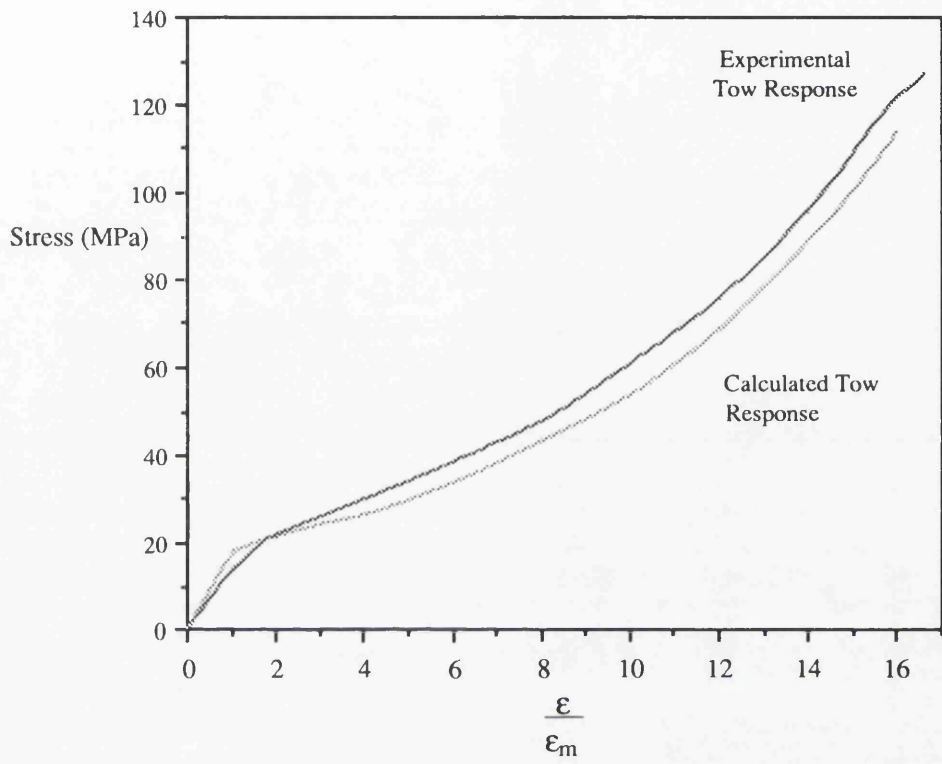


Figure 4.35 Comparison of average fibre stress using the calculated method and the unimpregnated experiment of the polyester tows

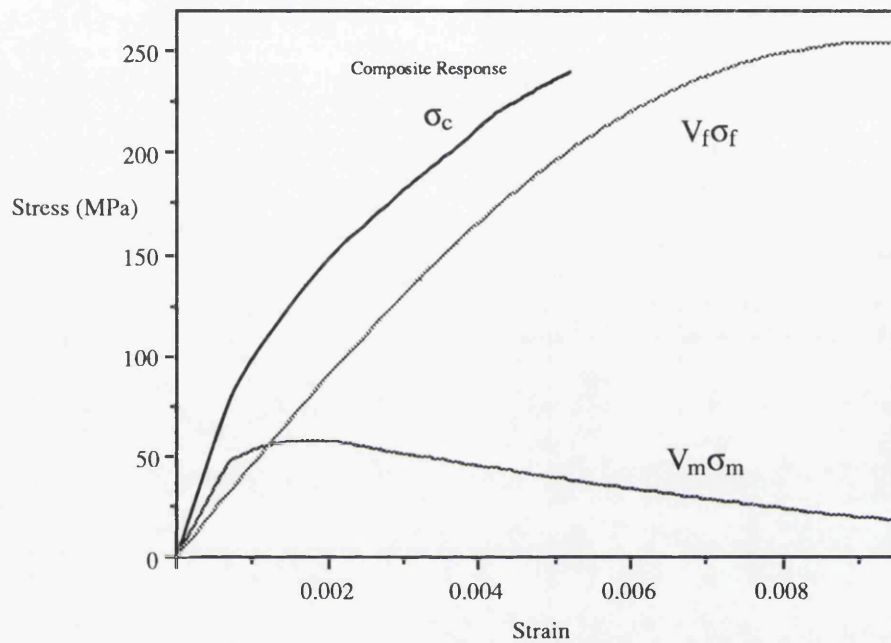


Figure 4.36 Comparison of the average fibre and matrix contribution to the composite stress for SiC-Alumina

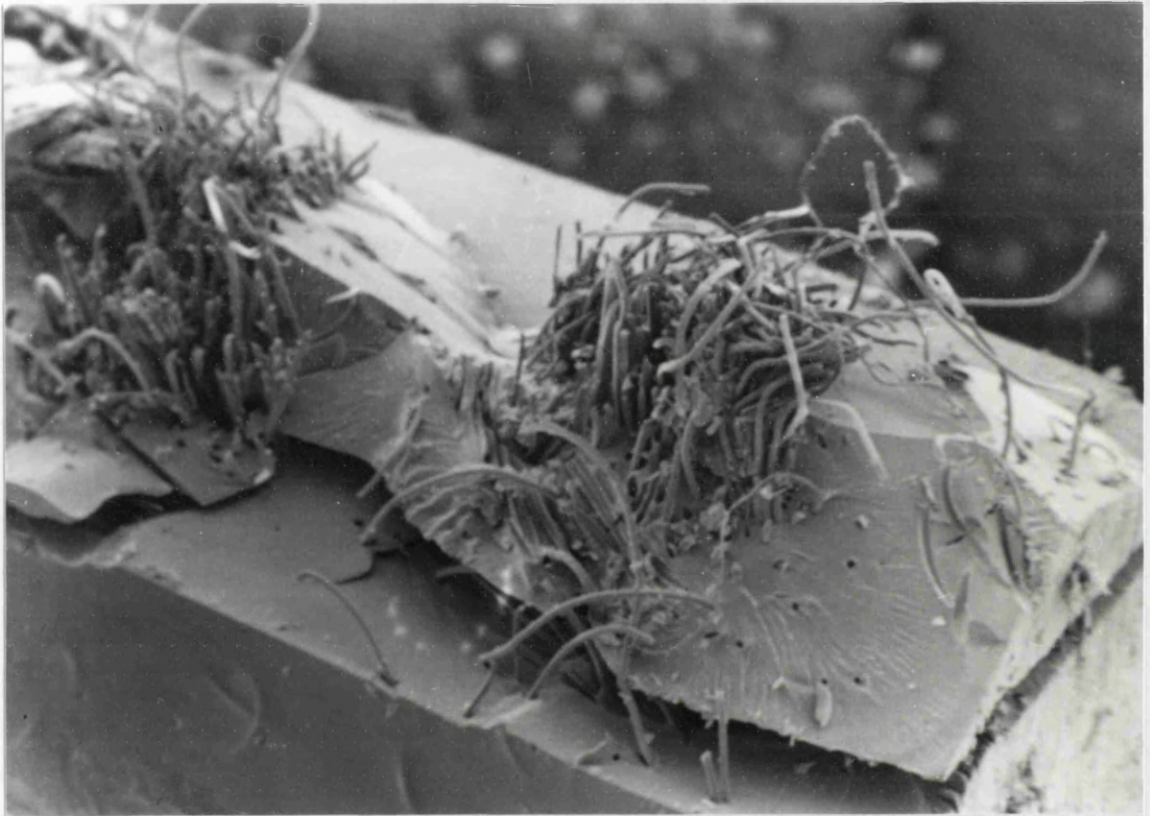


Figure 4.37 SEM photograph of the failure surface of a knitted polyester composite

5. Constitutive Model Development

5.1 Introduction

Ceramic composites were developed to provide a class of materials with enhanced toughness and ductility in comparison to monolithic ceramics. The effective use of such materials requires an understanding of their deformation mechanisms. This must be combined with an ability to represent the deformation modes in constitutive relations in a way which may be incorporated into finite element procedures.

The relevant micro-mechanisms of deformation have already been reviewed in earlier chapters. Significant advances have been made by incorporating the micro-mechanisms of fibre pullout and matrix micro-cracking into constitutive relations (Hayhurst et al 1991, Haddad et al 1991 and Marshall et al 1992) through damage mechanics. In the present work a combined experimental and computational approach has been adopted. The computational work follows a damage mechanics approach to describe the constitutive relations for a ceramic composites intended for an aero-engine application. This chapter aims to provide a basis for modelling and analysing ceramic composites, leading to its efficient use in engineering structures.

5.2 Micro-damage Model

In ceramic composites damage can be regarded as being of two distinct types. Firstly damage arises from the processing route. Typically this might comprise porosity due to incomplete vapour infiltration of the fibre architecture, as shown in Figure 5.1. Such damage is largely unaffected by subsequent mechanical loading. In contrast mechanical loading induces a second form of damage, typified by the matrix micro-cracking illustrated in Figure 5.2. In general, systems which exhibit a modulus or thermal expansion mismatch between matrix and fibre allow micro-cracking to develop during processing. Figure 5.3 shows a section of a SiC-Alumina composite as received from the manufacturer where micro-cracking of the matrix is in evidence. However in systems, such as SiC-SiC with no mismatch processing damage is usually limited to porosity as shown in figure 5.1.

The tensile deformation of brittle matrix composites originates from the ability of the matrix to sustain stable micro-cracks. In compression micro-cracking is not observed, and a crushing mode occurs at very much higher stress levels Sammis et al (1986). In order to represent micro-cracking in tension and crushing in compression, the material response was idealised in terms of intersecting yield or micro-cracking surfaces following Chen et al (1975). For tensile deformation of the model material the pre-micro-cracking response was initially taken to be isotropic linear elastic. To maintain generality and make contact with the known behaviour of other brittle materials (Chen et al 1975), a Mohr-Coulomb type micro-cracking criterion involving both the first and second stress invariants has been adopted. The stress system was limited to a small deformation description based on the equivalent stress $\bar{\sigma}$, and the mean hydrostatic stress $\sigma_{kk}/3$. The equivalent stress is conveniently expressed in terms of the stress deviators, s_{ij} .

$$s_{ij} = \sigma_{ij} - \sigma_{kk}/3 \quad (5.1)$$

$$\bar{\sigma} = \sqrt{\frac{3}{2} s_{ij} s_{ij}} \quad (5.2)$$

Micro-cracking in tension was taken to initiate at a Mohr-Coulomb criterion of the form.

$$f\left(\frac{\sigma_{ij}}{\sigma_t}\right) = \sqrt{\frac{3 s_{ij} s_{ij}}{2\sigma_t^2}} + \alpha \frac{\sigma_{kk}}{\sigma_t} - \beta(1 - f) = 0 \quad (5.3)$$

Where, α , β and σ_t are material properties, and f is the volume fraction of porosity. In the absence of porosity ($f = 0$) uniaxial tension defines the relationship

$$\beta - \alpha = 1 \quad (5.4)$$

To describe the tensile data of both the 0-90 SiC-SiC laminate, and the model material in the absence of processing damage, α was taken as 0.918 and β as 1.918 for tensile micro-cracking. The micro-cracking stress (σ_t) in uniaxial tension was 112 MPa for the ceramic composite and 40 MPa for the polymer system. The essential feature of the post micro-cracking behaviour in tension (Fu et al 1985), is that on unloading the total strains are largely recovered elastically, as illustrated in Figure 5.4. This corresponds to an elastically damaged material whose incremental elastic moduli are functions of the extent of micro-cracking, giving an overall non-linear response.

Following Chan et al (1990) and Abaqus (1992), micro-cracks are assumed to be capable of being formed on three intersecting planes which form an orthogonal system with axes $\alpha\beta\gamma$ corresponding to the directions of maximum principal strain. For micro-cracking on a single plane the normal to the crack plane is denoted α with the corresponding direct stress $\sigma_{\bar{\alpha}\bar{\alpha}}$ and strain $e_{\bar{\alpha}\bar{\alpha}}$. Here the bars over the subscripts are intended to override the usual summation convention (Abaqus 1992). Cracks are assumed to form at a direct strain $e_{\bar{\alpha}\bar{\alpha}}^{\text{open}}$. Before micro-cracking the stiffness C_{ijkl} is taken as the isotropic stiffness of the undamaged material. However when $e_{\bar{\alpha}\bar{\alpha}}^{\text{open}} \leq e_{\bar{\alpha}\bar{\alpha}}$ the damage is associated with the open micro-cracks and an elastic stress strain relation of the form is adopted.

$$\sigma_{\alpha\alpha} = \overline{C_{\alpha\alpha\alpha\alpha}} e_{\alpha\alpha} \quad (e_{\alpha\alpha} \geq e_{\alpha\alpha}^{\text{open}}) \quad (5.5)$$

The appropriate damaged stiffnesses were taken from the experimentally determined uniaxial stress-strain relation.

A characteristic of solids with an oriented array of micro-cracks is that strain is essentially produced normal to the crack plane, while terms involving Poisson's ratio are close to zero. Thus

$$\overline{C_{\alpha\alpha\beta\beta}} = 0 \quad (e_{\alpha\alpha} \geq e_{\alpha\alpha}^{\text{open}}, \alpha \neq \beta) \quad (5.6)$$

In compression the constitutive relation consists of a yield-flow surface based on classical concepts of plasticity. This theory allows the strain rate decomposition in compression to be written as:

$$e = e^{\text{el}} + e^{\text{pl}} \quad (5.7)$$

Here the total mechanical strain, e , is expressed as the sum of elastic, e^{el} , and plastic components, e^{pl} , with plastic flow arising from an associated flow rule with a compressive yield surface given by:

$$f\left(\frac{\sigma_{ij}}{\sigma_c}\right) = \sqrt{\frac{3}{2} \frac{s_{ij} s_{ij}}{\sigma_c^2}} + \gamma \frac{\sigma_{kk}}{\sigma_c} - \lambda(1 - f) = 0 \quad (5.8)$$

For the polymer system the material constants γ , λ and σ_c were taken as 0.1218, 1.1218 and 160 MPa respectively. The intersecting micro-cracking and compressive yield surfaces for the SiC-SiC composite are as shown in Figure 5.5 for plane stress conditions.

Processing damage in the form of voids has been assumed to degrade the strength of the material in a linear manner. More sophisticated models of the effect of porosity on the yield surface have been developed for metals (Gurson 1977) and for ceramics (Sammis et al 1986). However in the present context, interest centres largely on the micro-cracking behaviour as the stress systems in the components of engineering interest rarely involve the compressive failure modes, and this justifies the simplification. Processing

damage is assumed to be isotropic and is modelled by degrading both the yield surfaces and the elastic moduli linearly with porosity in an isotropic manner. In the computational models processing damage can be distributed spatially through a component in a way that reflects the processing. In the present work however interest is largely restricted to mechanically induced micro-cracking damage.

5.3 Reinforcement

Laminated ceramic composites generally have poor through thickness properties, which are dominated by the brittle matrix and the poorly bonded fibre-matrix interface. In the absence of modulus mismatch the composite is taken to be isotropic until micro-cracking occurs, after which an orthogonal array of cracks are set up. With the initial model it is possible to introduce anisotropy by introducing damage on any given plane. The modulus normal to the plane is reduced but the transverse direction is undamaged. This predamageing of the micro-cracking model is clumsy and computationally unstable. As a result the damage model may only be used to represent a laminated ceramic composite in stress systems in the absence of delamination.

In order to overcome these problems, one dimensional reinforcing elements were introduced into the original micro-damage model. The axial strain of the reinforcing element is identical to the element in which it is embedded. The reinforcement corresponds to the fibres or fibre tows which are effective only in the fibre direction. In the elastic case, axial loading in the direction of the reinforcing element produces a response dependent on the stiffness of the matrix (E_m) plus that of the reinforcement (E_f) and the corresponding volume fractions V_m and V_{f_i} of each phase given by:

$$E_{c(i)} = E_m V_m + E_f V_{f_i} \quad (5.9)$$

Here the subscript i is intended to denote that the reinforcement may be orientated in any direction (i). The subscript i thus refers to the direction of loading, where V_{f_i} can be zero if the applied load acts perpendicular to the reinforcing element. Here the use of the reinforcement allows the introduction of elastic anisotropy in the case of stiff fibres in a low modulus matrix.

This may be compared with the response of a composite where loading in the direction of the fibres results in stable micro-cracking of the matrix and load transfer from the matrix to the fibres. The transverse response up to

matrix micro-cracking in the reinforcing model is dependent on the undamaged elastic stiffness of the micro-damage model. A characteristic of the micro-damage model is the reduction to zero of the Poisson's ratio term after micro-crack initiation. It follows that post micro-crack response, transverse to the reinforcing direction, is matrix dominated with no contribution from the reinforcement. The numerical calculation of the strain in the reinforcing element is through a logarithmic strain increment. Computationally this strain increment is more commonly used in metal plasticity where motivation comes from the close similarity of the true stress for tension, compression and torsion. This is mathematically appropriate for materials where the elastic part of the strain is small.

A characteristic of fibre-matrix composites are the hysteresis loops observed during unloading and reloading after matrix micro-cracking has started. The hysteresis loops are formed due to a non-linear interaction between the fibre and the matrix resulting from failure of the fibre matrix interface accompanied by frictional sliding (Hutchinson et al 1990).

At a load point past matrix micro-cracking, stress gradients are present in the fibres and the matrix (Aveston et al 1971). Unloading the composite from this point initially produces an elastic response until sliding occurs in the opposite direction to that which occurred in loading. In many cases the unloading response is non-linear due to a directionally dependent interfacial shear resistance. Reloading produces forward sliding of the fibres out of the matrix. This is also non-linear, following a separate load path to the unload curve but returning the composite to the original state prior to the unload as shown in figure 5.6.

Figure 5.7 shows a schematic of the mechanics of this composite. The model comprises two springs of stiffness E_A and E_B . This model is constructed to imitate a composite whose constituents have different stiffnesses and volume fractions. The contribution of the constituents stiffness to the overall stiffness is weighted by the appropriate volume fractions. The springs in the model do not have a volume, and therefore have no volume fraction, but can be weighted against each other by appropriate factors. Volume fractions V_A and V_B are related such that the total volume of the model is unity ($V_A + V_B = 1$). This gives the stiffness of

the model E_c as:

$$E_c = V_A E_A + V_B E_B \quad 0 \leq \epsilon_c \leq \epsilon_s \quad (5.10)$$

Where the strain across each element is identical. Spring A is considered to be linear elastic up to a strain ϵ_s , followed by a decay in stiffness with strain as shown in figure 5.8. This spring has no inelastic strain components. Spring B is linear elastic up to a strain ϵ_s when the stress in the spring is $E_B \epsilon_s$. Past this strain sliding occurs in the friction element. The basic mechanism of sliding is such that an increase in displacement occurs at a constant load. The stress in spring B cannot exceed $E_B \epsilon_s$ with continued loading past ϵ_s resulting in an increased sliding or inelastic strain. Unloading of the spring will result in a residual strain of $(\epsilon - \epsilon_s)$ where ϵ is the applied strain as shown in figure 5.9. The corresponding model stiffness and response, shown in figure 5.10, are then linear elastic up to a strain ϵ_s as described by equations 5.10 and 5.11.

$$\sigma_c = V_A \sigma_A + V_B \sigma_B \quad (5.11)$$

Here σ_A and σ_B are the stress in springs A and B. The response past ϵ_s consists of a constant contribution from spring B, due to sliding, and a variable stress from spring A which depends on the applied strain.

$$\sigma_c = V_A \sigma_A + V_B E_B \epsilon_s \quad \epsilon \geq \epsilon_s \quad (5.12)$$

When the model is unloaded and reloaded a hysteresis loop is formed as shown in figure 5.10. This can be divided into four strain regions ϵ_c^I , ϵ_c^{II} , ϵ_c^{III} and ϵ_c^{IV} bounded by ϵ_{c1} , ϵ_{c2} , ϵ_{c3} and ϵ_{c4} . The notation uses the subscripts, numbered 1 - 4, to identify a position on the hysteresis loop. Subsequently the strain regions bounded by positions 1 - 2, 2 - 3, 3 - 4 and 4 - 1 are given by ϵ_c^I , ϵ_c^{II} , ϵ_c^{III} and ϵ_c^{IV} . This notation is consistently applied to the stiffness and the response in those regions.

The mechanics of the model are now considered. At an applied strain ϵ_{c1} , the stress is:

$$\sigma_{c_1} = V_A \sigma_{A_1} + V_B E_B \epsilon_s \quad (5.13)$$

When the model is unloaded from ϵ_{c_1} , spring A and spring B have stiffnesses $\frac{\sigma_{A_1}}{\epsilon_{c_1}}$ and E_B . The corresponding model stiffness (E'_c) is:

$$E'_c = V_A \left(\frac{\sigma_{A_1}}{\epsilon_{c_1}} \right) + V_B E_B \quad (5.14)$$

The stresses in springs A and B during unloading are shown in figures 5.8 and 5.9. The elastic unloading of the model continues without frictional sliding until a strain $\epsilon_{c_2} = (\epsilon_{c_1} - 2\epsilon_s)$. The model response in this region is given by:

$$\sigma'_c = V_A \frac{\sigma_{A_1}}{\epsilon_{c_1}} (\epsilon'_c) + V_B E_B [\epsilon_s - (\epsilon_{c_1} - \epsilon'_c)] \quad \epsilon_{c_2} \leq \epsilon'_c \leq \epsilon_{c_1} \quad (5.15)$$

At the strain ϵ_{c_2} spring B is subject to a compressive stress $-E_B \epsilon_s$ and reverse sliding starts. The subsequent contribution from spring B is constant and the corresponding model response σ''_c is:

$$\sigma''_c = V_A \frac{\sigma_{A_1}}{\epsilon_{c_1}} (\epsilon''_c) - V_B E_B \epsilon_s \quad 0 \leq \epsilon''_c \leq \epsilon_{c_2} \quad (5.16)$$

It follows that the strain when the applied stress returns to zero is

$$\epsilon_{c_3} (\sigma''_c=0) = \frac{V_B E_B \epsilon_s \epsilon_{c_1}}{V_A \sigma_{A_1}} \quad (5.17)$$

At $\epsilon_{c_3} (\sigma''_c=0)$ the stress in springs A and B are $\left(\frac{V_B}{V_A}\right) E_B \epsilon_s$ and $-E_B \epsilon_s$. If the model is reloaded the stiffness are described by equation 5.14. The model response is linear up to a strain $\epsilon_{c_4} = (\epsilon_{c_3} (\sigma''_c=0) + 2\epsilon_s)$ where the stress in spring B is $E_B \epsilon_s$ and forward sliding begins again. From reloading to the initiation of forward sliding the stress in the model is:

$$\sigma'''_c = V_A \frac{\sigma_{A_1}}{\epsilon_{c_1}} (\epsilon'''_c) + V_B E_B (\epsilon'''_c - \epsilon_{c_3} (\sigma''_c=0) - \epsilon_s) \quad \epsilon_{c_3} (\sigma''_c=0) \leq \epsilon'''_c \leq \epsilon_{c_4} \quad (5.18)$$

Once sliding begins again the contribution from spring B is constant and the response for the final section of the reload curve is:

$$\sigma_c''' = V_A \left(\frac{\sigma_{A1}}{\epsilon_{c1}} \right) \epsilon_c''' + V_B E_B \epsilon_s \quad \epsilon_{c4} \leq \epsilon_c''' \leq \epsilon_{c1} \quad (5.19)$$

This closes the hysteresis loop. The response past the strain ϵ_{c1} reverts to that described by equation 5.10.

Figure 5.6 shows the response of a polyester fibre matrix composite. The hysteresis loops shown have similar shape characteristics to the reinforcing model hysteresis. The model is now adapted to represent the response of specific composites. The overall stress in the composite can be separated into a fibre and a matrix contribution as shown in figure 5.11, and associated with the components of the reinforcing model. These can be determined using the average stress in the fibre ($\bar{\sigma}_f$) and matrix ($\bar{\sigma}_m$) as described in chapter 4 by:

$$\bar{\sigma}_f = \frac{\sigma_c}{V_f} - \frac{2\tau(L_s)}{R} + \frac{\tau}{R} \frac{\{L_s\}^2}{L} \quad (5.20)$$

$$\bar{\sigma}_m = \sigma_{mu} - \frac{\tau}{R} \frac{V_f}{V_m} \frac{\{L_s\}^2}{L} \quad (5.21)$$

In uniaxial tension the matrix is modelled by a spring in which matrix micro-cracking reduces the modulus with increasing strain. The frictional sliding of the tow-matrix interface is then modelled by the sliding element of the model. Hysteresis loops are produced by the fibre matrix interaction, and as a result reverse sliding inelastic strains are observed. The use of sliding spring elements to model the fibres is therefore a sensible option where inelastic strains occur and allows the ability to model hysteresis while capturing the essential physics of the deformation process.

The schematic composite model described by equations 5.10 to 5.19 and through figures 5.7 to 5.10 comprised an incrementally elastic element and a frictional element with a constant sliding stress. In comparison, the model of the polymer composite represented the stress contribution of the fibres and

the matrix by a frictional and an incrementally elastic element. These two models have subtle differences. In the schematic model the non-linear spring had a positive stiffness. This was coupled to a friction element with a constant sliding response. In the polymer model the non-linear spring response, representing the matrix, was linear up to a micro-cracking strain followed by a reduction in stress with increasing strain. The matrix response is however still incrementally elastic with no inelastic strain.

The friction element in the composite model representing the fibres exhibited a strain hardening response. It follows that the unload strain required in the sliding element to cause reverse sliding is no longer $2\epsilon_s$ but a function of the level of hardening. As a result of the strain hardening the strain to cause reverse sliding increases with applied strain. The fundamental mechanics of the two models remain similar. The difference in spring responses does not affect the loading characteristics however it does influence the unloading and reloading responses. The strain hardening friction element of the composite model poses a problem. The response of the composite model in unloading past micro-cracking is such that the hysteresis loop formed is linear as shown in figure 5.12. This is a direct result of the strain hardening increasing the strain to cause reverse sliding.

A Modification of the composite model was considered which would introduce hysteresis in both loading and unloading. This must be achieved without altering the overall composite response. In the composite model the transverse response is controlled by the incrementally elastic matrix element. For this reason it is desirable that the matrix element should be unaltered, and hence the reinforcing element was modified. The reinforcing element was split into two elements, the sum of which produces the loading response of the fibre contribution. The first element is a sliding element with no strain hardening and a constant reverse sliding component of strain. The second element was chosen to be a strain hardening element. The response of this friction element when summed with the constant friction element produced the stress contribution of the fibre as shown in figure 5.10 and hence does not affect the loading curve of the composite. From the mechanics of the original schematic model the combination of these two responses will produce hysteresis loops.

These two friction elements are then used to represent the reinforcing. When this is combined with the incrementally elastic element describing the matrix contribution the hysteresis loops produced will exhibit a decay at the same rate as the matrix modulus.

Using this approach to model the response of a fibre matrix composite has few limitations. The initial bound is that the response is the matrix element is fixed thus producing a more correct transverse response of the element. The remaining two element responses are variable but must sum to that of the fibre response. The variables that are therefore introduced to the model include the level of reverse sliding strain, the stiffness during initial unloading and the stiffness of the final unloading section. This allows the model to be mapped to the shape of a hysteresis loop from a single point of unloading.

5.4 Benchmarking the Constitutive Models

The constitutive relations validated in this section were the micro-damage and the micro-damaged model with reinforcement. The behaviour of the two models was compared with the polyester 0-90 continuous fibre-matrix composite laminate. A simple three element mesh was constructed from second order continuum plane stress elements with reduced integration using a total of eighteen nodes and run using the Abaqus finite element code on an IBM 3090. To demonstrate the characteristics of the constitutive models, the following tests were used.

- 1) A monotonically loaded uniaxial tensile and compressive tests.
- 2) A cyclic uniaxial tensile test followed by a transverse tensile loading cycle.
- 3) A cyclic uniaxial compressive test

The initial test focused on reproducing uniaxial data from the polyester model material. The cyclic analyses were intended to check the ability of the models to exhibit hysteresis and anisotropy. The uniaxial analysis was run beyond micro-cracking in tension and post yield stress compression using displacement boundary conditions. In no cases were the models taken beyond total failure in tension or compression.

The input for the micro-damage model was derived from the experimental uniaxial tensile and a compression tests described in chapter 4. The reinforcing model input was divided into a matrix and fibre contribution as described in section 5.4. A uniaxial micro-damaged response represented the average matrix contribution ($\bar{\sigma}_m$) as shown in figure 5.11. From section 5.4 the hysteresis of the model at micro-crack saturation was mapped to the uniaxial tensile experimental unloading curves. As a result the fibre reinforcing input was split into a perfectly plastic and a strain hardening response as shown in figure 5.13. The reinforcement data were chosen to fit the unloading response of the polyester shown in figure 5.6 from an applied tensile strain of 0.1. This coincides with matrix micro-crack saturation in the polyester composite. Combining these elements with the

matrix element gave the composite hysteresis loop shown in figure 5.14.

Figure 5.15 shows the results of the uniaxial tensile and compressive analysis response of the micro-damage model with the experimental results superimposed. The response of the reinforcing model in uniaxial tension and compression is shown in figure 5.16 with the transverse response shown in figure 5.17. Figure 5.18 compares the hysteresis loops of the reinforcing model with those measured on the polymer composite. From the cyclic results of the reinforcing model a secant modulus was calculated between the applied strain and the unloaded inelastic strain. This modulus was described as a function of the applied strain and compared with the results of the polyester composite normalised by the composite elastic modulus and the micro-cracking strain as shown in figure 5.19. In addition the inelastic strain as a function of the total strain was compared for the reinforcing model with the model material as shown in figure 5.20.

5.5 Discussion

The fundamental basis in the development of anisotropic constitutive models was initially to establish an isotropic micro-damage model. The results of the micro-damage model compared favourably with the tensile response of the model material. The behaviour in the transverse direction was identical to the response in the original loading direction before micro-cracking initiated in the transverse orientation. The results of a through thickness tensile test on the polymer are shown in figure 5.21 compared with the transverse micro-damage model response. From this diagram it is seen that micro-damage model overestimates the stress in the transverse direction by an order of magnitude. The response in the transverse direction of the micro-damage model would therefore be an unacceptable representation of out of plane loading of a laminate. In addition the cyclic loading in this orientation is incrementally elastic. This limits the use of the micro-damage model to predicting both the extent of micro-cracking damage and the load displacement response in geometries where the stress in the interlaminar direction does not exceed the matrix micro-cracking stress.

As a result of the limitations of the micro-damaged model, the reinforced model was developed. The compressive response of the reinforced model is heavily dependent on the matrix. The onset of compressive failure is arbitrary but may be selected such that the compressive stress field remains largely elastic as demonstrated in figure 5.16. In the model material compressive failure occurred at approximately twice the tensile micro-cracking stress and can be modelled accurately. However in a ceramic composite compressive failure occurs at significantly higher stress levels than in tension (Sammis et al 1986). The demonstration of the models ability to provide an elastic response in compression up to higher levels is therefore justified.

Figure 5.18 shows that the tensile response of the reinforced model in the direction of the reinforcement matched the results of the model material. Similarly the hysteresis loops of the reinforced model and the model material compared favourably. The characteristic form of the hysteresis loops

were imitated successfully, and the analysis showed an increase in the loop area comparable with those produced by the model material as shown in figure 5.18. Subsequently the decay of the secant modulus and the development of inelastic strain shown in figures 5.19 and 5.20 compared favourable with the analysis. However the experimental and computational results diverged at a strain ratio $\left(\frac{\epsilon}{\epsilon_t} = 10\right)$ when micro-crack saturation occurred and the load is transferred primarily to the fibres. This result is explained by considering the mechanics of the reinforced model. After matrix micro-crack saturation the stiffness of the composite becomes $V_f E_f$ with no increase in the load borne by the matrix (Aveston et 1971). Therefore in the reinforcing model an increase in the composite stress must be accompanied by an increase in the response of the reinforcing element as shown in figure 5.13. In this case the relevant reinforcing element is elastic plastic strain hardening. As the response of this element stiffens so the hardening rate of the element increases hence reducing the rate of inelastic strain with applied strain. In the reinforced model this results in a divergence between the predictions and the experimental results of rate of secant modulus depletion and inelastic strain of the composite shown in figures 5.19 and 5.20.

Figure 5.17 shows the transverse response of the reinforced model. The response is dominated by the matrix since past matrix micro-cracking the reinforcing elements only support load along their axis. The response therefore follows that produced by the average matrix stress input through the matrix element load curve. The results of the transverse experiments on the model material in figure 5.21 show the levels of stress to be much lower than those predicted by the reinforced model. Although the predicted curve of the reinforced model is higher than the experiment it should be noted that stress levels involved are very low and that the predicted response is a major improvement on the initial micro-damage model. The main result of the transverse analysis of the reinforced model is that it demonstrates its ability to model material with high levels of anisotropy and is suitable for the analysis of anisotropic materials in multiaxial stress fields.

5.6 Conclusions

A basic micro-damage model has been developed, which compared favourably with the model material in terms of damage and load displacement predictions. However in the through thickness direction the results were not encouraging. This limited the use of the micro-damage model to the analysis of components where the interlaminar stress did not exceed matrix micro-cracking. As a result of the limitations the model was refined by the introduction of reinforcement

The reinforced model gave numerical results which compared well with the experimental results in both the direction of the reinforcing and in the interlaminar orientation. In addition it has been demonstrated that the overall characteristic cyclic responses of the reinforced model can emulate the response of the model material. The results of the reinforced model are encouraging and allow it to be used to analyse fibre matrix components in terms of the prediction of deformation and the extent damage. Here the extent of damage is associated directly with strain and allows a crack density parameter to be attached to any stress system.

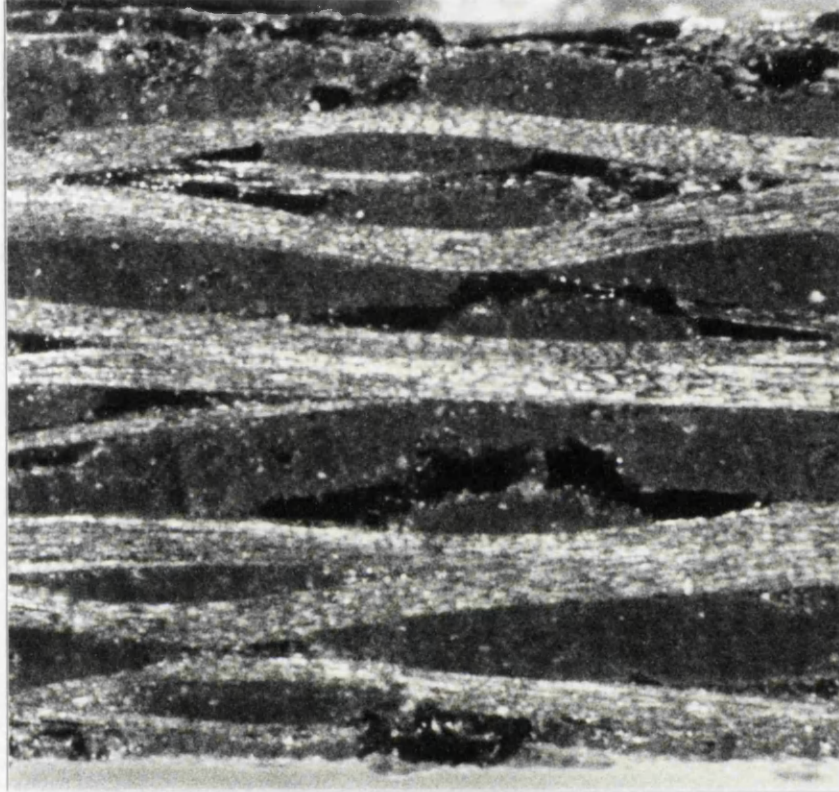


Figure 5.1 Photograph of porosity in SiC-SiC caused by incomplete densification during manufacture

Specimen in bending

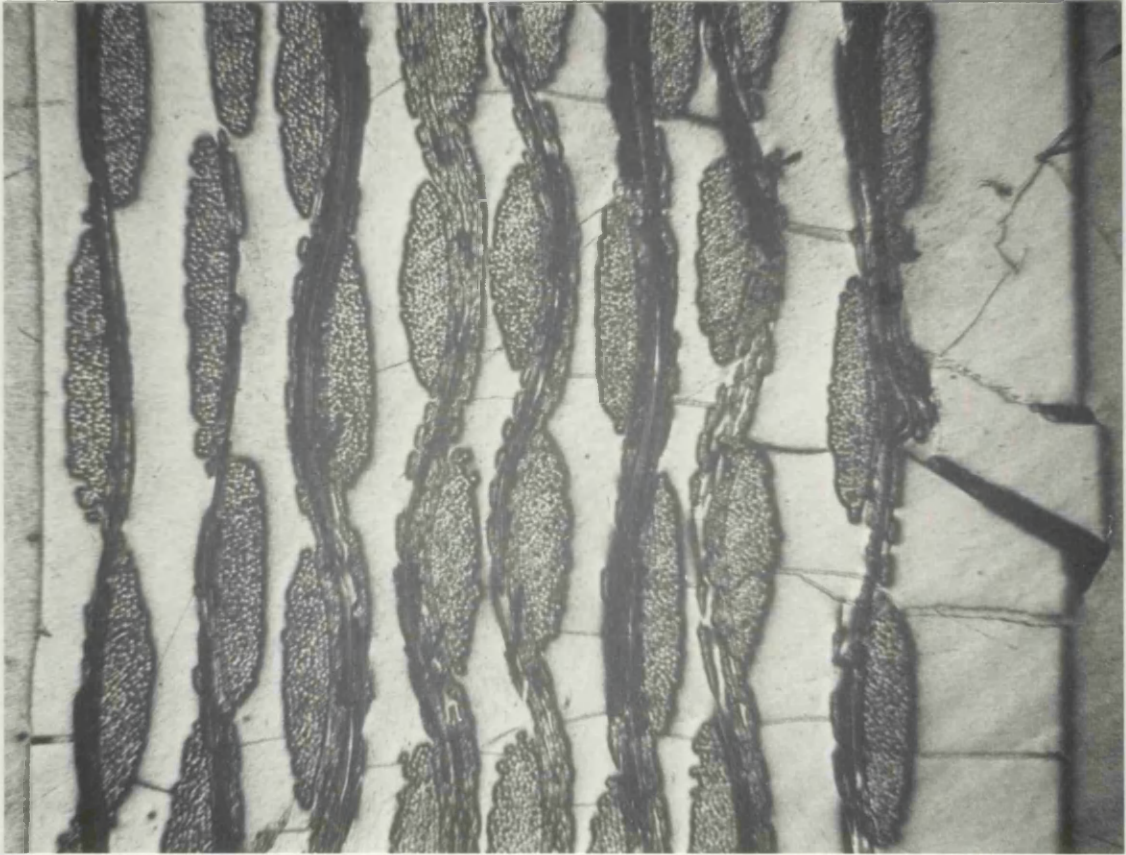


Figure 5.2 Photograph of matrix micro-cracking in the polyester composite.

Figure 5.3 Photograph of thermal induced micro-crack propagation in the matrix of the SiC-Alumina bond bar.

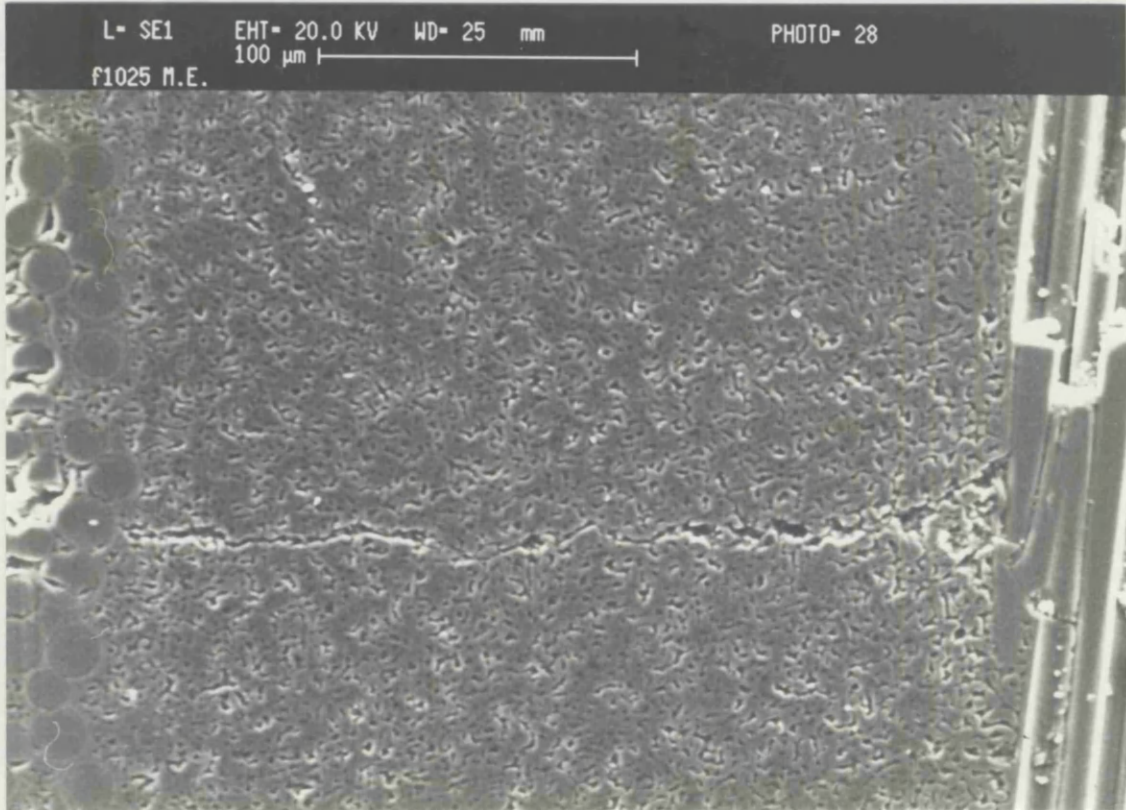


Figure 5.3 Photograph of thermal induced micro-crack propagation in the matrix of the SiC-Alumina bend bar.

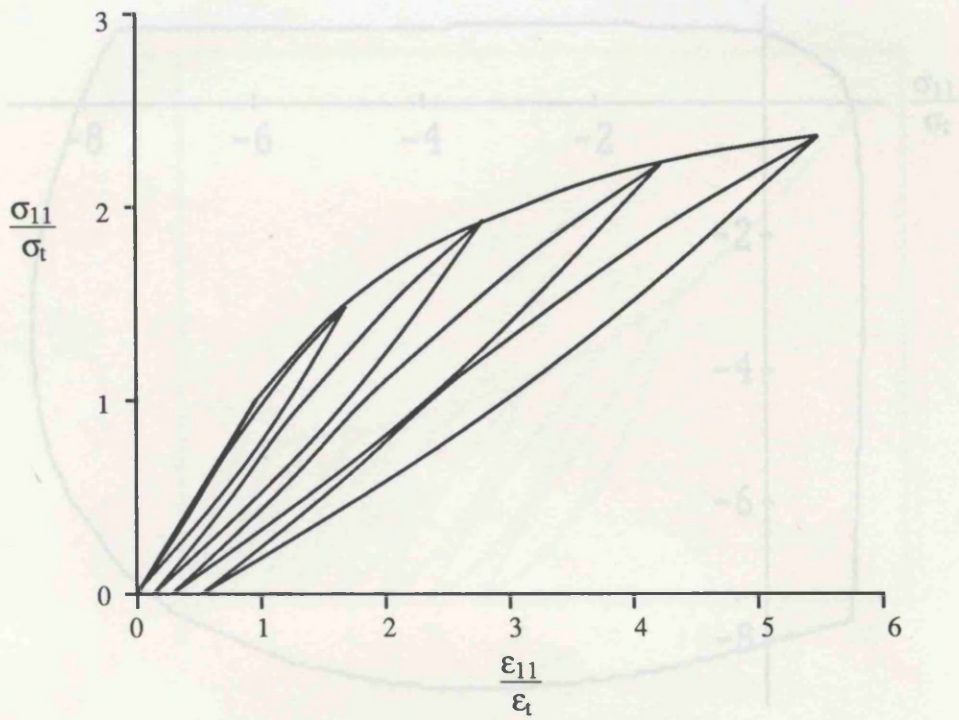


Figure 5.4 Tensile micro-crack response of a ceramic composite (Fu et al 1990)

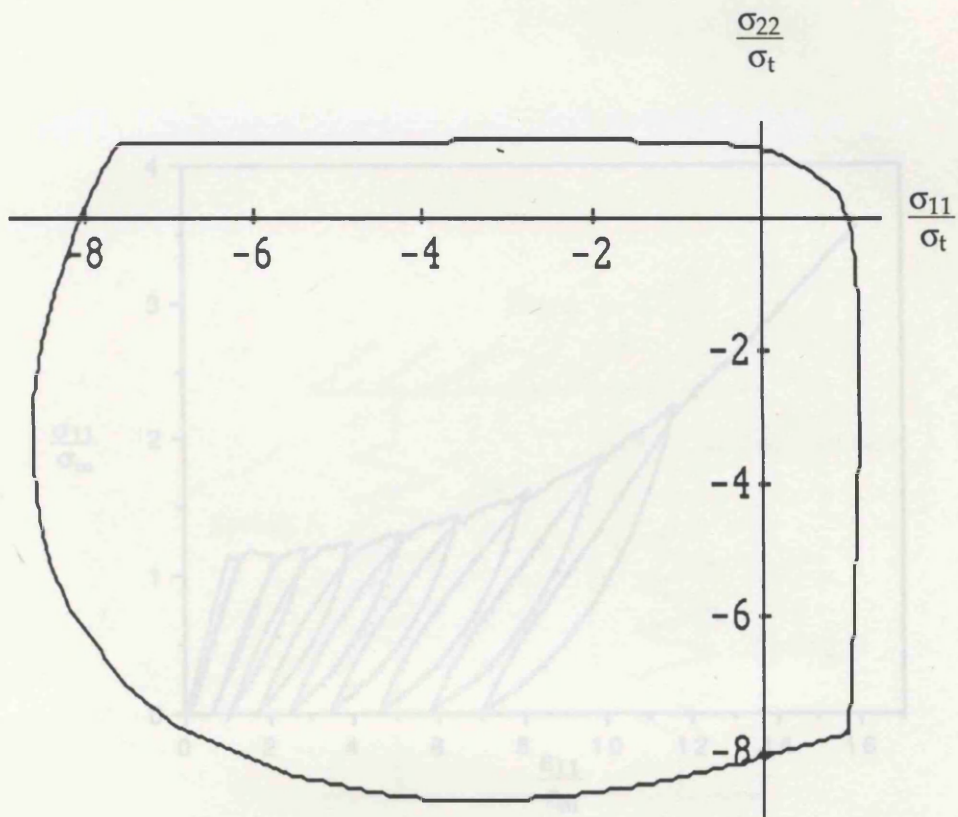


Figure 5.6 Stress Strain response of polymer system cycled in failure

Figure 5.5 Compressive and Tensile Mohr Coulomb Yield Surfaces

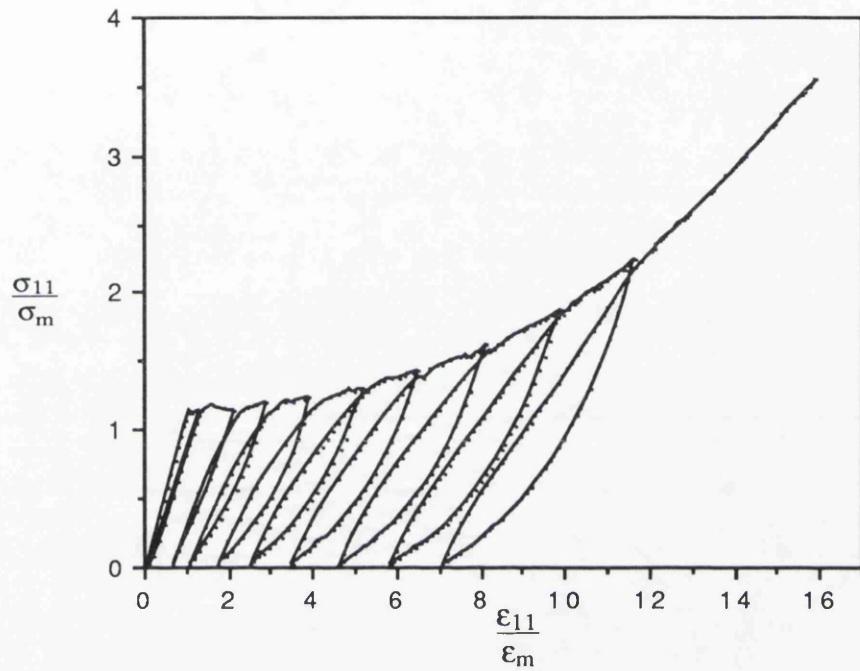


Figure 5.6 Stress Strain response of polymer system cycled to failure

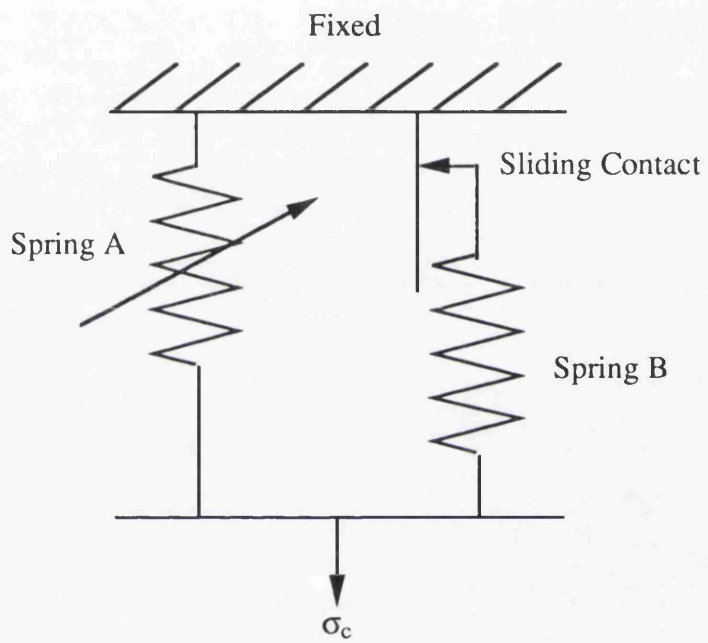


Figure 5.7 Spring Model System

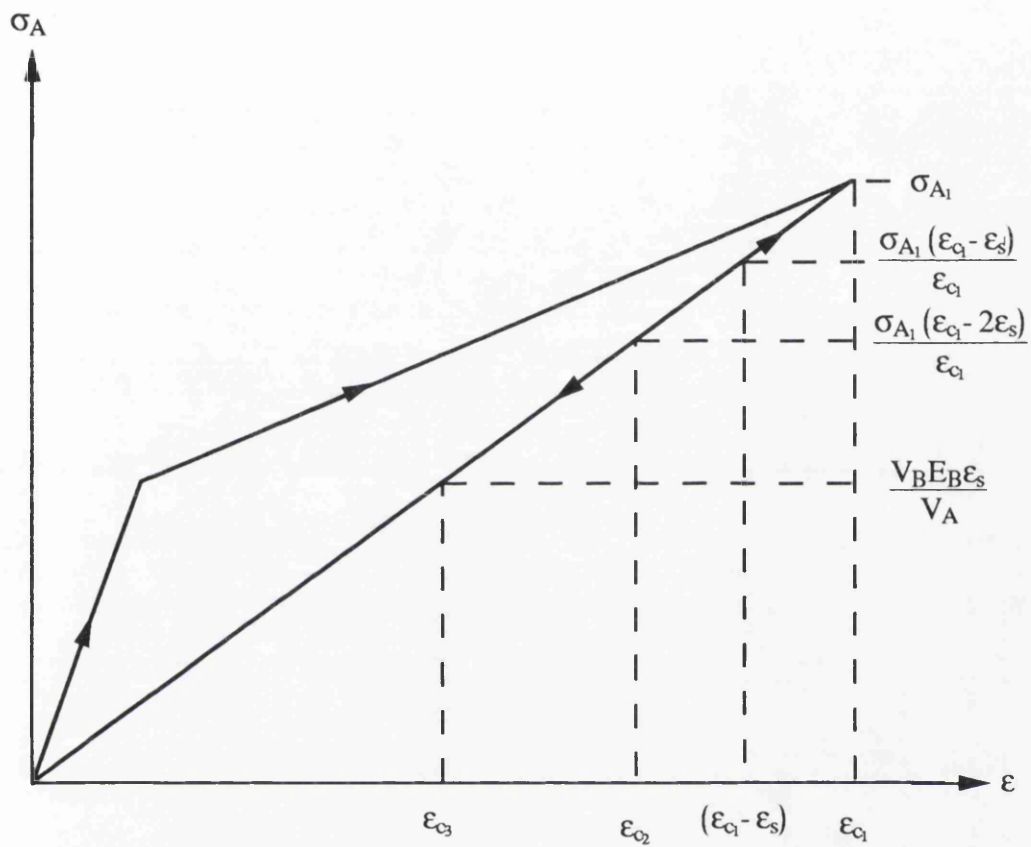


Figure 5.8 Spring A Response

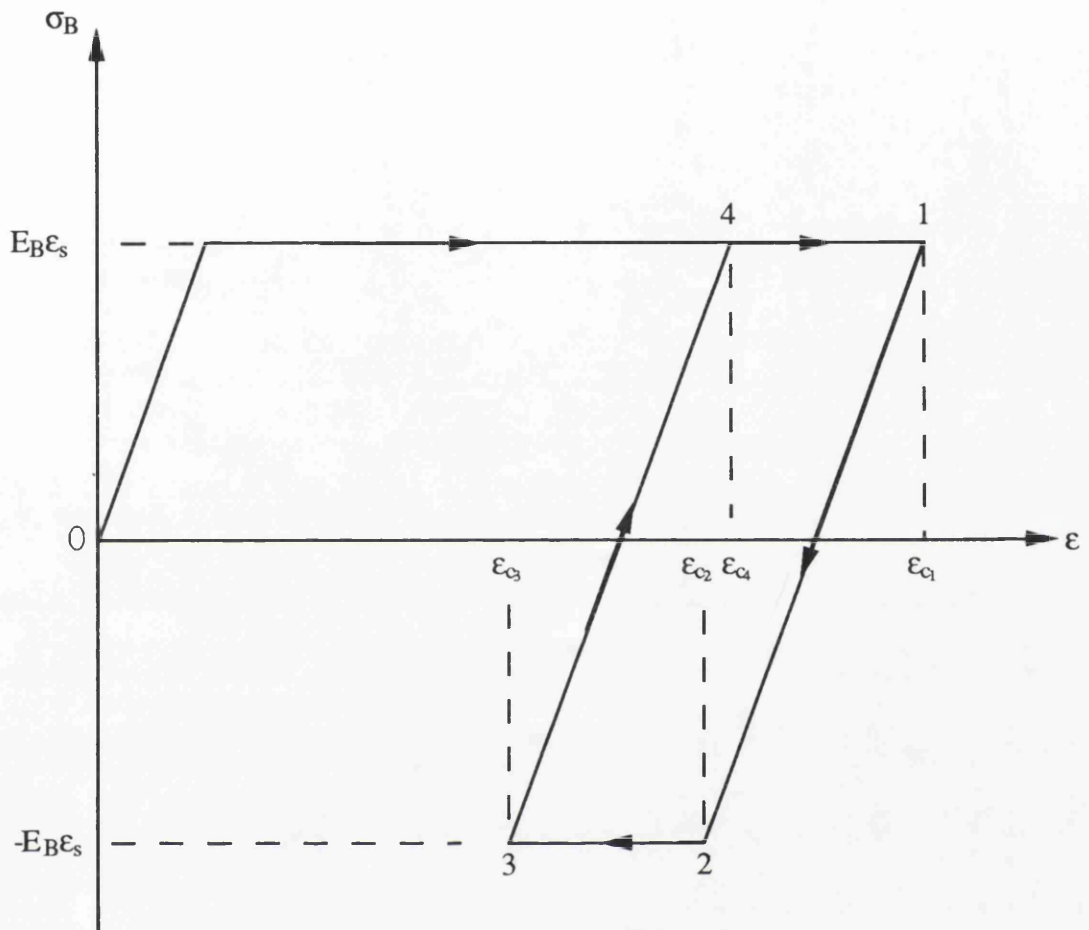


Figure 5.9 Spring B response

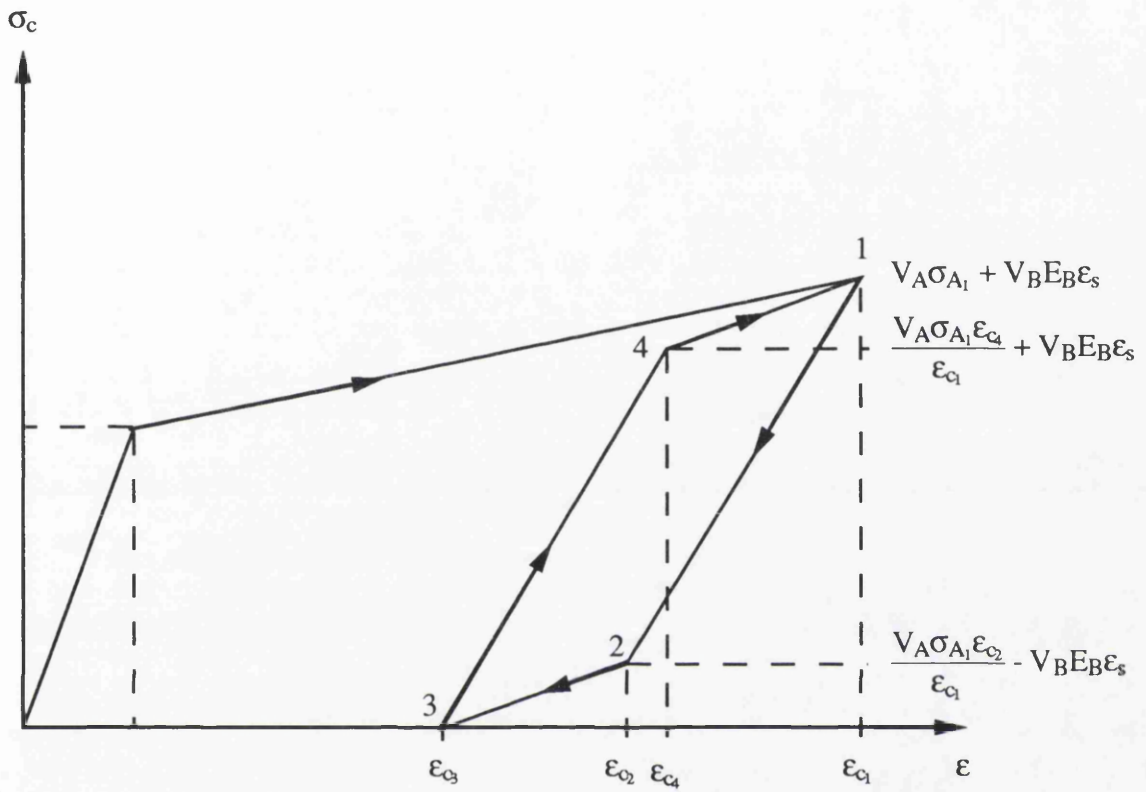


Figure 5.10 Model Response

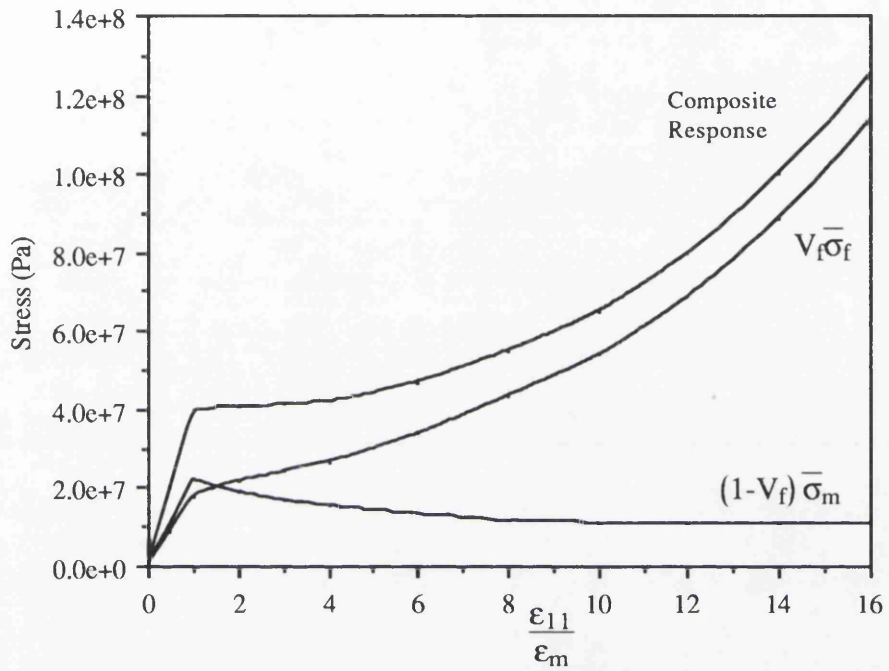


Figure 5.11 Average Stress Contribution from Fibres and Matrix Compared to the Polymer Composite Stress

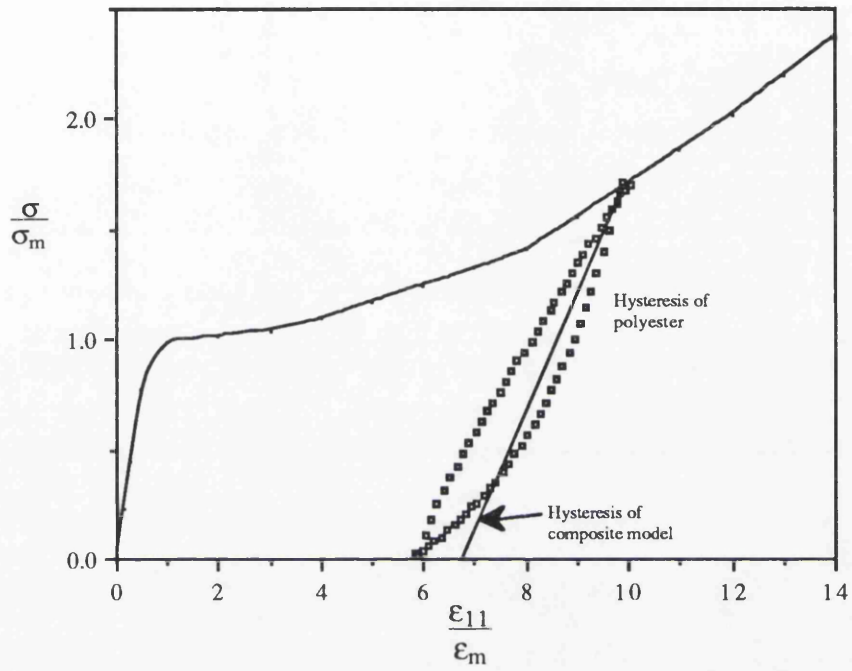


Figure 5.12 Comparison of the first composite reinforcing model with hysteresis data

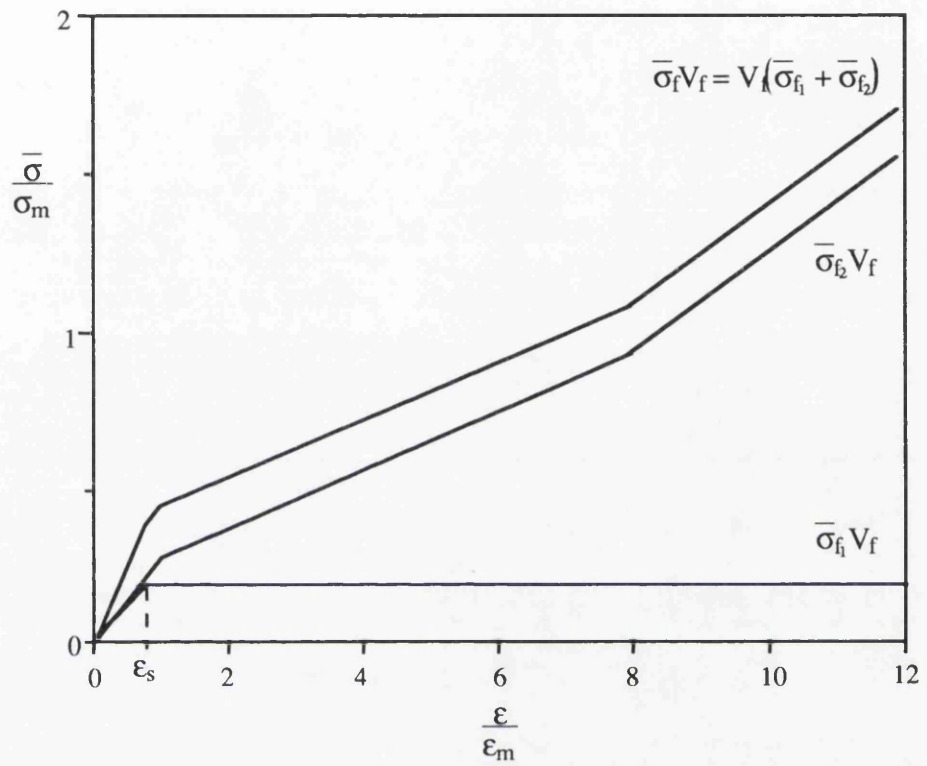


Figure 5.13 The response of the two elements combined to form the reinforcing element as a function of strain normalised by the micro-cracking stress and strain.

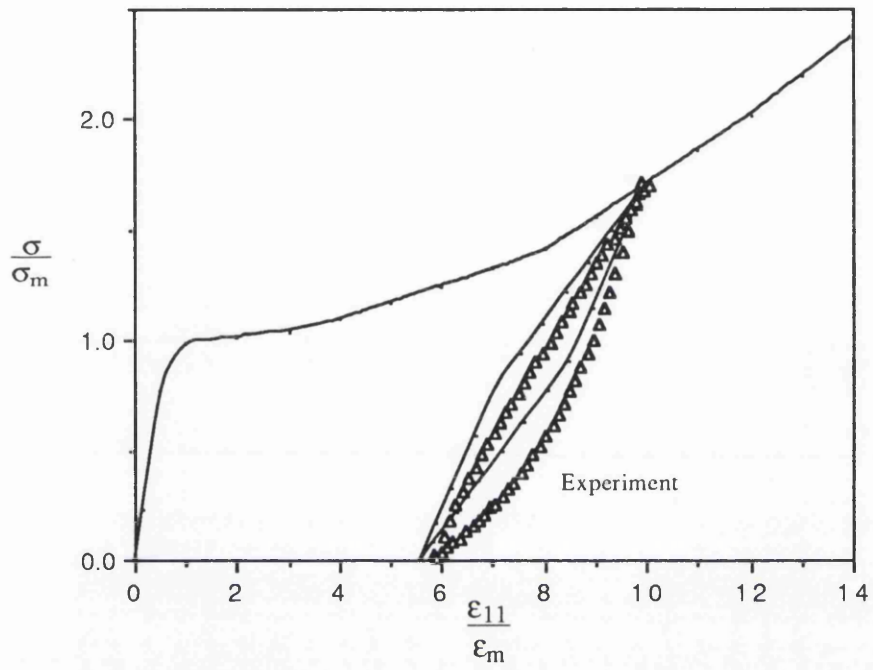


Figure 5.14 Cyclic comparison of the 2nd Composite reinforcing model with hysteresis data

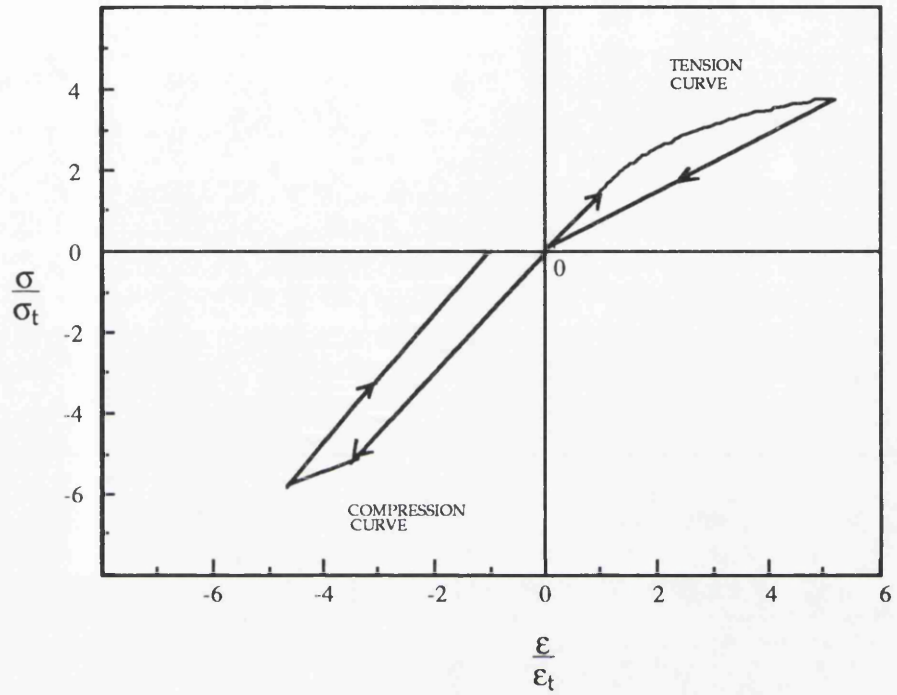


Figure 5.15 Response of Micro-damaged Model

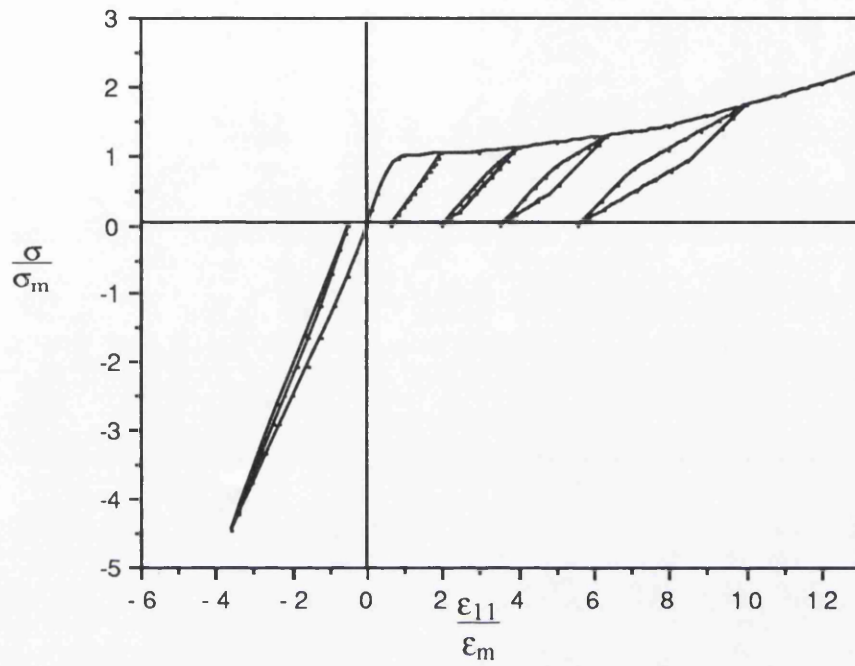


Figure 5.16 Cyclic response of the reinforcing model with hysteresis

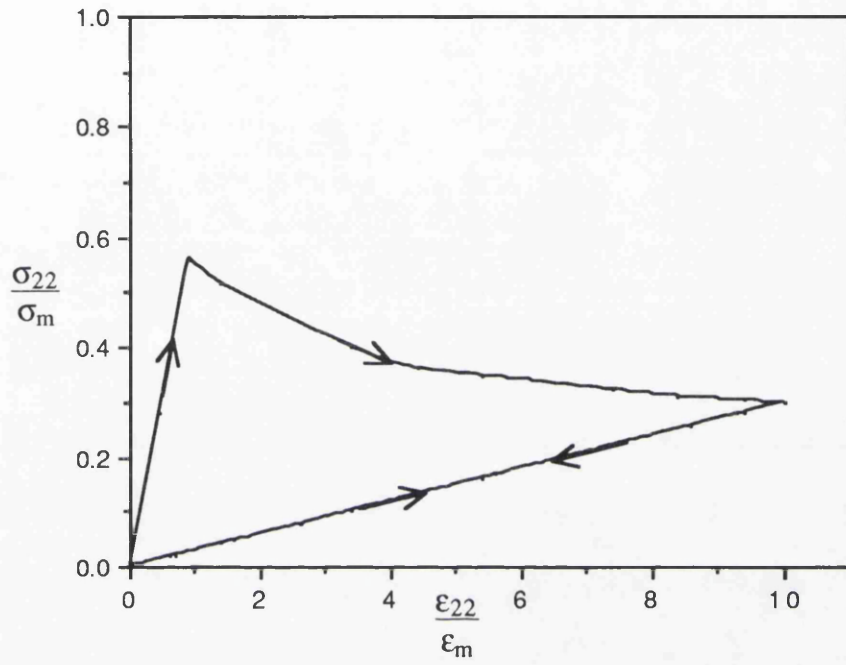


Figure 5.17 Reinforced model response perpendicular to the reinforcing element

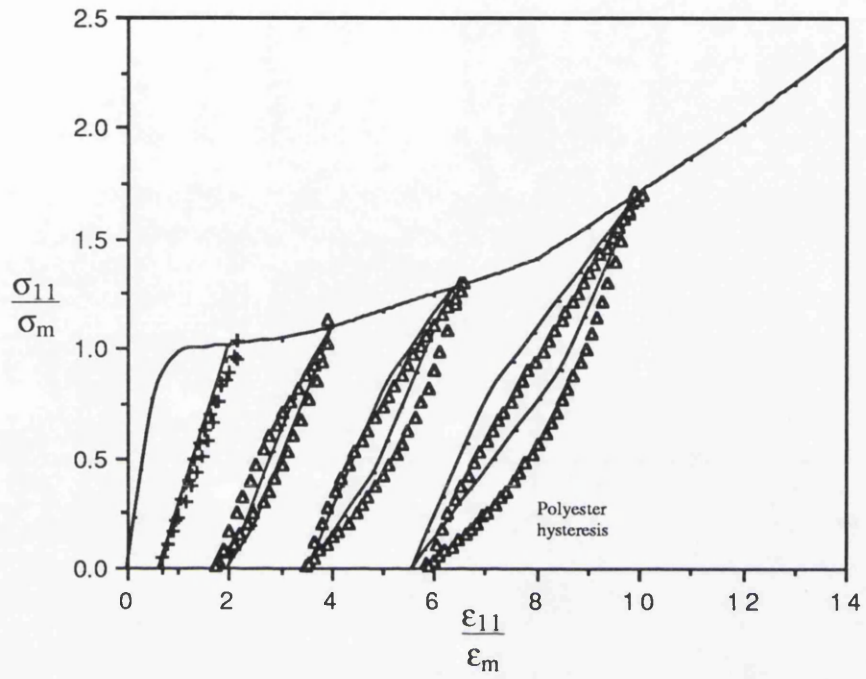


Figure 5.18 Cyclic comparison of the reinforcing model with the polyester uniaxial data

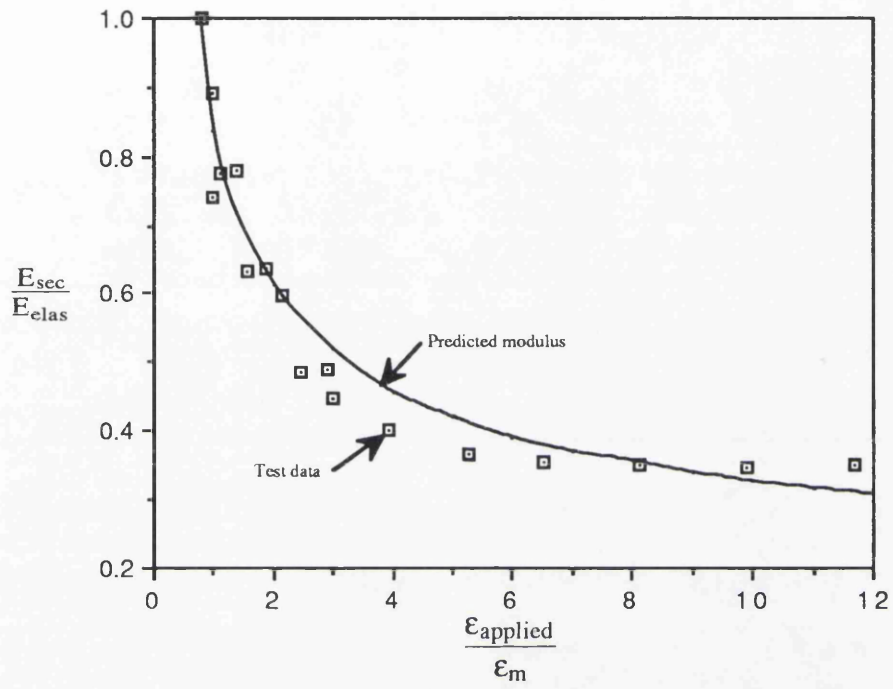


Figure 5.19 Secant Modulus against total strain for the computational model and the test data.

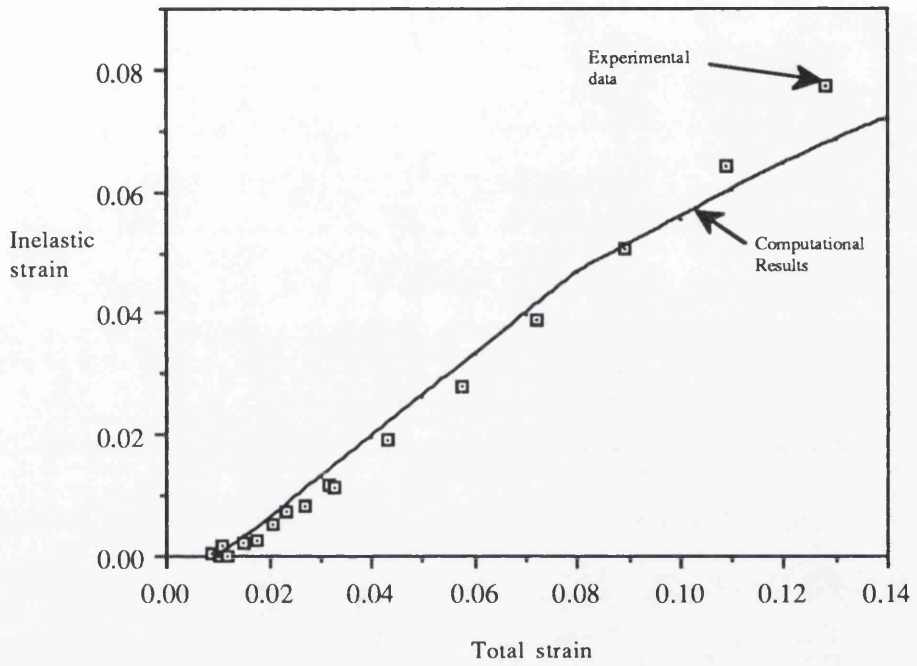


Figure 5.20 Inelastic Strain as a function of the applied Strain

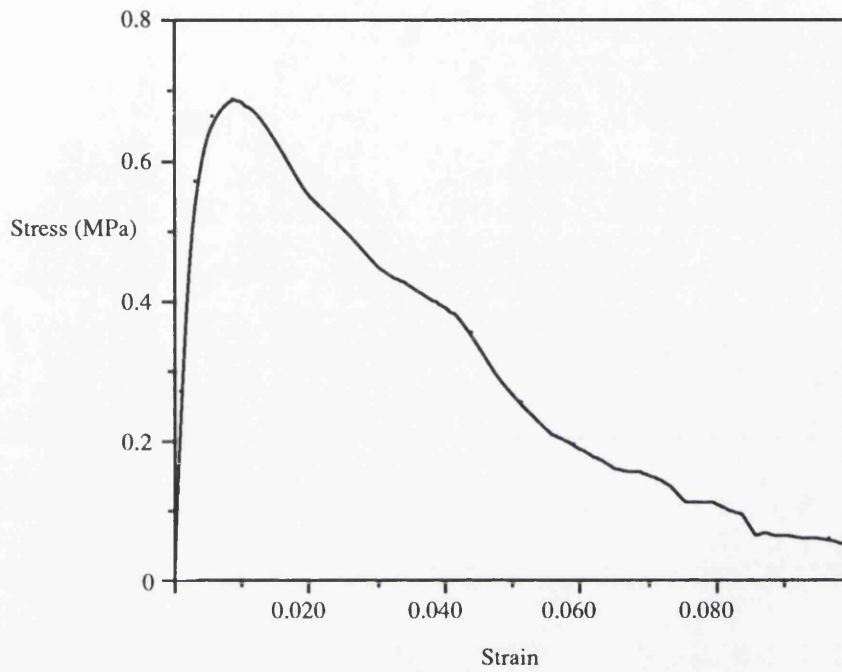


Figure 5.21 Interlaminar response of the polyester 0-90 laminate.

6. Sub-Element Analysis

6.1 Introduction

This chapter demonstrates the development of the reinforced model as a suitable numerical tool to analyse components manufactured from a fibre composite. Three generic specimens or sub elements were tested and the results compared to a computational analysis. The sub-elements included a bend bar, a 'T' beam and a thickened section to the dimensions shown in figures 6.1-6.3. The choice of the sub elements was intended to represent three geometries to be found in the design of an exhaust diffuser unit. The geometries were analysed to demonstrate the constitutive models in a range of stress systems to provide information for component design. The specimens were supplied by Rolls Royce and manufactured from SiC-Al₂O₃ using Nicalon fibres and the DIMOX process. In addition sub-elements of the polyester model material were supplied by Butler (1991). The initial analyses used the isotropic micro-damage relation. This was subsequently refined to incorporate reinforcement to allow the anisotropic effect of the fibre orientation to be modelled. In both constitutive models the analyses were used to predict the load-displacement response and the extent of micro-cracking.

6.2 Sub-Element Testing

6.2.1 Method

Three point bend tests were performed on a bend bar, a 'T' beam and a thickened section. The specimens were tested on a Lloyds 10000 testing machine, the test system and the ceramic specimen data were provided by Gibson (1993). The polyester specimens were manufactured with the 0-90 woven cloth fibres aligned parallel to the principal stress axis and a fibre volume fraction of 35%. The SiC-Al₂O₃ specimens were manufactured with a 0-90 array of continuous fibres aligned as in the model material specimens

with a fibre volume fraction of 36%. The three geometries were tested to varying levels of displacement. This provided load displacement data while optical microscopy established the extent and location of damage in the tests.

6.2.2 Results

The initial comparison of the numerical and experimental results was through the load-displacement (P-v) relation. A bend bar of length L, breadth B, depth w and second moment of inertia I subject to a load P is subject to an applied moment $M = \frac{PL}{2}$. This moment can be normalised by the moment M_t required to cause micro-cracking in the outer layer using simple bend theory, $M_t = \frac{2\sigma_t I}{w}$, where σ_t is the micro-cracking stress such that

$$\frac{M}{M_t} = \frac{PLw}{4\sigma_t I} \quad (6.1)$$

. Similarly the mid span displacement (v) was normalised by the displacement (v_t) to cause micro-cracking in the outer layer.

$$v_t = \frac{\sigma_t L^2}{12 E w} \quad (6.2)$$

Here E is the Youngs Modulus. Figures 6.4 and 6.5 show the normalised load displacement results of the model material and the ceramic bend bar experiments. For the ceramic sub-elements E and σ_t taken from data supplied by Merril (1992) are 108GPa and 78 MPa.

The load displacement results of the 'T' beam and thickened section were normalised in a similar way. In the case of the 'T' beam the applied moment was calculated at the initiation of the web fillet taking the beam length (L) in equations 6.1 and 6.2 to be 30.5 mm from the support. The moment M_t and displacement v_t were calculated as that required to cause micro-cracking in the outer layer of the specimen at the start of the fillet. The second moment of area I was therefore calculated using the dimensions of the specimen before the web fillet. Figures 6.6 and 6.7 show the normalised response of the 'T' section for both the model material and the ceramic.

Data from the thickened section tests were normalised by calculating the

applied moment at the start of the change in cross section where the beam length (L) in equations 6.1 and 6.2 is 20mm from the supports. Using simple bend theory the thickened section results were normalised by the moment (M_0) and the displacement (v_0) to cause micro-cracking in the outer layer of the beam at the initiation of thickened section where $L = 20\text{mm}$. In these calculations the second moment of inertia of the beam was determined at the cross section immediately prior to the thickening of the beam. The load displacement results of the thickened section for the model material and the ceramic are shown in figure 6.8 and 6.9

Inspection of the polyester composite bend bar showed localised micro-cracking initiating on the outer tensile layer of the specimen at the mid span extending laterally on the outer surface and through the specimen towards the compressive layer. To establish the extent of micro-crack growth in the model material through the thickness, the bend tests were halted at various levels of beam deflection. The specimens were then unloaded, sectioned and photographed. At a displacement ratio ($\frac{v}{v_t}$) of 3.3, micro-cracking was estimated, from the photograph shown in figure 6.10 to extend to a depth $\frac{x}{w} = 0.30$ where w is the beam thickness and x is the distance from the tensile surface. Photographs in figures 6.11 and 6.12 show micro-cracking at $\frac{x}{w} = 0.45$ and 0.55 at displacement ratios ($\frac{v}{v_t}$) of 4.7 and 6.1. In the polyester bend bar a distribution of micro-cracks extended laterally along the beam from the mid point of the tensile surface and normal towards the compressive surface.

In the ceramic bend bar a single crack was observed at the mid-span. Continued displacement showed the crack to propagate through the first laminate and then extend laterally with a delaminating type mode of deformation. This is shown in figure 6.13 with the beam at a displacement ratio ($\frac{v}{v_t}$) of 13.1. Further displacement showed cracking continuing through the specimen towards the compressive section of the beam at a displacement ratio ($\frac{v}{v_t}$) of 25.0 as shown in figure 6.14

Figure 6.15 and 6.16 show the damage in the model material 'T' beam at a displacement ratio $\frac{v}{v_t} = 7.5$, while figure 6.17 showing the damage at $\frac{v}{v_t} = 12.0$. These figures illustrate the way cracks were formed in the web, between the layers of fibres. Similar observations were made in the ceramic as shown in

figure 6.18, 6,19 where the specimens were at displacement ratios of 14.9 and 24.8. A consistent feature of both materials was the formation of delamination cracks in the matrix or the fibre tow. The position and orientation of the cracks therefore indicate that the interlaminar failure stress is significantly less than the uniaxial failure stress in the direction of the fibres. Complete failure of the polyester 'T' beam was not produced due the high levels of deformation required. In the ceramic 'T' beam failure was observed to occur by total delamination of the web as shown in figure 6.20 at a displacement ratio of 69.4.

In the thickened beam failure initiated at the change in cross section. Figures 6.21 and 6.22 show the model material thickened sections at displacement ratios of 11.2. and 15.0. Similarly the ceramic thickened sections are shown in figures 6.23 and 6.24 at displacement ratios of 18.4 and 73.6. To assess the mode of deformation the specimens were halted at varying level of displacement. Crack initiation again occurred on the tensile side of the specimen. Examination of the failed specimens indicated both tensile micro-cracking perpendicular to the fibre tows and shear cracks between the layers.

6.3 Computational Analysis

6.3.1 Method

For the purpose of numerical analysis, symmetry allows the test specimens to be represented by the half sections shown in figures 6.25, 6.26 and 6.27. Mesh generation was provided by Patran (1989) and analysed using Abaqus finite element code (Abaqus 1992, Appendix I) mounted on an IBM 3090. The bend bar was modelled with 215 nodes and 60 elements producing a problem with 430 degrees of freedom. The T-beam model consisted of 1109 nodes and 340 elements producing a problem with 2218 degrees of freedom. The thickened section model comprised 1577 nodes and 484 elements with 3154 degrees of freedom. All three models used second order continuum plane strain elements, with reduced integration and symmetry to represent the full specimen under displacement boundary conditions.

The initial analysis of the bend bar and the 'T' beam used an isotropic micro-damage constitutive relation as shown in figure 6.28. This was compared with the experiments in terms of the load-deflection response, as well as the position and extent of damage. In addition the results of the bend bar tests were compared with similar analysis using purely elastic and classical elastic-plastic constitutive relations. Subsequently the constitutive model was developed to incorporate anisotropy using the reinforcing model. The material input used the reinforcing model with the matrix and fibre contributions for the model material and the ceramic shown in figures 6.29 and 6.30. The orientation of the reinforcing elements were arranged in the same direction as the fibres in the specimens as shown in figures 6.31, 6.32 and 6.33 for the bend bar, the 'T' beam and the thickened section. Here the direction of reinforcement is described by the black broken lines in the deformed mesh. A typical Abaqus input deck for this analysis is shown in Appendix I

6.3.2 Results

The load-displacement response of the bend bar is compared for the micro-damaged model analysis data and the experimental results of the polymer system in figure 6.4. In this figure, the applied moment (M) and the displacement (v) is normalised by the moment (M_0) and deflection (v_0) to cause micro-cracking in the outer layer of the bend bar at the mid-span. Figure 6.34 compares the response of the micro-damage, the elastic and the classical elastic plastic model with the initiation of micro-cracking indicated.

The extent of micro-cracking in the computational analysis was determined from the tensile and compressive yield functions. Tensile and compressive yield was calculated separately and governed by functions of the micro-cracking stress (σ_c, σ_t) and the local stresses. In compression the appropriate function is given by:

$$f\left(\frac{\sigma_{ij}}{\sigma_c}\right) = \frac{\bar{\sigma}}{\sigma_c} + \gamma \frac{\sigma_{kk}}{\sigma_c} - \lambda \quad (6.1)$$

For the compressive field σ_c , γ and λ were taken as 105 MPa, 0.3635 and 0.8788. In tension a similar function, with different constants was used.

$$f\left(\frac{\sigma_{ij}}{\sigma_t}\right) = \frac{\bar{\sigma}}{\sigma_t} + \alpha \frac{\sigma_{kk}}{\sigma_t} - \beta \quad (6.2)$$

For the tensile field σ_t , α and β were 35MPa, 2.729 and 1.907 respectively.

Figures 6.35, 6.36 and 6.37 show the predicted extent of tensile micro-cracking and compressive yield functions of the polymer bend bar under the load point for displacement ratios ($\frac{v}{v_0}$) of 3.3, 4.7 and 6.1 for the micro-damaged constitutive relation. Here tensile micro-cracking or compressive yield are indicated by non negative functions. In all three cases there is no compressive failure, while tensile micro-cracking extended over 27, 41 and 52% of the beam width at displacement ratios ($\frac{v}{v_0}$) of 3.3, 4.7 and 6.1. The absence of compressive yield in the micro-damage model is a direct result of the high compressive yield to tensile micro-cracking ratio

Figure 6.38 shows the principal stress distribution through the polyester bend bar derived from the micro-damage model normalised by the bending stress (σ_b). This is described as a function of position through the beam thickness (x) normalised by the beam depth (w) under the load point. At the same displacement ratio the principal stress distribution of the elastic and the classical elastic plastic constitutive relations normalised by the bending stress are compared in figure 6.39. The absence of compressive failure in the micro-damaged constitutive relation is highlighted in figure 6.38. The absence of compressive yield has the effect of shifting the neutral axis towards the compressive side of the beam. In the case of the classical elastic plastic analyses the neutral axis remained at $\frac{x}{w}=0.5$ as a result of balanced yielding in compression and tension.

Using the isotropic micro-damaged constitutive relation the 'T' beam was analysed and compared with the normalised response of the polyester specimens as shown in figure 6.6. The isotropic computational analysis exhibited a significantly stiffer response than the specimen. Figures 6.40 and 6.41 show the strain distribution and the extent of micro-cracking in the isotropic micro-damage analysis of the polyester 'T' beam at a displacement ratio of 7.5. Comparing figures 6.40 and 6.41 with the photograph of the test specimen in figure 6.15 shows the predicted position of micro-cracking misplaced by the isotropic analysis. This is a result of the orientation of the fibres in the 'T' beam. Examination of figure 6.15 shows the formation of a delamination crack. From the numerical isotropic analysis the maximum stress concentration factor of 1.5 is located on the fillet radius of the 'T' beam. The orientation of the fibres in the specimen at the fillet radius and maximum stress concentration are in line with the principal stress. It is clear that the tensile delamination failure observed in the web, occurs at significantly lower stresses than the uniaxial failure stress in the direction of the fibres.

Figure 6.42 compares the normalised load-displacement response of the polyester bend bar with that predicted by the reinforced constitutive model. To demonstrate the hysteresis of the reinforced model the analysis was cycled at a displacement ratio of 3.5 to coincide with experiment as shown in figure 6.42. The ceramic bend bar response was normalised and compared with the

prediction from the reinforced model as shown in figure 6.5

Figures 6.6 compares the response of the model material 'T' beam with the predicted response of the polyester reinforced model. Figure 6.43 shows the principal strain distribution of the reinforced analysis of the model material at a displacement ratio of 7.5. This may be compared with the photograph of the specimen at the same displacement ratio shown in figure 6.15.

The ceramic 'T' beam response was compared with the ceramic reinforced model as shown in figure 6.7. Figure 6.44 shows the principal strain distribution of the ceramic 'T' beam reinforced model at a displacement ratio of 14.9. This is compared with the specimen at the same displacement ratio in figure 6.18.

The response of the model material thickened section is compared with the predicted response of the reinforced polyester model in figure 6.8. The principal strain distribution in the thickened section with the polymer reinforced model is shown in figure 6.45 at a displacement ratio of 15.0. This is compared with the specimen at the same displacement ratio in figure 6.22. The response of the ceramic thickened section compared with the reinforced model analysis is shown in figure 6.9. At a displacement ratio of 18.4 the predicted principal strain distribution of the ceramic thickened section shown in figure 6.46 is compared with the experiment in figure 6.23 at the same displacement.

6.4 Discussion

The predicted response of the bend bar using the basic micro-damage model compared well with the experimental response of the model material bend bar shown in figure 6.4. An essential feature of the micro-damage model was the absence of compressive failure. The effect of this on the bend bar response produces a beam which only incurred damage in tension as shown by the stress distribution in figure 6.38. This differs from the classical elastic plastic solution where yielding occurs in both tension and compression as shown in figure 6.39. A comparison of the response of the bend bar using the three constitutive relations is shown in figure 6.34, the micro-damage response is bounded by the response of the elastic and the plastic curves. Since the micro-damage model tends to be numerically unstable, the elastic and the plastic solutions which are computationally very stable may be used as upper and lower bounds for the load-displacement relation of a bend bar. The observed levels of micro-cracking shown in figures 6.10 to 6.12 also compared favourably with those predicted by the micro-damage model in figures 6.35 to 6.37. This demonstrates the use of the micro-damage model in the prediction of response and damage in bend specimens where the fibres are aligned in the direction of the principal stress.

The experimental response of the model material 'T' beam modelled with the isotropic micro-damaged model was not successful as illustrated in figure 6.6. The analysis followed the experimental response up to micro-cracking where the two curves diverged, with the computational solution showing a markedly stiffer behaviour. Examination of the failed 'T' beam shown in figure 6.15 showed failure to have occurred in the web. The isotropic analysis of the 'T' beam, shown in figure 6.40, indicated that the maximum stress concentration was located at the fillet. Examination of the failed specimens in figures 6.15 and 6.17 show that there were no fibres bridging the cracks thus indicating the mode of failure in both the ceramic and the model material to be tensile delamination.

At the location where delamination initiated the stress was approximately one quarter of the stress at the fillet. Since no tensile micro-

cracking occurred in the fillet this would predict delamination stresses less than 10MPa for the polyester composite and less than 20MPa for SiC-Alumina. Through thickness tensile tests on the polymer composite showed the delamination stress of the polyester to be of the order 1MPa. As a result of this the micro-damage model was extended by the introduction of reinforcement to incorporate anisotropy.

The first sub-element benchmark of the reinforced model was the bend bar. Hysteresis was incorporated into the polyester reinforced model. This compared well with the experimental results of the polyester composite as shown in figure 6.42.

In the polyester system the modulus of the matrix and reinforcement are the same such that the composite is elastically isotropic. In contrast the ceramic reinforced model is anisotropic elastic. Comparison of the ceramic numerical analysis with experiment showed good results up to initial microcracking of the specimen as shown in figure 6.5. The post cracking response of the ceramic did not exhibit the gradual softening as a result of micro-cracking as in the model material but indicated distinct points of failure. Examination of the failed specimen showed the number of failed lamina to be equal to the number of load drops. The uniaxial response of the ceramic in figure 6.47 shows no evidence of micro-crack saturation. This indicates either low fibre failure strains compared to that of the matrix or a high shear strength of the fibre matrix interface. Results of ceramic fibre tests showed the ceramic tows to have failure strains at least twice that of the composite. This suggests high interfacial shear terms which significantly increase the stress in the tows bridging the crack. In the ceramic bend specimen tensile micro-cracking occurred perpendicular to the principal stress but only under the load point. From this initial micro-crack interlaminar cracks formed outwards from the load point. The lack of multiple micro-cracking in the ceramic bend bar may therefore be attributed to the low fibre failure strains of the ceramic tows or high interfacial shear strength. Another possible explanation for single crack propagation is provide by considering the mechanics of matrix micro-cracking (Aveston et al 1971). During loading the matrix can only crack when the stress on the matrix is greater than the micro-cracking stress and when the matrix is of a length greater than $2L_s$. Where $2L_s$

is the maximum matrix block length at micro-crack saturation. In the case of the bend bar, the stress reduces as a function of distance from the load point. If after the initiation of cracking the stress at a distance L_s from the crack is less than the matrix micro-cracking stress then multiple matrix cracking will not occur.

Delamination cracks may occur be either tensile or shear delamination. Crack tip analyses of a tensile crack by Williams (1957) indicate the stress distribution at the tip of a mode 1 crack to be biaxial tension. This would favour tensile delamination cracks particularly if the delaminating stress is significantly less than the tensile micro-cracking stress. The extent of damage in the ceramic bend bar was predicted at displacement ratios ($\frac{v}{v_t}$) of 13.1 and 25.0 to be $\frac{x}{w} = 0.57$ and 0.75 . This was compared with the damage in the experiments in figures 6.13 and 6.14 to be $\frac{x}{w} = 0.38$ and 0.71 at the same displacement ratios. The predictions over estimate the damage observed in the ceramic bend bar at the lower displacement. This may be explained by examining figure 6.13. Here crack propagation occurred largely by delamination. It was demonstrated in chapter 4 for the polyester material that there was no significant difference between the fibre contribution to the composite response when calculated using the interfacial shear stress or by experiment. This is due to the low interfacial shear stress of the polyester. For the ceramic there is evidence to suggest that the interfacial shear stress is significantly higher than that of the polymer system. Since the response of the fibre contribution was determined using the tow experiments and not calculated using the shear stress it is therefore acceptable that ceramic matrix contribution is over estimated. This would give a stronger interlaminar response and not account for the low failure stress in the transverse direction as shown in the ceramic bend bar experiment. However overall results the ceramic bend bar analysis predict a favourable initial benchmark of reinforced model.

Numerical analysis of the polyester 'T' beam through the normalised load-displacement response in figure 6.6 was encouraging. However it was also necessary for the analysis to predict the deformation mode and extent of damage. Figure 6.43 shows the principal strain distribution of the model material 'T' beam at a displacement ratio of 7.5. Figure 6.48 shows the

elements in the reinforced 'T' beam which are predicted to micro-crack. In the numerical analysis micro-cracking started at the fillet but continued deformation resulted in a shift of the maximum strain to the web. The strain distribution shown in figure 6.43 indicates the web to contain maximum principal strains approximately 3.5 times greater than at the fillet. The shift in maximum strain from the fillet to the web can be explained by considering the orientation of the reinforcement. Prior to micro-cracking the model is almost isotropic and the fillet stress will always be above that of the web. After micro-cracking initiates at the fillet the response of the element at the fillet hardens as a result of the reinforcing fibres. However in the web the principal tensile stress acts perpendicular to the reinforced elements thus rendering the reinforcement mechanically ineffective. The behaviour of the element is therefore largely controlled by the matrix. The shift in the cracking from the fillet to the web occurs as a result of the effective reinforcement at the fillet until the initiation of delamination in the web. When tensile delamination begins the deformation of the web elements are such that the load to further deform them is small in comparison to that required to further strain the fillet elements resulting in a softening of the overall response of the modelled 'T' beam. This is shown by the normalised response in figure 6.6 where the final curve runs parallel to the experimental response but was delayed in its softening. Although the analysis predicted the start of micro-cracking in the fillet where none was observed, the extent of damage in web of the 'T' beam has been predicted with a degree of accuracy. This effectively supports the use of the reinforced micro-damage analysis. In addition the information gained from the testing showed the fibre architecture of the 'T' beam under the applied loading to be an unacceptable design. This is due the deformation modes dependence on the matrix response with no fibre bridging of the cracks resulting in an unreliable failure.

The ceramic 'T' beam response compared well with the analysis as illustrated in figure 6.7 over the initial non-linear section of loading. Past this point the two responses diverged. Inspection of the failed ceramic 'T' beam showed the formation of a dominant interlaminar crack in the web. No evidence of micro-cracking at the fillet was found. The interlaminar response of the element is dominated by the matrix response. The low levels in the

stress field at the crack suggest that the interlaminar response of the element is too stiff. The initial crack is indicative of tensile delamination but the sudden failure with continued load support suggests a sliding or shear delamination. However, the predictions of the location and extent of damage from the analysis are good. This combined with the prefailure comparison of the responses demonstrates the use of the ceramic reinforced model on the 'T' beam.

Figure 6.8 shows the response of the polyester thickened section compared to the analysis. The predicted load-displacement response compared well with the experiment. Figure 6.21 shows the damage in the polyester thickened section at a displacement ratio of 11.2 to be primarily through tensile micro-cracking. In figure 6.22 a similar specimen at a displacement ratio of 15.0 shows signs of interlaminar cracking in the tensile field. At a displacement ratio of 15.0 the analysis predicted interlaminar tensile strains sufficient to cause micro-cracking in the position of the delamination cracks shown in figure 6.22. Figure 6.45 shows the principal strain distribution of the polyester reinforced thickened section at a displacement ratio of 15.0. The predicted depth of micro-cracking was $\frac{x}{w} = 0.61$. Comparing this with figure 6.22 at the same displacement ratio shows micro-cracking to have occurred to a depth, $\frac{x}{w} = 0.65$. This confirms the ability of the analysis to predict the mode of deformation, the position and the extent of micro-cracking.

The load-displacement analysis of the ceramic thickened section is compared with the experiment in figure 6.9. As with the previous ceramic sub-elements there is good predictions of response well into the nonlinear portion of the loading past micro-cracking. This may be attributed to high interface shear strengths. Figure 6.24 shows the ceramic thickened specimen at a displacement ratio $\frac{v}{v_t} = 18.4$. From this photograph it can be seen that there is a single crack propagating from the tensile surface. This is followed by an interlaminar crack after which the crack continues towards the compressive surface. Figure 6.46 shows the principal strain distribution of the ceramic thickened section at a displacement ratio of 18.4. In this diagram micro-cracking is taken to occur in an element with a tensile strain greater than the ceramic matrix micro-cracking strain ($\epsilon_{mu} = 7.6 \times 10^{-4}$). This predicts the depth of micro-cracking to be $\frac{x}{w} = 0.46$. The experiment at the same displacement

showed micro-cracking through $\frac{x}{w} = 0.79$, shown in figure 6.23. This is not a particularly good result but may be reasonable explained again by high interfacial shear strengths.

6.5 Conclusions

Experimental tests of a number of sub-elements were compared with a numerical analysis using the reinforced model. Good comparisons were made between the predicted and observed load response, damage location, and the extent of micro-cracking thus confirming the use of reinforced constitutive model for the polyester sub-elements.

The analysis of the ceramic sub-elements using the ceramic reinforced model also compared well with the experiments. The predicted load response in all three sub-elements was good past initial micro-cracking and for extensive levels of damage. The location of damage was successfully predicted, while prediction of the extent of damage had limited success. However the overall predictions by the reinforced ceramic model were encouraging and confirmed its use as a constitutive model.

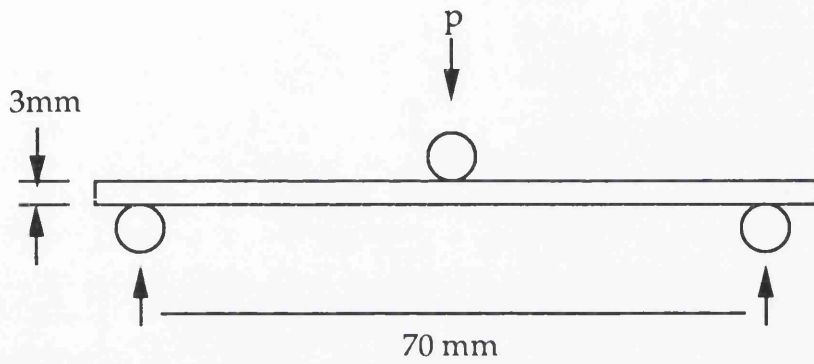


Figure 6.1 Bend Test Configuration for a Polyester fibre-Polyester Matrix Composite specimen 10mm deep

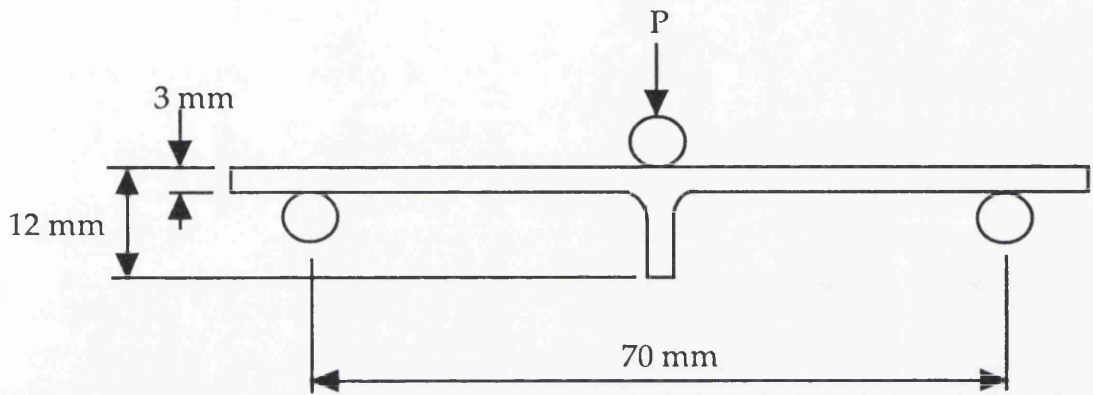


Figure 6.2 'T' beam Sub-element Dimensions with a beam breadth of 10 mm

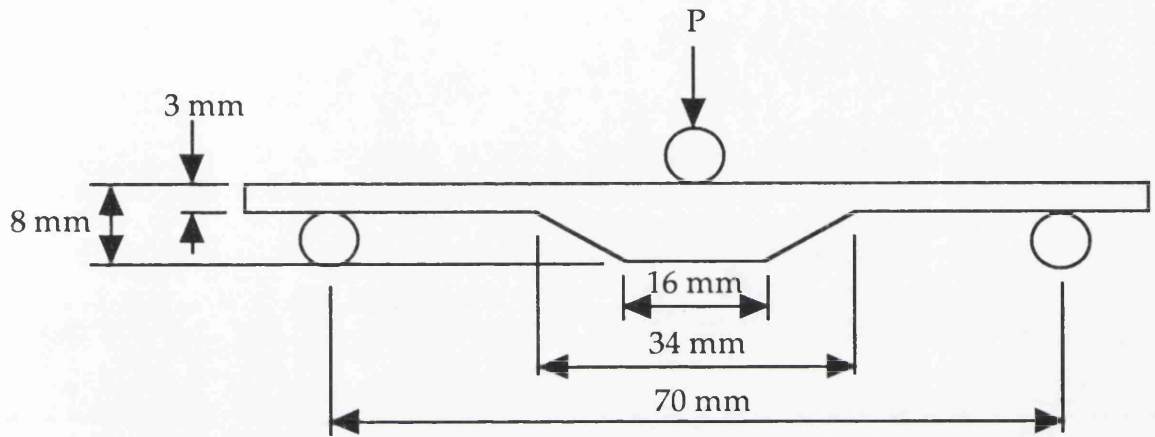


Figure 6.3 Thickened Beam Specimen Dimensions and loading configuration with a beam Breadth of 10mm

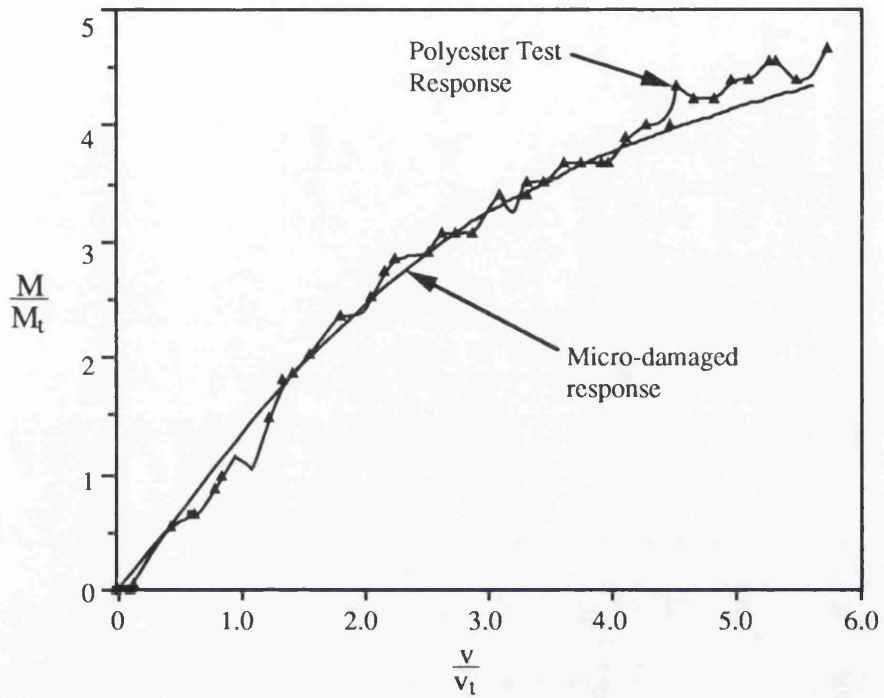


Figure 6.4 Normalised Response of the Polyester Bend Bar Compared with the Micro-damaged Analysis

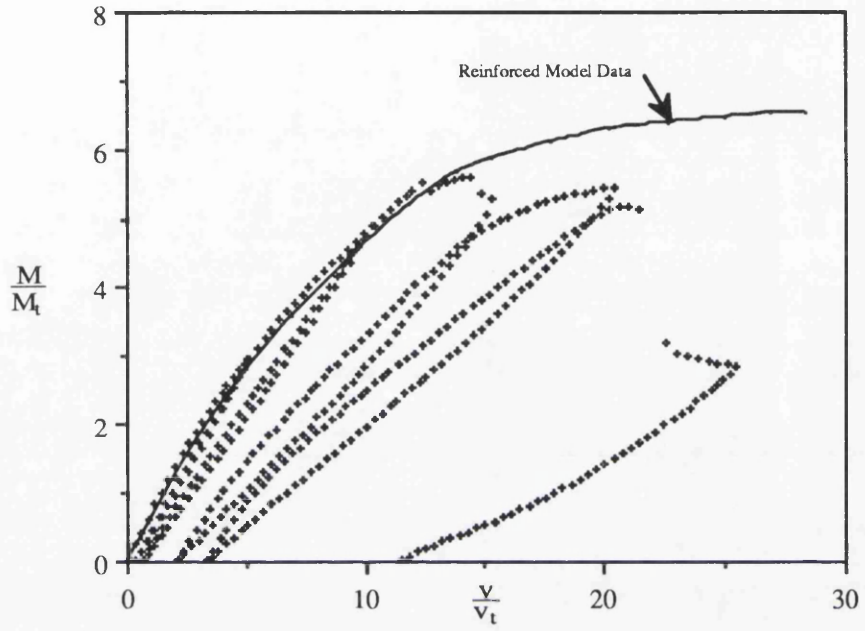


Figure 6.5 Normalised load-displacement comparison of the ceramic bend bar with the analysis

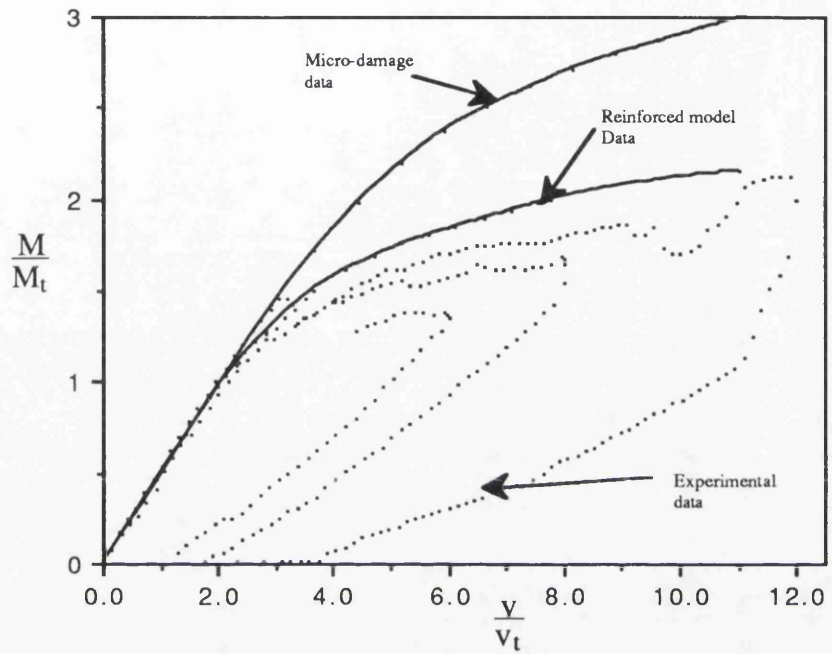


Figure 6.6 Model Material T beam experimental and computational results

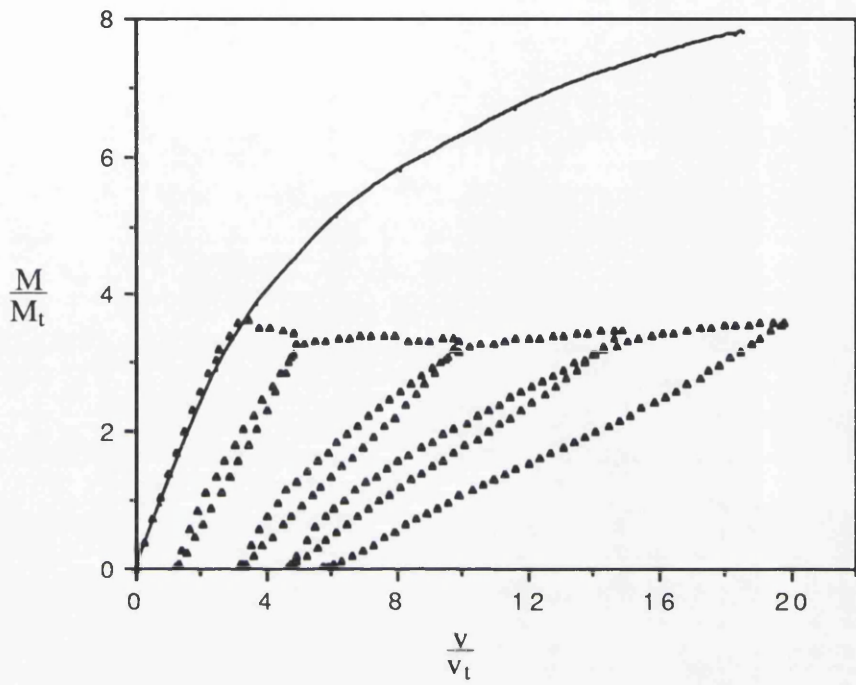


Figure 6.7 Normalised load-displacement response of the Ceramic 'T' beam comparing the analysis and experiment

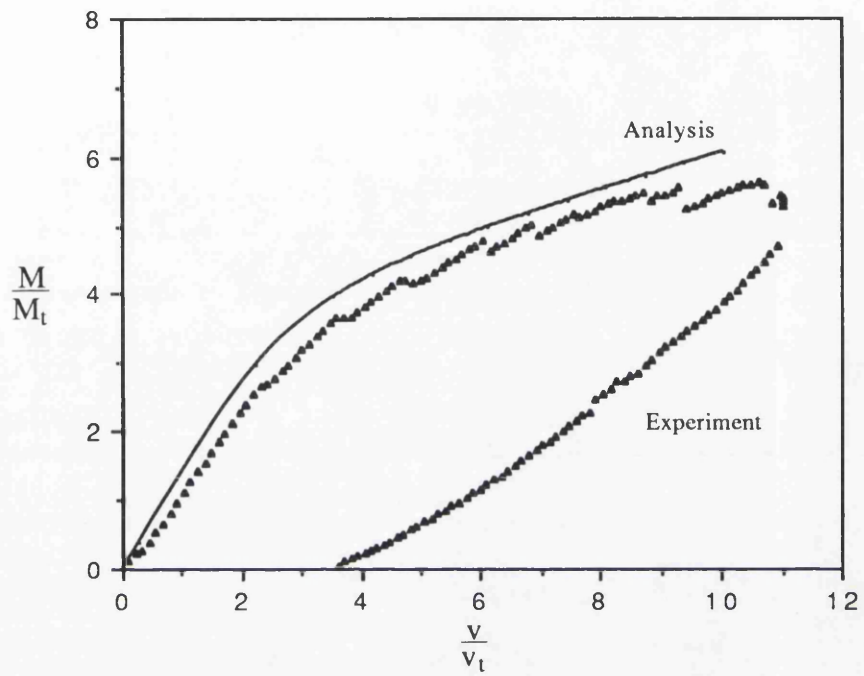


Figure 6.8 Normalised response of the thickened section compared to the analysis for the model material

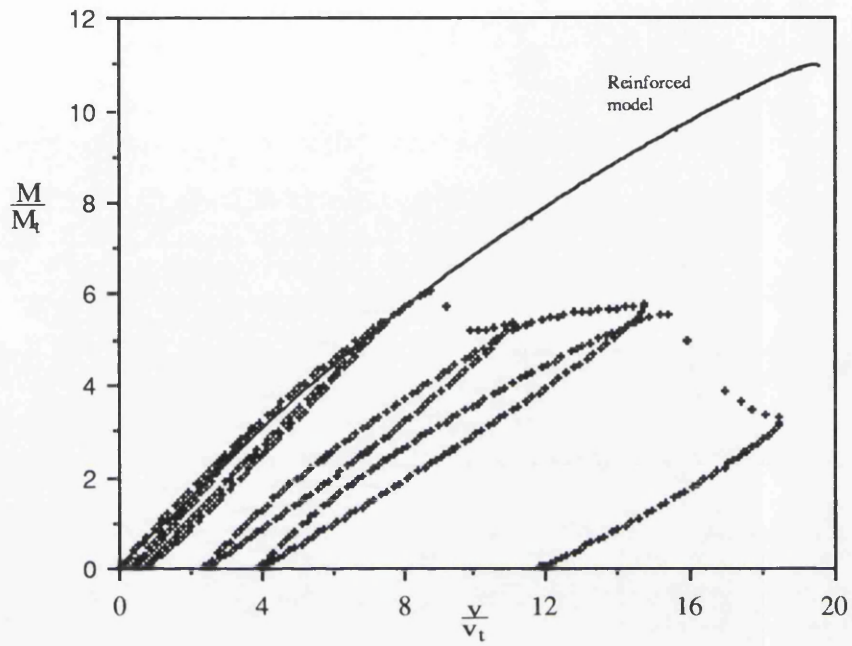


Figure 6.9 Normalised Response of the Ceramic Thickened Section against the Predicted Response of the Reinforced Model

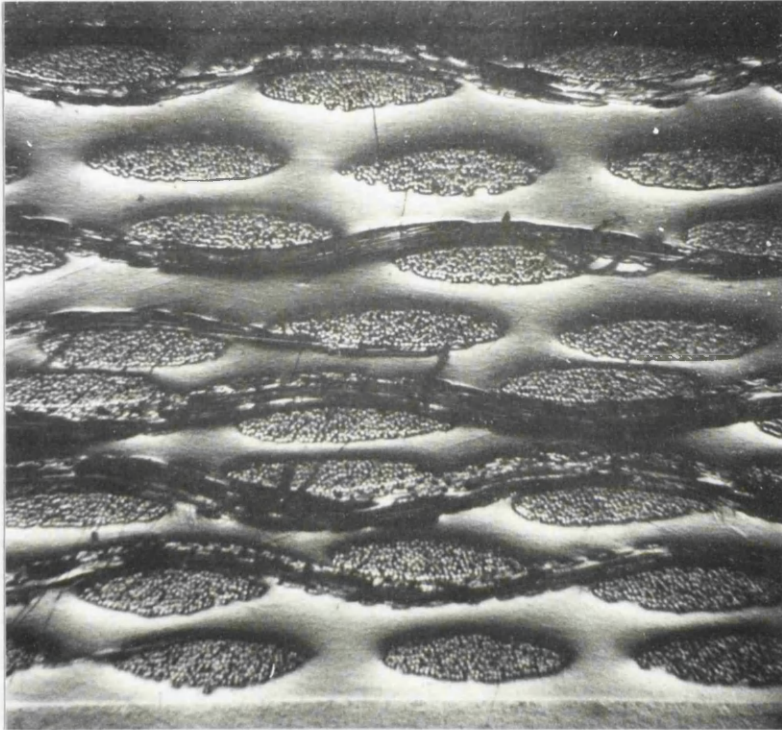


Figure 6.10 Photograph of micro-crack propagation through the polyester bend bar at a specimen rotation of 3.3..

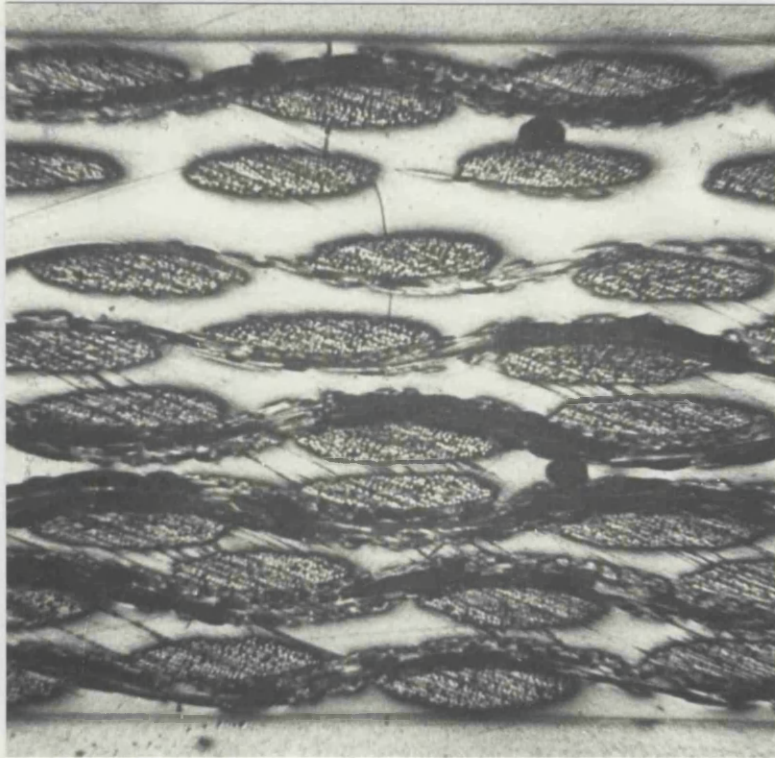


Figure 6.11 Photograph of micro-crack propagation through the polyester bend bar at a specimen rotation of 4.7.



Figure 6.12 Photograph of micro-crack propagation through the polyester bend bar at a specimen rotation of 6.1.

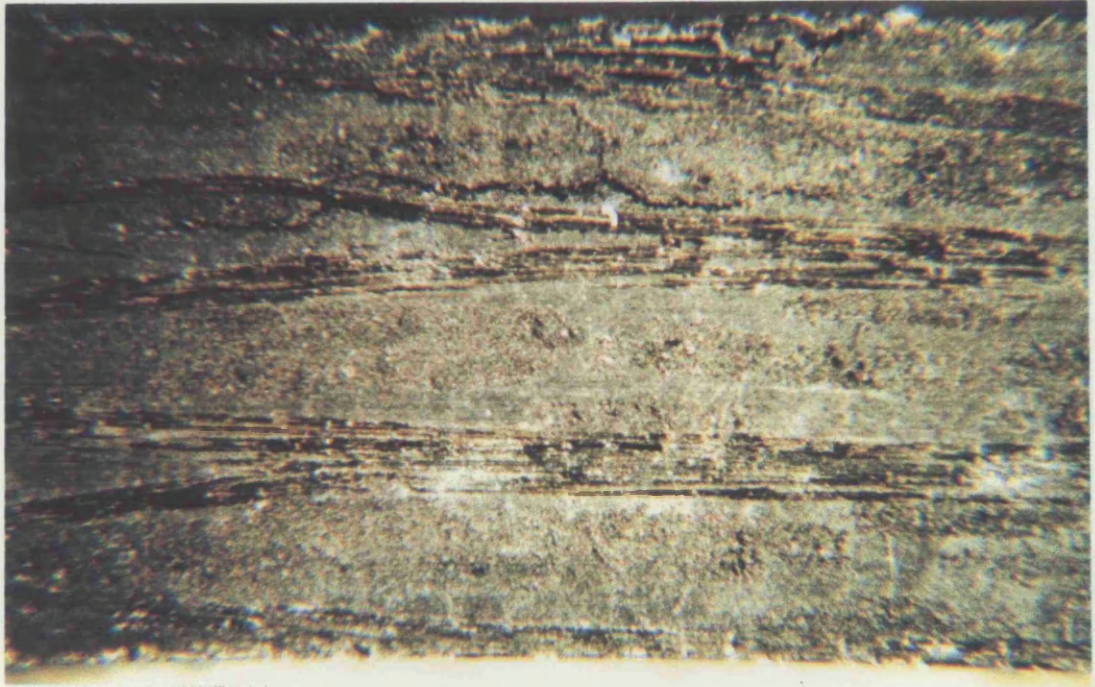


Figure 6.13 Photograph of micro-crack propagation through the ceramic bendbar specimen at a rotation of 13.1

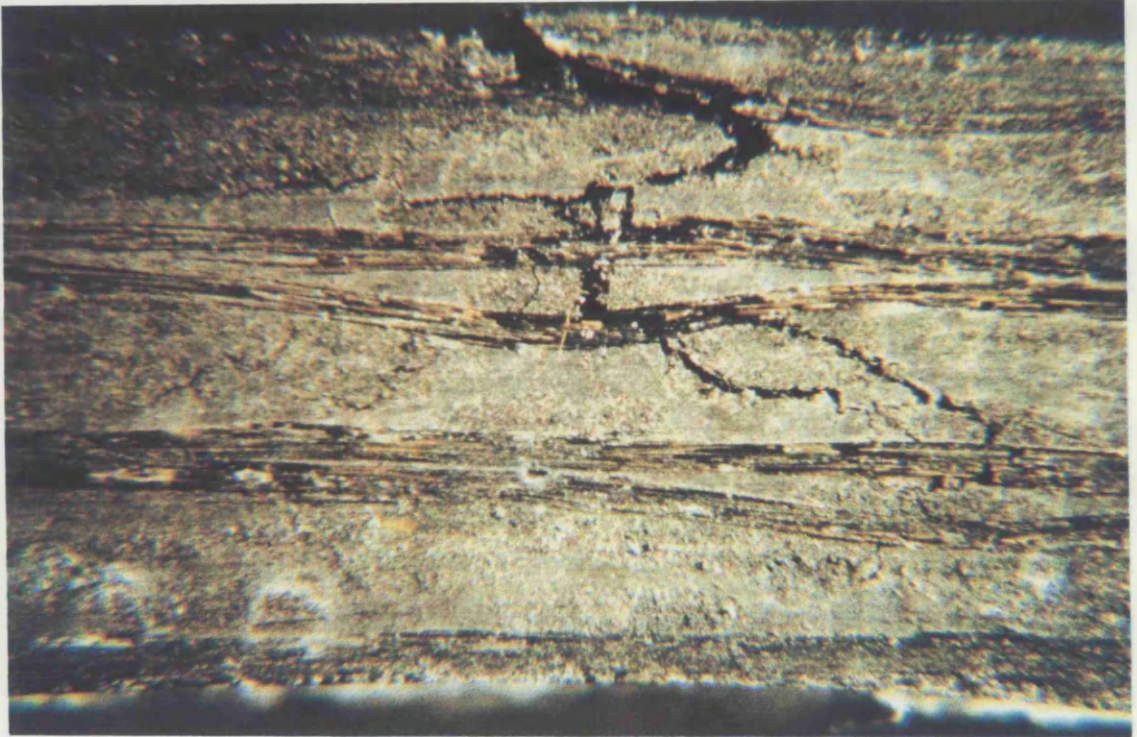


Figure 6.14 Photograph of micro-crack propagation through the ceramic bendbar specimen at a rotation of 25.0.

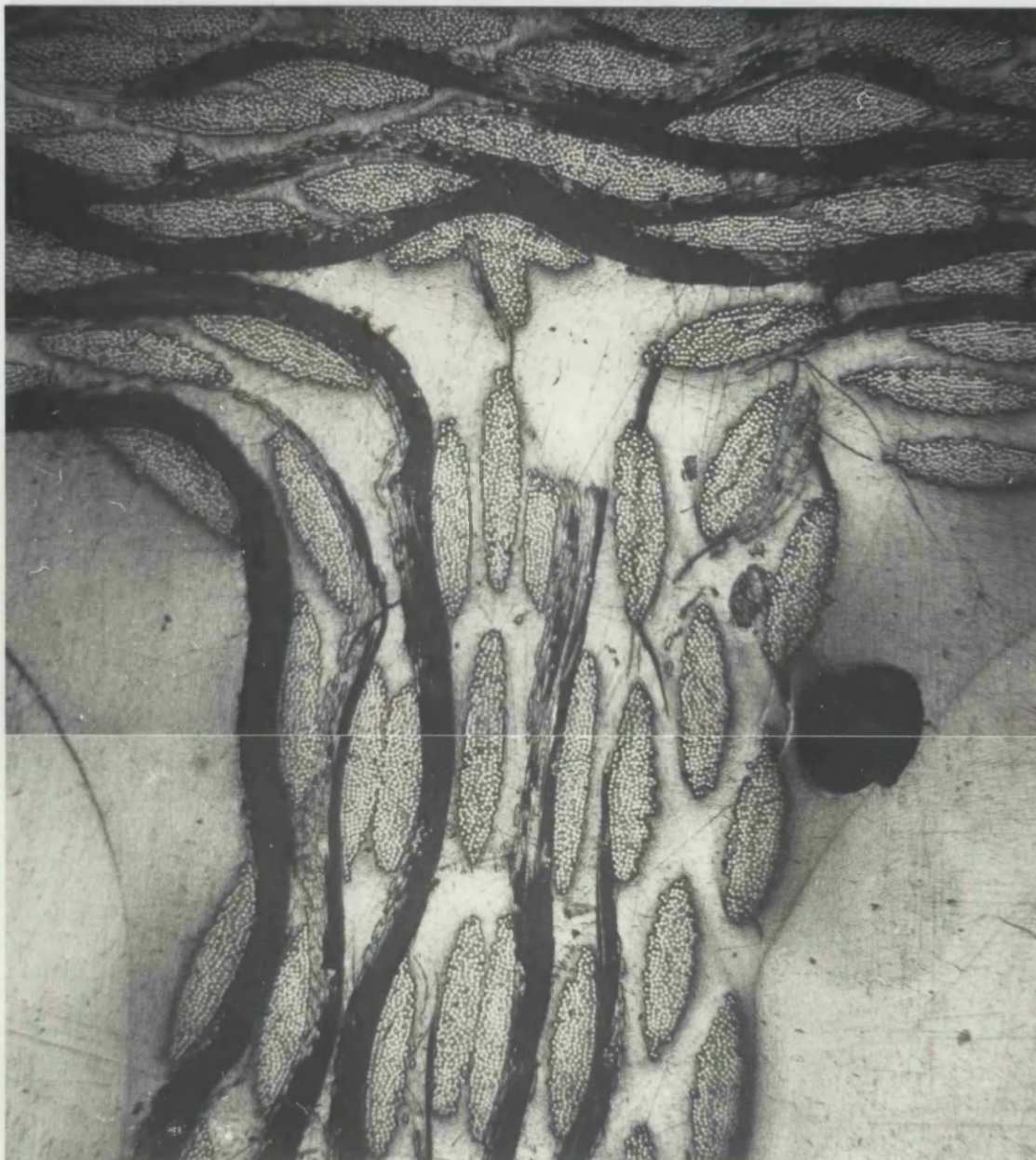


Figure 6.15 Photograph of micro-crack propagation through the polyester 'T' beam at a rotation of 7.5.

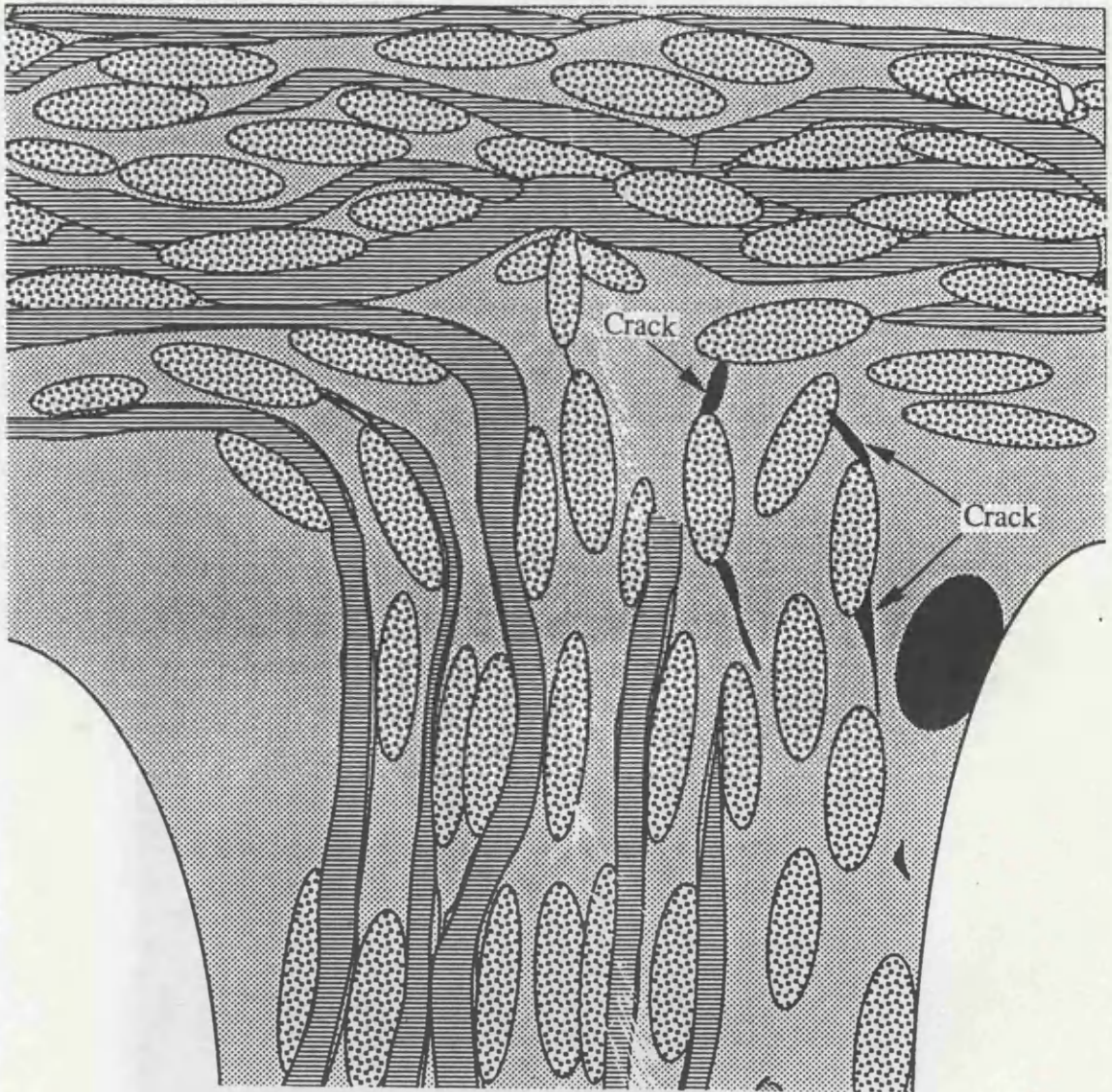


Figure 6.16 Schematic diagram of figure 6.15 showing the position of cracking in the T section.



Figure 6.17 Photograph of micro-crack propagation through the polyester 'T' beam at a rotation of 12.0.



Figure 6.18 Photograph of micro-crack propagation through the ceramic 'T' beam at a rotation of 14.9.



Figure 6.19 Photograph of micro-crack propagation through the ceramic 'T' beam at a rotation of 24.8.



Figure 6.20 Photograph of a failed ceramic 'T' beam at a rotation of 69.4.



Figure 6.21 Photograph of micro-crack propagation through the polyester thickened section at a rotation of 11.2

Figure 6.22 Photograph of micro-crack propagation through the polyester thickened section at a rotation of 15.0

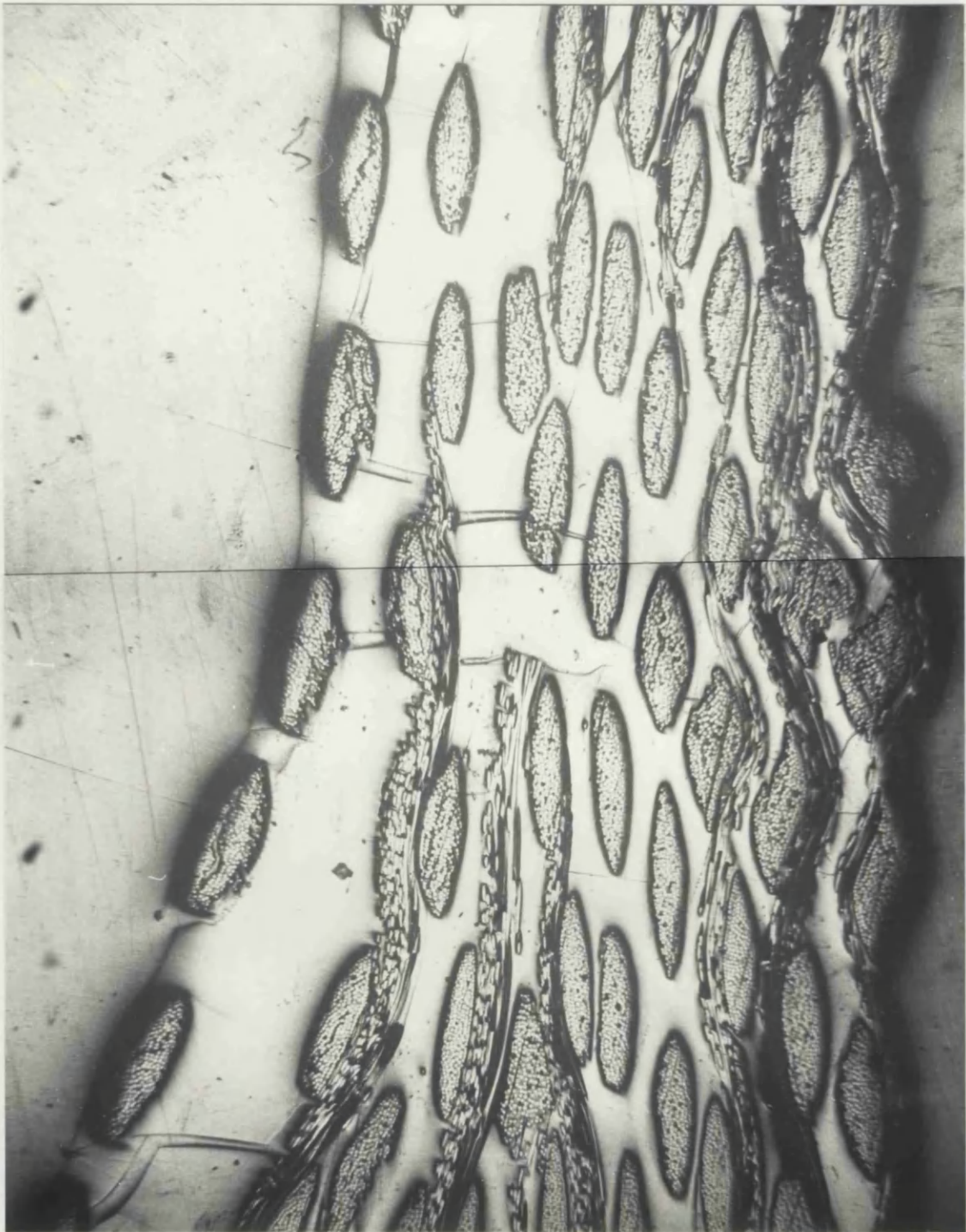


Figure 6.22 Photograph of micro-crack propagation through the polyester thickened section at a rotation of 15.0.



Figure 6.23 Photograph of micro-crack propagation through the ceramic thickened section at a rotation of 18.4

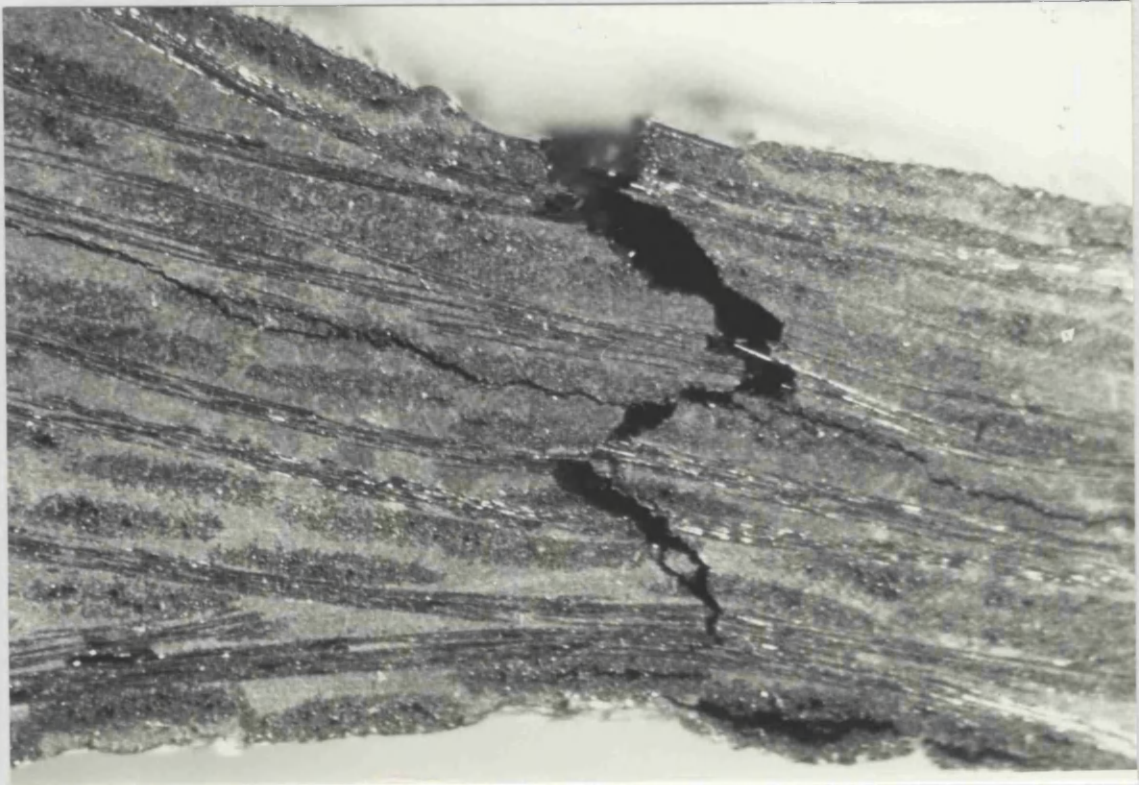


Figure 6.24 Photograph of a failed ceramic thickened section at a rotation of 73.6.

Figure 6.25 Band bar (full section finite element mesh)

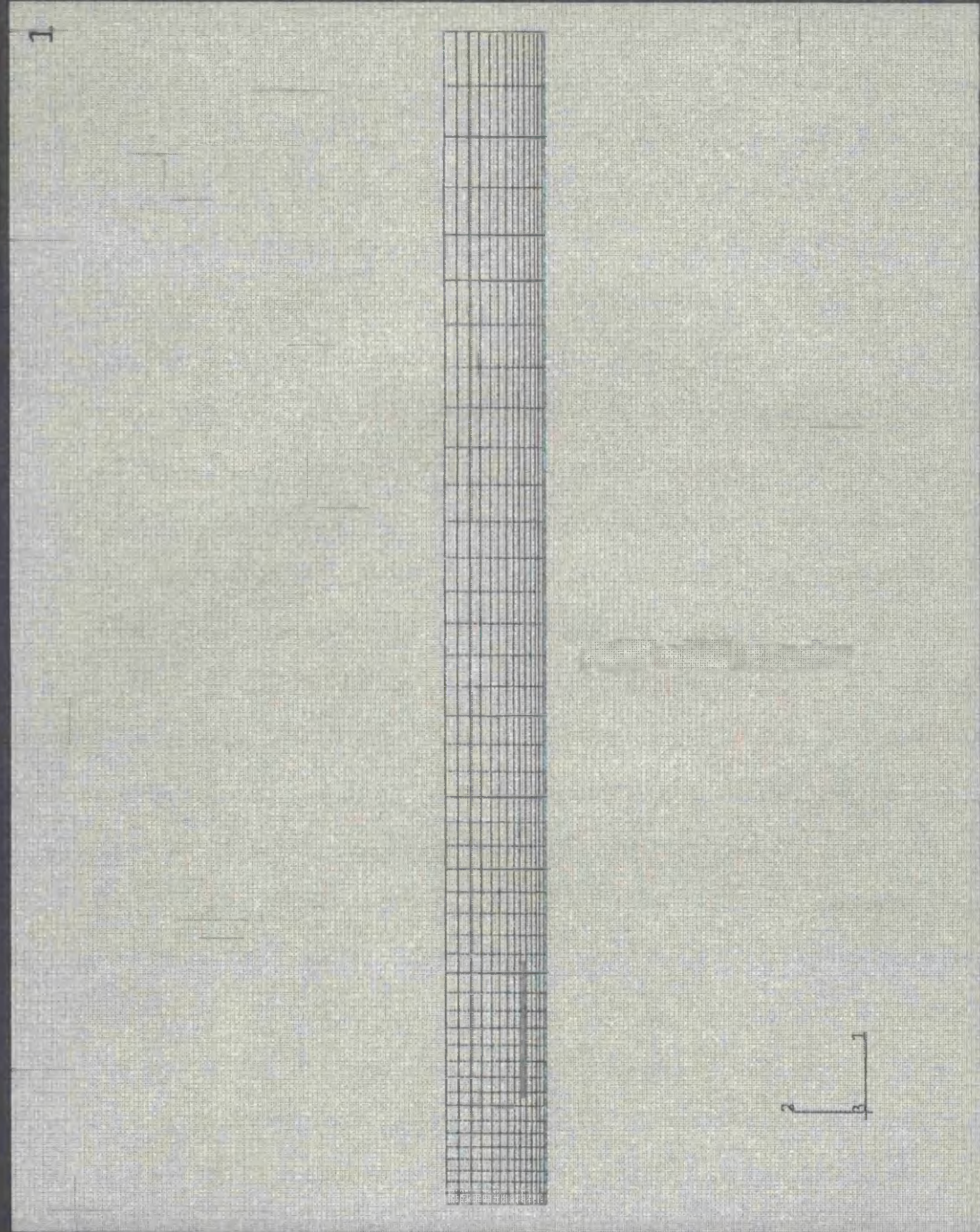


Figure 6.25 Bend bar half section finite element mesh.

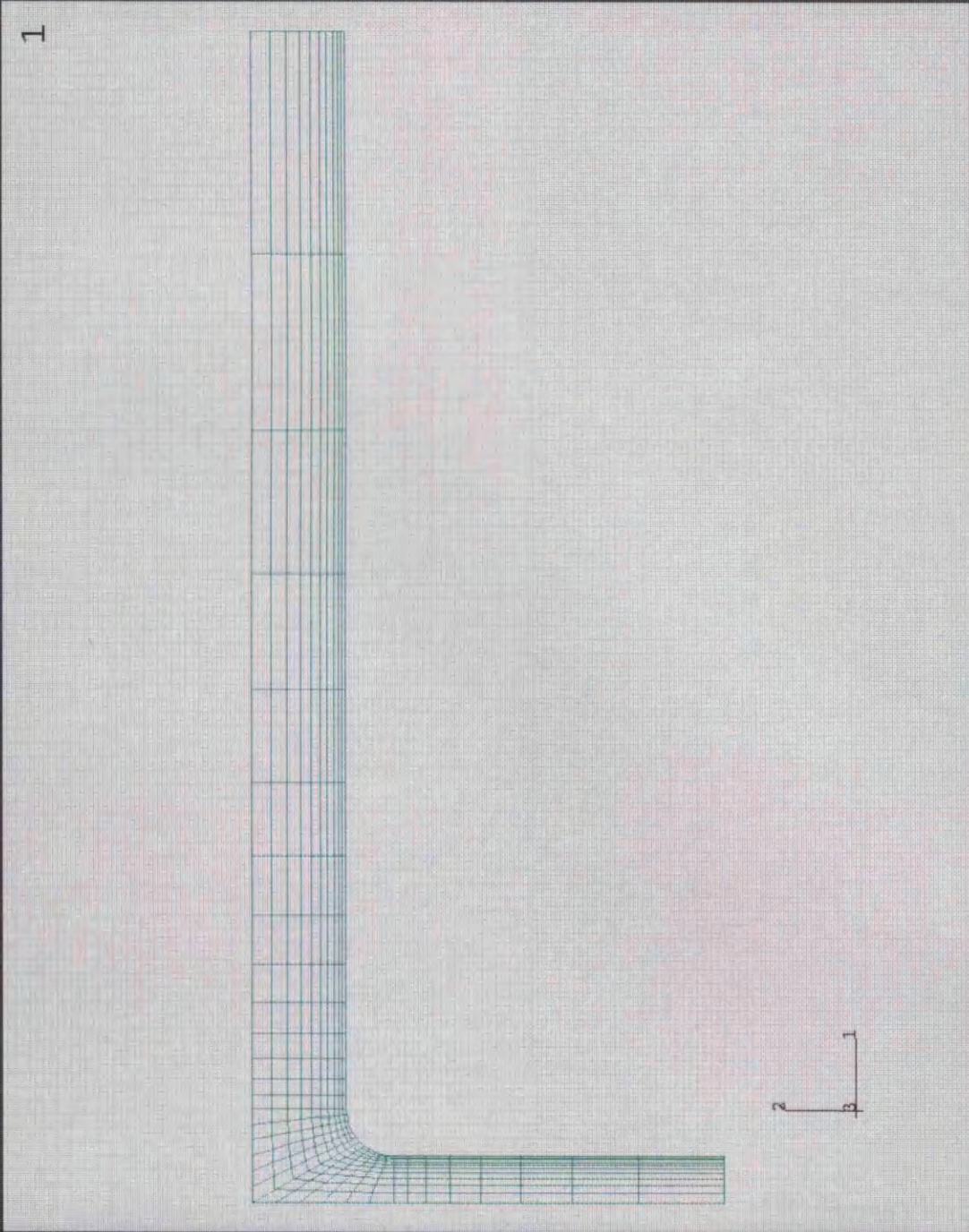


Figure 6.26 'T' Beam half section finite element mesh.

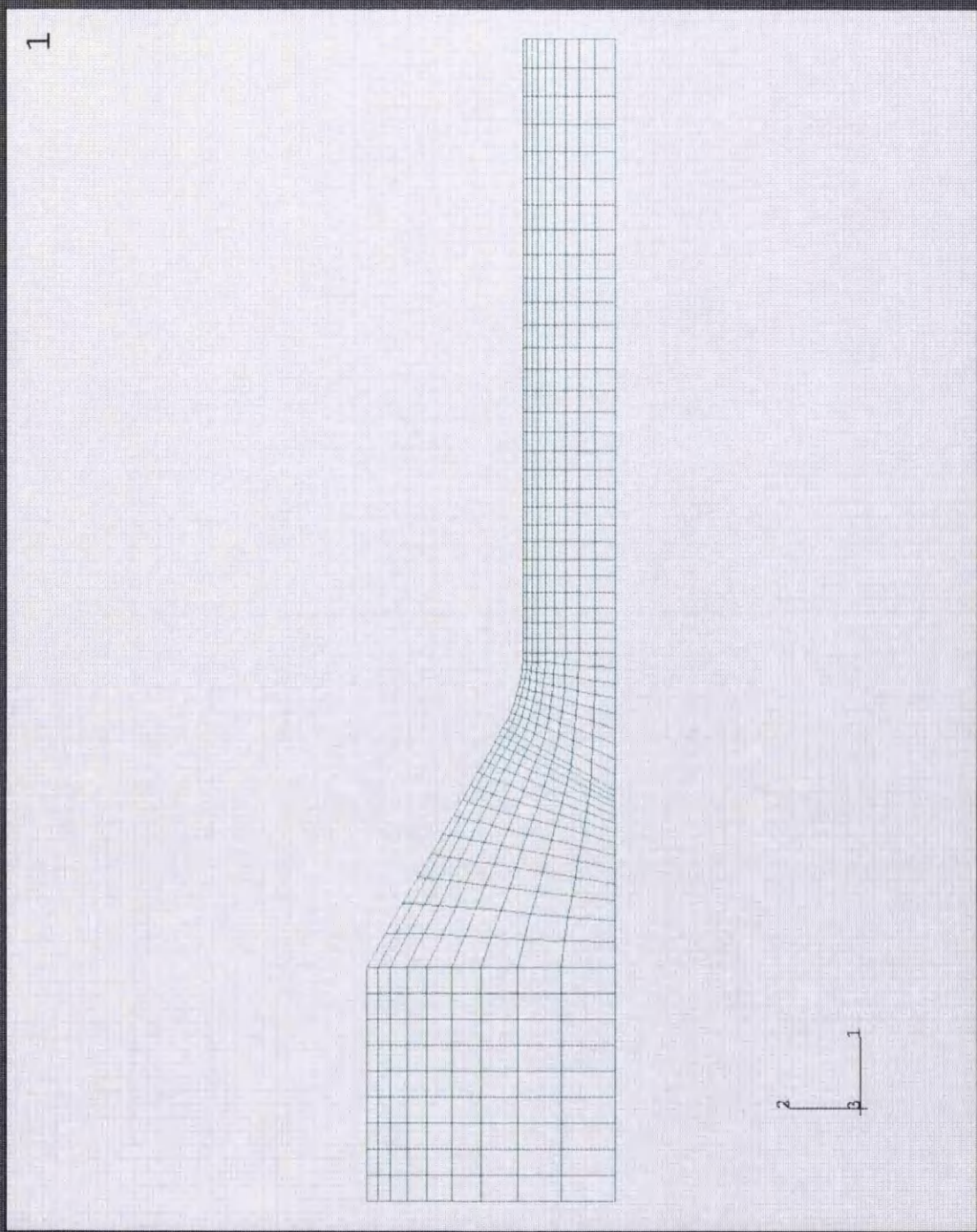


Figure 6.27 Thickened section finite element mesh.

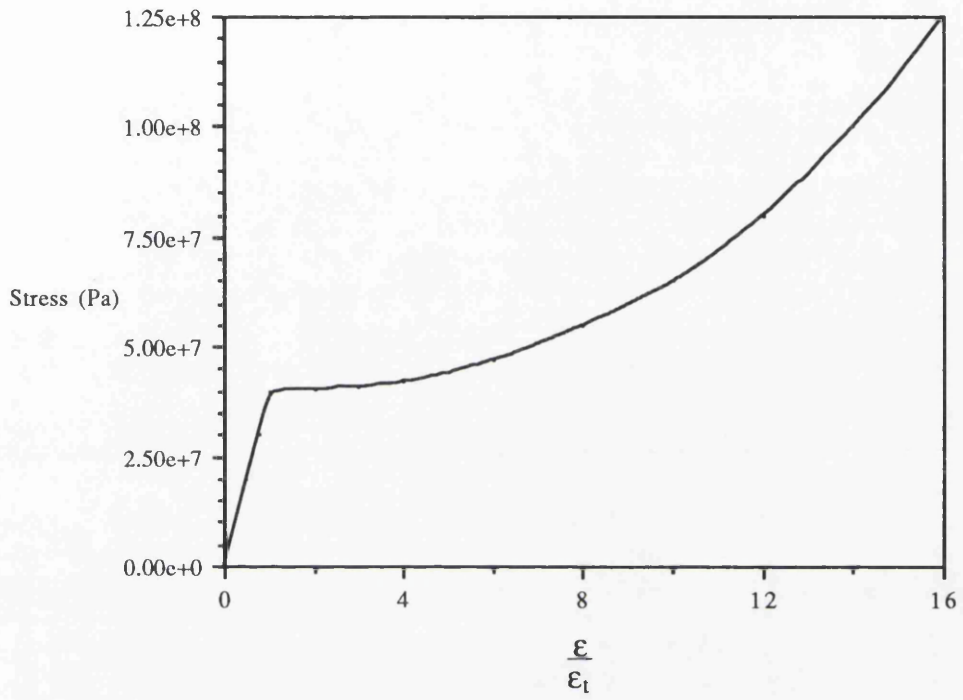


Figure 6.28 Material Input for the polyester micro-damage model

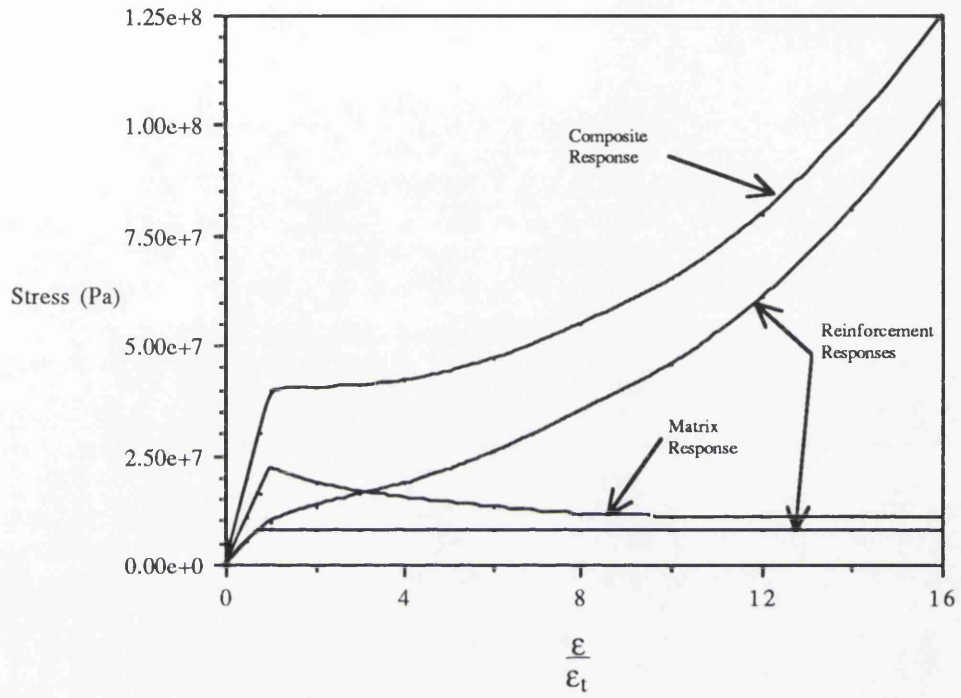


Figure 6.29 Material Input for the Polyester Reinforced Model

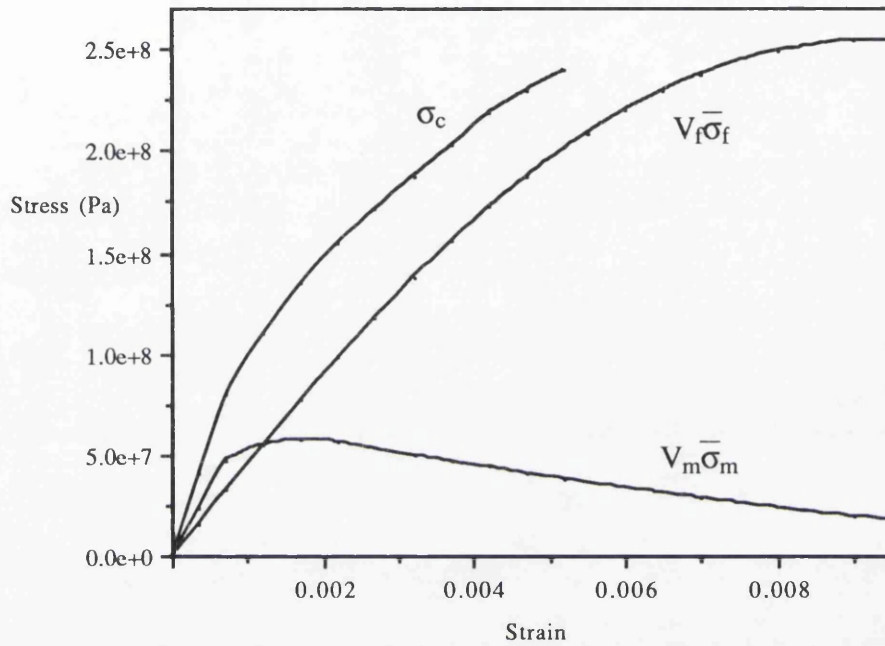
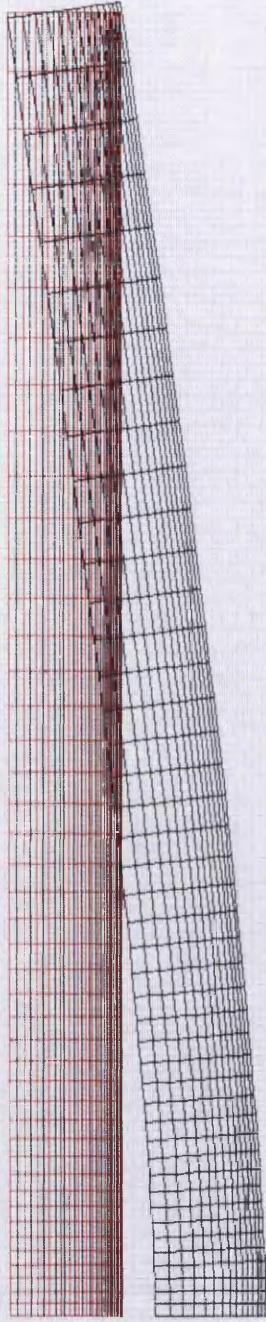


Figure 6.30 Comparison of the average fibre and matrix contribution to the composite stress for SiC-Alumina

1

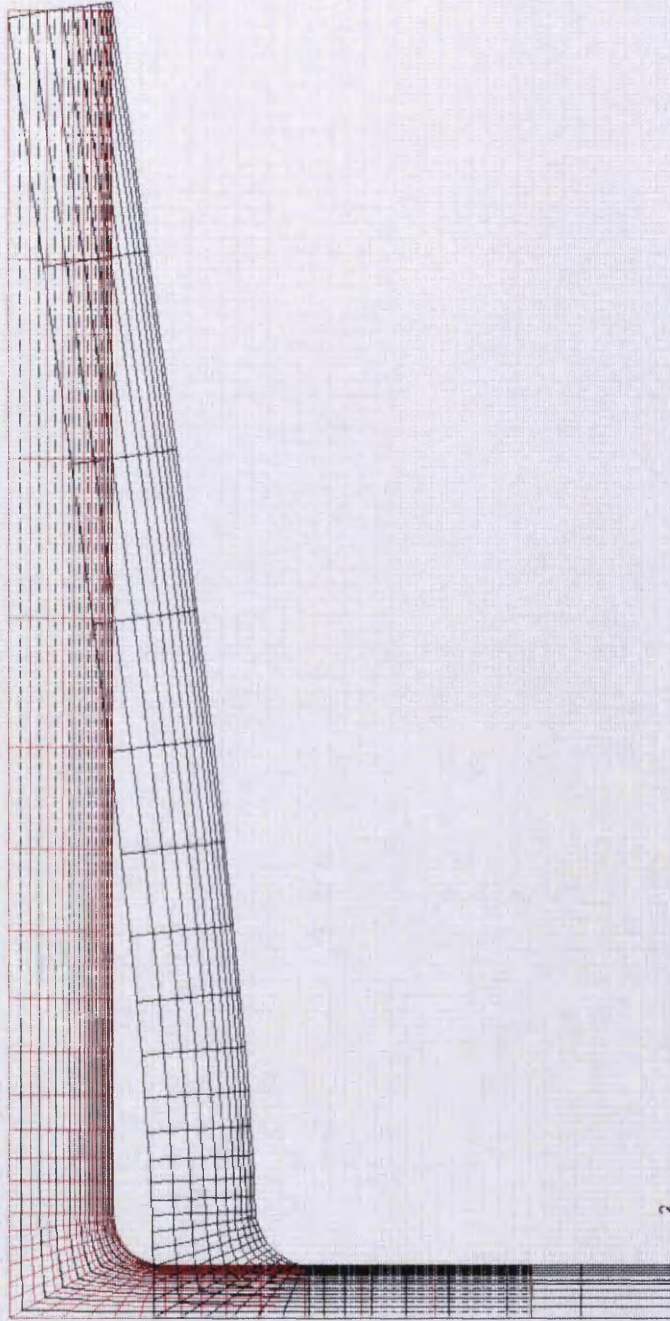


DISPLACEMENT MAGNIFICATION FACTOR = 1.53 ORIGINAL MESH DISPLACED MESH
TIME COMPLETED IN THIS STEP .635 TOTAL ACCUMULATED TIME .635
ABAQUS VERSION: 5.2-1 DATE: 16 SEP.93 TIME: 13:59:07 STEP 1 INCREMENT 40

dr
dr, displ

Figure 6.31 Deformed bend bar mesh and reinforcing elements in black superimposed onto the original mesh shown in red

1



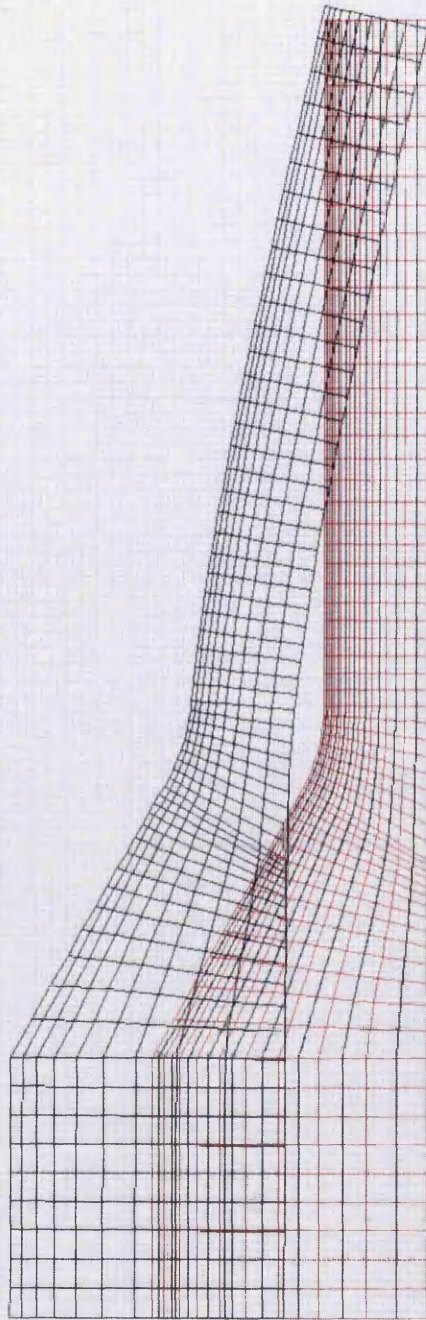
2
3

```
DISPLACEMENT MAGNIFICATION FACTOR = .816 ORIGINAL MESH DISPLACED MESH
TIME COMPLETED IN THIS STEP .425 TOTAL ACCUMULATED TIME .425
ABAQUS VERSION: 5.2.1 DATE: 08-JUL-93 TIME: 15:46:40 STEP 1 INCREMENT 21
```

dr, displ
Setting up edge list ...

Figure 6.32 Deformed 'T' beam mesh with reinforcing elements in black superimposed onto the original mesh shown in red.

1

2
3

DISPLACEMENT MAGNIFICATION FACTOR = .583 ORIGINAL MESH DISPLACED MESH
TIME COMPLETED IN THIS STEP .596 TOTAL ACCUMULATED TIME .596
ABAQUS VERSION: 5.2.1 DATE: 13-SEP-93 TIME: 23:22:32 STEP 1 INCREMENT 70

Figure 6.33 Deformed Thickened section mesh with reinforcing elements in black superimposed onto the original mesh shown in red.

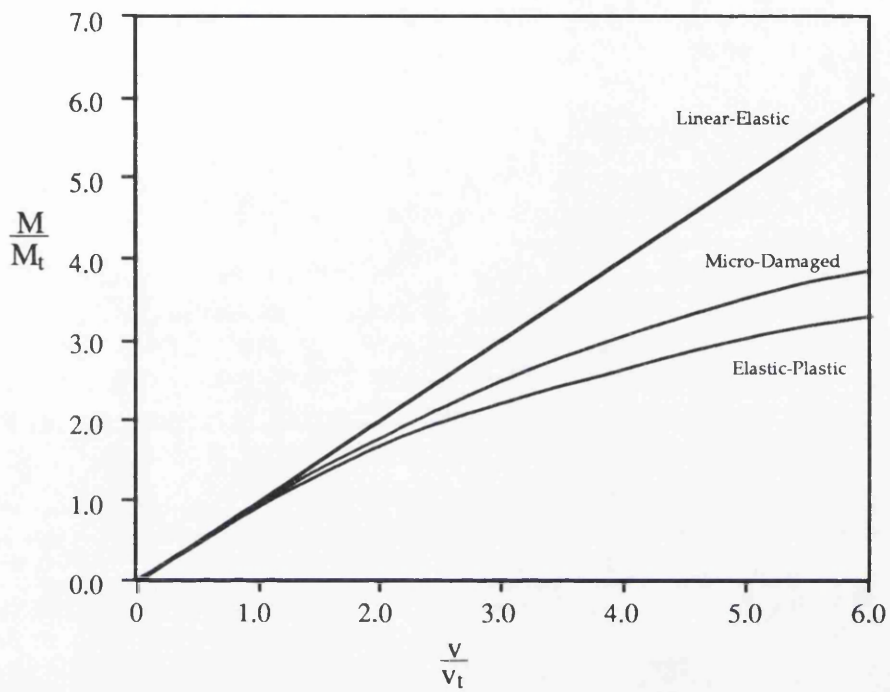


Figure 6.34 Normalised Response Micro-damaged Bend Bar Compared with the Elastic and Elastic-Plastic solutions

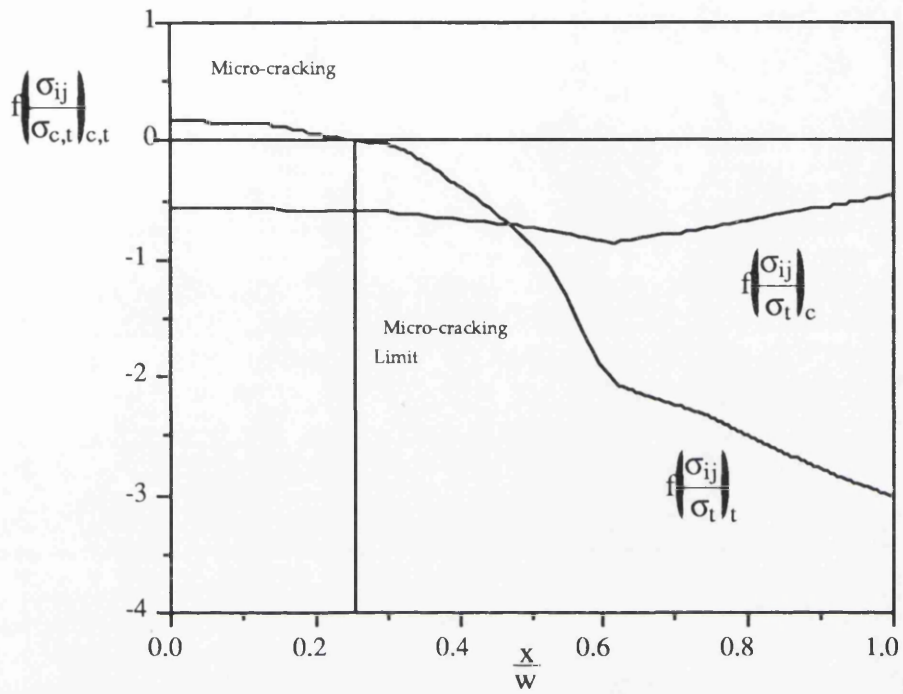


Figure 6.35 Tensile and Compressive Mohr Coulomb function for the three point bend bar analysis of the model material at a displacement ratio of 3.3

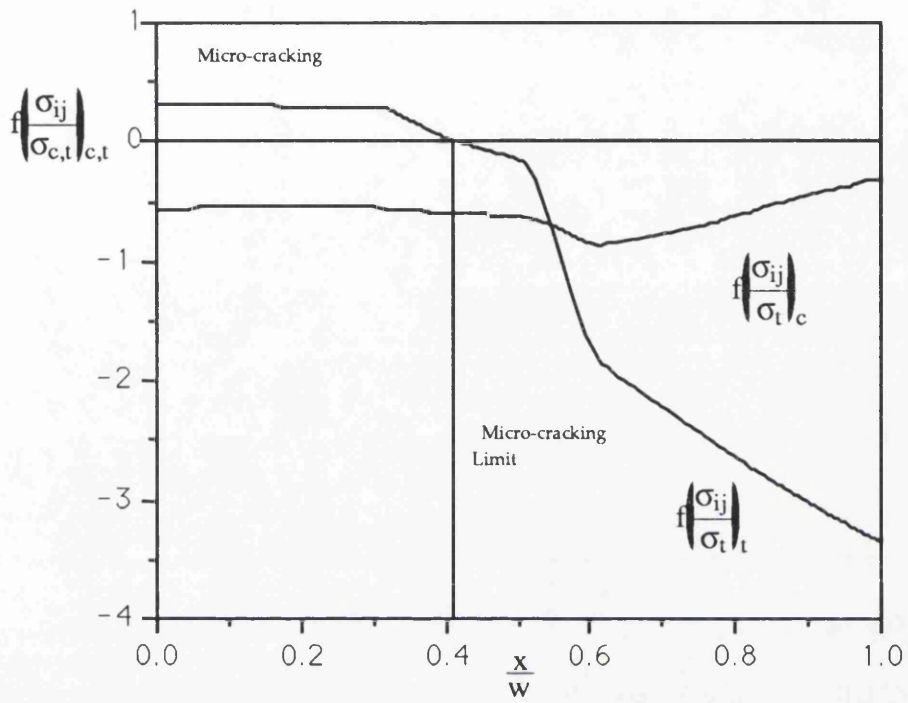


Figure 6.36 Tensile and Compressive Mohr Coulomb function for the three point bend bar analysis of the model material at a displacement ratio of 4.7

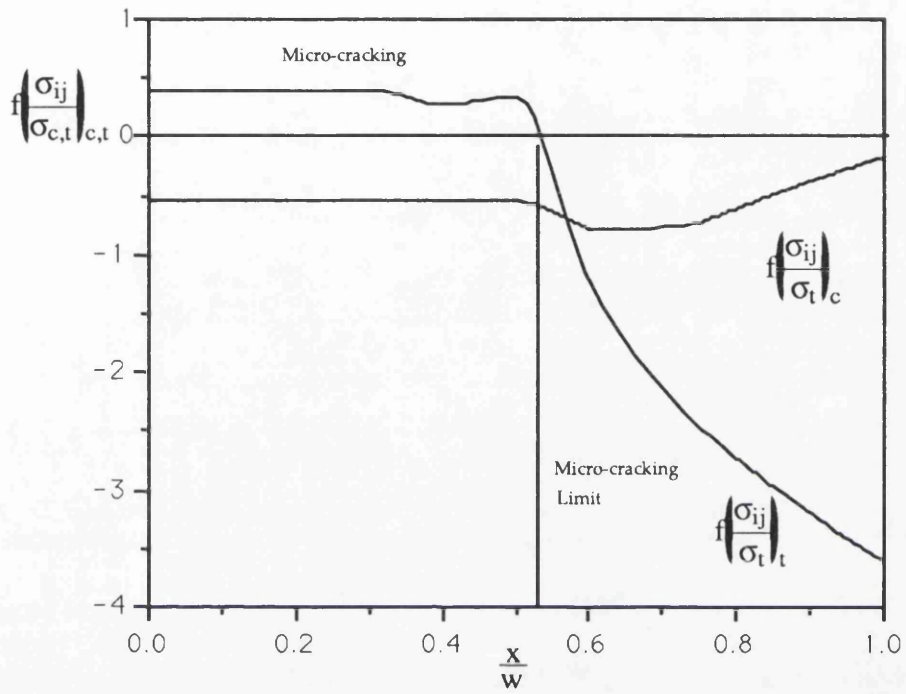


Figure 6.37 Tensile and Compressive Mohr Coulomb function for the three point bend bar analysis of the model material at a displacement ratio of 6.1

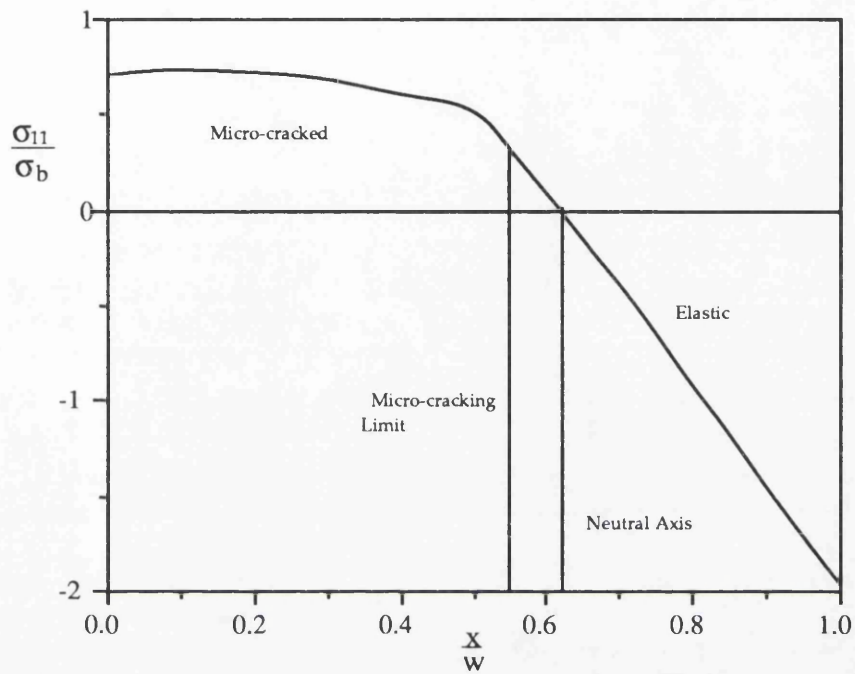


Figure 6.38 Principal Stress Distribution of the Bend Bar for the Micro-damaged Constitutive Model at a Displacement ratio of 6.1

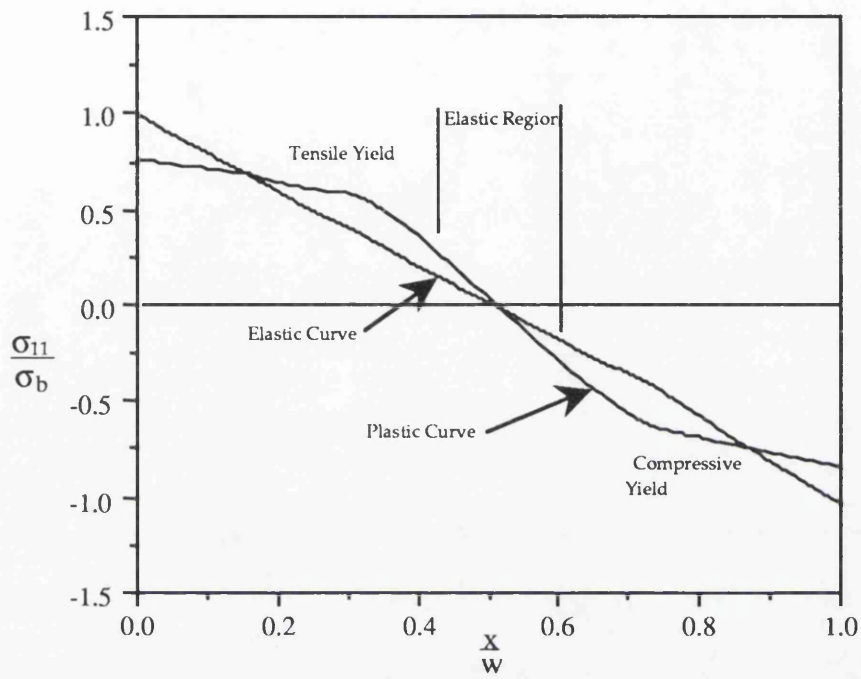
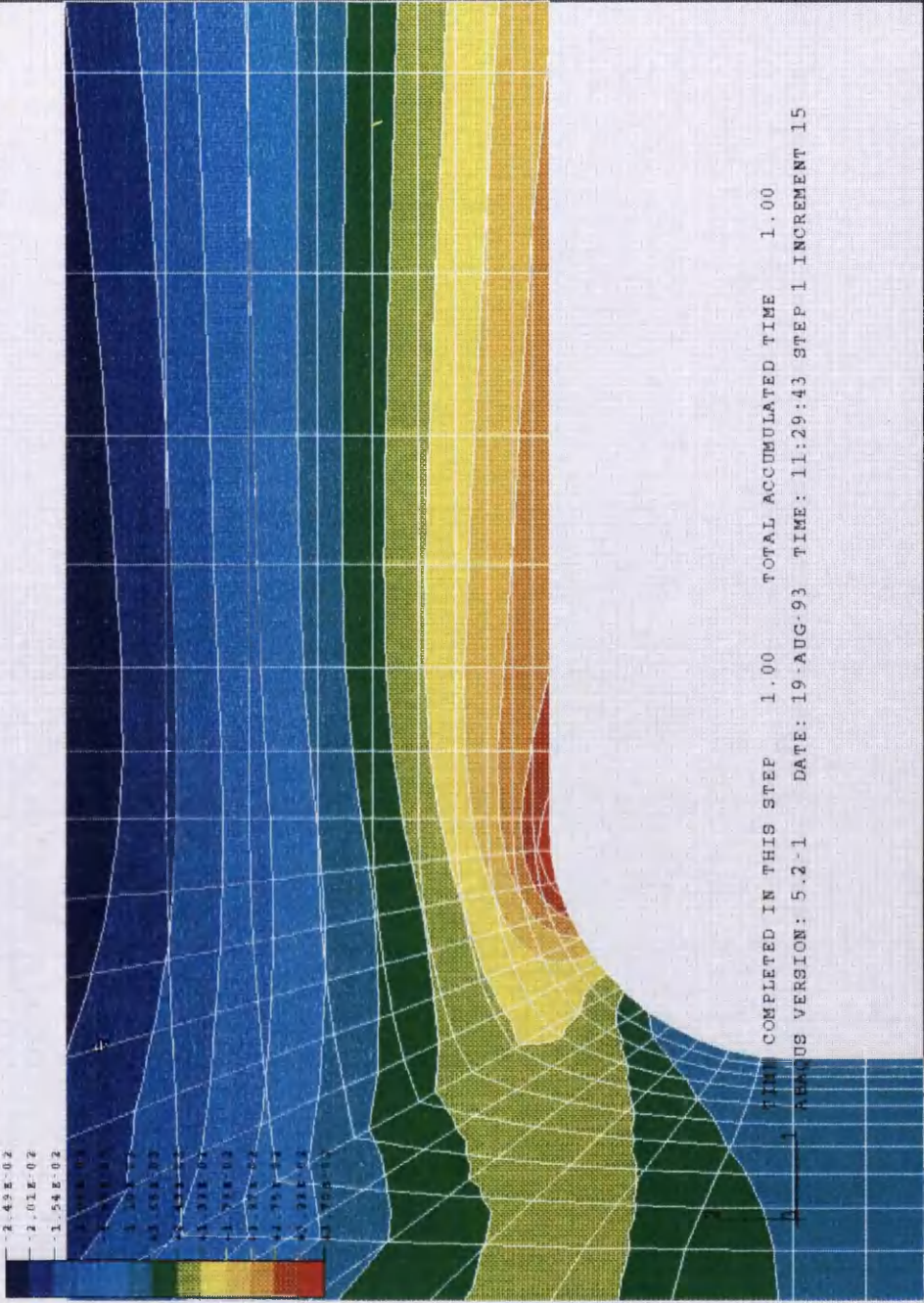


Figure 6.39 Principal Stress Distribution of the Bend Bar for the Elastic and Elastic-Plastic Constitutive Models at a Displacement ratio of 6.1

1

MIN	MAX	AVERAGE
-2.49E-02	0.000000	0.000000
-2.01E-02	0.000000	0.000000
-1.54E-02	0.000000	0.000000



TIME COMPLETED IN THIS STEP 1.00 TOTAL ACCUMULATED TIME 1.00
 ABAQUS VERSION: 5.2-1 DATE: 19-AUG-93 TIME: 11:29:43 STEP 1 INCREMENT 15

Figure 6.40 The strain distribution of a micro-damage analyses of a polyester 'T' beam at a displacement ratio of 7.5.

1

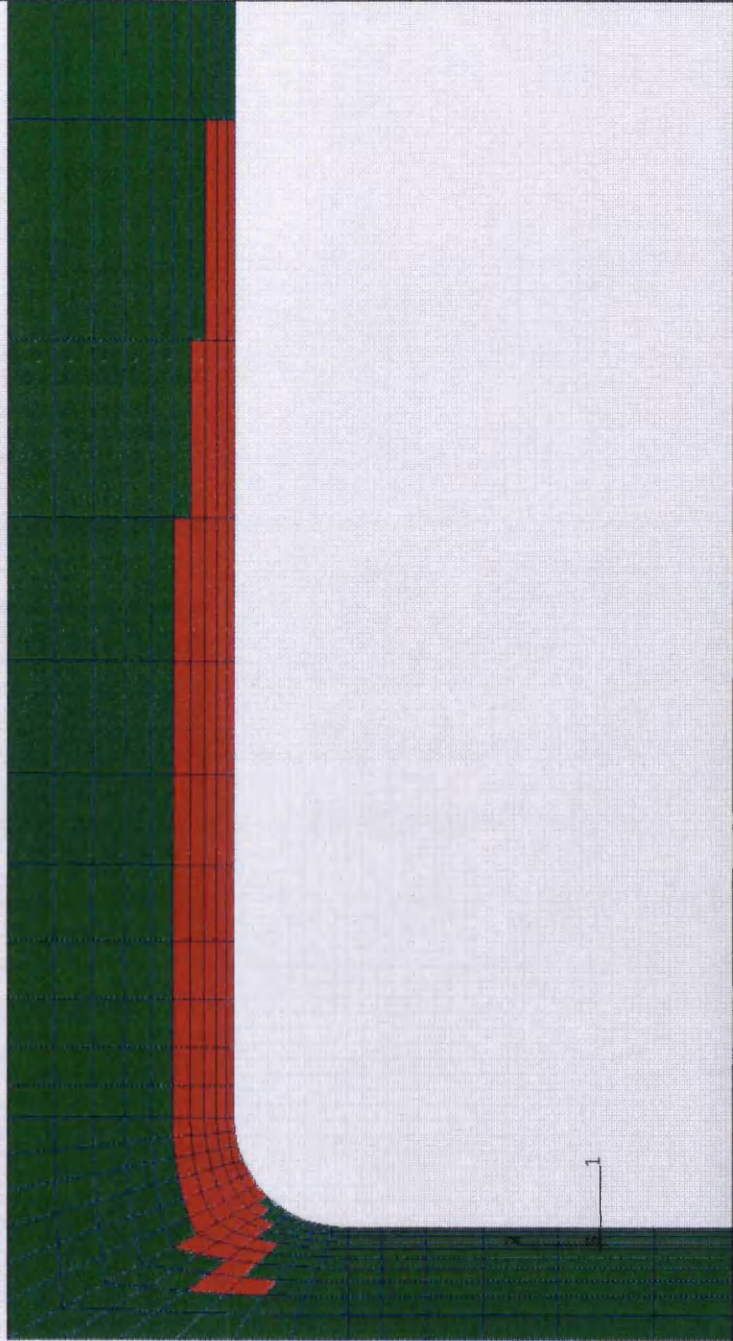


Figure 6.41 The distribution of micro-cracked elements (shown in red) following a micro-damage analyses of the polyester 'T' beam at a displacement ratio of 7.5.

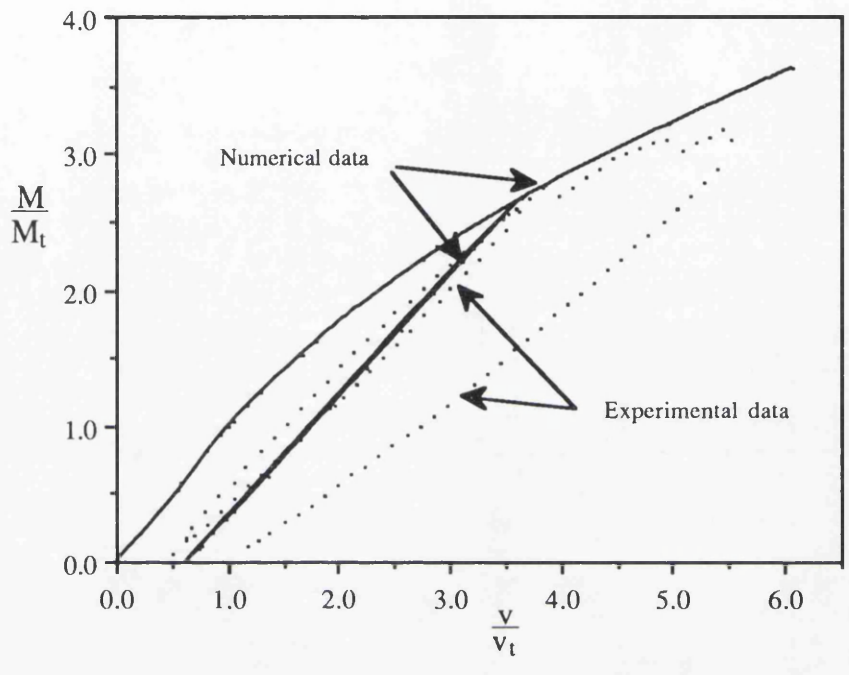
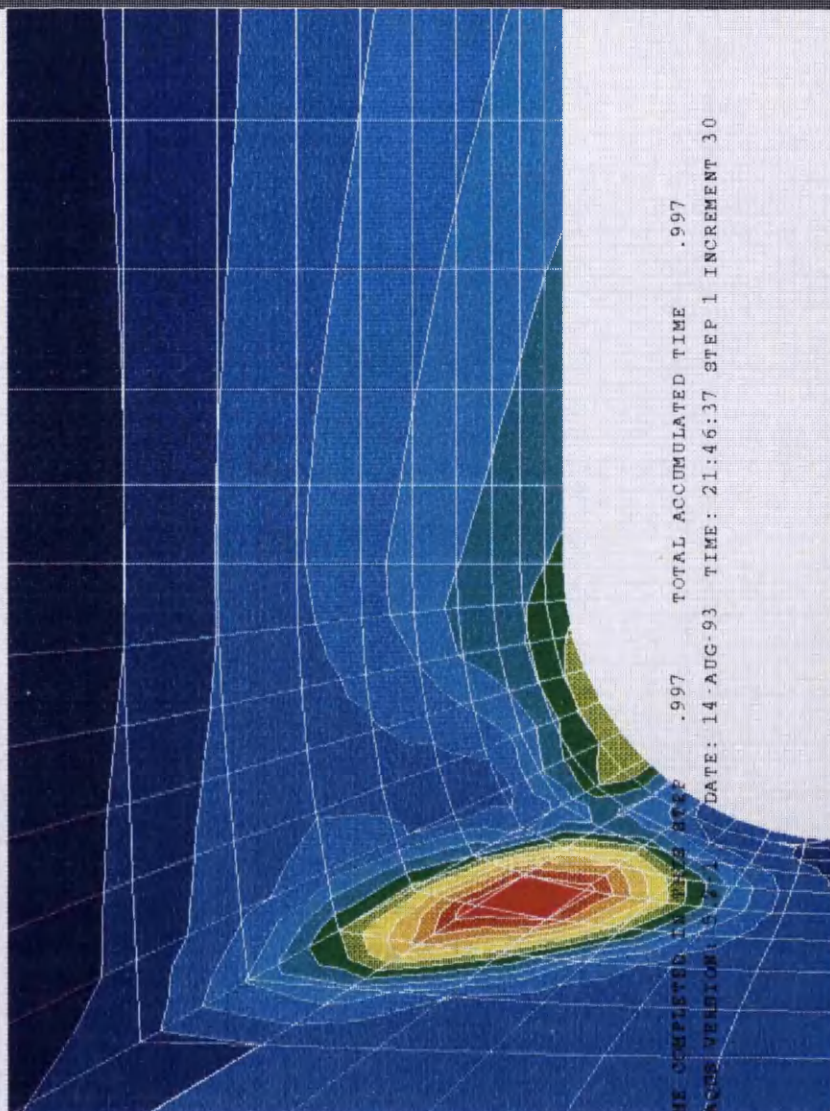
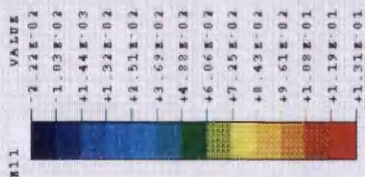


Figure 6.42 Polyester bend bar response compared to numerical data

1

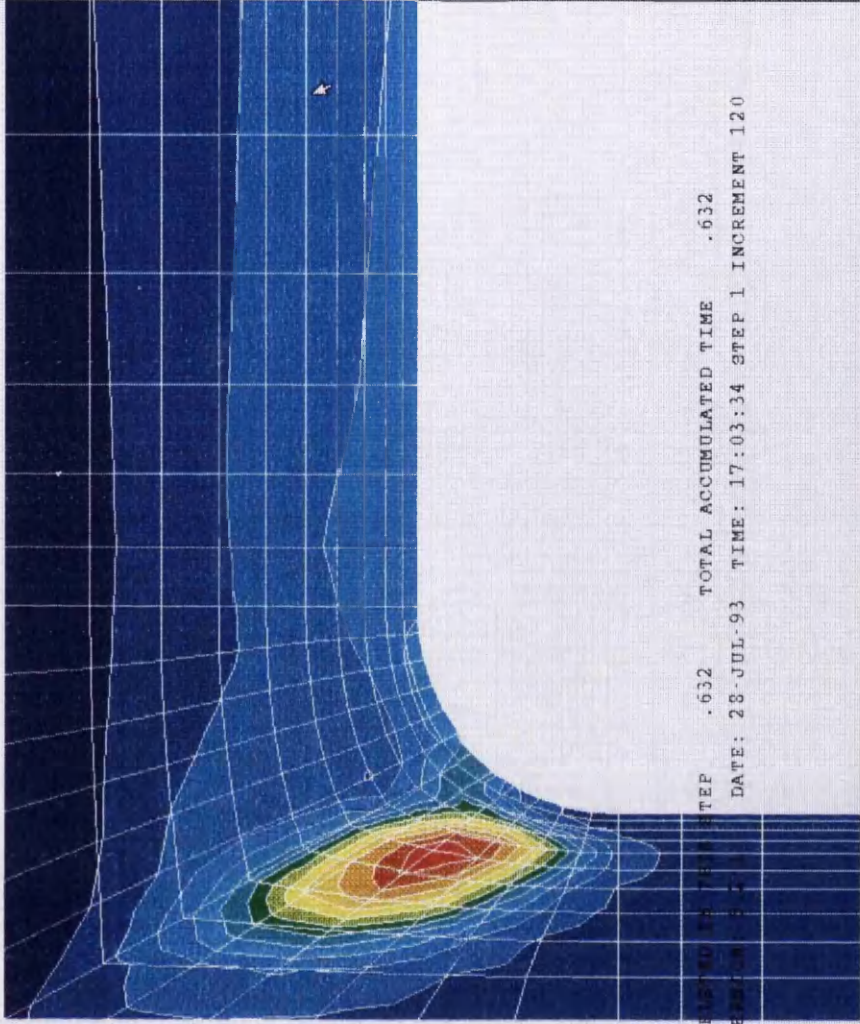


TIME COMPLETED IN THIS STEP .997 TOTAL ACCUMULATED TIME .997
 ABAQUS VERSION 5.7.1 DATE: 14-AUG-93 TIME: 21:46:37 STEP 1 INCREMENT 30



Figure 6.43 The strain distribution of the reinforced analyses of the polyester 'T' beam at a displacement ratio of 7.5.

1



TIME COMPLETED FOR THIS STEP .632 TOTAL ACCUMULATED TIME .632
DATE: 28-JUL-93 TIME: 17:03:34 STEP 1 INCREMENT 120
ABAQUS VERSION 5.2.1

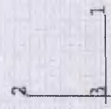


Figure 6.44 The strain distribution of a reinforced analyses of the ceramic 'T' beam at a displacement ratio of 14.9.

1

E11

VALUE
-2.99E-02
-2.03E-02
-1.97E-02
-1.14E-03
+8.45E-03
+1.80E-02
+2.76E-02
+3.72E-02
+4.68E-02
+5.64E-02
+6.60E-02
+7.56E-02
+8.52E-02
+9.48E-02
+1.04E-01
+1.14E-01
+1.24E-01
+1.34E-01
+1.44E-01
+1.54E-01
+1.64E-01
+1.74E-01
+1.84E-01
+1.94E-01
+2.04E-01
+2.14E-01
+2.24E-01
+2.34E-01
+2.44E-01
+2.54E-01
+2.64E-01
+2.74E-01
+2.84E-01
+2.94E-01
+3.04E-01
+3.14E-01
+3.24E-01
+3.34E-01
+3.44E-01
+3.54E-01
+3.64E-01
+3.74E-01
+3.84E-01
+3.94E-01
+4.04E-01
+4.14E-01
+4.24E-01
+4.34E-01
+4.44E-01
+4.54E-01
+4.64E-01
+4.74E-01
+4.84E-01
+4.94E-01
+5.04E-01
+5.14E-01
+5.24E-01
+5.34E-01
+5.44E-01
+5.54E-01
+5.64E-01
+5.74E-01
+5.84E-01
+5.94E-01
+6.04E-01
+6.14E-01
+6.24E-01
+6.34E-01
+6.44E-01
+6.54E-01
+6.64E-01
+6.74E-01
+6.84E-01
+6.94E-01
+7.04E-01
+7.14E-01
+7.24E-01
+7.34E-01
+7.44E-01
+7.54E-01
+7.64E-01
+7.74E-01
+7.84E-01
+7.94E-01
+8.04E-01
+8.14E-01
+8.24E-01
+8.34E-01
+8.44E-01
+8.54E-01
+8.64E-01
+8.74E-01
+8.84E-01
+8.94E-01
+9.04E-01
+9.14E-01
+9.24E-01
+9.34E-01
+9.44E-01
+9.54E-01
+9.64E-01
+9.74E-01
+9.84E-01
+9.94E-01
+1.00E-01

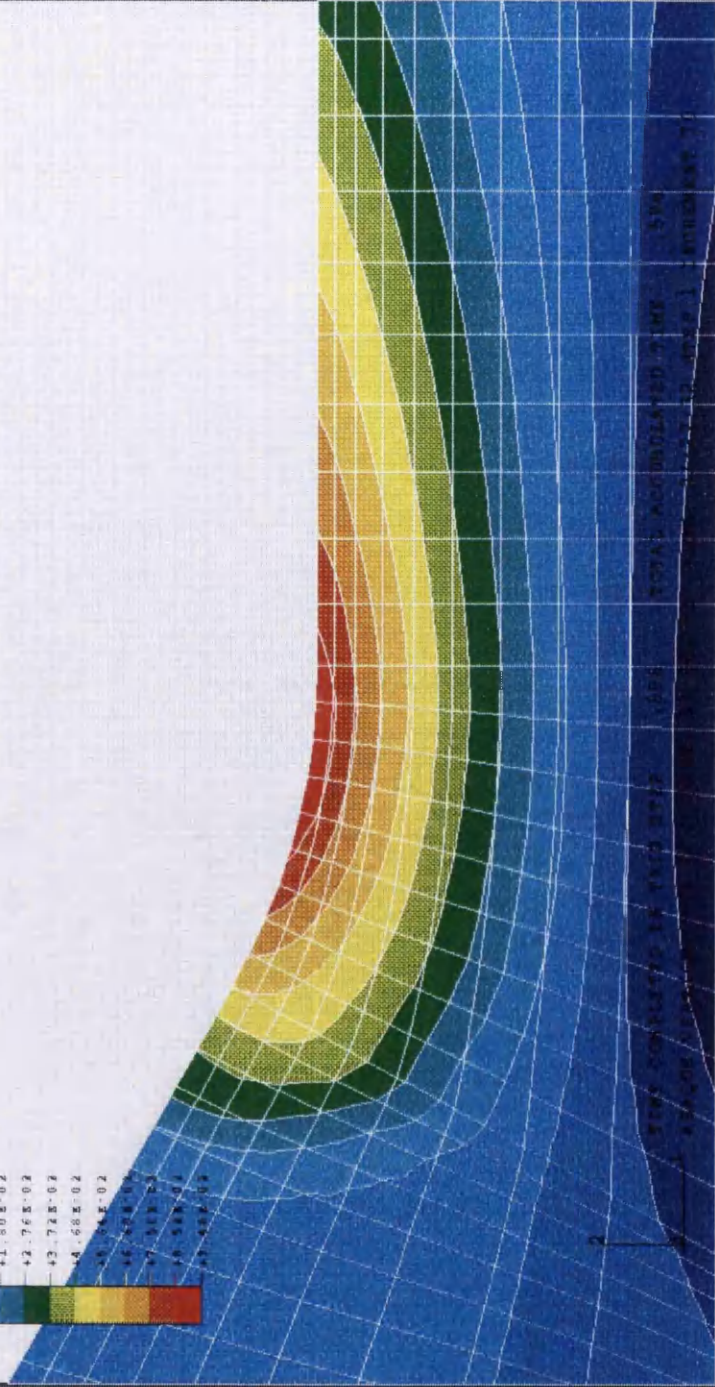
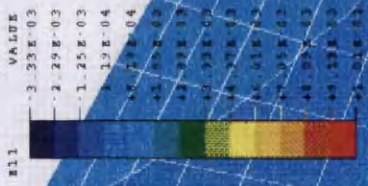


Figure 6.45 The strain distribution of a reinforced analyses of the polyester thickened section at a displacement ratio of 15.0.

1



TIME COMPLETED IN THIS STEP 5.878E-02 TOTAL ACCUMULATED TIME 5.878E-02
DATE: 16-SEP-93 TIME: 18:59:27 STEP 1 INCREMENT 20

Figure 6.46 The strain distribution of a reinforced analyses of the ceramic thickened section at a displacement ratio of 18.4.

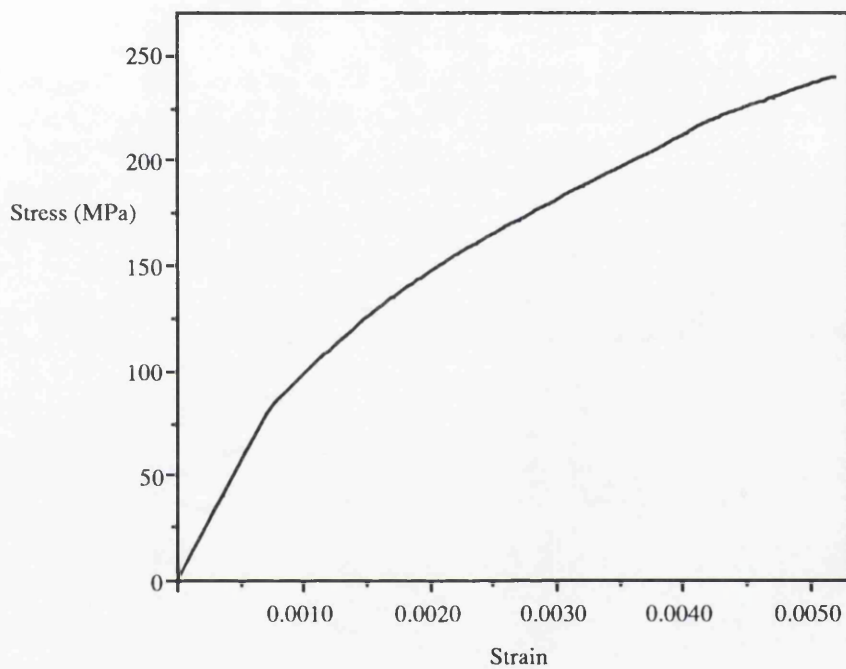


Figure 6.47 Uniaxial tensile response of SiC-Alumina

1

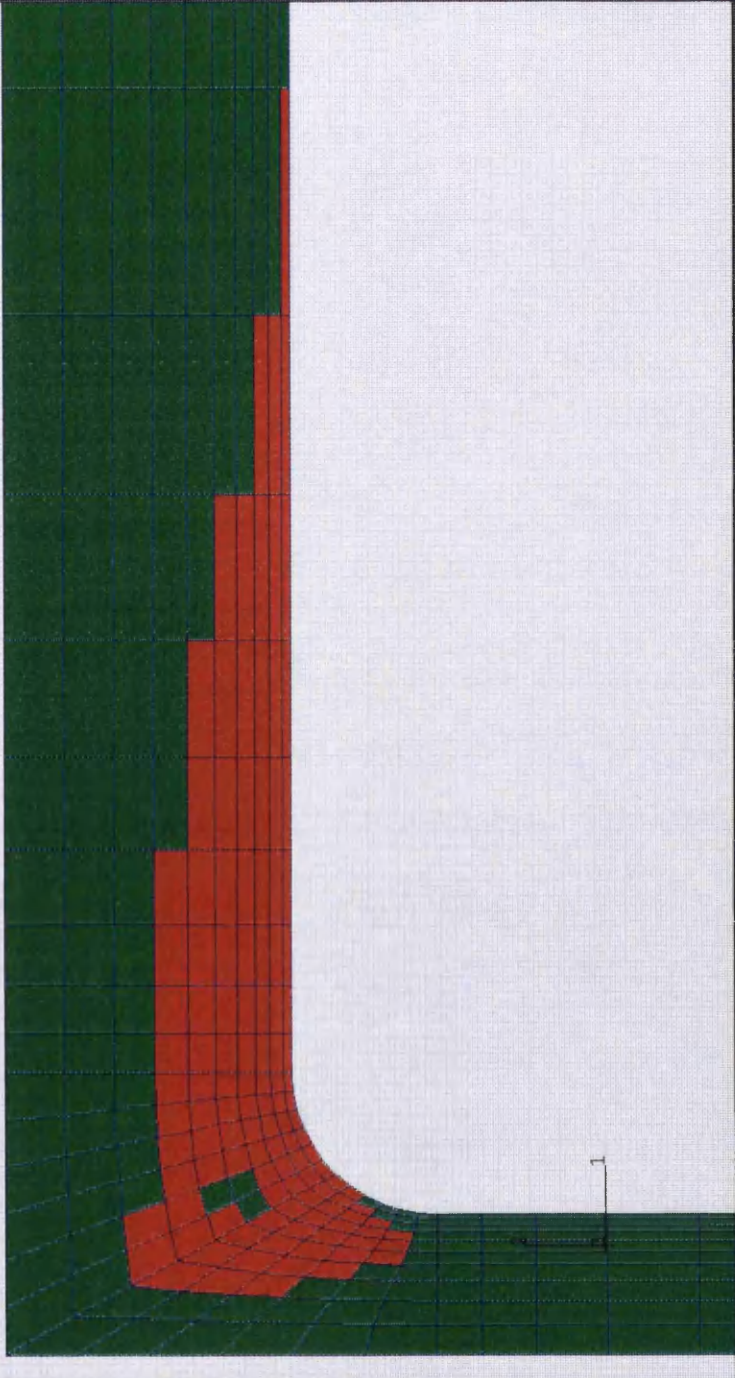


Figure 6.48 The distribution of micro-cracked elements in the reinforced analyses of the polyester 'T' beam at a displacement ratio of 7.5.

7 Design and Analysis of an Exhaust Diffuser Unit

7.1 Introduction

Fundamental thermodynamic considerations indicate that enhanced efficiency and thrust can be achieved by increasing the operating temperatures of air breathing engines. Such advances are limited by the performance, at temperature, of materials used in existing designs. These considerations, plus the need to minimise the weight of engine components has provided a powerful motivation for the use of ceramics. The current study is concerned with the redesign of an exhaust diffuser cone which is a non-critical engine component located in a high temperature environment.

The exhaust diffuser unit of a modern air breathing engine comprises a cone a heat shield and a set of vanes. The purpose of the cone is to ensure an aerodynamic flow of exhaust gas and in combination with the heat shield protect the rear bearing system of the engine, while the vanes are intended to eliminate swirl from the gas stream. Figure 7.1 shows a conventional double skinned design where the cone is actively cooled with air bled from the forward compressor. Here cooling air passes through the cavity between the inner and outer skins. This prevents both the cone and rear bearing assembly from exceeding their material and operating temperature limits as well as providing protection from hot spots generated by the inhomogeneous gas flow. The new design shown schematically in figure 7.2 was intended to eliminate the necessity for the cooling gas, replacing the double skinned metal structure of the exhaust cone with a lighter single skinned cone operating at temperatures of the order 1400K. This approach was intended to lead to an increase in engine operating temperature, an increase in engine efficiency and a reduction in weight.

The design provided the need to establish systematic material selection procedures, based on indices to compare the material's thermal shock resistance and resistance to fracture. Consideration was also given to material availability, ease of manufacture, cost of manufacture and operating temperature limits.

Candidate material data were incorporated into the analysis of thermally induced elastic stresses produced in the exhaust diffuser cone during start up. Subsequently, the behaviour of the cone during shut-down and restart was examined with a damaged based constitutive model which included the effect of thermally induced micro-cracking.

The effect of thermal cycling during engine start up and shut-down to ambient conditions was analysed to determine the extent of damage and residual stresses produced by using the micro-damaged model. To complete the analysis the thermal cycle was repeated.

The thermo-mechanical response may include ratcheting, or shakedown, where the material responds elastically after an initial damage cycle, as described by Jansson et al (1991b). The preferred option is shakedown because damage is limited and component life is prolonged. Concurrently the problem of stabilising the rear bearing temperature in the proposed design was addressed through the calculation of heat transfer rates across the bearing heat shield.

7.2 Material Selection

The design also provides a motive for re-examining and developing systematic material selection procedures for materials subject to thermally induced stresses (σ_{ij}). A dimensional argument shows that for a linear elastic material the stresses are proportional to the temperature gradient, the Young's Modulus (E), coefficient of expansion (α) and a geometric parameter with the dimensions of length $f(x)$.

$$\sigma_{ij} = E \alpha \frac{\partial T}{\partial x} f(x) \quad (7.1)$$

Given that the material fails at a critical tensile stress, σ_f , the highest resistance to steady state thermal gradients is attained by materials with a high value of $\frac{\sigma_f}{E \alpha}$. However when the temperature gradients in the material arise from externally applied heat sources and sinks, the temperature gradient within the material is reduced by a high thermal conductivity, k . This allows the resistance to steady state thermal gradients to be quantified by

the merit parameter:

$$\frac{k \sigma_f}{E \alpha} \quad (7.2)$$

The required properties are thus a high tensile strength and thermal conductivity, coupled with a low Young's modulus and coefficient of thermal expansion. A similar argument can be developed to allow the comparison of material performance, when a defect or flaw is present. In this case failure occurs when a critical stress intensity factor K_c is attained by the flaw. Here it is necessary in the absence of information to assume that all the candidate materials have similar flaws. On this basis the problem of a Griffith crack in a plate subject to a normal temperature gradient has been addressed by Hasselman et al (1986). The stress intensity factor again depends on the thermal expansion coefficient (α) the Young's modulus (E), the flaw size and the fracture toughness (K_c). The temperature gradient to cause unstable crack propagation, can then be established as a function of the material properties and a geometric constant. This leads to a merit parameter for toughness under thermally induced loading:

$$\frac{k K_c}{E \alpha} \quad (7.3)$$

This is essentially similar to the thermal strength merit parameter with strength σ_f now replaced by toughness, K_c . The present argument has been based upon the stress, or stress intensity, attained in steady state conditions. The argument is only slightly modified in the presence of thermal transients when the thermal conductivity is replaced by the thermal diffusivity α_d

$$\alpha_d = \frac{k}{\rho C_p} \quad (7.4)$$

where ρ is the density and C_p is the specific heat

Material selection criteria are based on maps, such as those discussed by Ashby (1982). The requirement is initially for a high value of the thermal-

strength merit parameter $\frac{k\sigma_f}{E\alpha}$. As the design requires the elimination of cooling, this must be combined with high melting points or decomposition temperatures. In terms of the material selection map shown in Figure 7.3 this indicates the ideal high performance material would be found towards the top right hand corner, where there is a combination of high melting point and excellent thermal shock resistance. The temperature requirement favours both monolithic and composite ceramics, such as silicon carbide and silicon nitride. Such materials also allow a major weight saving due to their low density, particularly when they enable a double skin design to be replaced by a single skin component.

In the absence of defects the monolithic ceramics have a particularly desirable combination of properties as demonstrated by in figure 7.3. In comparison the composites have poorer thermal shock resistance as a result of low thermal conductivity, particularly in the through thickness directions of laminated materials. This arises due to significant levels of porosity combined with weakly bonded interfaces which lower the thermal conductivity in this direction. The advantages of monolithic ceramics are largely predicated on the absence of flaws or defects, which is an unlikely and non-conservative scenario. In the presence of flaws the appropriate toughness parameter indicating a resistance to thermal shock in the presence of defects is $\left(\frac{kK_c}{E\alpha}\right)$, as shown in the map illustrated in Figure 7.4.

The advantage of the ceramic composites, such as SiC/SiC and SiC/Al₂O₃ becomes clear. It is however noteworthy that the arguments leading to Figures 7.3 and 7.4 are based on homogeneous materials, and thermally induced stresses occur within composites at a microscopic level due to the differences in elastic stiffness between the fibres and matrix. Such stresses lead to the occurrence of thermally induced micro-cracking in both fabrication and service. Such effects are minimised by composites such as SiC/SiC composites fabricated by chemical vapour infiltration, where the absence of modulus and expansion differentials between matrix and fibres inhibits thermal stress induced micro-cracking

7.3 Thermal Analysis

In the original double skinned design, cooling protects the exhaust diffuser cone and indirectly insulates the rear bearing assembly through an intermediate heat shield. The removal of cooling in the new design thus affects the temperature of the rear bearing system. In this context, a heat transfer analysis was required to determine temperature gradients of the cone and the heat shield. This was also a necessary precursor to determining the levels of thermo-mechanically induced stresses.

Heat transfer from the hot gas to the cone is governed by film coefficients. On the outer surface the hot exhaust gases at temperatures of the order of 1500C flow over the cone leading to high heat transfer rates. In contrast the inner surface of the cone is in contact with stagnant gas leading to convective boundary conditions and low heat transfer rates. The corresponding film coefficients are determined from the Nusselt number which is a function of the mass flow rate and the Reynolds number (Rogers et al 1980, White 1984). The film coefficients were calculated to be 1532W/m²K on the outside and 19W/m²K on the inside of the exhaust cone. These thermal boundary conditions are deliberately pessimistic, in particular the assumption that the exhaust gas on start up is instantaneously at 1500K. However on this basis, the temperature transients at the inner, centre and outer surfaces of the cone are shown in figure 7.5. The steady state temperatures are approached after approximately 140 seconds.

The thermal analysis of the heat shield protecting the rear bearings was set up in a similar manner. In the absence of active cooling the shield would reach a steady state temperature close to that of the cone after longer times. This is an unacceptable operating condition for the bearing. Although the design allows cooling to be removed from the cone, cooling must be ensured at the heat shield to allow the bearing to operate at temperatures less than 750K.

In order to calculate the mass flow rate of cooling air necessary to keep the inner surface of the heat shield below 750K, a heat transfer analysis of the shield wall was considered. At steady state the shield is subject to stagnant air within the exhaust cone at a temperature of 1500K, while the bearing side of the shield is subject to cooling. The problem is to determine the degree of cooling necessary. An iterative method of solution was adopted, by adjusting

the film coefficient, to determine the necessary gas flow to maintain the inner surface of the heat shield below 750K. The mode of heat transfer on the cone side was assumed to be natural convection. From this a heat transfer coefficient was calculated at 11W/m²K (White 1984). Flow over the bearing side of the heat shield was compared to forced flow over a flat plate. The subsequent heat transfer coefficient required to maintain the bearing operating temperature was calculated at 17.5W/m²K corresponding to a cooling gas velocity of 2 m/s.

7.4 Thermo-mechanical Analysis

7.4.1 Thermo-elastic analysis

To determine the thermally induced stresses the thermal analysis was coupled to a linear elastic finite element analysis. Shell and continuum finite element solutions, were used to represent the cone. Mesh generation was provided by Patran (1989) and the problem solved using the Abaqus (1992) finite element code mounted on an IBM 3090. The shell model comprised 48 second order elements and 97 nodes giving a problem with 291 degrees of freedom while the continuum model comprised of 231 elements and 821 nodes giving a problem with 3284 degrees of freedom. The reduction of computational times achieved by using shell elements is balanced for the present analysis by the inability of the shell elements to represent through thickness stress systems. This is an area of particular interest due to possibility of delamination.

Material data for the cone was taken from experiments reported by Hillier (1991) and Heraud et al (1990) for a SiC/SiC laminate. Young's modulus was taken as 200MPa, Poisson's ratio as 0.3 and density as 2500Kg/m³. A preliminary elastic calculation examined the effect of a rigid connection between the ceramic cone and the metal engine. This resulted in catastrophically high stress levels, so that subsequent analysis and design allowed the cone to expand freely.

Figure 7.6 shows the transient of the thermal induced stress on the inner, tensile surface of the cone. Remote from the edges of the cone the in-plane

stress system is essentially restrained bi-axial bending. The through thickness stresses were an order of magnitude lower than the in-plane stresses at all positions. This stress system allows the use of balanced 0/90 laminates, as the delamination stresses are low.

The peak stress occurred after approximately 1.6 seconds when there was the greatest temperature differential across the cone wall as indicated in Figure 7.5. At this time the outer and inner surface cone temperatures were 650K and 350K. Compressive stresses of the order 300MPa were generated on the outer surface while tensile stresses of the order of 140 MPa occurred on the inner surface. In SiC/SiC composites micro-cracking occurs at uniaxial stress levels of the order of 110 MPa (Hillier 1991) and Heraud et al (1990). In compression, yield occurred at levels between 800 and 900MPa. From this it can be seen that tensile microcrack initiation is possible but compressive yield is unlikely.

7.4.2 Damage Mechanics

The tensile toughness and strength of ceramic composites such as SiC/SiC depends upon their ability to tolerate micro-cracks, and fibre pull out, which lead to the enhanced toughness of this class of composite. It is therefore necessary to be able to understand and predict the extent and nature of micro-cracking and other forms of damage. Such problems have been addressed by the development of a damage mechanics approach. Although microcracking occurs in tension, a crushing mode develops at high compressive stress levels. Figure 7.7 shows the idealised uniaxial load/unload response in tension and compression for SiC/SiC composites.

In order to represent micro-cracking in tension and crushing in compression, the material response was idealised in terms of intersecting yield and micro-cracking surfaces following Chen (1975). For tensile deformation the pre-micro-cracking response was initially taken to be isotropic linear elastic. To maintain generality and make contact with the known behaviour of other brittle materials (Chen 1975) a Mohr-Coulomb type micro-cracking criterion involving both the first and second stress invariants has been adopted. Micro-cracking in tension was taken to initiate

according to a Mohr-Coulomb function of the stress deviators (s_{ij}) and the hydrostatic term (σ_{kk}) in the form.

$$f\left(\frac{\sigma_{ij}}{\sigma_t}\right) = \sqrt{\frac{3 s_{ij} s_{ij}}{2\sigma_t^2}} + \alpha \frac{\sigma_{kk}}{\sigma_t} - \beta = 0 \quad (7.5)$$

To describe the tensile deformation α was taken as 0.918, β as 1.918 and the micro-cracking stress (σ_t) as 112 MPa. The essential feature of the post micro-cracking behaviour in tension (Fu et al 1985), is that on unloading the total strains are largely recovered elastically. This corresponds to an elastically damaged material whose incremental elastic moduli are functions of the extent of micro-cracking, giving an overall non-linear response. Before micro-cracking the stiffness C_{ijkl} was taken as the isotropic stiffness of the undamaged material, however damage associated with open micro-cracks and an incrementally elastic damaged stress-strain relation was adopted.

The compressive constitutive relation utilised a compressive yield/flow surface based on classical concepts of Mohr-Coulomb plasticity with usual elastic-plastic strain rate decomposition where the total strain (e) is the sum of the elastic and plastic components of strain (e^{el} and e^{pl}).

$$e = e^{el} + e^{pl} \quad (7.6)$$

The compressive yield surface is described by the

$$f\left(\frac{\sigma_{ij}}{\sigma_c}\right) = \sqrt{\frac{3 s_{ij} s_{ij}}{2\sigma_c^2}} + \gamma \frac{\sigma_{kk}}{\sigma_c} - \lambda = 0 \quad (7.7)$$

For the ceramic composite the material constants γ , λ and σ_c were taken as 0.1218, 1.1218 and 800 MPa respectively. The results of this analysis describe the stress levels and extent of micro-cracking remote from the cone edge. Figure 7.8 shows the maximum principal stress distribution non dimensionalised by the micro-cracking stress ($\frac{\sigma_{11}}{\sigma_t}$) through the cone for linear elastic and micro-cracking model after 1.6 seconds from start up. In this figure the wall thickness is denoted w , and the distance from the hot outer wall is denoted x .

The elastic solution shows a non-linear stress distribution through the cone wall due to the non-linear temperature gradient. The damaged solution largely matches the elastic solution in the compressive part of the field where there is no damage, but diverges in the tensile field due to the occurrence of micro-cracking.

Figure 7.9 shows the modest stress levels that occur close to steady state conditions, while Figure 7.10. illustrates the residual stress distribution after a slow return to ambient temperature.

The level of damage corresponding to these stress distributions can be determined by reference to the tensile micro-cracking and compressive yield functions shown in figure 7.11, where a positive value indicates tensile micro-cracking or compressive yield.

During the thermal cycle, tensile micro-cracking occurred through approximately half of the cone wall thickness. This is indicated by positive values of the micro-cracking function ($f(\frac{\sigma_{ij}}{\sigma_t})$). In this analysis compressive yield was always absent as indicated by negative values of ($f(\frac{\sigma_{ij}}{\sigma_c})$). Subsequent thermal cycles produced identical stress levels to those of initial cycles indicating the occurrence of shakedown. However the presence of microcracks introduces the possibility of thermal degradation of the material properties due to oxidation of the fibre -matrix interface.

7.5 Conclusions

(1) A systematic material selection procedure based on deformation maps has suggested the use of ceramic composites such as SiC/SiC for the exhaust diffuser unit.

(2) Thermo-mechanical stress analysis indicates that the stress system is essentially bi-axial bending, combined with low through thickness stresses. This favours the use of a balanced 0-90 woven fibre architecture in SiC/SiC.

(3) Thermal analysis has shown the viability of an uncooled single skin design for the exhaust cone, provided that the rear bearing assembly is actively cooled.

(4) The ceramic composite is damage tolerant and may micro-crack approximately half way through the cone wall in a thermal cycle. Although repeated cycles lead to shakedown, the possibility of thermal degradation of micro-cracked composites is a cause for concern.

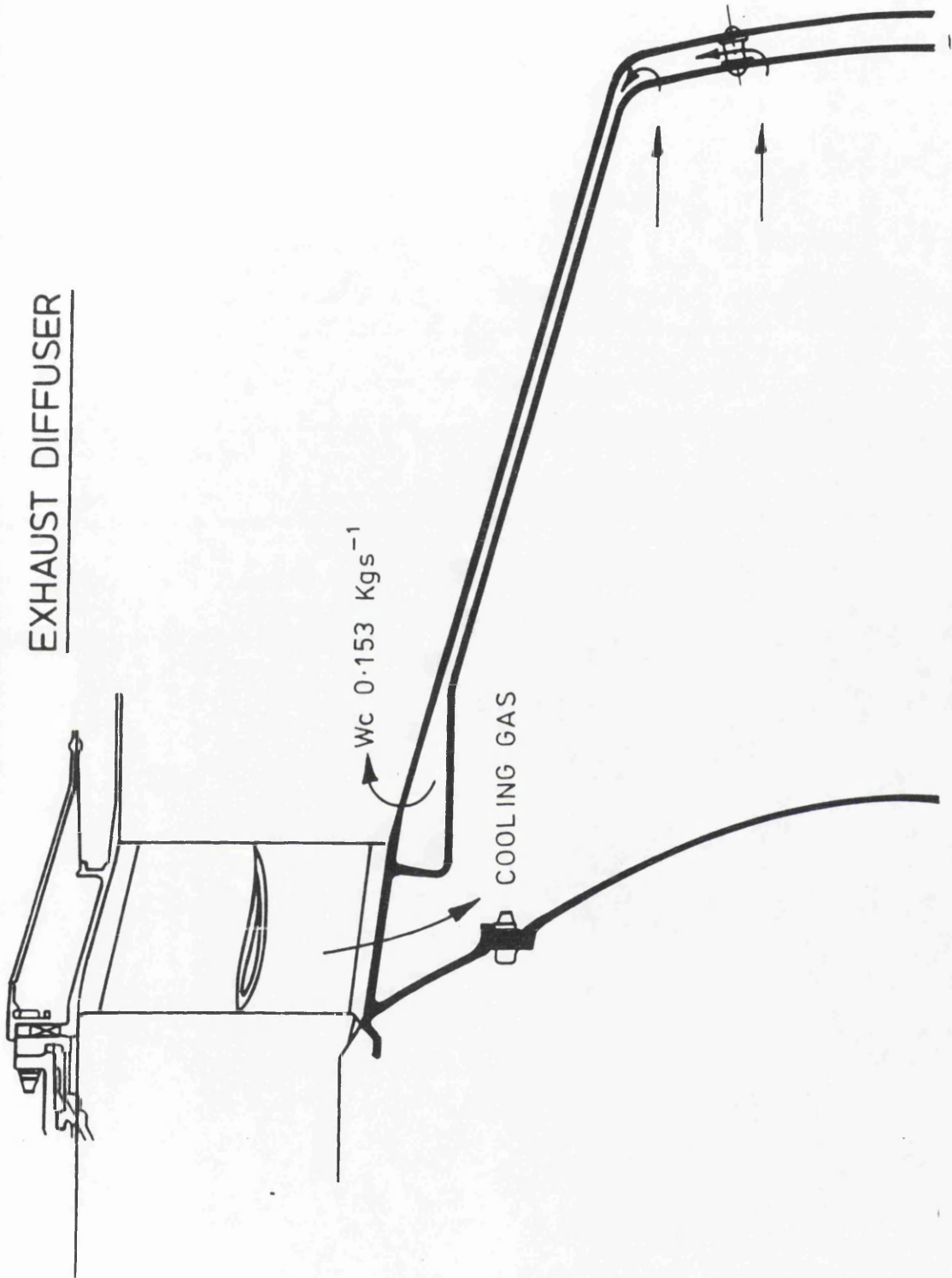


Figure 7.1 Double skinned actively cooled exhaust diffuser cone.

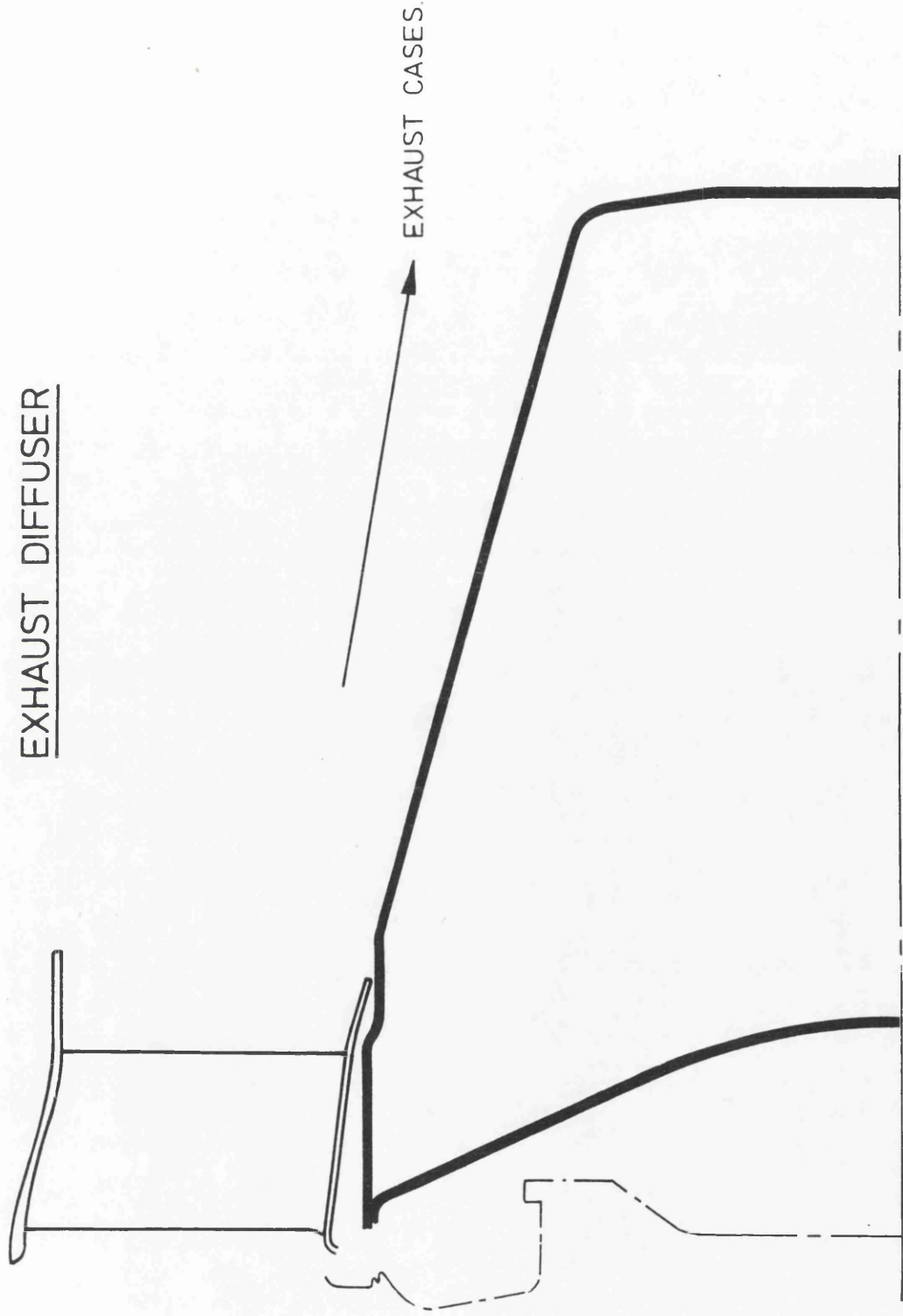


Figure 7.2 Proposed single skinned exhaust diffuser cone with no cooling

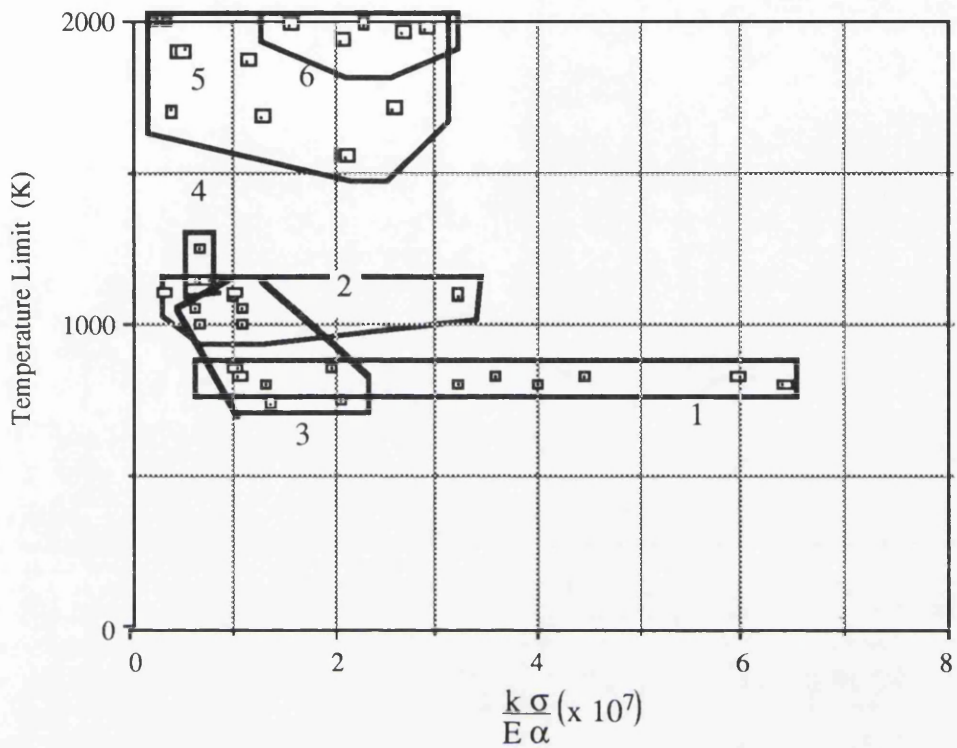


Figure 7.3 Thermal Shock index with the numbered areas indexed as below

1. Aluminium Alloys
2. Carbon
3. Base Metals
4. Super Alloys
5. Ceramic Composites
6. Silicon Carbide and Nitride

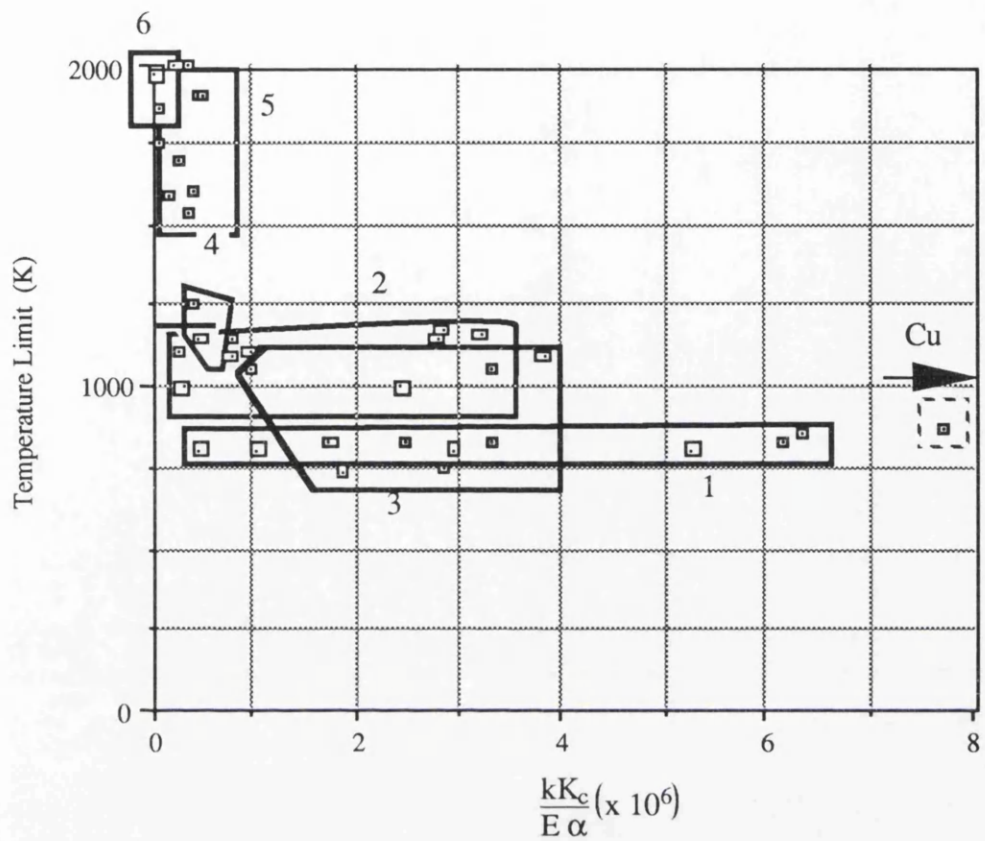


Figure 7.4 Thermal Fracture Index with the numbered areas indexed as below

1. Aluminium Alloys
2. Carbon
3. Base Metals
4. Super Alloys
5. Ceramic Composites
6. Silicon Carbide and Nitride

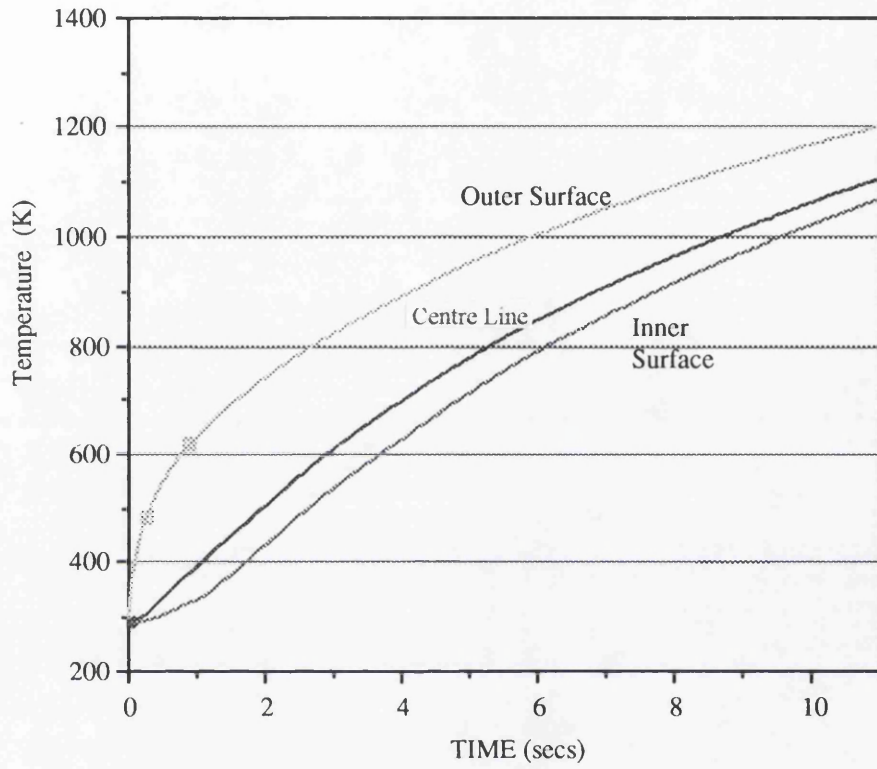


Figure 7.5 Temperature variation through the cone wall with time

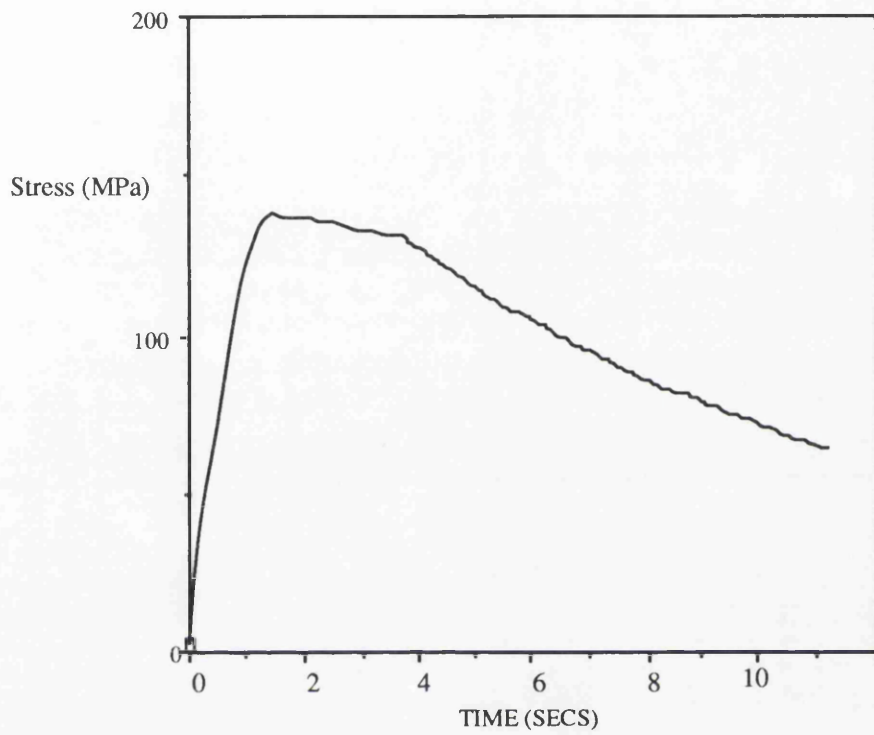


Figure 7.6 Axial stress distribution of cone

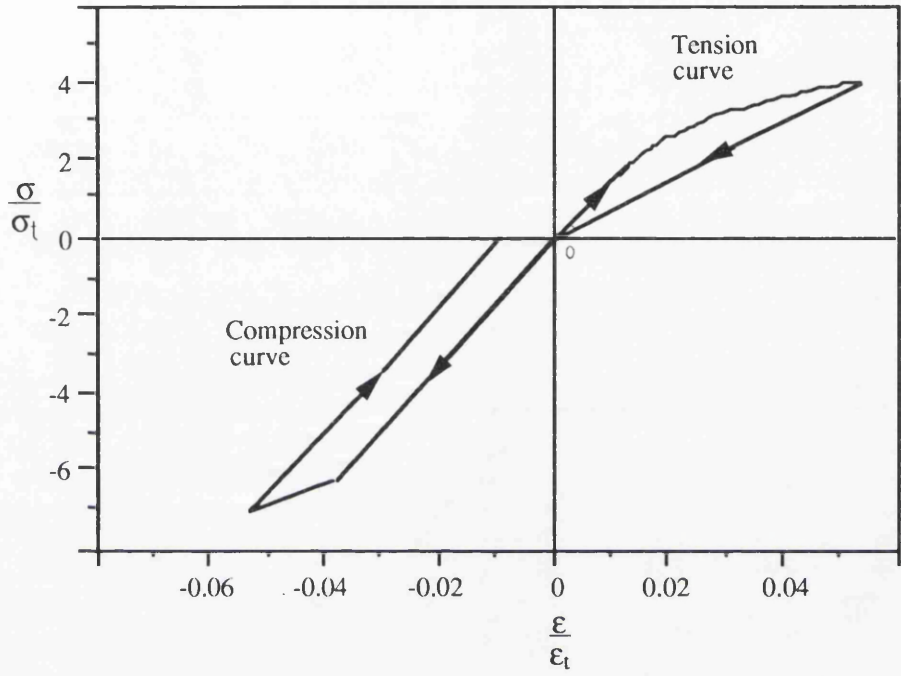


Figure 7.7 Ideal load/unload response of a SiC/SiC Composite

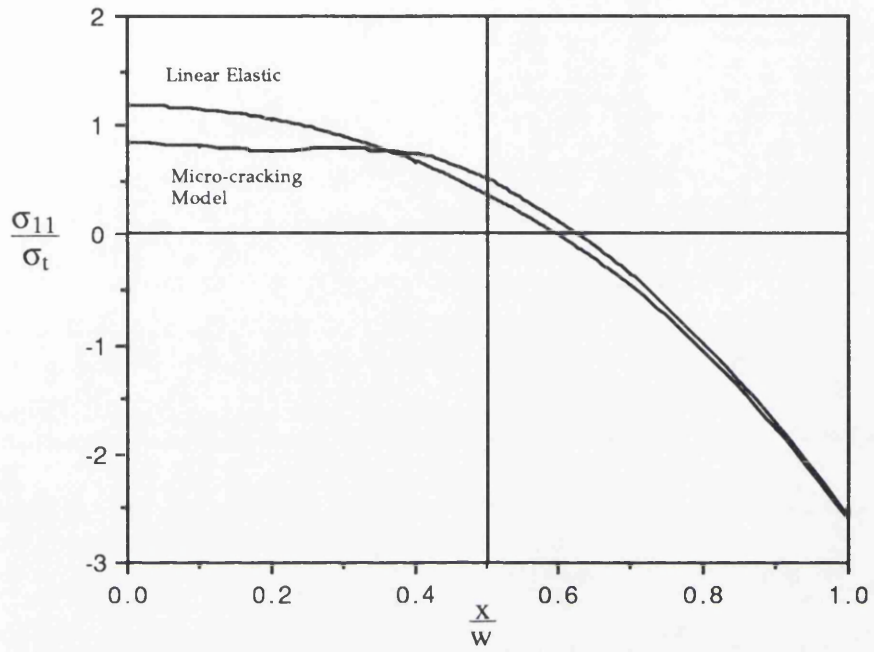


Figure 7.8 The principal stress distribution through the exhaust cone wall at the maximum temperature gradient during start up (t = 1.6sec)

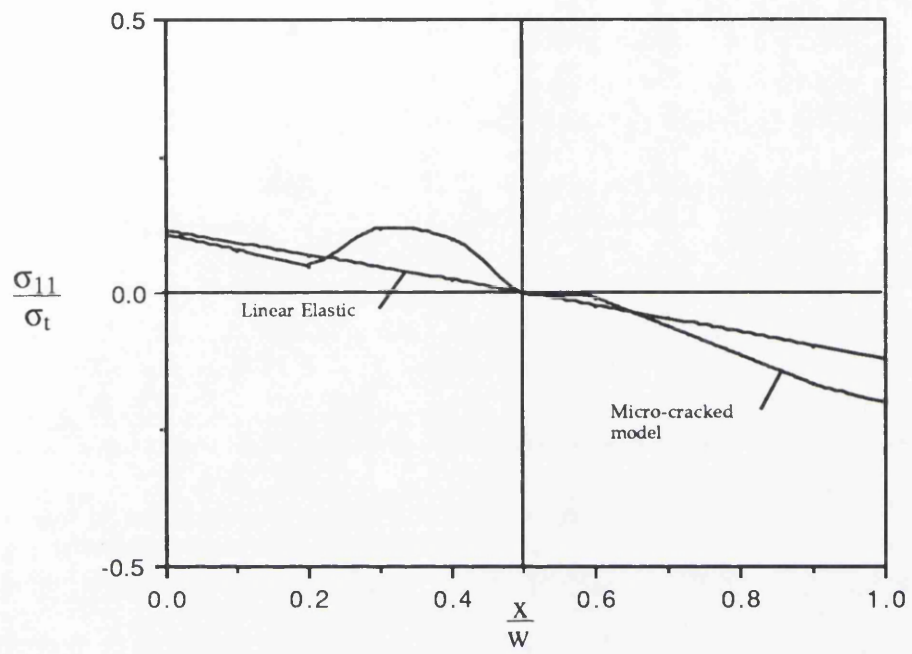


Figure 7.9 The principal stress distribution through the exhaust cone wall during steady state operating conditions, ($t > 140\text{sec}$)

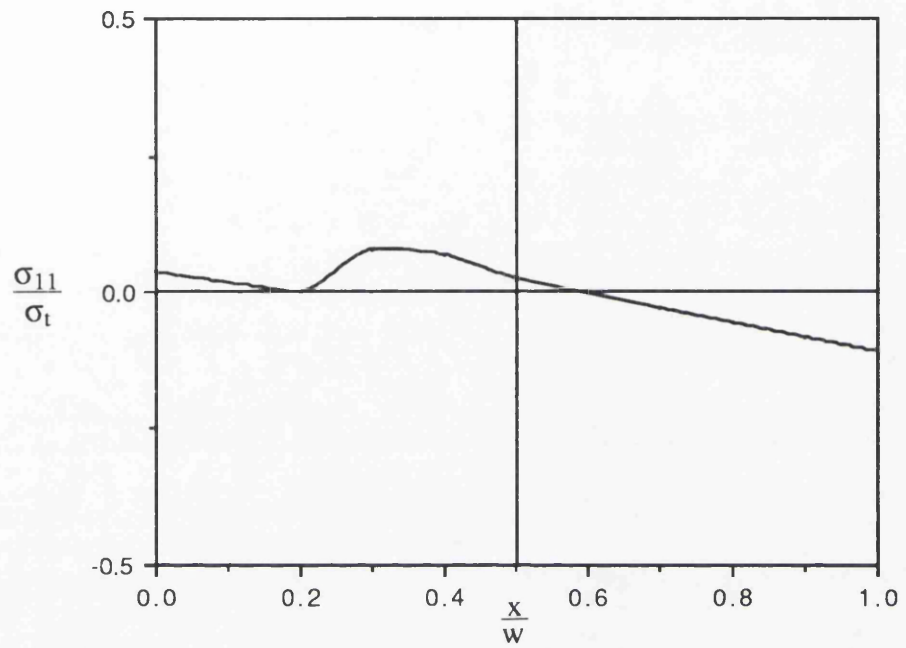


Figure 7.10 Principal stress distribution through the exhaust cone wall at ambient temperature

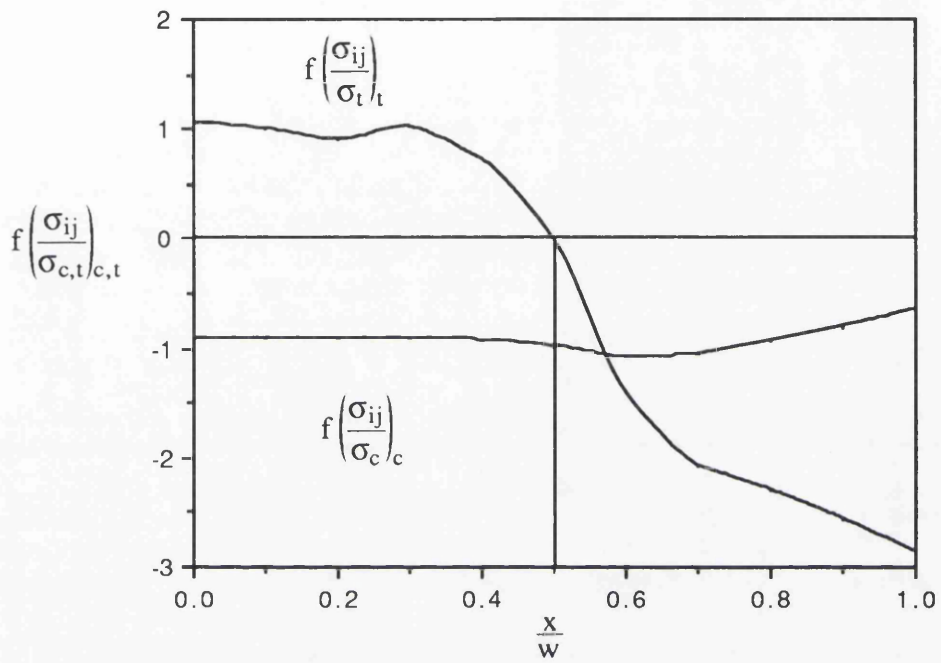


Figure 7.11 Tensile and Compressive yield function values through the cone wall at the maximum temperature gradient during start up

8 Single Dominant Crack Growth in a Ceramic Composite

8.1 Introduction

In a ceramic composite damage may occur in the form of multiple micro-cracking. The general case of composite loading allows the application of damage mechanics when the deformation is through multiple matrix micro-cracking. The Inherent characteristics of composites smear out the effects of a stress concentration at any individual micro-crack. In the sub-element analysis of the ceramic bend bar it was found that a single dominant crack was produced. This provides a case for the application of fracture mechanics.

The work in this report aims to use fracture mechanics to predict crack growth and the extent of matrix micro-cracking in a ceramic composite containing a macro-crack. The analysis adopts the damaged elasticity model and compares it with a linear elastic solution in a mode I loading.

8.2 Background

The purpose of fracture mechanics is to predict the onset and extent of crack propagation of a macro-scopic defect. This requires knowledge of the stress field surrounding the crack, the defect size and the material properties. The behaviour of a crack depends on its ability to resist propagation as measured by its fracture toughness. In a ductile material the available energy is absorbed by extensive tip blunting and plastic deformation. In contrast a brittle material has little energy absorption producing unstable crack growth.

To analyse these modes two fracture mechanics disciplines have been developed. These are Linear Elastic Fracture Mechanics (LEFM) and Elastic Plastic Fracture Mechanics (EPFM). LEFM regards local non-linearities as a minor perturbation of a largely elastic field. This study is primarily concerned with LEFM where the elastic stress field ahead of a crack as described by Williams (1957) is expressed by an asymptotic series:

$$\sigma_{ij} = A_{ij}(\theta) r^{-1/2} + B_{ij}(\theta) + C_{ij}(\theta) r^{1/2} + \dots \quad (8.1)$$

At the crack tip ($r = 0$) the first term is singular while the remaining terms are finite and bounded. The stress field close to the crack tip is dominated by the first term in the series which is usually written in terms of a stress intensity factor K :

$$\sigma_{ij} = \frac{K}{\sqrt{2\pi r}} f_{ij}(\theta) \quad (8.2)$$

Here the stress intensity factor (K) characterises the strength of the crack tip singularity.

Crack deformation can be analysed in terms of three distinct modes. These describe the relative movement of the crack faces. Mode I describes an opening of the crack faces. This is the most common mode in practice where the stress acts perpendicular to the crack faces. The remaining modes, mode II and mode III apply shear stresses across the crack faces causing in plane shear and out of plane shear.

Expanding equation 8.2, the in-plane stresses σ_{ij} at a radius r from the crack tip for a mode I loading as described by Irwin (1957) is:

$$\begin{Bmatrix} \sigma_{11} \\ \sigma_{12} \\ \sigma_{22} \end{Bmatrix} = \frac{K_I}{(2\pi r)^{1/2}} \cos(\theta/2) \begin{Bmatrix} 1 - \sin(\theta/2) \sin(3\theta/2) \\ \sin(\theta/2) \sin(3\theta/2) \\ 1 + \sin(\theta/2) \sin(3\theta/2) \end{Bmatrix} \quad (8.3)$$

The coordinate system used here is described in figure 8.1. The mode I stress intensity factor (K_I) characterises the intensity of the crack tip singularity. The associated cartesian displacements u_1 and u_2 are given by:

$$\begin{Bmatrix} u_1 \\ u_2 \end{Bmatrix} = \frac{K_I}{2G} \left(\frac{r}{2\pi}\right)^{1/2} \begin{Bmatrix} \cos(\theta/2) [\kappa - 1 + 2\sin^2(\theta/2)] \\ \sin(\theta/2) [\kappa + 1 - 2\cos^2(\theta/2)] \end{Bmatrix} \quad (8.4)$$

For plane strain κ is given by $(3 - 4\nu)$ and by $(3 - \nu)/(1 + \nu)$ for generalised plane stress where ν is Poisson's ratio.

In any cracked structure it is possible to define a circular region

surrounding the damaged produced by the stress concentration at the tip. Outwith this area the materials exhibit a linear elastic response. The displacement of this elastic boundary can be calculated using equation 8.2 thus defining a boundary layer formulation of crack tip deformation. Isolating the damaged area reduces computational times and more importantly removes geometry effects with an option for altering the loading using similar calculations for displacement for mode II and mode III configurations.

8.3 Numerical Method

A focused mesh used for the crack tip deformation modelling. Mesh generation was provided by Patran (1991) with solutions provided by Abaqus (1992). The mesh contained 360 four noded plane strain continuum elements consisting of 30 concentric rings of 12 elements. The mesh was refined that the radius of the first ring of elements was approximately 1 millionth of the radius of the outer ring. Symmetry and displacement boundary conditions were calculated using equation 8.2 and imposed on the outer radius of the mesh. An incrementally elastic non-linear constitutive relation was adopted for the analysis. This was compared to an isotropic elastic solution under identical displacements. Figures 8.2 and 8.3 show the hoop stress distribution ahead of and perpendicular to the crack ($\sigma_{\theta\theta}$) normalised by a micro-cracking stress (σ_0) as a function of the crack radius r from the crack tip.

8.4 Discussion

Figure 8.2 compares the linear elastic and the damaged elastic stress field down to non-dimensionalised distances of $25 \frac{r\sigma_0}{J}$ where J is given by $\frac{K^2(1-\nu^2)}{E}$. This is an important result as it predicts that for an incrementally elastic constitutive relation the stress field is dominated by the stress intensity factor K ahead of the crack even though the micro-scopic response is non-linear.

The stress distribution perpendicular to the crack ($\theta = \frac{\pi}{2}$) is shown in figure 8.3. This also demonstrates the dominance of the K term in the stress field. The shape of the damaged zone surrounding the crack was approximately circular with a radius of $90 \frac{r\sigma_0}{J}$. This indicates the stresses perpendicular to the crack are of the order to cause delamination.

8.5 Conclusions

Preliminary calculations indicate that Linear Elastic Fracture Mechanics may be applied to the crack analysis of a material exhibiting an incrementally linear elastic constitutive relation. Such a result would significantly simplify any crack analysis. In addition the stresses normal to the crack at the tip are of the order to cause delamination.

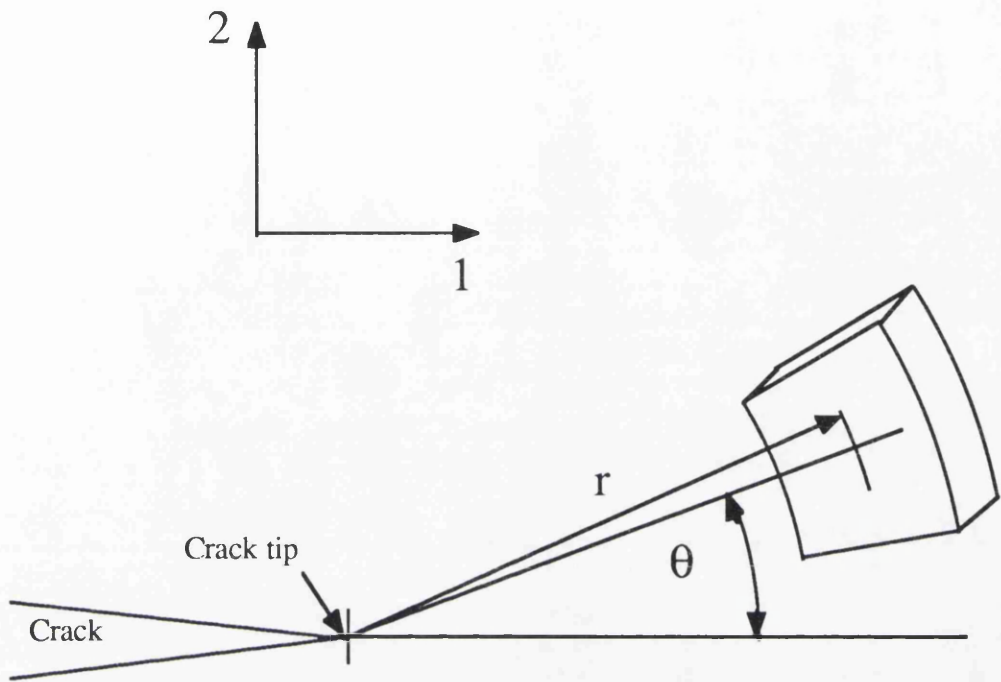


Figure 8.1 Coordinate system for the crack tip analysis

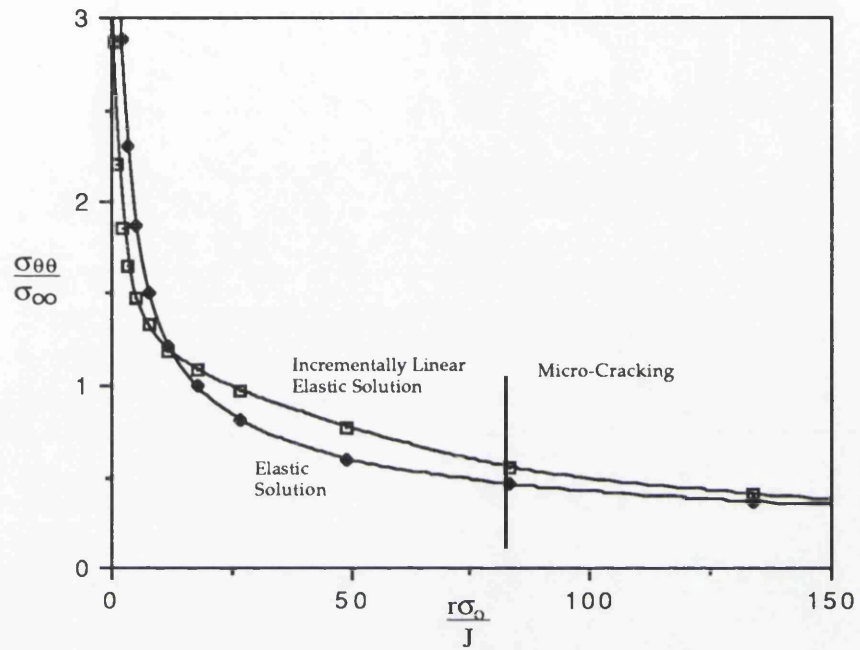


Figure 8.2 Normalised Stress Distribution Ahead of a Crack for an Incrementally Linear Elastic and a Linear Elastic Solution

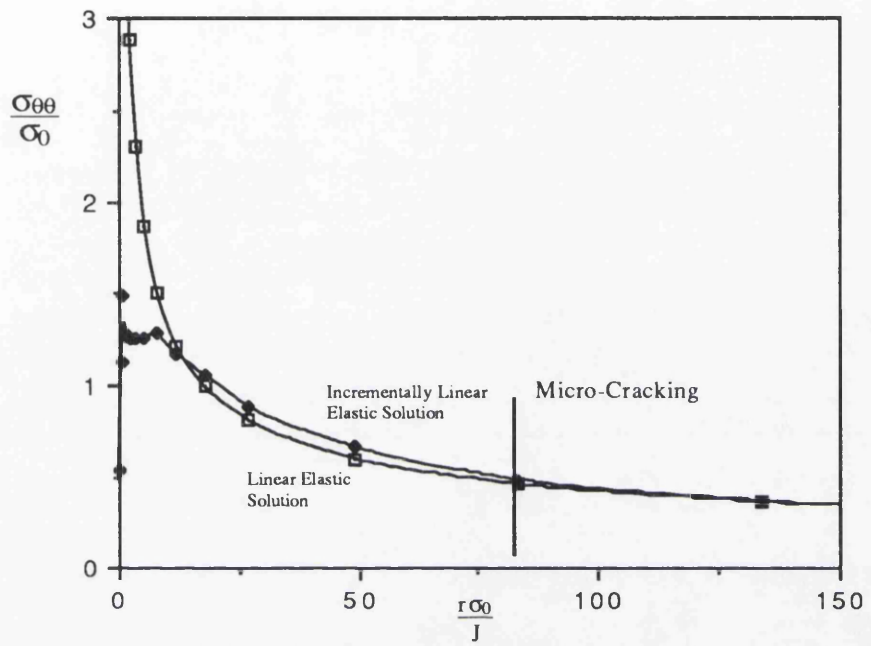


Figure 8.3 Normalised Stress Distribution at 90 Degrees to the Crack Face for an incrementally linear Elastic and a Linear Elastic Constitutive Relation

Conclusions

It has been demonstrated that the polymer system is a valuable tool with which to advance information on the design of ceramic composite components. The system provided an experimental model with which to appreciate the mechanics of deformation of ceramic composites. This understanding allowed the constituent contributions to the overall composite response of both the polymer and ceramic systems to be determined for use in the constitutive modelling.

A micro-damage model was developed which formed an orthogonal array of cracks normal to the direction of maximum principal strain. The micro-damage model was limited to simple stress systems and was used successfully in the exhaust diffuser and crack growth analysis. The exhaust diffuser analysis showed the viability of the uncooled single skin design and favoured 0-90 SiC/SiC as a suitable material for the cone. The crack growth analysis supported claims that the stress field normal to a single dominant crack was of the order to cause delamination in as seen in the ceramic sub-element tests.

The reinforced model was capable of modelling an anisotropic material with hysteresis and residual elongations. The development of a reinforced constitutive model utilised the polymer system through sub-element testing where damage and load responses were predicted successfully. The analysis of ceramic sub-elements also provided encouraging comparisons with experiments and confirmed its use as a constitutive model.

The analysis methods developed have provided a useful tool with which to begin to accumulate information on ceramic composite components. The future of the reinforced constitutive model is promising but requires work on computational stability. However it has demonstrated its use in analysing complex stress systems which is a significant fundamental step towards the computational analysis of ceramic components.

References

Abaqus, Version 5.2, Hibbitt Karlsson and Sorensen Inc, 1992.

Abbe F., Chermant J-L., Fiber-Matrix Bond-Strength Characterization of Silicon Carbide-Silicon Carbide Materials, *Journal of the American Ceramic Society*, 73 [8], pp 2573-2575, 1990.

Ashby M.F, *Materials Selection in Mechanical Design*. Pergamon Press, 1982.

Ashby M F, Blunt F J, Bannister M, Flow Characteristics of Highly Constrained Metal Wires, *Acta Metallurgica*, Vol 37, No 7, pp1847-1857, 1989.

Aveston J., Cooper G.A., Kelly A., Single and Multiple Fracture , In *Properties of Fibre Composites; Conference Proceedings, National Physics Laboratory*, p. 15, IPC Science and Technology Press, Guildford, UK, 1971.

Bao G, McMeeking R M, Fatigue Crack Growth in Fiber-Reinforced Metal Matrix Composites, Submitted to *Acta Metallurgica et Materialia*, April 1993.

Besmann T.M., Lowden R.A., Stinton D.P., Starr T.L., A Method for Rapid Mechanical Vapour Infiltration of Ceramic Composites, *Journal De Physique, Colloque C5, supplement au No 5, Tome 50, Mai*, 1989.

Bischoff E., Ruhle M., Sbaizero O., Evans A.G., Microstructural Studies of the Interfacial Zone of a SiC-Fibre-Reinforced Lithium Aluminum Silicate Glass-Ceramic, *Journal of the American Ceramic Society*, 72 [5], pp 741-745, 1989.

Bittence J.C., Strengthening Composites in Three Directions, *Advanced Materials and Process*, Vol 132 (1), p 45, 1987.

Buresch F.E., Structure Sensitivity K_{IC} and its Dependence on Grain Size Distribution, Density and Micro-crack Interaction, *Fract Mech. Ceram.* 4 835. 1978.

Butler E., Rolls Royce Plc, PO box 31, Moor Lane, Derby, 1991

Butler E., Private Communication, (Patent pending), Rolls Royce Plc, PO Box 31, Moor Lane, Derby, 1992.

Campbell G.H., Ruhle M., Dalgleish B.J., Evans A.G., Whisker Toughening: A Comparison Between Aluminum Oxide and Silicon Nitride Toughened with Silicon Carbide, *Journal of the American Ceramic Society*, 73 [3] pp 521-530, 1990.

Cao H.C., Dalgleish B.J., Deve H.E., Elliott C., Evans A.G., Mehrabian R., Odette G.R., A Test Procedure for Characterizing the Toughening of Brittle Intermetallics by Ductile Reinforcements, *Acta Metallurgica*, Vol 37, No 11, pp 2969-2977, 1989a.

Cao H.C., Evans A.G., An Experimental Study of the Fracture Resistance of Bimaterial Interfaces, *Mechanics of Materials* 7, pp 295-304, 1989b.

Cao H.C., Bischoff E., Sbaizero O., Ruhle M., Evans A.G., Marshall D.B., Brennan J.J., Effects of Interfaces on the Properties of Fiber-Reinforced Ceramics, *Journal of the American Ceramic Society*, 73, [6], 1691-1699, 1990.

Charalambides P.G., McMeeking R.M., Near Tip Mechanics of Stress-Induced Microcracking in Brittle Materials, *Journal of the American Ceramic Society*, 71 [6], pp 465-472, 1988.

Charalambides P.G., Evans A.G., Debonding Properties of Residual Stressed Brittle-Matrix Composites, *Journal of the American Ceramic Society*, 72 [5], pp 746-753, 1989.

Chan K.S., Davidson D.L., Effects of Interfacial Strength on Fatigue Crack Growth in a Fiber-Reinforced Ti-Alloy Composite, *Metallurgica Transactions A*, Vol 21A, pp 1603-1612, 1990.

Chen A.C.T and Chen W.F. ,Constitutive Relations for Concrete, *Trans. ASCE, Journal of Structural Engineering, Mechanics Division*, 101, 465, 1975

Ciba-Geigy Plastics, Duxford, Cambridge, England, 1991

Clough R.B., Biancianiello F.S., Wadley H.N.G., Kattner U.R., Fiber Interface Fracture in Single Crystal Aluminum/SiC Fiber Composites. *Metallurgica Transactions A*, Vol 21A, pp 2747-2757, October 1990.

Clyne T.W., Withers P.J., An Introduction to Metal Matrix Composites, Cambridge Solid State Science Series, Cambridge University Press, 1993

Cooper G.A., Kelly A., Tensile Properties of Fibre-Reinforced Metals: Fracture

Mechanics, J. Mech. Phys. Solids, Vol 15, pp279-297, 1967.

Cox B.N., James M.R., Marshall D.B., Addison Jr R.C., Determination of Residual Stresses in Thin Sheet Titanium Aluminide Composite, Metallurgica Transactions A, vol 21A pp 2701-2707, 1990.

Cox B.N., Marshall D.B., Crack Bridging in the Fatigue of Fibrous Composites, Fatigue Fract. Engng Mater. Struct, Vol 14, No 8 pp847-861, 1991

Daniels H E, The Statistical Theory of the Strength of Bundles of Threads, Proc. R. Soc. A183, p405, 1945.

Dauskardt R.H., Ritchie R.O., Cox,B.N., Fatigue of Advanced Materials: Part I, Advanced Materials & Processes , pp 26-30, Aug 1993.

Enka, Filament Yarn, Diolen Type 174ss High Tenacity Polyester Filament Yarn, Enka UK Ltd, Enkalon house, Regent St, Leicester, Leicestershire, LE1 9AF, 1990

Evans A.G., Burlingame N., Drory M. /kriven W.M., Martensitic Transformations in Zirconia-Particle Size Effects and Toughening, Acta Metallurgica, 29, 447, 1981.

Evans A.G., On The Formation Of A Crack Tip Microcrack Zone, Scripta Metallurgica Vol 10, pp 93-97, 1976

Evans A.G., McMeeking R.M., On the Toughening of Ceramics by Strong Reinforcements. Acta Metallurgica, Vol. 34, No 12, pp 2435-2441, 1986.

Evans A.G., He M.Y., Hutchinson J.W., Journal of the American Ceramic Society, 72 [12] pp 2300-2303, 1989a

Evans A.G., Marshall D.B., The Mechanical behaviour of Ceramic Matrix Composites, Acta Metalurgica, Vol 37. No 10, pp 2567-2583, 1989b.

Evans A G, Zok F W, Cracking and Fatigue in Fiber-Reinforced Metal and Ceramic Composites, Engineers Guide to CompositeMaterials, American Society for Metals, Metals park , Ohio 44073, 1991

Fitzer E., Gadow R., Fibre Reinforced Silicon Carbide, American Ceramic Society, 65 (2), pp 326-335, 1986.

Flinn D.B., Ruhle M., Evans A.G., Toughening in Composites of Al₂O₃

- Reinforced with Al, *Acta Metallurgica*, Vol 37, No 11, pp 3001-3006, 1989.
- Fu Y, Evans A.G., Some Effects of Micro-cracks on the Mechanical Properties of Brittle Solids-I. Stress, Strain Relations, *Acta Metall* Vol 33 No 8 pp 1515-1523, 1985.
- Gerberich W.W., Fracture Mechanics of a Composite with Ductile Fibres, *J. Mech. Phys. Solids*, Vol 19, pp71-87, 1971.
- Gibson R., Private Communication, James Watt Building, University of Glasgow, 1993.
- Gonzalez-Doncel G., Sherby O.D., High Temperature Creep Behaviour of Metal Aluminium-SiC Composites, *Acta Metall. mater.*, Vol 41, No 10, pp 2797-2805, 1993.
- Gurson A.L., Continuum Theory of Ductile Rupture by Void Nucleation and Growth: Part 1 - Yield Criteria and Flow Rules for Porous Ductile Media. *Trans. ASME, Journal Engg. Mater. Tech.*, 99:2 1977.
- Haddad S.H., Hayhurst D.R., Leckie., Design of uniaxially loaded components fabricated from tough fibre reinforced ceramic matrix composites, *Proceedings Royal Society London A*, 434, p383, 1991.
- Hayhurst D.R., Leckie F.A., Evans A.G., Component Design Based Model for the Deformation of Tough Fibre-Reinforced Ceramic Matrix Composites., *Proceedings Royal Society London A*, 434, p 369, 1991.
- Harris B, Habib F A, Cooke R G, Matrix cracking and the mechanical Behaviour of SiC-CAS composites, *Proc. R. Soc Lond. A*, 437, pp109-131, 1992.
- Hasselmann D.P.H, Singh J.P, Criteria for the Thermal Stress Failure of Brittle Structural Ceramics, 1986.
- Heraud. L, Spriet. P, High Toughness C-SiC and SiC-SiC Composites in Heat Engines, SEP, Bordeaux, France. 1990.
- Hillier R, Rolls Royce Plc, PO Box 31, Moor Lane, Derby, 1991.
- Hoagland R.G., Embury J.D., Green D.G., On the Density of Micro-cracks Formed During the Fracture of Ceramics, *Scripta Metallurgica*, 9, 907, 1975.

Hull D, An Introduction to Composite Materials, Cambridge University Press, 1981.

Hutchinson J W, Plastic Stress and Strain Fields at a Crack Tip, J, Mech. Phys. Solids, Vol. 16, pp337-347, 1968.

Hutchinson J.W., Jensen H.M., Models of Fiber Debonding and Pullout in Brittle Composites with Friction, Mechanics of Materials, 9, pp 139-163, 1990.

Hyde A.R., Fibre Reinforced Glass and Ceramic Composites, GEC Journal of Research, Vol. 6, No. 1., 1988.

Irwin G.R., Journal of Applied Mechanics, Vol 24, p 361, 1957*

Ishikawa T., Chou T.W., Stiffness and Strength Behaviour of Woven Fabric Composites, Journal of Materials Science 17, pp3211-3220, 1982.

Jansson S., Deve H.E., Evans A.G., The Anisotropic Mechanical Properties of a Ti Matrix Composite Reinforced with SiC Fibers, Metallurgica Transactions A, Vol 22A, pp 2975-2984, 1991a.

Jansson S., Leckie F.A., Mechanical Behaviour of a Continuous Fibre-Reinforced Aluminium Matrix Composite Subjected to Transverse and Thermal Loading, J. Mech. Phys. Solids Vol 40 No 3 pp 593-612, 1991b.

Jones RM, Mechanics of Composite Materials, Scripta book company, Washington D.C. 1975.

Kaute D.A.W., Shercliff H.R., Ashby M.F., Delamination, Fibre Bridging and Toughness of Ceramic Matrix Composites, Acta Metall mater., Vol 41, No 7, pp 1959-1970, 1993.

Kelly A., Strong Solids, Clarendon Press, Oxford, 1966

Kelly A., Macmillan N.H., Strong Solids, Monographs on the Physics and Chemistry of Materials, Oxford Science Publications, Clarendon Press, Oxford, 1986.

Kimber A.C., Keer J.G., On the Theoretical Average Crack Spacing in Brittle Matrix Composites containing Continuous Aligned Fibres, Journal of Material Science Letters, 1, pp 353-354, 1982.

Kinra V.K., Wren G.G., Rawal S.P., Misra M.S., On the Influence of Ply -

Angle on Damping of ELasticity of a Metal-Matrix Composite., Metallurgica Transactions A, Volume 22A, pp 641-651, March 1991.

Klein A.J., Which Weave to Weave, Advanced Materials and Processes, 2 [3], pp 40-43, 1986.

Ko F.K., Textile Structural Composites, Elsevier, Essex, UK, 1988.

Ko F.K., Preform Fiber Architecture for Ceramic-Matric Composites, Ceramic Bulletin, Vol 68, No. 2, 1989.

Laird II G., Kennedy T.C., Crack Wake Toughening Mechanisms on a Whisker-Reinforced Ceramic. Finite Elements in Analysis and Design 9, pp113-124, 1991.

Llorca J., Elices M., Fracture Resistance of Fibre-Reinforced Ceramic Matrix Composites, Acta Metall. Mater. Vol 38, No 12, pp 2485-2492, 1990.

Lu G., CVD Diamond Films Protect Against Wear and Heat, Advanced Materials & Processes, pp 42-43, Dec, 1993.

McClintock F.A., Argon A.S., Mechanical Behaviour of Materials, Addison-Wesley Publishing Company, Inc, Reading, Massachusetts, USA, 1966.

McColm I.J., Clark N.J., Forming, Shaping and Working of High-Performance Ceramics, Blackie and son Ltd, Glasgow, 1986

McMeeking R.M., Evans A.G., Matrix Fatigue Cracking in Fiber Composites, Mechanics of Materials 9, pp217-227, 1990.

Marshall D.B., Cox B.N., The Mechanics of Matrix Cracking in Brittle-Matrix Fiber Composites, Acta Metallurgica, Vol 33, No 11, pp 2013-2021, 1985.

Marshall D.B., Cox B.N., Tensile Fracture of Brittle Matrix Composites Influence of Fiber Strength, Acta Metallurgica, Vol 35, No 11, pp 2607-2619, 1987.

Marshall D.B., Analysis of Fiber Debonding and Sliding Experiments in Brittle Matrix Composites, Acta Metall. Mater., Vol 40, No 3, pp427-441, 1992.

Matthews F.L., Rawlings R.D., Composite Materials: Engineering and Science, Printed by The Alden Press, Oxford, 1994.

Merril G., Rolls Royce Plc, PO Box 31, Moor Lane, Derby, 1992.

Meyer D.W., Cooper R.F., Plesha M.E., High Temperature Creep and the Interfacial Mechanical Response of a Ceramic Matrix Composite, *Acta Metall. mater.*, Vol 41, No 11, pp 3157-3170, 1993.

Morrell R., *Handbook of Properties of Technical and Engineering Ceramics*, Part 1, HMSO, 1985.

Morris W.L., Cox B N, James M.R., Localized Surface Deformation of an Al 4% Cu Alloy in Fatigue, *Acta Metall*, Vol 37, No 2, pp 457-464, 1989.

Naslain R., *Fibrous Ceramic-Ceramic Composite Materials Processing and Properties*, *Journal De Physique, Colloque C1*, supplement au No 2, Tome 47, 1986.

Naslain R., Langlais F., Fedou R., The CVI-Processing of Ceramic Matrix Composites, *Journal De Physique, Colloque C5*, supplement au No 5, Tome 50, mai, 1989.

Newkirk M.S., Leshner H.D., White D.R., Kennedy C.R., Urquhart A.W., Claar T.D., Preparation of Lanxide Ceramic Matrix Composites: Matrix Formation by Directed Oxidation of Molten Metals, Presented at the 11th Annual Conf. on Composites and Advanced Ceramic Materials, Cocoa Beach, Florida, 1987.

Ochiai S., Osamura K., Influences of Matrix Ductility, Interfacial Bonding Strength and Fibre Volume Fraction on Tensile Strength of Unidirectional Metal Matrix Composite, *Metalurgica Transactions A*, Volume 21A, pp 971-977, 1990.

Patran Release 2.4, PDA Engineering, Sept 1989.

Pergan, VBR Polyester resin, Spectra Brands PLC, Treloggan Industrial Est, Treloggan Rd, Newquay, Cornwall, TR7 2SX, 1991.

Reed J.S., *Introduction to the Principles of Ceramic Processing*, John Wiley & Son, Inc, 1987.

Rogers and Mayhew *Thermodynamics and Transport Properties of Fluids*, Third Edition, Basil Blackwell, 1980.

Ronald T.M.F., NASP Lanches New Materials, Advanced Materials & Processes, pp 24-27, Sept, 1993.

Rosen B W, Thermo-Mechanical Properties of Fibrous Composites, Proc. R. Soc A319, 79, 1970.

Rossignol J.Y., Langlais F., Naslain R., A Tentative Modelization of Titanium Carbide CVD within the Pore Network of Two-Dimensional Carbon Carbon Composite Preforms, Proc 9th Int. Conf. CVD, The Electrochem. Soc., Pennington, pp. 596-614 1984.

Rossignol J.Y., Quenisse J.M., Naislain R., Mechanical Behaviour of 2D C-C/TiC Composites made from a 2D C-C Preform Densified with TiC by CVI, Composites, Vol 18, No 2, pp 135-144, 1987.

Ruhle M., Evans A.G., High Toughness Ceramics and Ceramic Composites, Progress in Materials Science, Vol 33, pp85-167, 1989

Ruhle M., Intercrystalline Cavitation and embrittlement in copper materials, Metalurgica et al, Vol 30, No 5, pp 416-474, 1976

Sammis C.G., Ashby M.F., The Failure of Brittle Porous Solids under Compressive Stress States, Acta Metalurgica, Vol 34, pp511-526, 1986

Schiroky G.H., Urquhart A.W., Sorenson B.W., Ceramic Composites fro Gas Turbine Engines Viaa New Process., Presented at the Gas Turbine and Aeroengine Congress and Exposition, 1989.

Sigl L.S., Fischmeister H.F., On the Fracture Toughness of Cemented Carbides, Acta Metalurgica, Vol 36, No 4, pp 887-897, 1988

Spectra, Polyester hardener Spectra Brands PLC, Treloggan Industrial Est, Treloggan Rd, Newquay, Cornwall, TR7 2SX, 1991.

Thouless M.D., Evans A.G., Effects of Pull-Out on the Mechanical Properties of Ceramic-Matrix Composites, Acta Metallurgica, Vol 36, No 3, pp 517-522, 1988.

Thouless M.D., Sbaizero O., Sigl L.S., Evans A.G., Effect of Interface Mechanical Properties on Pullout in a SiC-Fiber-Reinforced Lithium Aluminum Silicate Glass-ceramic, Journal of the american Ceramic Society, 72 [4], pp 525-532, 1989.

Van Den Breckal C.H.J., Fonville R.M.M., Van Der Straten P.J.M., Verspui G., Proc. 8th Int. Conf. CVD-Paris, The Electrochem. Soc., Pennington, pp 142-156, 1981

White F.M, Heat Transfer, Addison and Wesley Publishing Company Inc 1984.

Williams M.L., On the Stress Distribution at the Base of a Stationary Crack, Journal of Applied Mechanics, Vol 24, p 109-114, 1957

Xia Z.C., Carr R.R., Hutchinson J.W., Transverse Cracking in Fiber Reinforced Brittle Matrix, Cross-Ply Laminates, Acta Metall. mater., Vol 41, No 8, pp 2365-2376, 1993.

Yang J.M., Ma C.L., Chou T.W., Fiber Inclination Model of Three-Dimensional Structural Composites, Journal of Composite Materials, Vol. 20, Sept, 1986.

Zok F., Jansson S., Evans A.G., Nardone V., The Mechanical Behaviour of a Hybrid Metal Matrix Composite, Metallurgica Transactions A, Vol 22A, pp 2107-2117, September 1991.

APPENDIX I

The problem documented here is the plastic collapse of a square concrete slab supported in the vertical direction at the corners. The slab is reinforced in two directions, at 75 percent of its depth. The method of reinforcing is identical to that used in the reinforcing model as described in Chapter 5. One quarter of the slab is modelled with symmetry using eight node shell elements, with reinforcing represented by the REBAR statement.

*HEADING

CORNER SUPPORTED TWO-WAY SLAB TESTED BY MCNEICE

*NODE

1,0.,0.

7,18.,0.

61,0.,18.

67,18.,18.

*NGEN,NSET = Y-SYM

1,7

*NGEN,NSET = X-SYM

1,61,10

*NGEN,NSET = LX2

61,67

*NGEN,NSET = LY2

7,67,10

*NGEN

11,17,2

21,27

31,37,2

41,47

51,57,2

*ELEMENT,TYPE = S8R,ELSET = SLAB

1,1,3,23,21,2,13,22,11

*ELGEN,ELSET = SLAB
1,3,2,1
1,3,20,3
2,3,20,3
3,3,20,3
*SHELL SECTION
1.75,9
*REBAR,ELEMENT = SHELL,GEOMETRY = ISOPARAMETRIC
SLAB,.014875,1.,-.435,4
SLAB,.014875,1.,-.435,1
*MATERIAL,ELSET = SLAB
*ELASTIC
4.15E6,.15
*CONCRETE
3000.,0.
5500.,.0015
*FAILURE-YIELD RATIOS
1.16,.0836,1.16,.0836
*TENSION STIFFENING
0.,8.E-4
*MATERIAL,ELSET = SLAB,REBAR
*ELASTIC
29.E6
*PLASTIC
50.E3
*BOUNDARY
Y-SYM,YSYMM
X-SYM,XSYMM
67,3
*STEP,INC = 30,SUBMAX
*STATIC,PTOL = 50.,RIKS
.05,1.,.01,.1
*CLOAD
1,3,-5000.
*EL PRINT,FREQ =10
*END STEP